

Ruben Heimböckel

High Surface Area Nanoporous Carbons for Energy-Related Applications

Dissertation

Zur Erlangung des Grades

Doktor der Naturwissenschaften (Dr. rer. nat.)

an der Fakultät für Mathematik, Informatik und Naturwissenschaften

im Fachbereich Chemie der Universität Hamburg

Oktober 2019

Die vorliegende Arbeit wurde im Zeitraum von April 2014 bis Oktober 2019 in der Arbeitsgruppe von Prof. Dr. Michael Fröba am Institut für Anorganische und Angewandte Chemie im Fachbereich Chemie der Universität Hamburg angefertigt.

- | | |
|--------------|-----------------------------|
| 1. Gutachter | Prof. Dr. Michael Fröba |
| 2. Gutachter | J.Prof. Dr. Simone Mascotto |

Tag der Disputation: 08.11.2019

Eidesstattliche Erklärung

Hiermit versichere ich an Eides statt, die vorliegende Dissertation selbst verfasst und keine anderen als die angegebenen Hilfsmittel benutzt zu haben. Die eingereichte schriftliche Fassung entspricht der auf dem elektronischen Speichermedium. Ich versichere, dass diese Dissertation nicht in einem früheren Promotionsverfahren eingereicht wurde.

Hamburg den 07.10.2019

Ruben Heimböckel

Danksagung

Ich möchte mich zunächst einmal bei Herrn Prof. Dr. Michael Fröba für die Aufnahme in den Arbeitskreis und die Möglichkeit zur Promotion bedanken. Außerdem bedanke ich mich für das mir entgegengebrachte Vertrauen und die Freiheit zur Bearbeitung meines Themenfeldes.

Herrn JProf. Dr. Simone Mascotto danke ich für die Übernahme des Zweitgutachtens. Herrn Prof. Dr. Volker Abetz und Herrn PD Dr. Christoph Wutz danke ich für die Bereitschaft zur Teilnahme der Prüfungskommission meiner Disputation.

Ich möchte mich sehr herzlich bei Dr. Frank Hoffmann dafür bedanken, dass er meine Arbeit Korrektur gelesen hat und für die Betreuung in der Batterie/Kohlenstoff/Wasserstoff/Hydrid/Sonstiges-Untergruppe.

Ich danke meinen ehemaligen Laborkollegen Dr. Boris Ufer und Dr. Michael Sartor für die gute Aufnahme als Neuling ins Labor.

Ein großer Dank gilt Dawid Sturm. Du warst der perfekte Laborbuddy und wenn es mal schlecht lief, haben wir unsere legendären Playlists ausgepackt. Es lief dann vielleicht nicht immer im Labor besser, aber wir konnten dabei lachen.

Ganz besonders möchte ich mich bei meinen Bürokollegen Dr. Sebastian Kraas, Dr. Michael Dreifke, Timo Stein und Natascha Speil bedanken. Wir haben „213“ zu einer echten Marke gemacht die für maximale Konzentration und Arbeitsleistung steht. Natürlich haben wir uns auch ab und zu in lockerer Atmosphäre unterhalten können. Das werde ich sehr vermissen.

Ich bedanke mich bei meinen Praktikanten und Hiwis Inga, Leon und Roman für deren Unterstützung im Labor.

Ohne die zahlreichen Messungen die an meinen Proben durchgeführt worden sind, hätte ich meine Arbeit nicht durchführen können. Daher bedanke ich mich ganz herzlich bei Sandra König, Isabelle Nevoigt, Uta Sazama, Cornelia Bretzke und Renate Walter. Außerdem möchte ich mich bei deren Stellvertretern bedanken, die das während ihrer Promotionszeit gemacht haben.

Ich möchte mich bei allen aktuellen und ehemaligen Mitgliedern des AK Fröba bedanken. Ich wurde sehr gut aufgenommen und es herrschte bei uns immer eine enorm hohe Hilfsbereitschaft und freundliche Unterstützung.

Ich hatte das Glück, während meiner Studienzeit viele nette Menschen kennenzulernen und neue Freunde zu finden. Ohne euch hätte ich das Studium so nicht geschafft und es tat gut, auch an der Uni mal über andere Dinge zu reden.

Brad, thank you for reading.

Meine Familie und besonders meine Eltern haben mich von der ersten Sekunde an unterstützt und immer an mich geglaubt. Ohne euer Vertrauen hätte ich es wahrscheinlich nicht soweit geschafft. Ich bin euch für immer dankbar.

Die beiden wichtigsten Menschen in meinem Leben sind meine eigene kleine Familie. Larissa, danke dafür, dass du mich seit Jahren intensiver als irgendein anderer Mensch liebevoll unterstützt hast. Das hat mir immer Kraft und Mut gegeben den Weg weiter zu gehen. Hugo, danke, dass du da bist.

Table of contents

1	Introduction.....	1
1.1	Porosity	2
1.2	Carbon	4
1.3	Porous carbons.....	6
1.3.1	Carbon materials via direct carbonization.....	7
1.3.2	Carbon precursor	8
1.3.3	Ordered mesoporous carbons	8
1.3.4	Phenolic resins	10
1.3.5	Friedel-Crafts cross-linking	12
1.3.6	Activation of carbons	14
1.3.7	KOH activation of novolac based carbons	18
1.4	Capacitors.....	19
1.4.1	Electric double layer capacitors.....	20
1.4.2	Electrode materials for electric double layer capacitors.....	26
1.4.3	Role of surface area on the capacitance of EDLCs.....	33
1.4.4	Role of the pore size on the capacitance of EDLCs.....	34
1.5	Hydrogen storage of porous carbons	39
1.5.1	Hydrogen storage of porous materials	42
2	Analytical methods	44
2.1	Gas physisorption.....	44
2.2	Powder X-ray diffraction (p-XRD).....	56
2.3	Raman spectroscopy	57
2.4	Electrochemical measurements.....	58
3	Motivation	65
4	Results and Discussion	67
4.1	Synthesis and characterization of formaldehyde resin based carbons and their investigation as energy storage materials	68
4.1.1	Synthesis of PF-resin based carbons.....	69
4.1.2	Influence of the activation reactant	70
4.1.3	Influence of the semi-carbonization temperature	98
4.1.4	Influence of the activation temperature	122
4.1.5	Combining low activation reactant and semi-carbonization.....	141

4.1.6	Influence of activation and semi-carbonization temperature	159
4.1.7	Influence of the carbon precursor	177
4.1.8	Cross-linking of formaldehyde resins via Friedel-Crafts alkylation	194
4.2	Influence of the pore size on capacitance	215
4.2.1	Mining the data.....	215
4.2.2	Simulation of capacitance using EDLC models	221
4.2.3	Influence of pore size on capacitance retention	248
4.2.4	The perfect pore size for supercapacitors?	258
4.3	Influence of pore size on hydrogen uptake capacity	263
4.3.1	Mining the data.....	263
4.3.2	Simulation of hydrogen uptake capacities	266
4.3.3	Applicability of the new model	272
5	Summary	276
6	Zusammenfassung	281
7	Experimental Section	287
7.1	Material syntheses	287
7.1.1	Synthesis of phenol formaldehyde-resins	287
7.1.2	Synthesis of PF resins based carbons	287
7.1.3	Synthesis of phenol resorcinol formaldehyde resins	287
7.1.4	Synthesis of PRF resin based carbons.....	288
7.1.5	Synthesis of FC-cross-linked PRF resins	288
7.1.6	Synthesis of FC cross-linked PRF resin based carbons.....	288
7.2	Characterization methods.....	289
7.2.1	Physisorption	289
7.2.2	Scanning electron microscopy	289
7.2.3	Powder X-Ray diffraction	289
7.2.4	Raman spectroscopy	290
7.2.5	Thermal analysis	290
7.2.6	Cell preparation and electrochemical measurements	290
8	Bibliography	293
9	Appendix	308
9.1	Further information to the chapter “results and discussion”	308
9.2	Safety.....	322

9.3	Publications	324
-----	--------------------	-----

List of Abbreviations

ACN	acetonitrile
BET	Specific Surface area according to Brunauer, Emmet und Teller
BJH	Barrett, Joyner and Halenda
CDC	charge/discharge
CMK	Carbon Mesostuctured by Korea Advanced Institute of Science and Technology
CV	Cyclic voltammetry
DFT	Density functional theory
DR	Dubinin-Radushkevich
EDL	electric double layer
EDLC	electric double layer capacitor
EIS	electrochemical impedance spectroscopy
EISA	evaporation induced self-assembly
EMImBF ₄	1-Ethyl-3-methyl-imidazolium tetrafluoroborate
F	Formaldehyde
FC	Friedel-Craft
HK	Horváth and Kawazoe
HSAC	High surface area carbon
IHE	inner Helmholtz plane
IUPAC	International Union of Pure Applied Chemistry
MCM	Mobil Composition of Matter
NLDFT	Non-local density functional theory
NMP	<i>N</i> -Methyl-2-pyrrolidione
NOV	Novolac
OHP	outer Helmholtz plane
PEIS	potentiostatic electrochemical impedance spectroscopy
PF	Phenol/Formaldehyd
PVDF	Polyvinylidenfluoride
PSD	Pore size distribution
QNNLS	quick non-negative least square method
QSDFT	Quenched solid density functional theory
R	Resorcinol
RF	Resorcinol/Formaldehyde
SEM	scanning electron microscopy
SDA	structure directing surfactant
TEABF ₄	Tetraethylammonium tetrafluoroborate
TGA	Thermal gravimetric analysis
XRD	X-Ray diffractometry

1 Introduction

The use of energy has been crucial in the history of humanity for millennia. The use of fire, with wood as an energy source, was the first significant advance in the development of humankind.^[1] In the following millennia humanity learned to use many different energy sources (e.g. oil) or forms of naturally occurring energy (e.g. currents in water and wind).

In the future, renewable energies are expected to provide the majority of the world's energy supply. This is due to the finite nature of resources and the environmental problems associated with the use of existing primary energy sources, such as fossil fuels. Burning fossil fuels produces large amount of carbon dioxide, which is the greenhouse gas that causes climate change and global warming in a large extent. Although wind power, hydropower, solar energy and biomass will likely be the primary energy sources in the future, efficient storage of these renewable energies remains difficult. Wind energy and solar energy in particular do not constantly supply the same amount of energy, as the supply depends on the time of day and the season. Stationary energy storage systems are therefore required, which store the excess solar and wind energy and release it on demand. In addition, the energy generated by the sun and wind will also be used in the future for mobility, e.g. for cars, for which similar energy storage technologies are required. Energy storage systems, such as lithium-ion batteries and capacitors, have therefore been the focus of scientific research for several years. One focus of energy storage research is on porous materials, like porous carbons. They have a multitude of advanced properties such as electrical conductivity and high adsorption capacity, which is why they are particularly well suited as electrode materials.^[2] Applications in the field of capacitors are particularly interesting. Porous carbons with a high specific surface area are the electrode material used in commercial capacitors, which rely on capacitive storage mechanisms with liquid electrolytes.^[3] These are also called electrochemical double layer capacitors and are the subject of the latest research.

Furthermore, the search for alternative energy sources is of great importance. Today, hydrogen is perceived as the best energy carrier for harnessing energy, as it is abundantly available and is a clean fuel with zero, or near zero, emissions. It is the lightest element of the periodic table, and proves to be the best combustible at the

parameter of the highest chemical energy stored per unit mass.^[4] It is especially interesting as an alternative fuel for the transport sector, which is consuming almost 60 % of the world energy.^[5] Along with production and distribution, hydrogen storage is an important factor in using hydrogen as an energy source. To date, the extensive utilization of hydrogen as a fuel is being hindered by lack of effective hydrogen storage solutions. Ideally, the amount of hydrogen should be carried as a small volume and light weight. But so far, the common practice is to pressurize hydrogen gas into a steel cylinder, which has been rated to a maximum of 700 bar. Despite such high pressures at 700 bar, sufficient amount of hydrogen still requires a storage tank with a volume of about 150 L. Therefore purely pressurized hydrogen is not considered economically viable option for hydrogen storage.^[6] The solid-state storage in solid materials, like porous carbons, is safe, can reach acceptable mass or volume densities and can be used both for stationary and portable applications.

1.1 Porosity

Porous materials are found in many places in our daily lives. Sponges, various rocks and human bones are just a few examples. When it comes to porosity characterization, the International Union of Pure and Applied Chemistry (IUPAC) divides porous materials by pore size: pores smaller than 2 nm in diameter are called micropores. Pores with a size between 2 nm and 50 nm are called mesopores, while pores with diameters above 50 nm are called macropores. In addition to this classical classification, there is also the term nanopores, which covers all pores with a diameter below 100 nm.^[7] Besides the pore size, the pore shape and the pore connectivity is an important factor for the characterization of porous solids, since it can influence the properties of the solid. Different types of pore connection have been defined, and are displayed in Figure 1. The closed pores have no access to the surface, unlike the open pores. Blind pores have only one access to the surface, whereby some pores have a larger cavity. These pores are also known as blind ink-

bottle-shaped pores. Pores that have multiple entries to the surface are called through pores. When these are connected, they are called cross-linked pores.

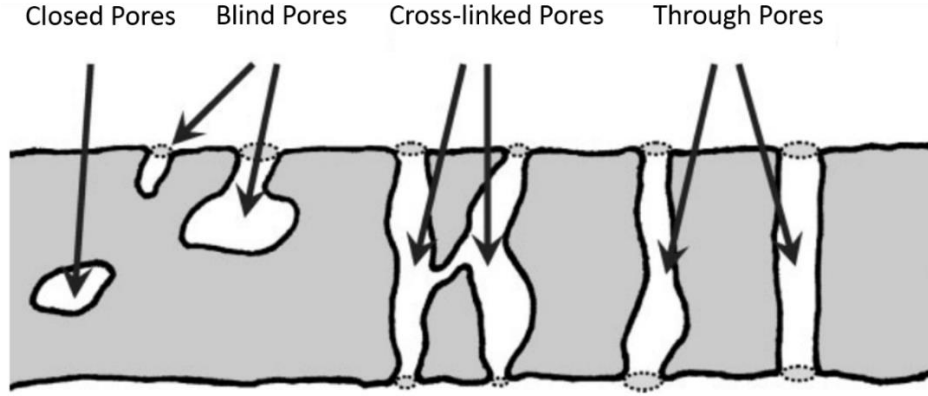


Figure 1: Schematic representation of different pore connectivities. Adapted from Giesche.^[8]

The porosity Φ indicates the ratio of cavity volume to the total volume of a substance or mixture of substances. It is dimensionless and a measure of the actual cavities of the corresponding material. The density ρ (for solids) or the bulk density (for bulk powder) as well as the true density ρ_0 define the porosity. The exact relationship is shown in equation (1).

$$\Phi = \frac{1 - \rho}{\rho_0} \quad (1)$$

The density is the geometric density of a body including the cavities. The true density indicates the skeleton density of a body and thus is an indication of the volume of the body without cavities. An alternative representation of porosity is also the ratio of the pore volume V_C (cavity volume) and the total volume V , which is composed of the true volume V_S (solids volume) and the pore volume.

$$\Phi = \frac{V_C}{V_C + V_S} \quad (2)$$

The total porosity is the sum of the cavities or the sum of the pores respectively. The cross-linked pores form the open porosity or the effective porosity respectively and the closed pores form the closed porosity.

1.2 Carbon

Carbon can occur both bound and elemental in nature. In bound form, carbon plays such an important role that research in several sub-areas of chemistry, organic chemistry and biochemistry is conducted almost exclusively on compounds of carbon. However, inorganic carbon compounds are also important. An outstanding example is CO_2 , which is indispensable for the growth of plants. Also as a greenhouse gas, it has a great influence on atmospheric processes.^[9]

Elemental carbon occurs naturally in two modifications, as diamond and as graphite. The difference between these modifications is the hybridization of carbon. In diamond, each carbon atom is connected to four additional carbon atoms. Therefore, there is a sp^3 hybridization. In graphite, each carbon atom has only three σ bonds to other carbon atoms, which corresponds to a sp^2 hybridization; the fourth bond is a π bond. This leads to two different structures with completely different properties. Carbon in diamond form has a three-dimensional structure and a density of $3.514 \text{ g}\cdot\text{cm}^{-3}$. In graphite the density is lower ($2.24 \text{ g}\cdot\text{cm}^{-3}$), and it has a layered structure. The individual layers of graphite (also called graphene layer) consist of a two-dimensional network of carbon, in the form of fused six rings. Van-der-Waals forces hold the individual layers together.

Compared to graphite, carbon in diamond is hard, chemical stable, has a high melting point and is an electrical insulator. Diamond occurs either in cubic structure (Figure 2 a) or hexagonal diamond structure, while the cubic structure is the regular diamond structure and analogous to the sphalerite structure (ZnS).

Figure 2 b shows the α graphite (also called hexagonal graphite). This is the most common graphite form. For the layers there is a stacking sequence of AB, so the layer of every third layer corresponds to the first one. Furthermore, there is a graphite form with the stacking sequence ABC, where every fourth layer is above the first. This graphite is known as β graphite (rhombohedral graphite). A stacking sequence AA is not known for graphite.

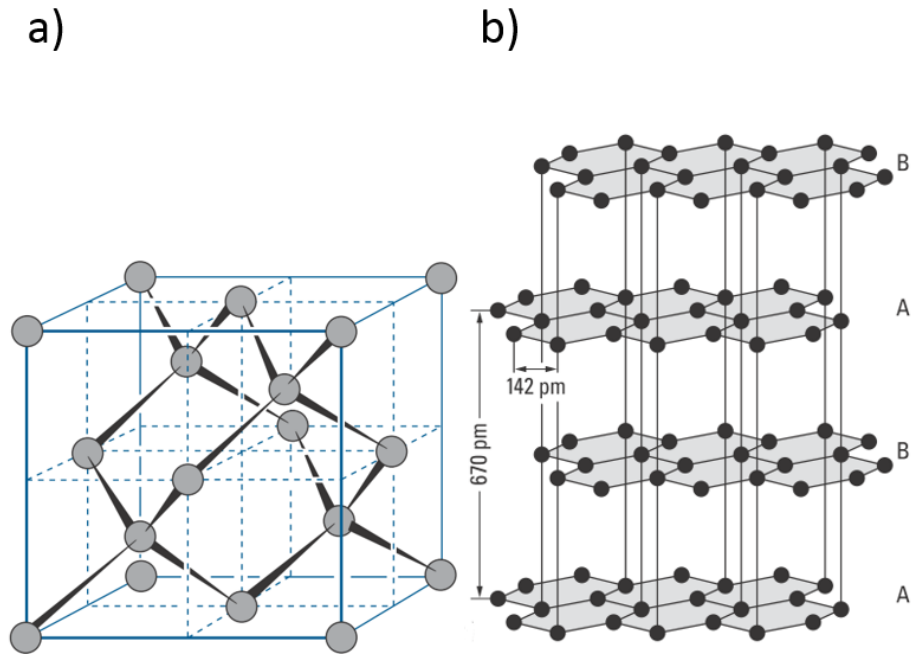


Figure 2: (a) Cubic crystal structure of diamond. (b) Hexagonal structure of α graphite.

Under standard conditions, graphite is the more thermodynamically stable modification of carbon. Due to defects, misalignments, heteroatoms and other impurities, synthesized and naturally occurring carbon is not available as pure graphitic carbon. Usually, only small domains of graphitic carbon exist in bulk material, which are randomly bound to each other. This macroscopic structure is called amorphous. With increasing synthesis temperature, the order of the carbon and thus the size of the graphitic zones increases until pure graphite is formed at approximately 2000 K.

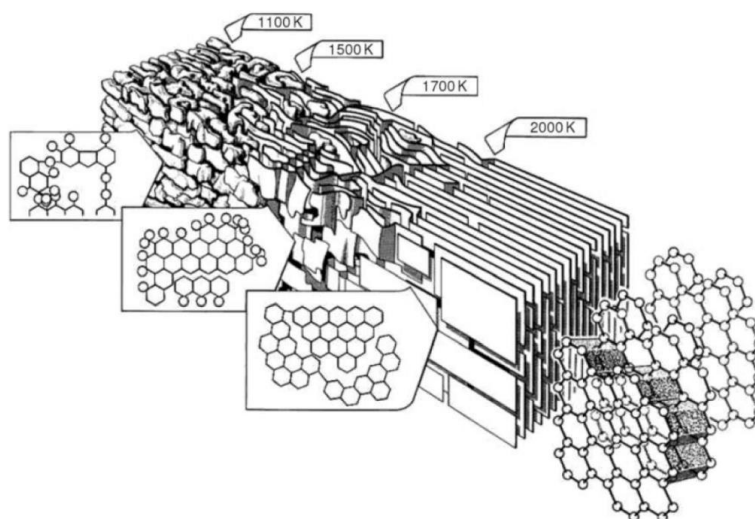


Figure 3: Temperature dependency of the carbon order. With increasing temperature the structural order of the carbon increases until pure graphite is formed at approximately 2000 K. Adapted from Bentur and Mindess.^[10]

Besides the natural occurring diamond and graphite, there are other carbon modifications. For example, single graphene sheets, fullerenes or carbon nanotubes (CNT). However, these are all modifications, which need to be technically synthesized but are often used as energy storage materials.^[11–17]

1.3 Porous carbons

Carbon black and activated carbons are a few examples for porous carbons with industrial applications. Carbon black is produced by the incomplete combustion, or thermal decomposition of gaseous or liquid hydrocarbons under controlled conditions. Activated carbons are produced from carbonaceous source materials, which can also be hydrocarbons, but also biosource materials like bamboo or coconut shells. The carbon is then activated in its property by a targeted increase in porosity. This is achieved by physical or chemical activation. The most important area of application for carbon blacks is as a filler and reinforcer for various synthetic materials and rubber products, e.g. car tires and conveyor belts. Additionally, carbon black pigments are added to paint, lacquers and coatings, where they have a coloring effect, and influence flow properties.^[18,19] In recent years, carbon blacks have been also applied in the field of energy storage, e.g. as conductive additive^[20,21], electrode materials^[20,21] and catalysts for fuel cells.^[22] Activated carbons have a good electrical conductivity, possess great chemical stability, are of low cost, are

easily available and possess a high specific surface area.^[23,24] Activated carbons are especially used as adsorbents due to their high surface area. They are used, for example, to remove impurities from solutions and gases. In this context, carbons are also being used in gas masks, for drinking water treatment and medically for detoxification of the intestines.^[18,19] In addition, activated carbons are also used, similar to carbon blacks, as catalyst supporting material or in the area of energy storage as electrode material in capacitors.^[25,26] They are also promising storage materials for greenhouse gases.^[27,28]

1.3.1 Carbon materials via direct carbonization

Carbonization is the thermal treatment of organic substances (the carbon precursor compounds) at high temperatures in an inert gas atmosphere (usually argon or nitrogen). In this treatment, the carbon content of the material increases while the content of heteroatoms decreases. Carbonization can take place via the solid, liquid or gaseous state. The product of carbonization must necessarily be a solid.^[19,29] During carbonization via solid state, a macromolecular substance is decomposed by the high-temperature treatment. During this process, various low-molecular gases and liquids such as carbon dioxide, water or methanol are released. The morphology of the material is basically retained, so that the resulting carbon is an image of the starting material, but has a lower density. The nature of the precursor compound and the temperature of carbonization determine the internal structure of carbon. During the decomposition of the starting material by the thermal treatment, the remaining carbon atoms move over short distances in order to occupy more energetically favorable positions. This gradually forms a network of carbon atoms, some of which already contain carbon rings. Depending on the temperature, this network contains remaining heteroatoms, especially hydrogen. The spaces created by the release of heteroatoms, followed by the movement of carbon atoms and the formation of bonds between them, determine the structure and intrinsic porosity of the resulting carbon. The impact of the raw material results from its characteristic type of decomposition. The influence of temperature is more complicated: at higher temperatures, the resulting network of carbon atoms initially stabilizes and its expansion rises to a maximum at which the porosity also passes through a maximum. If the temperature increases further, only the interconnection of the individual atoms increases, whereby the porosity and the accessibility of the pores decrease again. The temperature at which the porosity of the carbon is the largest, is again specific

for the starting material, but is usually above 800 °C. Precursor compounds, which usually undergo this carbonization process, are sugars and polymers with little or no aromatic content.

1.3.2 Carbon precursor

In general, activated carbons are synthesized by carbonization of different starting materials or precursors as described in section 1.3.6.^[30,31] Very often so called bio-source materials are chosen for carbon precursors such as wood, coconut shell residues, leaves or hydrochar.^[32–37] During the carbonization process of the precursors, mainly micropores are being formed, which lead to high specific surface areas. Another often-used class of precursors are synthetic polymers or mixtures thereof.^[38–40] The precursors determine the morphology, surface chemistry and have a strong influence on the porosity of the activated carbon materials. Therefore, a controlled synthesis of the precursor is desirable, to tailor the porosity, morphology and surface chemistry of the activated carbon. The most commonly used polymer precursors are formaldehyde resins, synthesized via polymerization with phenol or resorcinol.^[41–43] Besides phenol- and formaldehyde derivatives, poly(divinylbenzene)^[44], polyacrylonitrile^[45] and polypyrrole^[46] are possible polymer precursor materials.

1.3.3 Ordered mesoporous carbons

Classical activated carbons are mainly microporous and amorphous. For some applications, larger mesopores and an ordered pore structure are desired. This is achievable with template-based synthesis methods to generate ordered mesoporous carbons.^[47] They differ from the other carbonizations in that a porous or amphiphilic template is used in the synthesis. The precursor is carbonized along with the template and thus obtains a porous structure, whereby the pore geometry and size can be specifically controlled by the use of certain templates. There are two different ways to template carbon solids. One method, nanocasting, was developed, in which a temperature-stable raw material like silica, with an ordered nanoporous structure is impregnated with a carbon precursor. After the carbonization, the template is removed and the nanoporous carbon remains as a replica.^[48] As an example, Figure 4 shows the synthesis of carbon CMK-3.^[49] The template used is the silica SBA-15, which has a hexagonal structure. Sucrose is then impregnated in an aqueous solution and polymerized with H₂SO₄. The filled silica template is carbonized at 800 – 1100 °C to obtain a silica-carbon composite. In the final step, the template

is dissolved in ethanol with NaOH to complete the synthesis of the ordered, porous carbon. The structure of the CMK-3 corresponds to the negative replication of the SBA-15, which can also be detected by SEM images and X-ray powder diffraction. Since the negative replication of the "honeycomb structure" of the SBA-15 are only isolated nano rods, they must still be cross-linked with each other in order for the structure to remain stable in the material. This is explained by connecting pores in the pore walls, which enable the connecting strands in the CMK-3.^[50]

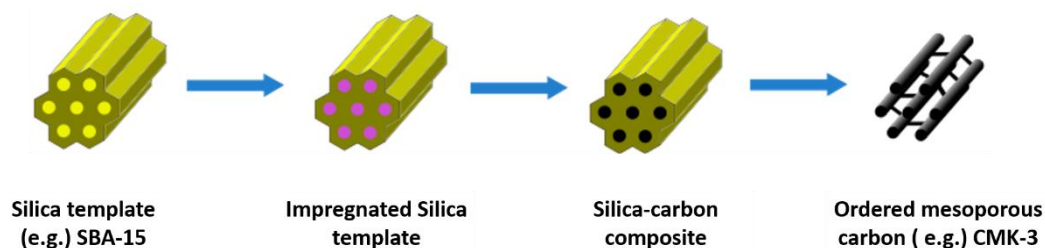


Figure 4: Scheme of the synthesis procedure of the ordered mesoporous carbon CMK-3 via nanocasting.

The structure of the carbon is determined by the template that is used, which enables the synthesis of different carbons with different ordered structures, high porosity and a narrow pore size distribution. However, nanocasting requires many synthesis steps, especially since the template has to be synthesized first and removed later.

The second method is based on the use of amphiphilic surfactants (e.g. block co-polymers). Under the synthesis conditions, phase separation occurs between the surfactant and the carbon precursors (hydrophobic polymers with a low degree of polymerization, usually based on phenol-formaldehyde resins). An example is shown in Figure 5. At first a self-assembly of the surfactant takes place and the carbon precursor compound can be polymerized around the micelles. The template is removed during the carbonization process.

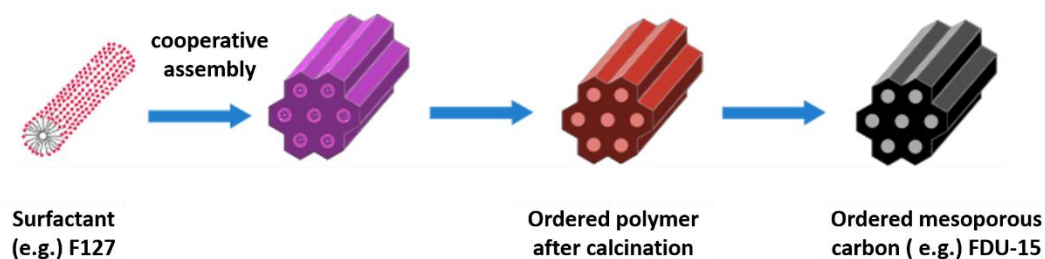


Figure 5: Scheme of the synthesis procedure of the ordered mesoporous carbon FDU-15 via direct synthesis.

A methodological variant of this is also known as the EISA process (evaporation induced self-assembly) where the micelle formation is induced by evaporation of the solvent.^[51–55] Ordered mesoporous carbons are promising materials as their interconnected and ordered pore structure offers diffusion pathways for adsorbed molecules in different sizes, which is why ordered mesoporous carbons are widely investigated as host materials. However, the synthesis is expensive, time consuming and inscalable. Whenever template-free synthesized carbons are a possible alternative, their use is preferred.

1.3.4 Phenolic resins

Phenol/formaldehyde (PF)-resins are one of the most used polymers for the direct synthesis of porous carbon materials. Depending on the reaction condition, different polymers with different material properties can be produced. The PF polymer was already presented as Bakelite and used as a material at the beginning of the 20th century.^[56] It is therefore one of the first known synthetic polymer materials. The mechanism of polycondensation of phenolic resins is an electrophilic substitution. Due to the +M effect of the hydroxyl group, electrophilic substituents react preferably at the ortho and para positions of the phenol. The polymerization is classified as a polycondensation, which means water is released during the reaction. Depending on the reaction conditions, a distinction is made between two different mechanisms and the resulting phenolic resin classes (Figure 6). If the reaction is base-catalyzed, then it is a resol. When the synthesis is acid-catalyzed, a novolac is formed.

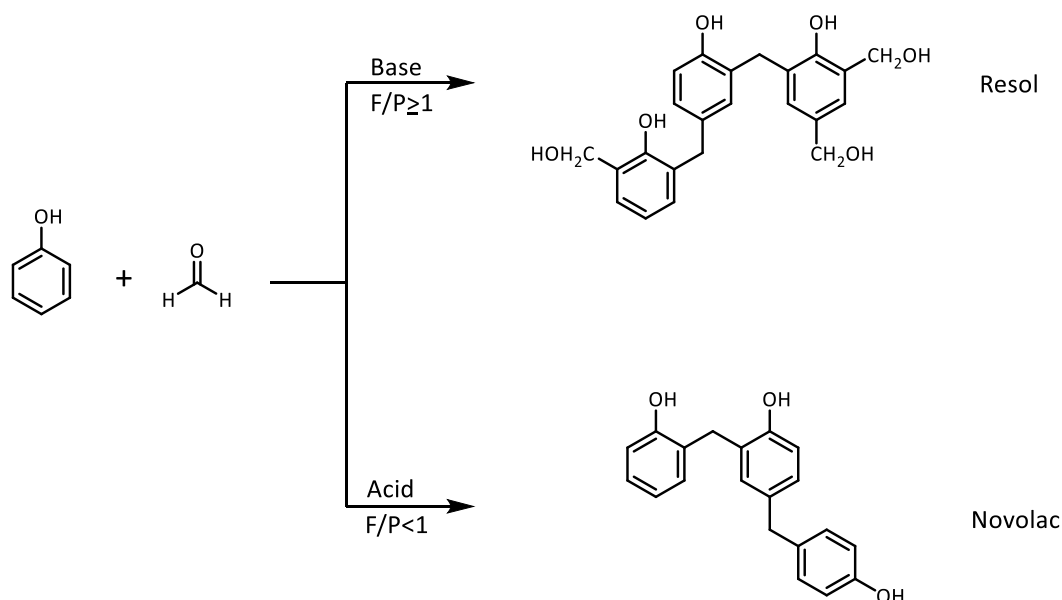


Figure 6: Polymerization of phenol and formaldehyde with acidic and alkaline conditions. Adapted from Pilato.^[57]

For the respective products, the formaldehyde-phenol ratio (P/F ratio) is also important in addition to the catalysis conditions. To obtain a duroplastic resol, the F/P ratio must be greater or equal to 1. For a thermoplastic novolac, the F/P ratio must be less than 1. The synthesis mechanism of acid novolac synthesis follows the Lederer-Manasse reaction (Figure 7). After an electrophilic addition of formaldehyde, a phenylethanol (4-hydroxymethyl phenol) derivative of phenol is formed. Acid catalyzed rearrangement results in an intermediate product of phenol with terminal ethylene functionality, which can react with a phenol molecule. Finally, two phenol molecules are connected via a methylene bridge to form 4,4'-methylenediphenol.^[58] As soon as one phenol molecule has reacted with another, the intermediate product formed is able to react with another phenol molecule. However, the oligomers cannot polymerize further. In order for the polymer to cross-link further, a formaldehyde source is necessary, otherwise the novolac cannot react further. The base-catalyzed reaction also leads to the formation of an intermediate. First, the phenolate is formed, which then reacts with formaldehyde in the ortho or para position to 2-(hydroxymethyl)phenolate. The trisubstituted (2-hydroxybenzene-1,3,5-triyl)timethanol can then be formed by further reaction with formaldehyde.

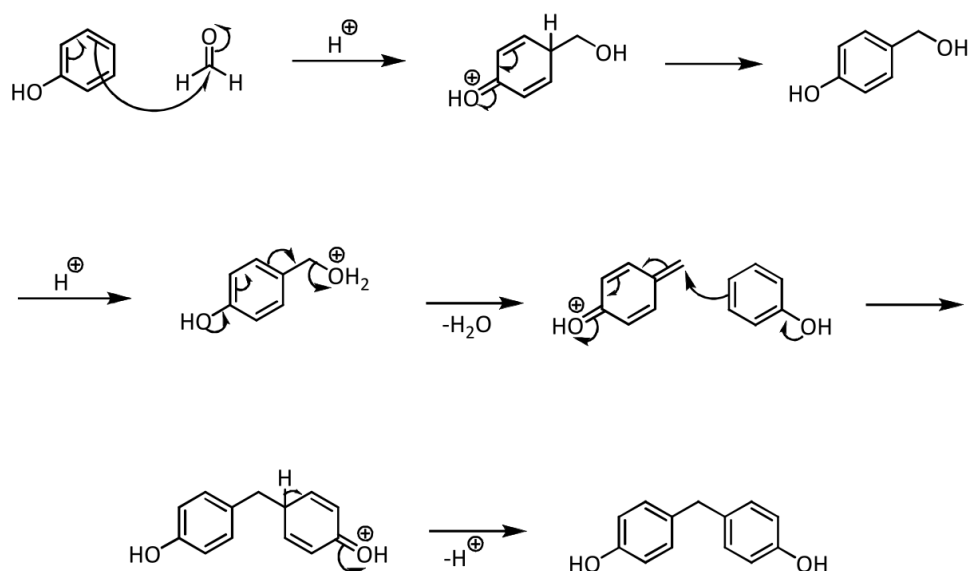


Figure 7: Lederer-Manasse-reaction of the acid catalyzed polycondensation of phenol and formaldehyde to a novolac.

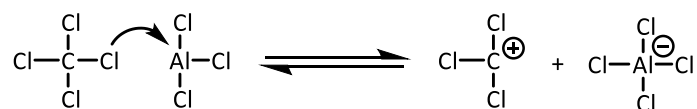
In addition to phenol, resorcinol and phloroglucinol are frequently used together with formaldehyde to form a formaldehyde resin.^[59,60] Resorcinol has a higher reactivity compared to phenol, due to its additional hydroxyl groups. The reactivity of phloroglucinol is even higher, which enables the possibility to perform a polymerization under mild reaction conditions (neutral pH value, low reaction temperature). Nevertheless, the control of the synthesis is more difficult with phloroglucinol, which is why phenol and resorcinol are often used as precursor compounds.^[61,62]

1.3.5 Friedel-Crafts cross-linking

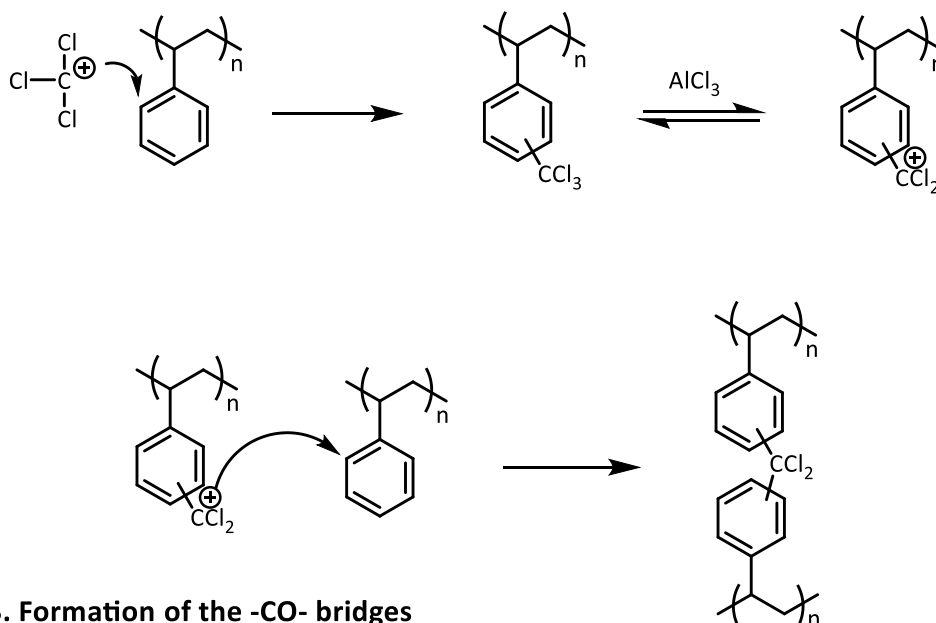
Carbon precursors not only determine the morphology and surface chemistry of the resulting carbon materials, but also influence the pore size and shape. A structural modification prior to the chemical activation of the synthetic polymer is therefore a possible approach for tailoring pore sizes and shapes. Wu et al. cross-linked polystyrene chains via Friedel-Crafts alkylation which were further carbonized to obtain a hierarchically structured carbon electrode material.^[63] The mechanism of the cross-linking is shown in Figure 8. CCl_4 is used as solvent and cross-linking reagent and AlCl_3 is used as acidic Friedel-Crafts catalyst. First, the AlCl_3 abstracts a chloride anion from the CCl_4 as Lewis acid, so that a carbocation is formed. This reacts in an electrophilic substitution with an aromatic ring of polystyrene. From

the CCl_3 group on the aromatic ring, a chloride anion is again abstracted by AlCl_3 , forming a dichloro(phenyl)methyl cation. This reacts in an electrophilic substitution with another aromatic ring so that they cross-link the aromatic rings via a chlorinated methylene bridge. Finally, the chlorinated methylene bridge is hydrolyzed to a carbonyl bridge by adding water. The polymer produced in this way is cross-linked via carbonyl bridges.

1. Formation of the carbocations



2. Formation of the $-\text{CCl}_2-$ cross-linking



3. Formation of the $-\text{CO}-$ bridges

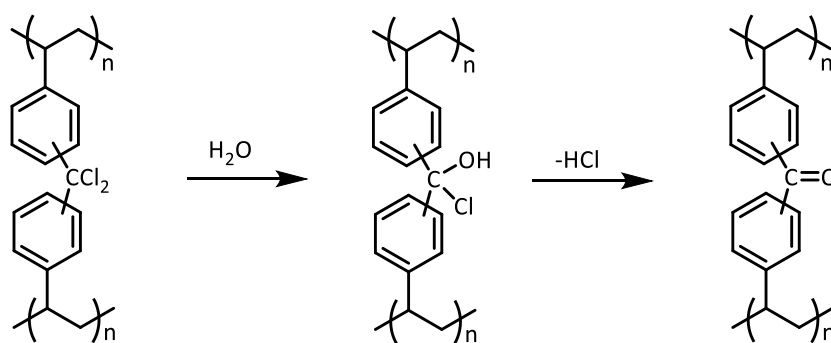


Figure 8: Reaction mechanism of the cross-linking of polystyrene. Adapted from Li et al.^[64]

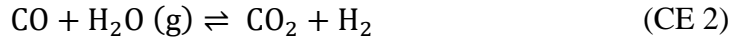
1.3.6 Activation of carbons

The activation of carbons is a widely used method to increase the porosity, by removing carbon atoms from the carbon structure via physical or chemical processes. The aim is to enlarge pores and increase the specific pore volume and surface area of the carbon materials.^[65]

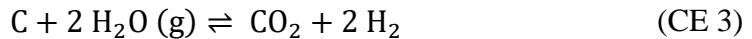
In general, the activation process can be divided into physical and chemical activation. At a physical activation, the source material is treated with hot gases and thus developed into activated carbons. The carbonized material or the raw material is exposed to oxidizing atmospheres, which can be steam, air or carbon dioxide at temperatures of 800 to 1100 °C.^[29,66] The steam activation of carbon is based on the steam-carbon reaction (CE 1).^[18]



The steam-carbon reaction is endothermic, which is why high temperatures are necessary to drive the reaction towards the product side. A continuous flow of the activation gas removes carbon monoxide and hydrogen from the reaction environment and enhances the activation even further. Another occurring equilibrium reaction is the water-gas shift reaction, which is also an essential part in steam reforming process for the production of hydrogen (CE 2).^[18]



This reaction is exothermic and its equilibrium constant is equal to 1 at a temperature of 830 °C.^[18] The chemical potential of carbon monoxide is higher than the chemical potential of hydrogen below 830 °C. During the steam activation of carbon, the water-gas shift reaction is at equilibrium, because carbon monoxide is a product of CE 1 and a reactant of CE 2. The chemical equations 1 and 2 can be combined to CE 3, which is an endothermic reaction and therefore easy to control via temperature.



As long as carbon remains in the reaction system, carbon dioxide and carbon monoxide coexist in equilibrium. The reaction is known as the Boudouard-reaction, named after the French chemist O.L. Boudouard.



At the physical activation with air, the carbon substrate reacts with oxygen during the reaction process to form carbon dioxide (CE 5):

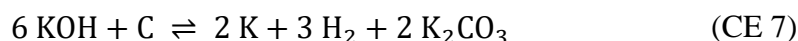


Both reactions displayed in the chemical equations 4 and 5 are in equilibrium, since carbon dioxide is reagent in CE 4 and product in CE 5. Both equations can be combined to CE 6, which is exothermic, and therefore difficult to control. For this reason the physical activation of carbon with oxygen is rarely used.^[29]



At the chemical activation of carbons, the raw material or carbonized substrate is impregnated with a chemical reactant, which is typically an acid, strong base or salt. The chemical activation, can be either a one or a two-step process.^[67,68] That means, the carbonization can be performed during or prior to the activation process. The most common activation reactants are potassium hydroxide (KOH), sodium hydroxide, zinc chloride, phosphoric acid, potassium carbonate and sulfuric acid.^[34,65,69] The advantage of the chemical activation compared to the physical activation is that it can be performed at lower temperatures, and the yield of the highly porous products is often very high. In addition, impurities caused by biomass derived carbons can be lowered, but the activation reagents are often corrosive and they must be removed at the end of the reaction with an additional washing step.

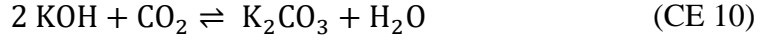
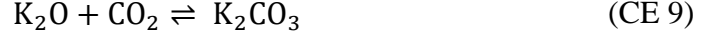
KOH is the most widely used chemical activation reactant, as the resulting porous carbons have achieved the best results in terms of increased porosity and high specific surface area.^[70–72] Other influencing factors for the chemical activation are the precursor, the ratio of activation reactant and substrate as well as the temperature. The influence of the carbonization temperature prior to the activation will be discussed in the next section 1.3.7. The substances formed during the KOH activation are hydrogen, potassium carbonate, carbon dioxide, carbon monoxide, water and metallic potassium.^[70–72] With thermodynamic calculations, and considering the activation temperature, it is possible to show that the reaction shown in CE 7 is a plausible overall chemical reaction of the activation process with KOH. All reaction products were experimentally proven, and the standard Gibbs free energy change above 570 °C is negative.^[65,71]



It is assumed that the first step of the chemical reaction starts at 400 °C with the dehydration of KOH, which is finished at approximately 600 °C.^[65]

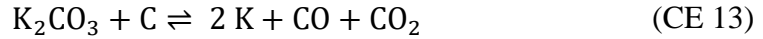


The formed water can react with the carbon substrate according to CE 1 to CE 3. Carbon dioxide reacts with potassium oxide (CE 9) or KOH (CE 10) to potassium carbonate.

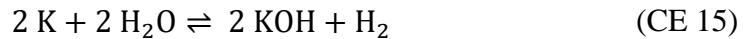


The decarboxylation of potassium carbonate begins at 700 °C and is completed around 800 °C. It is assumed, that the reaction is catalyzed by carbon.^[65,71]

The formation of metallic potassium is based on the reduction of potassium oxide with hydrogen (CE 11) and/or carbon (CE 12).^[70] Another possibility is the reduction of potassium carbonate with carbon (CE 13)^[73] or (CE 14), which proceeds above 700 °C.^[65]



Metallic potassium can react with water (CE 15) and carbon monoxide (CE 16).^[73] The formed products support the activation process.



It is assumed that as-prepared metallic potassium intercalates in the lamellar structure of the graphene layers of the carbon. Therefore, the distance between the layers is increased. After the removal of the intercalated potassium with the washing step or reaction with water during the activation (CE 15), the structure remains as the carbon lattice cannot return in its original nonporous structure, resulting in an increase of pore sizes for subnanometer pores.^[74] With hydrogen being formed during the activation, the formation of methane from carbon and/or carbon dioxide is possible.^[75] Furthermore, it was shown that KOH and potassium carbonate

catalyze the formation of methane from carbon and steam in a temperature range of 500 to 600 K.^[76] As mentioned above, chemical KOH activation of carbons is the most widely used method for the production of activated carbons. Various synthetic polymers and biomass derived substrates were used as precursors for carbons followed by a chemical activation for gas storage and energy storage applications.^[65,77–83]

1.3.7 KOH activation of novolac based carbons

Depending on the organic precursor, the obtained activated carbons differ in surface area, pore size, pore volume and surface chemistry. As mentioned in section 1.3.4, PF resins are widely used organic precursor for generating carbon materials, like ordered mesoporous carbons and carbon aerogels.^[54,84,85] The degree of polymerization of PF resins can be controlled very well and by the use of a soft templating method, a mesoporous PF resin can be formed leading to a variety of carbons with tailored pore sizes and shapes.^[86–88] In the recent years, ordered mesopores gained scientific interest for various applications. However, the use of structure directing agents (SDA) is time consuming and expensive, as mentioned above. Another possible approach to create small mesopores is via chemical activation of carbons, without the use of structure directing agents, as mentioned in section 1.3.6. Chemical activation of ordered mesoporous carbons to increase the specific surface area is possible, but it is very likely the ordered mesoporous structure will be heavily damaged during the activation process.^[42] Recent studies showed PF based carbons synthesized under acidic conditions possessed an exceptional resistance to a wide range of activation reactants and activation temperatures.^[83,89,90] This is attributed to the high cross linking of the rigid polymer network promoted by the acidic synthesis conditions. The preservation of ordered mesopores with respect to chemical KOH activation was found to be dependent of the carbonization temperature prior to the chemical activation. When ordered mesoporous carbons based on PF resins are carbonized at a temperature of 700 °C or higher, the carbons keep most of the ordered mesoporous structure.^[91] Therefore the carbonization temperature prior to the activation is crucial for the chemical and thermal stability of the carbons. With a higher carbonization temperature, the carbonaceous framework has a more rigid structure, which can withstand the KOH activation process for a possible preservation of ordered pore structures.^[92] However, a lower carbonization temperature prior to the chemical activation can increase the effectiveness of the pore creating

activation procedure, due to the less rigid structure of the carbonaceous framework.^[32,64,69,93] Another parameter for the activation process is the activation temperature, as described in section 1.3.6. With the carbonization temperature, the activation temperature and the amount of the chemical activation reactant there are three parameters which influence the pore size and thus surface area and pore volume. By varying these parameters, carbons with tailored porosity can be obtained which are suitable for studies, regarding adsorption mechanisms for gas storage or electrochemical energy storage.

1.4 Capacitors

Capacitors are devices, which are able to store electric charges along with the corresponding energy and release it at a later stage. Thus, capacitors can be used as electric energy storage devices. The energy storage mechanism is based on the separation of charges, which accumulate at a charged electrode. A simple capacitor setup is the plate capacitor, which is built up of two electrically conductive plates and an insulating dielectric medium.^[94] By applying a positive and a negative charge on the plates respectively, charge carriers accumulate at the electrode surfaces and an electric field is developed in the dielectric media. The classic dielectric media usually provides fixed charge carriers in the field. The amount of charges Q , which is storable at the plates, depends on the applied voltage U and the capacitance C .

$$Q = C \cdot U \quad (3)$$

The storable amount of charge is linear proportional with the applied voltage.^[95] The capacitance itself depends on the surface area A of the plates, the distance d of the plates and the relative permittivity ϵ_r of the dielectric medium, as well as ϵ_0 . The capacitance increases, with a larger surface area, a smaller distance of the plates and a larger relative permittivity of the dielectric medium, which is a measure of containing the developed electric field.

$$C = \epsilon_r \epsilon_0 \frac{A}{d} \quad (4)$$

1.4.1 Electric double layer capacitors

Electric double layer capacitors (EDLC) are electrochemically energy storage devices. In general, EDLCs consist of two electrodes, an electrolyte and a separator. The electrode material is coated on a current collector. The storage mechanism is based on the formation of an electric double layer of electrolyte ions on the interface of the electrode and the electrolyte.^[39,96,97] If a voltage is applied to the electrodes, one electrode is charged negatively and the other one positively, the electrolyte ions diffuse towards the electrode surface and form an electric double layer. In comparison to batteries, the charge storage in EDLCs is of purely physical character and no redox reactions or other faradaic charge transfer reactions occur at the electrode surface. This is the main difference to the battery as its charge storage mechanism is based on redox reactions at both electrodes. The disadvantage of the battery compared to the EDLC is therefore that in the following of the redox reactions on the electrode surfaces, a diffusion process occurs, as a result of which reduced and oxidized species diffuse away from the electrode and new charge carriers accumulate on the electrode surface.^[98] Although the specific energy density of batteries is higher, EDLCs can store and release energy faster, resulting in a higher power density, as seen in the Ragone plot in Figure 10. Different classes of electrochemical capacitors are pseudocapacitors, as seen in Figure 10. Pseudocapacitors use rapid and reversible surface redox reactions for charge storage, or redox reactions of the electrolyte species on the surface of pristine carbon electrodes. The pseudocapacitance, is induced by pseudocapacitive materials such as transition metal oxides, heteroatom-enriched carbons and conducting polymers.^[99–101]

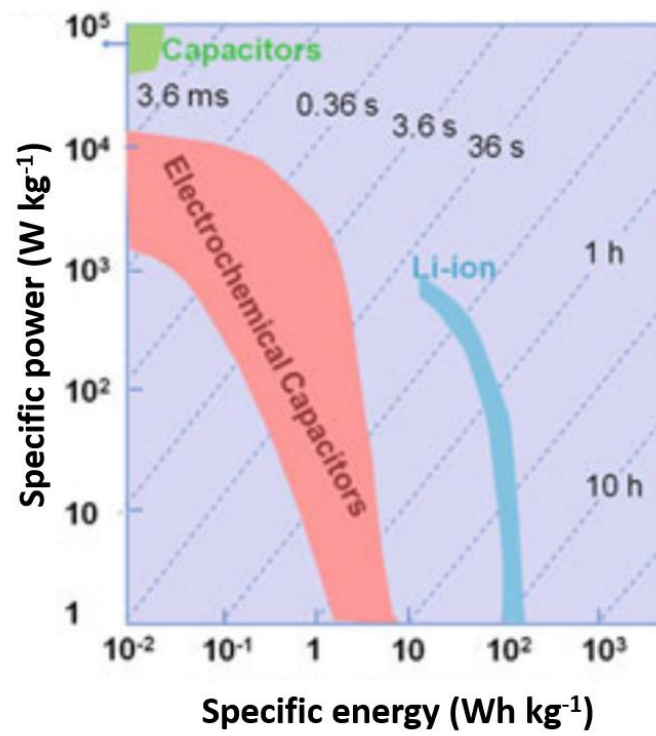


Figure 9: Ragone plot of different electrochemical storage systems. [102] Copyright 2016, Springer Nature.

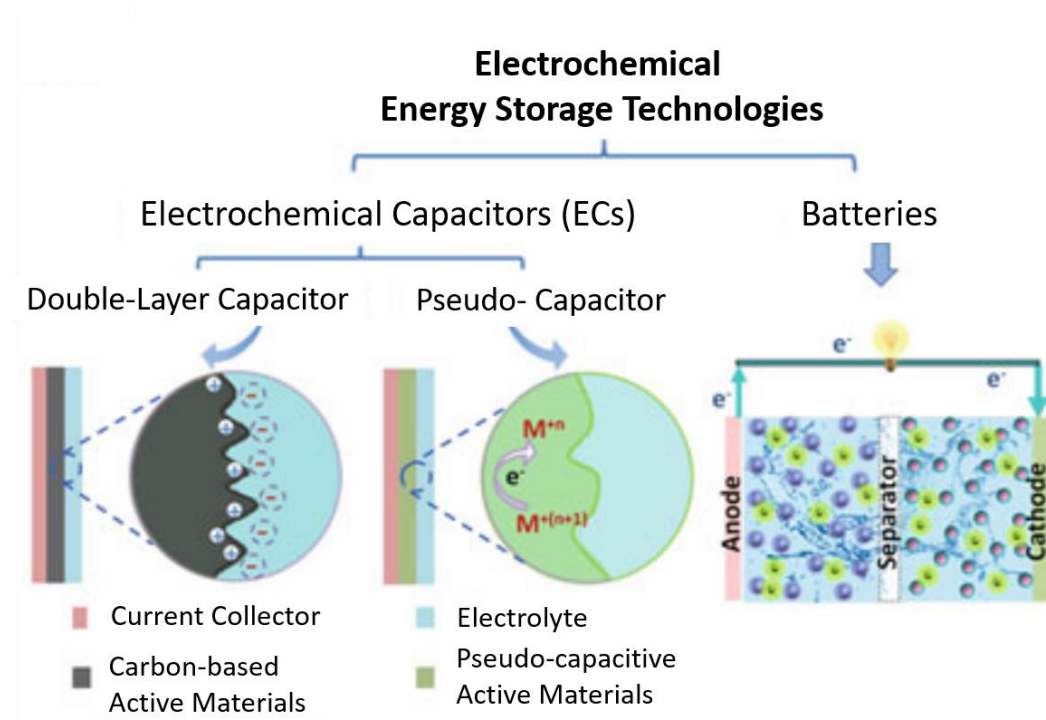


Figure 10: Mechanisms of different energy storage technologies, including double layer capacitor, pseudocapacitors and batteries. Adapted from Liu.^[102]

There are three classic descriptions of the electric double layer (EDL) on the electrode surface.^[103] Helmholtz originally proposed the concept of a double layer on a charged solid surface, which consists of a rigid single layer of adsorbed counter ions on the electrode surface.^[104,105] Thereby, a rigid layer of charge carriers in the solid phase is compensated with a rigid layer of electrolyte ions of the opposite charge, at a distance d , which is also known as the double-layer thickness. The capacitance can be calculated according to equation (4). Gouy and Chapman developed another double-layer model. The Gouy-Chapman model involves the diffusion and mixing of ions in the solvent. A thermal movement of the counter ions in the electrolyte is assumed, which form a diffuse layer and thus lead to a diffuse double layer on the electrode surface.^[106,107] Stern combined both models to the Stern double-layer model. He proposed a rigid double layer on the electrode surface and diffuse double layer, followed by the bulk electrolyte as seen in Figure 11.^[108]

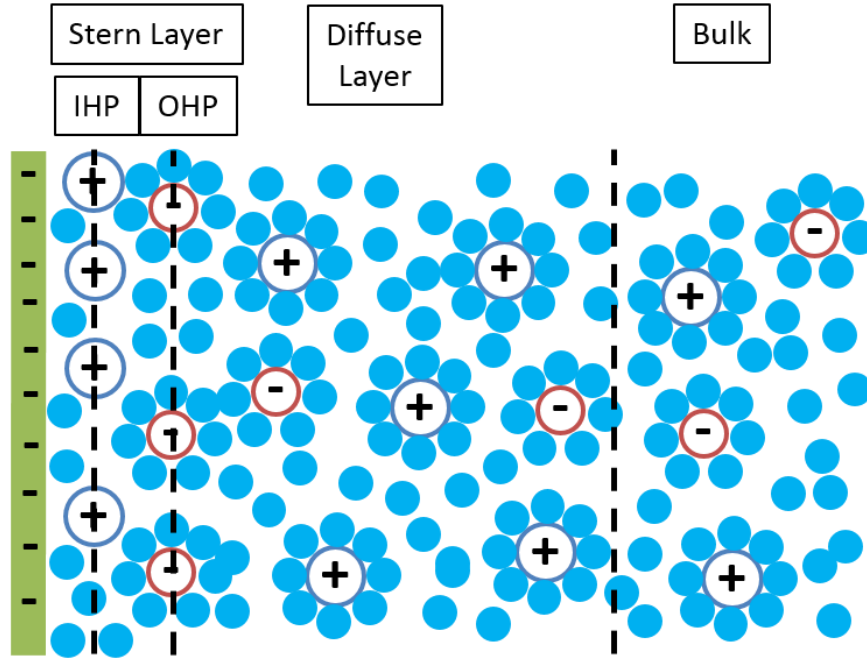


Figure 11: Scheme of the Stern model for the electric double layer capacitor.

The Stern layer can be further divided into the inner Helmholtz plane (IHP) and the outer Helmholtz plane (OHP). The IHP is the rigid layer of adsorbed ions on the interface of the electrode surface and is essentially the original Helmholtz double layer. The OHP is a rigid layer of solvated electrolyte ions with the same electric charge as the electrode surface. The diffuse layer begins at the OHP.^[103,109] The electrochemical potential curve is shown in Figure 12. The potential decreases linearly from the electrode surface ψ^0 to the IHP ψ^i . The potential decreases linearly again, but with a larger slope to the OHP ψ^d . Within the diffuse layer, the electrochemical potential decreases exponentially until the bulk potential is reached.^[110] The energy is mainly stored in the Stern layer, especially in the IHP. Charge transfer of specific adsorbed ions or solvent molecules at the electrode surface can additionally occur, not only in pseudocapacitive systems, but also as side reactions in EDLCs, which then increases the capacitance.^[111]

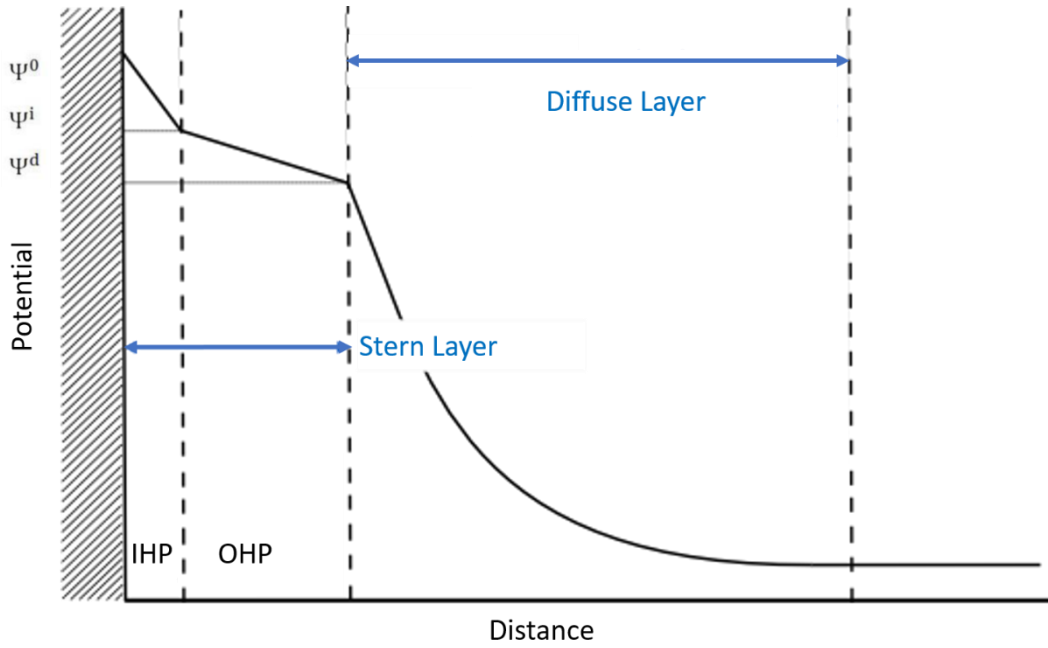


Figure 12: Electrochemical potential curve of the double layer according to Stern.

The capacitance of the EDLCs is magnitudes larger than the capacitance of conventional capacitors, due to the small double layer thickness d (~ 1 nm), and the larger relative permittivity of the solvent molecules. The ability to enhance the electric field between the charges of the solvent molecules is larger than that of conventional dielectrics and solvent molecules possess often an additional dipole moment.^[112] A larger capacitance is associated with a larger energy density, which is the reason EDLCs are often referred to as supercapacitors. Pseudocapacitors and hybrid systems of EDLCs and batteries are also referred to as supercapacitors.^[113]

$$E = \frac{1}{2}CU^2 \quad (5)$$

Equation (5) shows energy is proportional to the capacitance and depends on the applied cell voltage U . The maximum power P is described by the means of the following equation.

$$P = \frac{U^2}{4R_{\text{ESR}}} \quad (6)$$

The achievable power depends on the cell voltage as well. Another different component is the series equivalent resistance R_{ESR} . It reflects the bulk resistance of the electrolyte, contact resistance of electrode material and current collector as well as

intrinsic resistance of the electrode material. The general aim for an EDLC setup is achieving a high cell voltage along with a high capacitance and a low equivalent series resistance.

Capacitance, cell voltage and resistance of a capacitor are material dependent. Aluminum is often used as the current collector. It conducts electricity well and is cost-effective. The separator must be mechanically strong to increase the stability of the capacitor cell. It also needs to have ionic conductivity, prevent particle migration of the electrode material and have an electronic insulating effect. Polyolefins, cellulose paper, ceramics and glass wool are often used as separators.^[95,109] The electrolyte system is a crucial component in the EDLC setup. It should have a high ionic conductivity, and needs to be electrochemically stable, to provide a high cell voltage. In general, there are three types of electrolyte systems, which are used commercially or for research purposes. Aqueous electrolytes (e.g. KOH, H₂SO₄, Na₂SO₄), organic electrolytes (e.g. ACN, propylene carbonate) with a conducting salt (e.g. tetraethylammonium tetrafluoroborate, TEABF₄) or ionic liquids (e.g. 1-ethyl-3-methyl-imidazolium tetrafluoroborate, EMImBF₄) are frequently used as electrolyte systems.^[114–116] The electrolyte systems have different advantages and disadvantages. Aqueous electrolytes have the highest conductivity among all presented electrolyte systems (540 to 750 mS·cm⁻¹).^[117] However, the electrochemical stability of water is rather low, as it decomposes at a voltage of 1.23 V and the operative voltage window for aqueous electrolytes is often as low as 1 V. A lot of research is dedicated to increasing the operating voltage window of aqueous electrolytes. A promising approach is the use of pH-neutral salts, like Li₂SO₄ or LiNO₃ and the variation of the respective concentration. It was possible to increase the voltage window up to 1.5 V by increasing the excess potential for the oxidation and reduction of water.^[118–120] By variation of the pH-Value and the use of a mixture of conducting salts it was even possible to increase the voltage window up to 2.1 V. However, the system is quite sensitive to pH change and requires cautious assembly.^[121] The operating voltage windows of ionic liquids are the highest among all discussed electrolyte systems (ΔU 4 V).^[117] The conductivity on the other hand, is very low, due to the high viscosity (e.g. EMImBF₄: 15.5 mS·cm⁻¹). As a consequence, the resistance of the capacitor device is increased. Furthermore, ionic liquids need to be free from water residues and are the most expensive electrolyte

systems. Organic electrolytes have a high voltage window (2.5 to 3 V) and a moderate conductivity (TEABF₄ 59.9 mS·cm⁻¹). Both energy and power of a capacitor are dependent on the voltage. The resistance, on the other hand, influences the maximum power of the capacitor only. For this reason, a system with a higher voltage is preferred over a system with a higher conductivity. Organic electrolyte systems are the most commonly used and commercially most established systems.^[13,98,109,113]

1.4.2 Electrode materials for electric double layer capacitors

The electrode materials are important components in the EDLC, as they have a significant influence on the operating properties of the device. To achieve a high capacitance, the electrode material should provide a high electrode surface and accessibility to electrolyte ions.

Carbons are the most promising and widely used electrode materials for EDLCs, due to their high specific surface area, good electrical conductivity and mechanical stability. A high surface area is especially beneficial for a high capacitance, because more access is granted for electrolyte ions to participate in the double layer formation.^[122,123] In addition, the porosity can be controlled, which is important for ion accessibility of the carbon surface and ion diffusion within the carbon network. Metal oxides and conducting polymers are frequently used as electrode materials in pseudocapacitors and hybrid capacitor systems, but have no significant role as electrode materials in EDLCs, as they store and release energy via physical ion adsorption and desorption only.^[101,113,124–126] As shown in Figure 13, commonly used electrode materials for EDLCs are conventional activated carbons, carbon nanotubes and graphene based carbons. Activated carbons possess the highest surface area among the used carbon materials and are therefore preferred electrode material in commercial EDLC devices. Another advantage is the cost efficiency and facile synthesis method of activated carbons, as described in section 1.3. Therefore, activated carbons are used as electrode materials in commercial EDLC devices and very often coconut shell derived carbons.^[13,26,98,113]

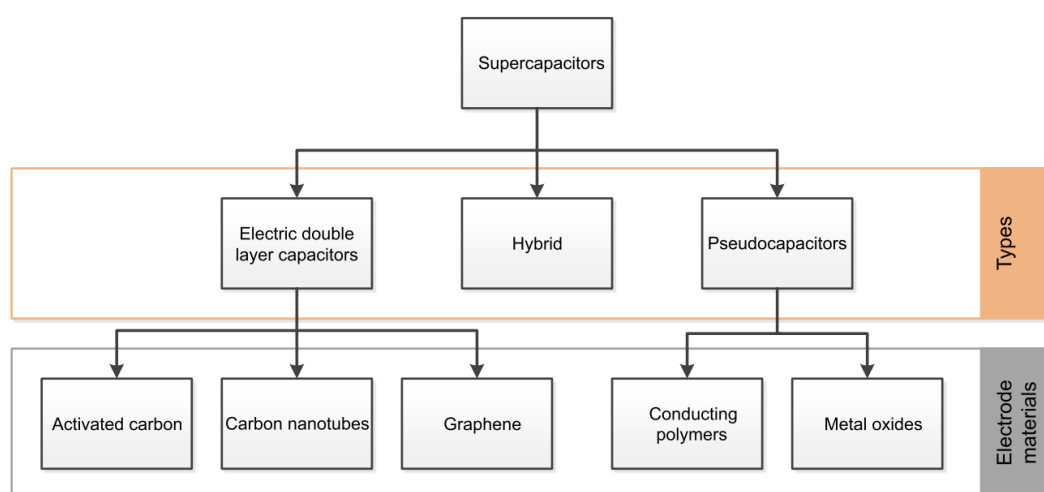


Figure 13: Classification of different supercapacitors and their electrode materials.^[113] Copyright 2014, Elsevier.

In most commercial EDLCs, activated carbons are used as electrode materials along with organic electrolytes. These devices reach operating cell voltages of 2.7 V and a specific capacitance of 100 to 120 F·g⁻¹.^[16,127] In research, many different activated carbons were presented and used as electrode materials. Very high cell capacitances of up to 240 F·g⁻¹ have been achieved, but these referred exclusively to the pure electrode material and not to the entire device.^[128,129] Furthermore, the retention of the capacitance, or rate capability at higher currents is a decisive factor. As standard, the capacitance of an EDLC is measured over larger current ranges (1 to 20 A·g⁻¹). Although the double layer formation at the electrode surface in the ideal capacitor should be independent of the diffusion of the electrolyte ions, it is observed that the capacitance decreases at higher currents. This is attributed to the limited diffusion of the electrolyte ions in the micropores of the carbon, which is subject to kinetic inhibitions at higher currents and thus leads to lower capacitance at higher currents.^[130] In addition to the diffusion of electrolyte ions through the pore channels, surface diffusion through small pores leads to frictional resistances, which ultimately reduces the capacitance.^[131] Therefore, electrode materials need to ensure not only high surface areas for a large capacitance, but also provide pores large enough to ensure a high rate capability, because this ensures the EDLC can be employed over a wide power range and that mainly depends on the pore sizes of the activated carbons.

There were also many attempts to use carbons based on chemically or physically activated formaldehyde resins for supercapacitor electrodes.^[41,132–137] Lei et al. for example, used a hexamine cross-linked phenolic resin as carbon precursors, which was activated with CO₂, as EDLC electrode materials and achieved a gravimetric capacitance of 160 F·g⁻¹ in organic electrolyte at a low current density.^[138] The capacitance value of the carbon sample, which they referred to as C-46, was high, but the retention of the capacitance with respect to higher current densities was only about 50 % due to the high content of micropores below 1 nm, which inhibit fast ion diffusion at higher current densities. Chen et al. used a commercial PF-resin as the carbon precursor and obtained the carbon sample PC-6 after chemical activation via KOH and ZnCl₂.^[134] The achieved capacitance in organic electrolyte was 142 F·g⁻¹ at a low current density of 120 mA·g⁻¹. The retention of capacitance was 71 %, but the highest current density was rather low with 2 A·g⁻¹. The reason for the low retention is the low content of pores that are larger than 1 nm. Carbons based on formaldehyde resins were additionally used with aqueous electrolytes. Du et al. synthesized hollow mesoporous carbon spheres, based on 3-aminophenol/formaldehyde resins, which achieved a high capacitance of 429 F·g⁻¹ in 6 M KOH at a current density of 0.5 A·g⁻¹.^[139] A high retention of capacitance with 79 % was obtained due to the presence of mesopores.

Carbide derived carbons (CDCs) are porous carbon materials with a very narrow pore size distribution. Pore sizes of CDCs are often in the micropore range below 1 nm. CDCs are prepared by high temperature extraction of metal ions from carbides serving as precursor, like SiC, TiC or ZrC. The most common method for production of CDCs is high temperature chlorination (Figure 14) and vacuum decomposition.^[140–143] They are considered as promising EDLC electrode materials because carbide precursors allow the fine-tuning of porous networks and good control over surface functional groups more so than activated carbons.^[140,144] It is possible to tailor the porous network of CDCs by varying the precursor composition. Each CDC precursor has an individual variation of distribution of carbon atoms and therefore leads to a different porous network. Independently of the carbide precursor used, an increasing synthesis temperature reveals a common trend of increasing pore size. The porous structure often collapses if the synthesis temperature exceeds 1300 °C whereas the graphitization of carbon occurs at temperature higher than

1000 °C.^[145,146] With regard to the carbide precursor, a comparison can be established between titanium and silicon carbide carbons, which shows that the same synthesis temperature of 1200 °C leads to a narrower pore size distribution and a smaller average pore size of the Si-CDCs due to the different distribution of carbon atoms of the CDC precursor.^[147,148] The use of CDCs as electrode materials for EDLCs has shown that the capacitance is governed by the CDC structure accordingly, along the rate performance as both values are significantly pore size dependent.^[149] Permann et al. synthesized different titanium CDCs and their respective capacitance values were between 100 and 130 F·g⁻¹, depending on the synthesis condition.^[150]

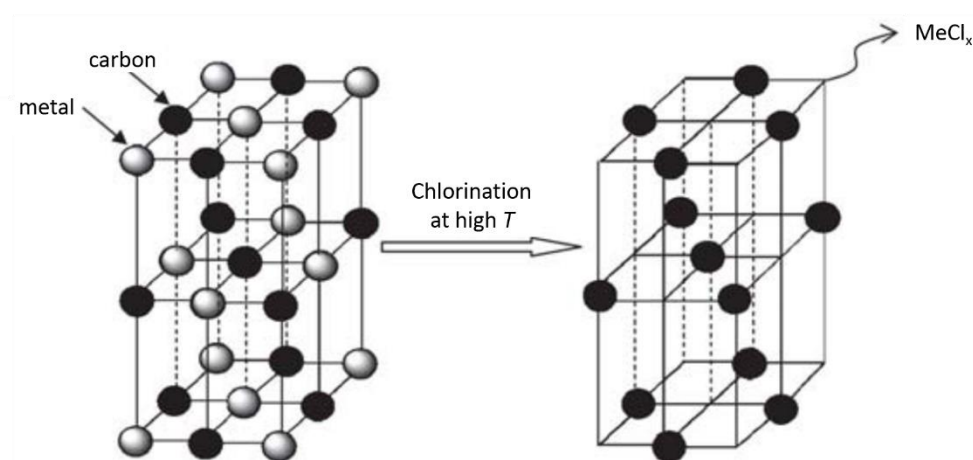


Figure 14: Selective high-temperature chlorination of a metal carbide lattice with an fcc structure (such as TiC and ZrC). Adapted from Sevilla and Mokaya.^[141]

An important observation was the capacitance values of a series of Ti-CDCs, which were synthesized at different temperatures of 600 to 1200 °C. The electrochemical investigations have shown the contributions to the capacitance of pores below 2 nm are significantly higher than the contributions of larger pores. The maximum contribution to the capacitance was provided by the pores, which had the size of the non-solvated electrolyte ions.^[151,152] It was postulated that the electrolyte ions can penetrate into small pores, partially or completely removing their solvate shell as shown in Figure 15.^[153] By doing so, the electrolyte ions experience no screening of charge of the solvent molecule and the distance to the electrode surface is shortened and thereby decreasing the double layer thickness. This results in an increase of the capacitance, which can be deduced from equation (4). It should be noted, that

the distance between the two plates d in equation (4), is now addressed as the double layer thickness.

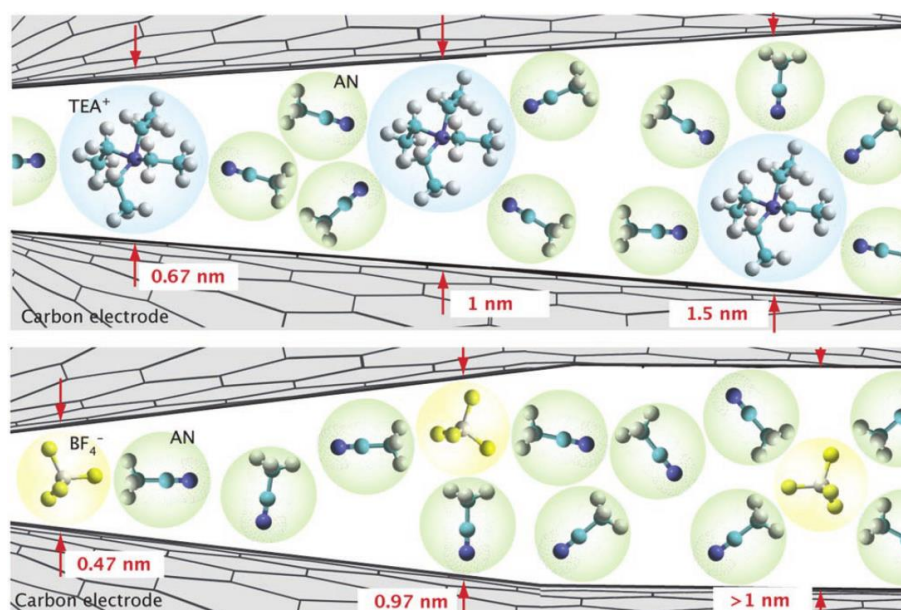


Figure 15: Geometric confinement of ions in extremely small pores. Both anions (BF_4^-) and cations (TEA^+) can enter the pores partial or full removal of the solvent-molecule (acetonitrile, AN) and no screening of charge occurs at pore sizes below 1.5 and 1 nm, respectively.^[153] Copyright 2008, Wiley-VCH Verlag GmbH & Co. KGaA. Reproduced with permission.

CNTs and carbon nanofibers are mainly produced by catalytic decomposition of hydrocarbons.^[13,154] So called single-walled carbon nanotubes and multi-walled carbon nanotubes can be prepared, depending on the synthesis parameters. These have a fully accessible external surface and high electric conductivity, which is why they are candidates for electrode materials in EDLCs.^[11,13,98,154] The specific capacitance of CNT based electrodes is greatly influenced by the purity and the morphology of the CNT material. It is possible to deposit CNT perpendicular to the current collector, thus producing a so-called CNT forest, in which the diameter of the CNTs determine the porosity of the electrode as well as the distance between the CNTs. Thus, increasing the distance between the tubes on the electrode could increase the capacitance retention at high currents, but an increased distance between the tubes decreases the amount of CNTs on the current collector and therefore the effective surface of the electrode.^[155] The specific capacitance of purified CNT powders in aqueous electrolytes is comparatively low in the range of 20 to 80 $\text{F}\cdot\text{g}^{-1}$, and is mainly attributed to the hydrophobic property of the CNT surface, which hinders

the accumulation of water-solvated electrolyte ions.^[155] The capacitance can be increased by a subsequent oxidative process up to $130 \text{ F} \cdot \text{g}^{-1}$. These oxidative treatments modify the surface chemistry and introduce additional functional oxygen groups that are able to contribute to pseudocapacitance as it is described in more detail later in this section.^[26,156]

Graphene is a one-atom thick layer of graphite, which corresponds to the basal plane, and can be considered to be building blocks of many structured carbons like CNTs or graphite.^[157] Graphene based carbon materials can be 2-D structured and can exhibit a flake-like shape and, in theory, can provide specific surface areas above $2500 \text{ m}^2 \cdot \text{g}^{-1}$ depending on the orientation and length of the flakes, yet in practice is often below $500 \text{ m}^2 \cdot \text{g}^{-1}$ for graphene based electrodes.^[158–160] Graphene can be prepared by thermal exfoliation of graphite oxide or by reduction of suspended graphite oxide sheets, which are agglomerated into graphene particles after the reduction.^[161,162] Multilayer graphene films have often been the focus of research, as they possess valuable properties, like their high intrinsic electric conductivity, which enables low internal resistance of the electrode, leading to high power densities. Additionally possess a structural flexibility and are lightweight.^[163–165] Many research efforts have been dedicated to exploring novel processing methods to obtain graphene-based films, such as spin-coating, layer-by-layer deposition, vacuum filtration, and interfacial self-assembly.^[166,167] Besides the decrease of accessible surface area and reduction of ion diffusion rate, the agglomeration and restacking due to the strong π - π interactions between the layers is a critical issue. Many attempts have been undertaken to solve this processing bottleneck, by using template-assisted growth of the sheets or adding spacers between the graphene layers.^[168] Nevertheless, the latter also limits the access of ions to the active surface on the graphene planes, even if the bridges favor the reduction of graphene sheets aggregation.^[102] Introducing additional porosity in the graphene framework layer is a possibility to enhance ion diffusion and increasing the accessible surface area. Recently, Xu et al. reported freestanding holey graphene frameworks, also called graphene nanomesh, with efficient ion transport pathways.^[169] The graphene frameworks were prepared through hydrothermal reduction of graphene oxide with simultaneous etching of graphene at around 200°C , owing to the presence of H_2O_2 molecules. Due to the formation of nanopores in the graphene sheets, the 3-D self-assembled structure enables to reach high capacitance values ($298 \text{ F} \cdot \text{g}^{-1}$) and a high

retention of capacitance at high currents of 83 % in organic electrolyte. Although the electrochemical performance of the holey graphene framework was good, the material was quite far from intact graphene, as it was formed by removing a large number of carbon atoms from graphitic planes. Zhu et al. proposed a similar approach. Graphite oxide was treated via microwave to obtain exfoliated graphene sheets.^[170] The sheets were chemically activated with different amounts of KOH and highly porous graphene sheets, called activated microwave enhanced exfoliated graphite oxide, were produced with BET surface areas up to $3100 \text{ m}^2 \cdot \text{g}^{-1}$, which is unusually high for graphitic carbons. Regarding the electrochemical performance, high capacitance values of $166 \text{ F} \cdot \text{g}^{-1}$ were achieved for current densities between 0.7 and $5.4 \text{ A} \cdot \text{g}^{-1}$. However, the retention of capacitance for high current densities is an important factor and was not reported. It may be stated that promising graphene based electrode materials are similar in porous properties to activated carbons. The latter are still preferred because they cost significantly less, although the electrical conductivity of graphene-based materials is higher.^[120]

Doping carbonaceous materials with nitrogen induces changes in their physical, chemical and electrochemical properties. Moreover, nitrogen doping can alter the electronic and chemical structure of the carbons, enhancing their chemical stability, surface polarity, electrical conductivity and electron-donor properties. Therefore, nitrogen-doped carbons are promising electrode materials supercapacitors.^[171,172] The most common method for the synthesis of nitrogen-doped carbons is the use of nitrogen-containing precursors.^[173,174] A new method is the combination of carbonization, nitrogen functionalization and activation into one single process.^[175,176] In general, there are four types of doped nitrogen in carbons depending on the bonding environments, including pyrrolic, pyridinic, quaternary N/graphitic N and nitrogen oxides of pyridinic nitrogen, as shown in Figure 16a. Whereas quaternary nitrogen enhances the electric conductivity of the doped carbon material, pyridinic, pyrrolic and pyridonic nitrogen will improve the capacitance of the material via faradaic charge transfer reactions, as shown in Figure 16b. The overall capacitance in aqueous electrolytes can be improved with increasing nitrogen content in alkaline and acidic media.^[177,178] Significant improvement of capacitance in organic electrolytes was not observable, since there are no protons for the charge transfer available.^[179] Oxygen doping is also a possibility to enhance the capacitance.^[115] A common method to achieve a highly oxygenated carbon is to choose a suitable oxygen-rich

precursor for carbonization or to treat carbon in a strongly oxidative atmosphere. The high value of capacitance is related to charge transfer reactions on quinone, phenol and ether groups.^[180,181]

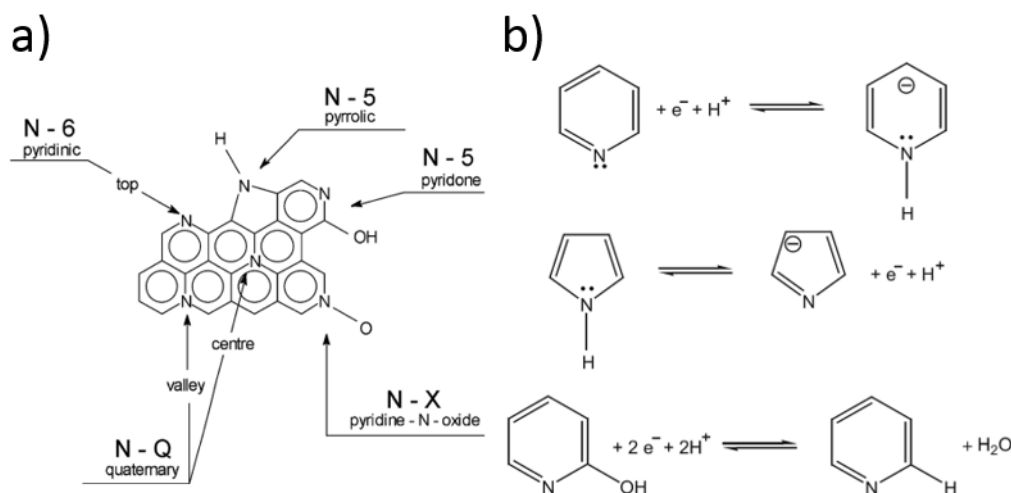


Figure 16: (a) Bonding configuration for nitrogen atoms in nitrogen-doped carbons.^[182] Copyright 2003, Elsevier. (b) Possible redox reactions associated involving pyridinic, pyrrolic and pyridone-type nitrogen species.^[171] Copyright 2016, reproduced by permission of the Royal Society of Chemistry.

1.4.3 Role of surface area on the capacitance of EDLCs

The surface area of activated carbon electrode materials is a crucial factor regarding the total capacitance of EDLCs. The capacitance increases with a higher specific surface area, as equation (4) suggests. The general trend of an increasing capacitance with increasing surface area is limited, as a saturation of capacitance is observable for BET surface areas above 2500 m²·g⁻¹, determined by gas physisorption.^[115] As mentioned by Centeno and Stoeckli and their co-workers, the use of the BET method to determine the specific surface area can be misleading, because it easily overestimates the surface area of microporous activated carbons.^[183–185] The density functional theory (DFT) method is widely used and is currently the most advanced methodology to extract porosity data from gas sorption isotherms and effectively avoids the limitations of the BET theory.^[7,186,187] Results of the DFT method are the pore size related cumulative pore volume and the cumulative specific surface area. The obtained DFT surface area reflects the probably most reliable value for the carbon, but the same trend of the saturation of capacitance with increas-

ing surface area was observable, as shown in Figure 17. Therefore, the electrochemically active surface area can be determined by subtracting the surface of pore sizes that are inaccessible to electrolyte ions from the total surface area. Taking for example the ion size of tetraethylammonium (0.67 nm) and tetrafluoroborate (0.45 nm) into account, pores smaller than these values are inaccessible to the ions, which results in a reduction of the accessible surface area as shown by Jäckel et al.^[188,189] It was demonstrated the surface capacitances, which are based on the specific surface accessible for the electrolyte ions, are not clearly dependent on the pore sizes.

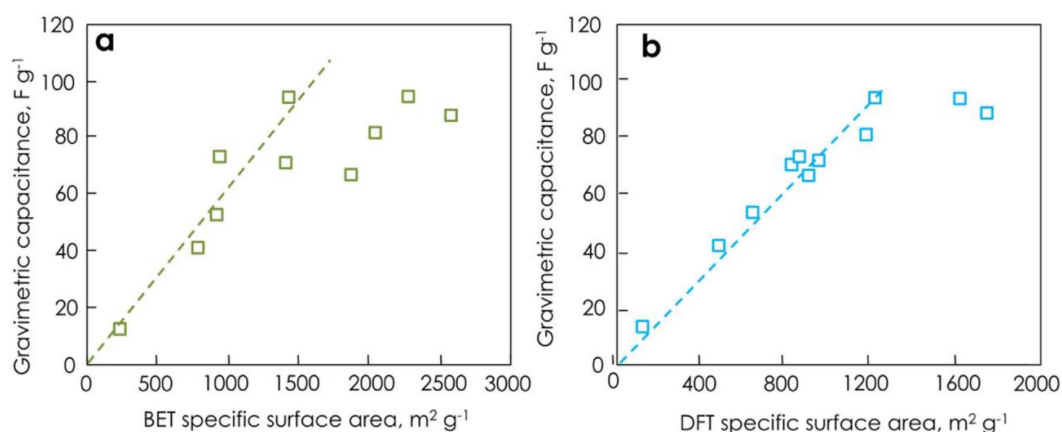


Figure 17: Gravimetric capacitance vs (a) BET and (b) DFT specific surface area of a series of activated carbons.^[120] Copyright 2018, Elsevier.

1.4.4 Role of the pore size on the capacitance of EDLCs

As mentioned in section 1.4.2, Chimola et al. observed an anomalous increase of surface area normalized capacitance for subnanometer pores with the size of the bare electrolyte ion (around 0.7 nm).^[152] The validity of the confinement effect has been subject of discussion in recent years. Some researchers assume the capacitance is independent of the pore size, which is described by a “regular pattern”.^[184,185,190,191] Regarding these studies, results from various scientific papers were taken into account and compared, in which the carbons were used as electrode materials in organic electrolytes. The normalized capacitance values were calculated using the BET specific surface area and the electrochemical active surface area generated by pores larger than 0.63 nm, which reflects the usable surface area of the carbon electrodes where capacitive charge storage is possible. The capaci-

tance values were plotted against the average micropore size calculated by the Dubinin-Radushkevich (DR) method as shown in Figure 18. The capacitance values normalized by the BET specific surface area show an anomalous increase of capacitance for the smallest accessible pores around 0.7 nm, which would confirm previous observations (Figure 18 a). The capacitance values normalized by the electrochemically active surface area on the other hand, show no clear trends, for the entire pore range from 0.7 to 2 nm, hence behaving in a “regular pattern”. The normalized capacitance values scatter around $0.094 \pm 0.011 \text{ F} \cdot \text{m}^{-2}$ (Figure 18 b). Therefore the authors assume the anomalous increase of capacitance for pores around 0.7 nm is a result of the capacitance normalization with the inaccurate BET surface area. What is also important to note is that these studies represent the dependence of the capacitance of the volume-weighted average micropore size. Even microporous carbons do not have a narrow and monomodal pore size distribution, instead they are rather multimodal. Therefore, the pore size specific influences on the capacitance cannot be obtained from the studies. This requires different approaches.

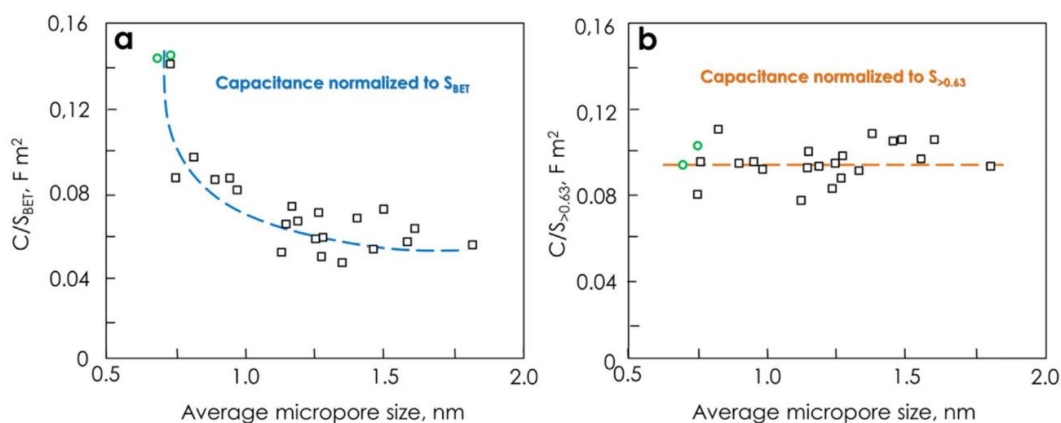


Figure 18: Variation of normalized capacitance in TEABF₄/ACN vs. average micropore size for a variety of porous carbons: (a) normalized to BET surface area; (b) normalized to the electrochemical active surface area $S_{>0.63 \text{ nm}}$ for pores larger than 0.63 nm.^[120] Copyright 2018, Elsevier.

The introduction of the electrochemical active surface area is an important factor for the proper determination of the influence on pore size and the capacitance. However, one problem of the previous investigations was that the dependence of the capacitance was determined only against an average pore size, which does not reflect the actual pore size distribution of most carbons as it only indicates an average

value. Chemically activated carbons usually have additional mesopores and therefore a multimodal pore size distribution, which is why the relation between the average pore size and the specific capacitance only is very inaccurate.^[189,192]

Although the subject is widely discussed, it was experimentally proven that partially of fully desolvated ions participate in the formation of the electric double layer.^[193] The confinement effect of partial or full removal of the solvation shell of ions, entering subnanometer pores is therefore possible. The Helmholtz model of the rigid double layer can be used for flat plate configurations and can describe the pore size-dependent thickness of the double layer in perfectly ordered slit pores, but is inaccurate for nanopores with different degrees of curvature caused by different pore geometries. Therefore, new models of capacitors have been proposed to describe the double layer formation in a curved and highly nanoporous carbon network in porous carbons. Depending on the synthesis, nanoporous carbons can have various pore shapes, such as slit, cylindrical and sometimes spherical types.^[52] Huang et al. adapted the classic Helmholtz model to develop a concept based on cylindrical mesopores (2 to 50 nm) and micropores (< 2 nm). In the mesopore regime, solvated ions enter the pores and approach the pore walls to form electric double-cylinder capacitors as shown in Figure 19 a.^[194,195] The surface area normalized double-cylinder capacitance is given by the following equation:

$$\frac{C}{A} = \frac{\varepsilon_0 \varepsilon_r}{b \ln[b/(b-d)]} \quad (7)$$

where b is the radius of the cylinder pore and d the double-layer thickness. In such case, the effect of the pore size and pore curvature becomes prominent compared to the double-layer thickness d . In the micropore regime, partially or fully desolvated ions enter the pores and line up to form electric wire-in-cylinder capacitors, as shown in Figure 19 b and its capacitance is given by the following equation:

$$\frac{C}{A} = \frac{\varepsilon_0 \varepsilon_r}{b \ln(b/a_0)} \quad (8)$$

where the key quantity is a_0 , the effective size of the ion (the extent of electron density around the ions).^[103,194,195] These models can be combined to simulate the

total capacitance of a carbon electrode material with a multimodal pore size distribution using equation (8) for micropores, equation (7) for mesopores and (4) for macropores with their respective surface areas.

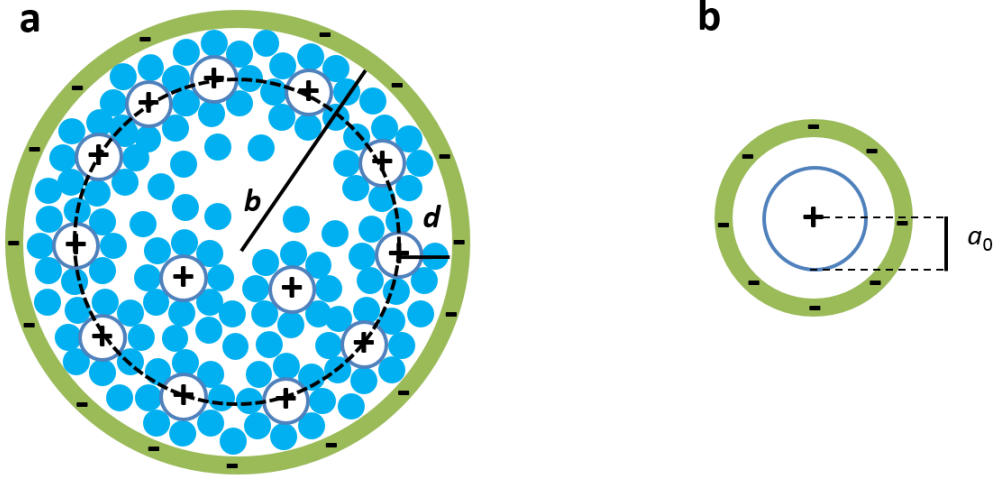


Figure 19: Scheme of the (a) electric double-cylinder capacitor model with the pore radius b and the double layer thickness d and the (b) electric wire-in-cylinder capacitor model with the effective size of the ion a_0 or ion radius.

The electric double cylinder-capacitor and electric wire-in-cylinder capacitor models assume a cylindrical pore shape for micro- and mesopores and alternative models have been proposed for other pore geometries. If the mesopores have a spherical shape, the geometric configuration of adsorbed electrolyte ions would differ, leading to the following equation derived by Wang et al.:^[196]

$$\frac{C}{A} = \frac{\varepsilon_0 \varepsilon_r}{d} \left(\frac{b-d}{b} \right) \quad (9)$$

Although the electric double-cylinder capacitor model assumes a cylindrical pore geometry for micropores, it is supposed that micropores in carbon materials are rather slit pores, which can also show a curvature of pore walls.^[197] Feng et al. suggested that micropores are too narrow for electrolyte ions to experience the effect of pore wall curvature on the electric double layer. They adjusted the classic flat plate model, assuming slit-shaped micropores, to account for the confined double layer leading to a sandwich-type capacitor model, as described in equation (10) and

shown in Figure 20.^[198] Furthermore, the effective double-layer thickness d_{eff} was introduced, which is the distance between the pore wall and the outer electron shell of the electrolyte ion.

$$\frac{C}{A} = \frac{\varepsilon_0 \varepsilon_r}{b - a_0} \quad (10)$$

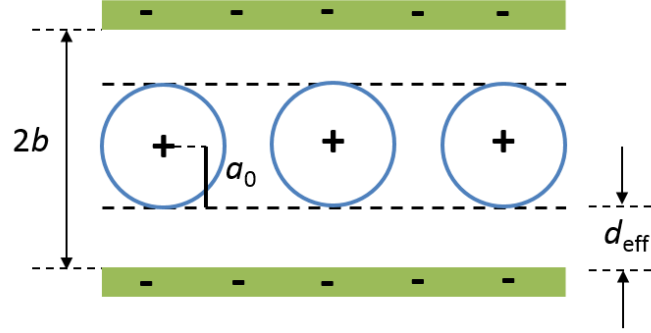


Figure 20: Sandwich-type capacitor model for confined slit-shaped micropores with the pore diameter of the electrode material $2b$, the effective ion radius a_0 and the effective double-layer thickness d_{eff} .

With the effective double-layer thickness, it is possible to describe the anomalous increase of capacitance for subnanometer pores very well. Hsieh et al. used the new capacitor model for slit pores (Figure 20) in combination with the electric double-cylinder capacitor model for mesopores (Figure 19 a) to simulate the capacitance of activated carbons based on data derived from physisorption measurements.^[199] The relative permittivity of the solvent also plays a decisive role for determining the influence of the pore size on the capacitance. It is assumed that in confined spaces, e.g. in small pores, this permittivity is significantly smaller compared to bulk space. This is due to the restricted mobility of the solvate molecules, which leads to the fact that the electric field between electrolyte ions and electrode surface is maintained to a lesser extent due to the limited orientation polarization of the solvent molecules. Consequently, they proposed a pore size dependent dielectric permittivity, which increases linearly up to a pore size of 2 nm. According to equation (10), the capacitance increases with increasing pore size, considering the increase of relative permittivity. However, since the term $(b - a_0)$ becomes larger with increasing pore size, the capacitance is reduced. These two counteracting effects

lead to a constant capacitance for the entire range of micropores. Despite this approach, which contradicts the anomalous increase of capacitance at subnanometer pores, experimental and simulated capacitance values matched reasonably for organic and aqueous electrolytes. Just recently, Zuliani et al. evaluated different combinations of double layer capacitor models. They used the electrical wire and sandwich type pore model for micropores and the cylinder and spherical model for mesopores for various activated carbons, and compared the simulated capacitance with the measured capacitance.^[200] Using high resolution scanning electron microscopy (SEM) for investigation of the pore shape it was found that the activated carbon materials had curved mesopores. Furthermore, they observed the best match of simulated and measured capacitance for a combined model of slit-shaped pores for micropores and cylindrical shaped pores for mesopores, confirming the approach of Hsieh et al.

1.5 Hydrogen storage of porous carbons

Hydrogen is an ideal clean energy vector since H_2 is both carbon- and pollution-free and its burning product is only water, while the combustion of fossil fuels generates carbon dioxide and a variety of pollutants.^[201] Moreover, hydrogen is one of the most abundant elements and makes up 75 % of normal matter by mass, which provides rich sources for H_2 generation.^[202] Hydrogen storage is therefore a highly investigated field in scientific research. The solid state hydrogen storage is a promising approach. This can be achieved through sorption of H_2 on or in a solid substrate, relying on two principle mechanisms, which is either adsorption on the substrate surface via physisorption or dissolved hydrogen atoms forming chemical bonds on the substrate surface via chemisorption. As shown in the energy potential diagram in Figure 21, the combination of terms of long-range attractive forces and short-range repulsive forces lead to a broad minimum in the potential energy curve which corresponds to the physisorption process. In contrast, the energy minimum of chemisorption has a larger value, but requires an activation energy of molecular dissociation, whereas physisorption has no energy barrier. Therefore the physisorption process is non activated and fast kinetics are characteristic for physical adsorption, thus being a promising approach in storing hydrogen on porous host materials.^[203] When porous host materials are used for hydrogen storage, physisorption is commonly used for storage. H_2 molecules are adsorbed at

temperatures higher than their boiling point (20.4 K), caused by the weak interaction forces, namely van-der-Waals-forces between the H_2 molecules and the adsorbent surface. (For further details of physisorption mechanism see section 2.1) Therefore, the average heat of adsorptions are rather small and low temperatures around 77 K are required for storage materials to adsorb hydrogen. These temperatures are technically very difficult to realize for various applications.^[204]

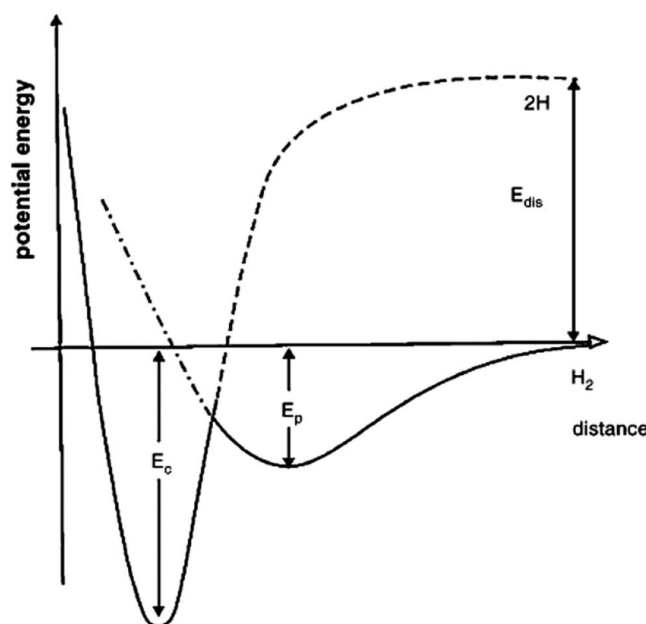


Figure 21: Potential energy diagram for chemisorbed E_c and physisorbed E_p hydrogen as a function of the distance from the surface of the adsorbent.^[203] Copyright 2005, Elsevier.

Hydrogen storage via physisorption is completely reversible and exhibiting very fast kinetics which is mandatory for efficient hydrogen storage and release, and porous carbons are one of the most promising host materials.^[4,6,201,202] The surface area of storage materials is an important factor. Activated carbons are therefore well suited as host materials, as they usually have very high specific surface areas. It is reported that an approximately linear relationship exists between the hydrogen uptake capacity of hydrogen at 77 K and the specific surface area of the porous carbon material, independent of the nature of the carbon materials as shown in Figure 22 a.^[203,205–207] It is estimated, that the gravimetric uptake of hydrogen on porous carbons at 77 K and 35 bar is about 1 wt% H_2 per $500 \text{ m}^2 \cdot \text{g}^{-1}$ of the specific BET surface area.^[208] The surface area is an important factor, but the pore sizes are crucial for the uptake capacity optimization. A linear correlation is usually obtained

when relating the hydrogen uptake capacity to the micropore volume.^[209] As shown in Figure 22 b, various observations stated the dominating capacity provided by subnanometer pores below 0.7 nm.^[206,207,209–211] For micropores in general, the interaction energy between H₂ molecules and carbon adsorbents can be enhanced in narrow pores due to the overlap of the potential fields from both sides of the pore wall. This means adsorption enthalpies decrease as pore size increases, limiting the attractiveness of larger pores to physisorption. Furthermore, the density of pores decreases with the square of pore size increases and the saturation limit for hydrogen storage in a physisorption based nanoporous material at cryogenic temperature can be estimated as the product of the micropore volume and the density of liquid H₂ in the pores.^[212]

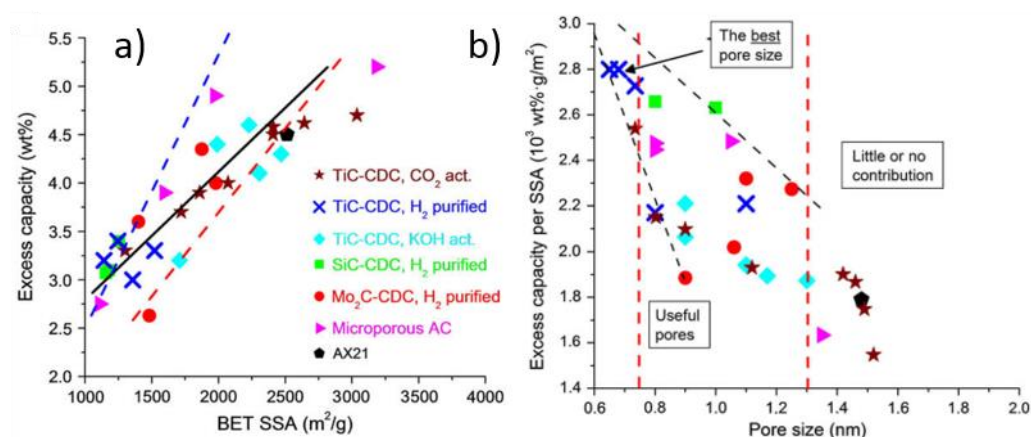


Figure 22: (a) Excess hydrogen capacity of different carbons at 77 K, 60 bar vs BET surface area. (b) Excess capacity normalized to surface area vs. average pore size for the samples in (a).^[210] Copyright 2009, Elsevier.

Carbons based on synthetic polymers have been widely investigated as host materials for hydrogen storage. High hydrogen storage capacity values at 77 K and 1 bar were always achieved when the porous carbons possessed a combination of high specific surface area and high micropore volume. The carbon sample NAC-1.5-600 based on imidazolium chloride form Sethia and Sayari reached a gravimetric hydrogen storage capacity of 2.96 wt%.^[213] Zhang et al. obtained even better results when they cross-linked a phenyltrimethylsilane-based polymer, which was carbonized and activated afterwards.^[78] The gravimetric hydrogen uptake of the carbon sample CHCPB-K-700 was 3.25 wt.% at 1.13 bar and 77 K. Carbons based on biosource materials are also frequently used as host materials.^[128]

Blankeship II and Mokaya synthesized cigarette butt-derived carbons, with an exceptional high BET surface area of $4310 \text{ m}^2 \cdot \text{g}^{-1}$ ($3867 \text{ m}^2 \cdot \text{g}^{-1}$ micropore surface area) and ultra-high pore volume of $2.09 \text{ cm}^3 \cdot \text{g}^{-1}$ ($1.71 \text{ cm}^3 \cdot \text{g}^{-1}$ micropore volume). The gravimetric hydrogen uptake at 77 K and 1 bar of the sample SF-4700 was one of the highest measured uptakes with 4.0 wt% so far, and is mainly attributed to the high specific surface area and high content of micropores below 1 nm. In addition to pore sizes, doping of the carbon framework is considered to enhance the hydrogen uptake, especially observed for nitrogen doped carbons.^[214,215] The influence of oxygen is still unclear, but the presence of oxygen functional groups may enhance the hydrogen uptake capacity likewise.^[216] Blankeship II et al. synthesized oxygen-rich carbon, derived from chemical activated hydrochar, with oxygen contents up to 22.8 wt%.^[217] The gravimetric hydrogen uptake was as high as 3.9 wt%, but the sample had a very high specific surface area and a very high content of micropores smaller than 1 nm. Therefore, a direct relation from the high hydrogen uptake to the high oxygen content could not be drawn.

1.5.1 Hydrogen storage of porous materials

Metal-organic frameworks have also been in the focus of research for host materials for hydrogen storage.^[218,219] Due to their ordered network of channels or pores, small molecular gases such as carbon dioxide and hydrogen can be reversibly captured and released from the framework pores. Additionally, tailoring of pore size and surface area of metal organic frameworks is possible as well as the addition of specific functions, such as open metal sites.^[220] As one of few examples, a multitligand approach for the synthesis of metal organic frameworks lead to increased surface areas of the resulting porous materials like the porous metal organic framework UMCM-2, consisting of Zn_4O metal clusters linked together by two linear dicarboxylates and four trigonal planar ligands arranged in an octahedral geometry.^[221] The UMCM-2 possessed a high BET surface area of $5200 \text{ m}^2 \cdot \text{g}^{-1}$ and a high hydrogen uptake capacity of 6.9 wt% at 77 K and 4.6 MPa. A mesoporous metal organic framework using a secondary linker to stabilize a highly open framework structure, lead to a hydrogen uptake of 5.64 wt% at 77 K and 5 MPa.^[222] Another example is the polyhedral mesoporous metal organic framework NOTT-116 with a BET surface area of $4664 \text{ m}^2 \cdot \text{g}^{-1}$, which was synthesized by the formation of isophthalate-sustained cubaoctahedra, which prohibited framework interpenetration. The hydrogen uptake capacity of NOTT-116 was up to 9.2 wt% at 77 K and

5 MPa^[223]. Just recently it is suggested, that Li-ion doping of metal-organic frameworks can increase the uptake capacity, where Li-doped MOF-519 reaches a capacity of 2.27 wt% at 77 K and 1 bar.^[224] Zirconium-based metal-organic frameworks have proven to be suited for understanding and gaining insights into the structural and textural storage mechanisms of hydrogen storage under cryogenic conditions. The metal-organic framework NU-1103 displayed a high capacity of 14.4 wt%.^[225] In general, metal organic frameworks emerge as an important class of porous materials regarding the hydrogen storage with different approaches, like light metal doping and post functionalization.

Other porous materials have been investigated for their application as host materials for hydrogen storage. Boron nitride exhibits good thermostability and resistance to chemicals. It has been theoretically suggested that boron nitride surface has a stronger interaction with hydrogen molecules, compared to a carbon surface due to the heteropolar band between boron and nitrogen atoms.^[226] Some storage properties of boron nitride nanostructures have been reported, like multiwalled boron nitride nanotubes, which can store up to 2.6 wt% of H₂ at 298 K and 10 MPa.^[227] Under similar conditions, collapsed boron nitride nanotubes had a gravimetric hydrogen storage capacity of 4.2 wt%.^[228] A different approach was the synthesis of oxygen-doped boron nitride nanosheets of 2 to 6 atomic layers by a sol-gel method.^[229] The material had a storage capacity of 5.7 wt% at 5 MPa and 298 K, which is one of the highest capacity values ever reported for boron nitride materials. The high hydrogen storage capacity is attributed to the oxygen-doping of the nanosheets, which exhibited increased hydrogen adsorption energies compared to pure boron nitride nanosheets.

In principle, the topic of hydrogen storage in nanoporous materials has been investigated in many ways. Besides hydrogen storage via physisorption in nanoporous materials like carbons, metal-organic frameworks, boron nitrides or organic polymer networks different approaches are possible like the storage via chemisorption in nanostructured hydrides or nanomaterials like ordered mesoporous carbons as function support for hydrides.^[230,231] However, the focus of this work, will remain on the hydrogen storage via physisorption in nanoporous carbons.

2 Analytical methods

2.1 Gas physisorption

Gas physisorption is an analytical method, which investigates the porous character of materials. Gas adsorption is particularly interesting, as a large range of pore widths can be easily measured without damaging the material during the measurement. In addition to pore widths, further information such as specific surface area and specific pore volume can be determined. In gas adsorption, a distinction is made between physical and chemical adsorption, whereas the physical adsorption is mainly used for the characterization of porous materials. A fluid (adsorptive) is passed on a surface (adsorbent) and physisorption occurs, whereby non-adsorbed gas and adsorbed gas are distinguished. The adsorbed gas is called adsorbate. Physisorption is basically reversible, the process of adsorption of a gas to a surface is called adsorption and the removal of the gas from the surface is called desorption (see Figure 23).^[232] The interactions between the gas and the surface are based on van-der-Waals forces. In porous materials, the physisorption is determined by the fluid-wall and fluid-fluid interactions, as well as the limited or confined pore space, which has an influence on the thermodynamic stability and the state of a fluid in the pore.

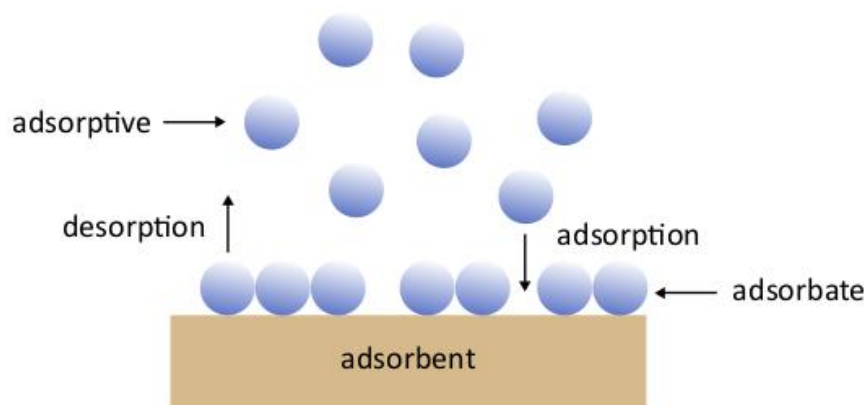


Figure 23: Scheme of the physisorption processes.

Physisorption measurements are carried out at a constant temperature, which is adapted to the used gas. There are two possibilities to obtain the isotherms of a physisorption measurement. The gravimetric and the volumetric measurements are

possible, with the latter being the more common method for many gases. The standard gases for volumetric gas adsorption are nitrogen and argon. Typically, isotherms are measured for both gases at their respective boiling temperatures, 77 K for nitrogen and 87 K for argon. The determinable pore widths lie between 0.3 and 100 nm in a measuring range of $10^{-7} \leq p/p_0 \leq 1$, with p/p_0 being the relative pressure. Physisorption often refers to pore widths rather than pore diameters, as there are different pore geometries. The pore width of a cylindrical pore corresponds to the diameter of the cylinder; in the case of slit pores, the pore width describes the smallest distance between the pore walls. It is particularly important for gas adsorption to remove adsorbed gas from the sample before measurement. This is done in a vacuum at elevated temperatures. Especially for carbons with very small pores, a thorough activation is necessary, because otherwise the already adsorbed gases adulterate the results of the measurement.

An isotherm usually includes the adsorption and desorption of a gas. To measure the adsorption isotherm, the pressure of the adsorptive on the sample is increased to the saturation vapor pressure and the adsorbed gas volume is determined. In order to subsequently measure the desorption isotherm, the sample is evacuated step by step after reaching the saturation vapor pressure. At low relative pressures, the micropores are filled first. In these, the adsorption potentials of opposing pore walls overlap, so that adsorption is mainly controlled by the interactions of the molecules with the pore wall. The smallest micropores (< 0.7 nm, also called ultramicropores) are already filled at relative pressures of $p/p_0 < 0.01$. In the range of $0.01 \leq p/p_0 \leq 0.2$ larger micropores, also called supermicropores, are filled. First, a monolayer of gas molecules is formed on the surface of the adsorbent, on which further layers (multilayers) can form as a result of van-der-Waals interactions between the adsorbate molecules. Due to the weak interaction of adsorbent and adsorbate in large micropores, further adsorption takes place mainly due to interactions between the adsorbate molecules. At relative pressures of $p/p_0 > 0.2$ only multilayer adsorption takes place. As long as the adsorbed film is still thin, it is stabilized by the adsorption potential of the walls. However, the influence of surface tension and curvature increases with the thickness of the adsorbed film. If the film exceeds a certain thickness, stabilization is no longer possible and the gas begins to condense inside the pore. This process is called capillary condensation and occurs only in pores larger than micropores. The larger the pore in which the adsorption takes place, the larger

the relative pressure at which capillary condensation occurs. The successive filling of pores of different sizes with increasing relative pressure is used to determine the pore size distribution of a material from the isotherm.^[232]

Depending on the material at which the physisorption takes place, different physisorption isotherms are obtained. The IUPAC distinguishes between six isotherm types (type I to VI), with two variants of type I and type IV (type I(a) and (b) and type IV(a) and (b)).^[7,233,234] Figure 24 shows the different types of isotherms. A type I isotherm is characteristic for micropores. The initial gradient is very large due to the strong interactions between adsorbent and adsorbate. For micropores smaller than 1 nm in diameter, type I(a) isotherms are obtained, while micropores and small mesopores with pore diameters between 1 and 2.5 nm lead to type I(b) isotherms with a slightly less steep slope. For non-porous and macroporous materials, the result is a type II isotherm in which multilayer adsorption can be observed in a large relative pressure range. Type III isotherm is a special case of type II isotherm, which occurs when the interactions between adsorbate and adsorbent are weak. Type IV isotherm is typical for mesoporous materials. The steep increase in the isotherm at higher relative pressures is due to capillary condensation. For pores whose diameter is larger than about 4 nm, a hysteresis occurs in the isotherm curve and the isotherm can be assigned to type IV(a). For smaller mesopores this hysteresis cannot be observed, resulting in the type IV(b) reversible isotherm. The reasons that lead to the occurrence of hystereses are explained in more detail in the next paragraph. Type V isotherm is a special case of type IV(a) isotherm if there are weaker interactions between adsorbate and adsorbent. A type VI isotherm occurs with layered adsorption on uniform, non-porous surfaces like graphitized carbon black.

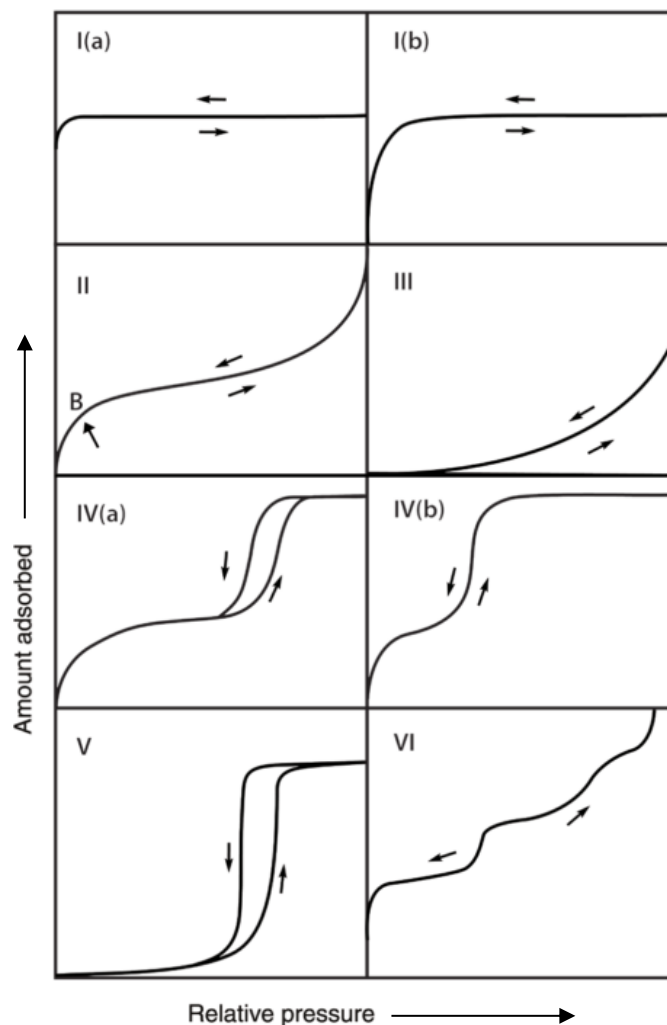


Figure 24: Classification of physisorption isotherms adapted from Thommes *et al.*^[7]

The hysteresis that occurs when larger mesopores are present can be explained by the mechanism of the capillary condensation during the adsorption. Some of the initially formed films form metastable bridges instead of growing films during adsorption and the nucleation of liquid compounds is inhibited, which delays the condensation of the adsorbate and occurs at higher relative pressures considering the actual pore size. During desorption, however, evaporation of the adsorbate takes place without the need for nucleation. This is in thermodynamic equilibrium and can be correlated directly with the pore diameter. Thus, adsorption and desorption branches of a type IV(a) isotherm do not overlap.^[187,235] In fact, hystereses can also occur for various other reasons and therefore differ in their profile. The IUPAC

distinguishes six forms of hysteresis (H1 to H5), where the H2 Type has the variants H2(a) and H2(b). The different forms of hystereses are shown in Figure 25.

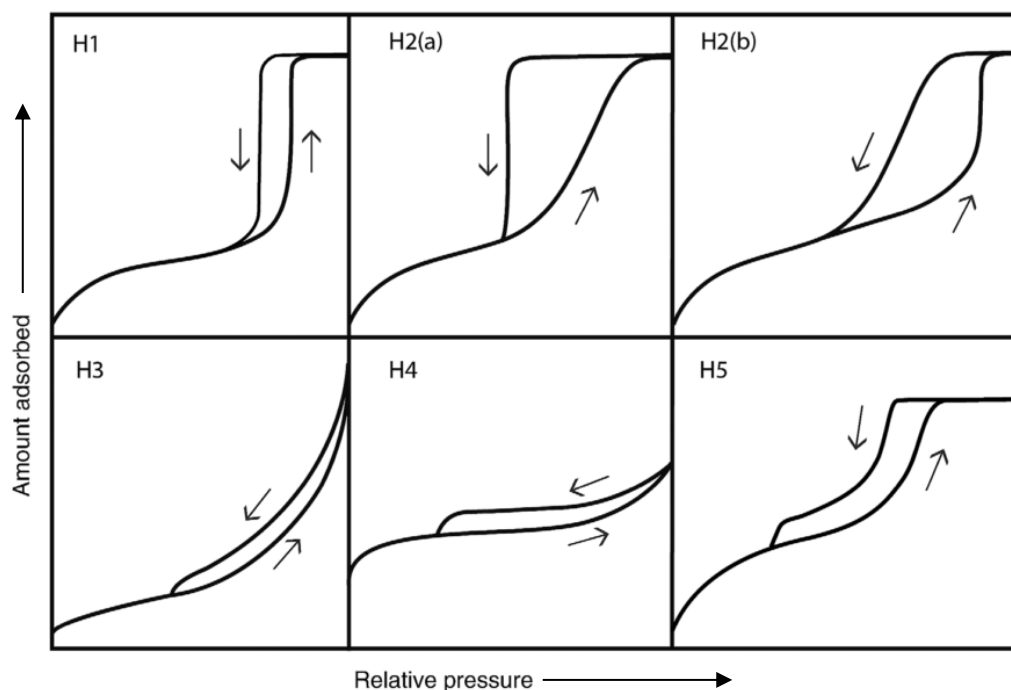


Figure 25: Classification of hysteresis loops adapted from Thommes *et al.*^[7]

The shape and geometry of the pores can be partially deduced from the shape of the hysteresis. For example, H1 hysteresis is characteristic of uniform, often cylindrical pores with narrow pore size distribution in which delayed adsorption occurs. H2 type hystereses are typical for pores that show pore entries smaller than the actual pores. Hysteresis of form H2(a) occurs when the pore entries show a narrow size distribution, while the form H2(b) is typical for pore entries broad a wide size distribution. Hystereses of type H3 usually occur when aggregates of plate-shaped particles are present or when there is a network of macropores that are not completely filled with condensate. The form of the H4 hysteresis is similar to the H3 hysteresis, but the isotherm tends to take the shape of a Type I isotherm in the range of higher relative pressures. It is often observed for aggregates of micro- or mesoporous zeolite crystals. In addition, hystereses of the forms H3 and H4 can be associated with a phenomenon called cavitation, which is described below. Hysteresis type H5 is characteristic of materials in which part of the pores are freely accessible for the adsorbent and another part is "blocked" by smaller entries.^[232,236] If a material is structured in such a way that access to large pores in a porous network is restricted

by smaller pores, so-called bottleneck pores, desorption of the adsorbate can take place in two different ways. Both desorption mechanisms differ from the simple pressure-dependent evaporation that occurs in uniform pores. The type of mechanism depends on the diameter of the pore entries. If the diameter is larger than a certain critical diameter, which is about 5 to 6 nm for nitrogen, the actual pore is emptied at the relative pressure at which the adsorbate evaporates in the pore entries. Even if evaporation in the large pore would actually take place at higher relative pressures, this is not possible if the pore is blocked by the adsorbate in the smaller entries. For this reason, the term "blocked pores" is also used. If the pore diameter is smaller than the critical diameter, desorption takes place via a cavitation mechanism. This means gas bubbles spontaneously form within the condensate in the pore, which can diffuse through the pore entry without emptying it. In contrast to the mechanism with blocked pores, the relative pressure in the cavitation mechanism does not depend on the size of the pore entries, but exclusively on the properties of the fluid in the pore. The same gas is therefore always desorbed at a similar relative pressure.^[187,232,236,237] Adsorption, on the other hand, proceeds normally regardless of the size of the pore entries. This means that considering the delayed condensation, it is possible to determine the actual pore size distribution from the adsorption, while the size of the pore entries can be determined from the desorption in the case of blocked pores. When cavitation occurs, the pore size cannot be determined from the desorption branch, and only a gas-specific value is obtained. Figure 26 provides an overview of the profile of isotherms in the different mechanisms of delayed condensation.

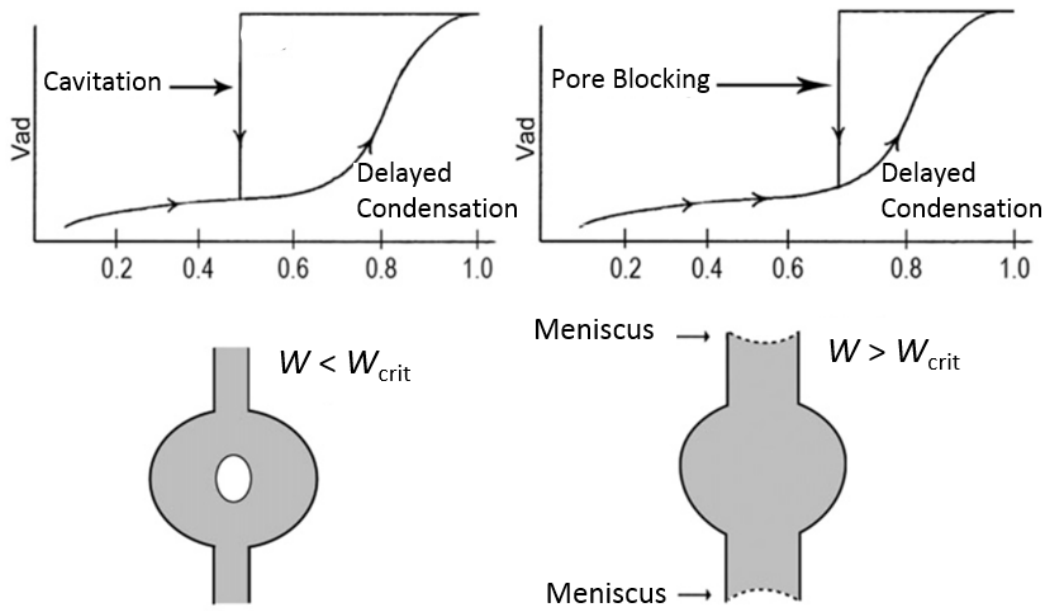


Figure 26: Scheme of cavitation and pore-blocking phenomena. W is the size of the pore neck and W_{crit} is the critical neck size at which cavitation occurs if W falls below. Adapted from Thommes *et al.*^[187]

In the case of blocked pores, the shape of the hysteresis differs depending on the size distribution of the pore entries: If there is a narrow size distribution of the pore entries, the isotherm shows an almost triangular appearance (hysteresis type H2(a)), since the desorption of the gas takes place in a very small pressure range. Whether the actual pore shows a narrow or wide size distribution only influences the pressure range by adsorption. If, on the other hand, there is a narrow size distribution of the actual pores and a broad distribution of pore entries, an almost inverse form of H2(a) hysteresis is obtained, the H2(b) hysteresis, in which the desorption drops over a larger pressure range.^[7,187] This is illustrated in Figure 27.

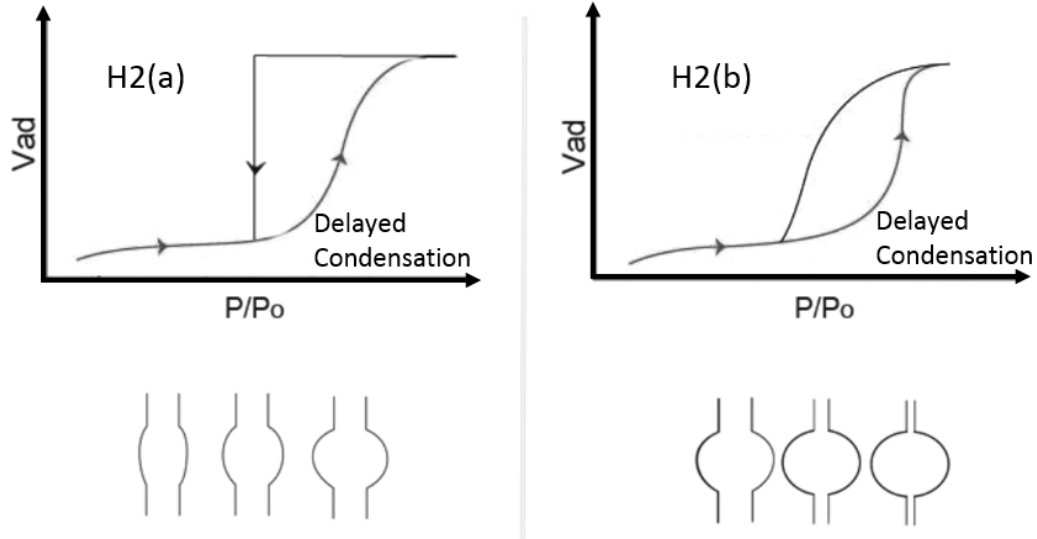


Figure 27: Scheme of the influence of the size distribution of the pore entries and the actual pores on the course of the isotherm when blocked pores occur. Varying actual pore sizes with narrow pore entries (left) and varying pore entries with narrow actual pore size (right). Adapted from Thommes *et al.*^[232]

The surface area of a solid can also be determined from the sorption isotherm. The Brunauer-Emmet-Teller (BET) method can be used to determine the surface area.^[238] It is assumed that a monolayer of gas molecules is initially formed on the surface. Further molecules can then be adsorbed onto the initial layer, which are bound by van-der-Walls forces. The velocities of ad- and desorption are constant at thermal equilibrium and the adsorbed gas amount n_{ads} can be described by equation (11).

$$n_{\text{ads}} = \frac{n_{\text{mono}} \cdot C \cdot \frac{p}{p_0}}{\left(1 - \frac{p}{p_0}\right) \left[1 + (C - 1) \cdot \frac{p}{p_0}\right]} \quad (11)$$

Here n_{mono} is the amount of substance of a monolayer, p/p_0 the relative pressure and C a constant, which is described by equation (12).

$$C = \frac{k_{\text{ads},1} \cdot k_{\text{des}}}{k_{\text{ads}} \cdot k_{\text{des},1}} \cdot \exp\left(\frac{E_{\text{ads},1} - E_{\text{ads}}}{R \cdot T}\right) \quad (12)$$

In this equation $k_{\text{ads},1}/k_{\text{des},1}$ are the velocity rate constants of the ad- and desorption, $E_{\text{ads},1}$ the adsorption energy of the first layer, E_{ads} the adsorption energy of the other layers, T the temperature and R the ideal gas constant. The indices for the velocity

rate constants indicate the first adsorbed layers starting with zero, and then counting. Since the following layers are interacting via van-der-Waals forces of the adsorbate only, the following applies to all layer with $i > 1$: $k_{ads,2}/k_{des,2} = k_{ads,3}/k_{des,3} = \dots = k_{ads,i}/k_{des,i}$. Equation (11), which describes the amount of adsorbed gas, can be transformed into the linear equation.

$$\frac{\frac{p}{p_0}}{n_{ads} \cdot \left(1 - \frac{p}{p_0}\right)} = \frac{1}{n_{mono} \cdot C} + \frac{C - 1}{n_{mono} \cdot C} \cdot \frac{p}{p_0} \quad (13)$$

Here $(C-1)/(n_{mono} \cdot C)$ is the slope and $1/(n_{mono} \cdot C)$ the ordinate of the straight line. Assuming the formation of the monolayer is complete before the multilayer formation begins, it can be defined that $C \gg 1$ and from the slope and the ordinate of the straight line, it is possible to determine the amount of adsorbed gas of the monolayer. According to equation (14), the specific surface area S_{BET} can be calculated by multiplication of the adsorbed amount of gas of the monolayer, the Avogadro constant N_A and the surface σ occupied by a single gas molecule of the monolayer.

$$S_{BET} = n_{mono} \cdot N_A \cdot \sigma \quad (14)$$

It is also possible to determine the pore size distribution (PSD) of an adsorptive from the sorption isotherm. One of the classic methods is based on the Kelvin equation. The Kelvin equation describes the phenomenon of capillary condensation for cylindrical pores by providing a relationship between the relative pressure and the radius of the condensed phase. Based on this, Barrett, Joyner and Halenda (BJH) developed a model for determining the pore size distribution in 1951.^[239] In 1964, Dollimore and Heal presented a refined theory.^[240] Both models are based on the assumption of cylinder pores and determine the pore size distribution from the desorption branch. This takes into account that a progressive reduction of the relative pressure initially results in desorption of the condensed phase and consequently a multilayer of the adsorbate remains on the pore surface. The actual pore diameter is thus composed of the proportion calculated according to the Kelvin equation and that of the remaining multilayer. This is called the modified Kelvin equation. Theories based on this falsely assume that the condensed phase has the same thermophysical properties as the condensed bulk adsorptive. For example, the surface tension, which is a parameter of the Kelvin equation, depends on the curvature of the

surface.^[241] In addition, the critical point of the adsorbate shifts in the spatial restriction of the porous adsorbent to smaller values. The simplified model results in considerable deviations from the actual pore sizes in the lower mesopore region. It was suggested, that the BJH-method should be used to determine pore sizes larger than 7.5 nm.^[242,243]

The adsorption mechanism in micropores differs from the capillary condensation of adsorbate that occurs during the adsorption process in mesopores. The adsorption of nitrogen in general is based on the van-der-Waals interaction of the adsorbent, which is described by the Lennard-Jones potential. In micropores, these adsorption potentials of opposite pore walls overlap, so the adsorption potential also increases with decreasing pore size. The thermodynamics of the adsorption process in micropores is described by the Dubinin-Radushkevich equation (DR equation)^[244,245] based on the work of Polanyi, which introduced the adsorption potential.^[246] The DR equation correlates the adsorption potential with the volumetric component of the adsorbate-filled pores in the total pore volume. An application of physisorption data according to a linearized form of the DR equation, which is called a characteristic adsorption equation, provides the adsorption energy or the total pore volume from its slope or ordinate section.^[247] For an ensemble of pores with different adsorption energies, several straight lines are thus obtained. Each of these straight lines can be assigned a total pore volume originating from pores with the same adsorption energy. Since, in the case of micropores, the adsorption energy correlates with the pore size-dependent Lennard-Jones potential, the pore size distribution can be determined from that. This process is suitable for chemically homogeneous, lightly activated carbons with a narrow pore size distribution. More highly activated carbons have a wider pore size distribution, as the walls between neighboring pores are partially removed during the activation process. This and a strong chemical inhomogeneity have the consequence that the linearity of the application according to the DR equation is necessarily given. Dubinin and Stoeckli refined the DR equation to account for chemical inhomogeneity of carbons.^[248] Horváth and Kawazoe (HK) presented a more precise method for determining the micropore size distribution.^[249] This is a semi-empirical method developed for carbon materials with slit pores, such as activated carbons. It is based on the work of Everett and Powl, who calculated the potential of noble gas atoms between graphene layers.^[250] The HK

approach assumes an average potential between adsorbent and adsorptive and establishes a correlation between effective pore size and the relative pressure at which the respective pores are filled with adsorptive. It means adsorption takes place in pores of a certain shape and size at a characteristic relative pressure. However, this is a simplified assumption, as the adsorption process is discontinuous. As described above, it cannot be assumed that the adsorbate behaves like the bulk adsorptive. Further developed theories also exist from the HK model.^[251]

A more sophisticated method that is suitable for the determination of the pore size distribution is based on the density functional theory (DFT). Compared to the "classical" methods, they offer the advantage that a simultaneous analysis of micropores and mesopores can be carried out. The DFT is based on statistical mechanics and describes the system of adsorbent, adsorbate and adsorptive through the grand canonical ensemble. In a physisorption experiment, the equilibrated states represent the minimum at different relative pressures. The large canonical ensemble is represented as a functional of the density of the adsorptive. The basis of the DFT is therefore the minimization of the grand canonical ensemble, which provides the equilibrium distribution of the adsorptive as its density within the porous structure of the adsorbent. In 1989, a DFT method for the determination of PSD was presented for the first time by Seaton et al.^[252] In the following years, this approach was further developed and is known as non-local density functional theory (NLDFT).^[253] The surfaces of carbon materials were initially considered flat and graphitic. Surface roughness and chemical inhomogeneity, as it occurs on activated carbons, could therefore not be taken into account. Furthermore, these NLDFT models are one-dimensional, which means the adsorptive adsorbent potential and adsorbent density vary only orthogonally to the pore wall. As a result, theoretically calculated isotherms each have one stage at the transition to adsorption of the next multilayer.^[254] This subsequently distorts the determined pore size distribution. In reality, multilayer adsorption of geometrically and chemically inhomogeneous carbons is not gradual but continuous. There are two- and three-dimensional NLDFT models, which consider a geometric and chemical inhomogeneity. However, these result in a considerably higher computational effort. In 2006, Ravikovitch and Neimark presented the quenched-solid density functional theory (QSDFT).^[255] This is based on a one-dimensional DFT approach with comparatively low calculation effort. The geometric inhomogeneity (surface roughness) of the adsorbent is taken

into account by considering solid atoms of the adsorbent as quenched components of the solid-fluid mixture with a fixed density distribution. Thus, the grand canonical ensemble, describes a two-component system and is a functional of both the adsorbent and the adsorptive density. Its minimization is provided by a theoretically calculated isotherm without artificial stages. According to equation (15), the Generalized Adsorption Isotherm equation, the experimental sorption isotherm $N_{\text{exp}}(p/p_0)$ can be represented as a superposition of theoretical isotherms $N_{\text{QSDFT}}(p/p_0, W)$ from the pore size range from W_{min} to W_{max} , where $f(W)$ is the function of pore size distribution. The entirety of theoretical isotherms is called kernel.^[256,257]

$$N_{\text{exp}}\left(\frac{p}{p_0}\right) = \int_{W_{\text{min}}}^{W_{\text{max}}} N_{\text{theo}}\left(\frac{p}{p_0}, W\right) \cdot f(W) dW \quad (15)$$

The PSD can be determined according to equation (15) from the experimental sorption isotherm $N_{\text{exp}}(p/p_0)$, by calculating the function of the PSD $f(W)$. The quick-non-negative least square method (QNNLS) can be used on that occasion.^[258] Specific QSDFT kernels were developed for different pore geometries. For mesoporous materials, which sorption isotherms show hysteresis phenomena, it should be considered, whether the kernel describes the ad- or desorption process as described earlier.

The standard adsorptive for the determination of specific surfaces and pore size distributions of porous materials is nitrogen at 77 K. However, nitrogen has proven to be less suitable for the analysis of micropores, as it interacts differently with different adsorbents due to its quadrupole moment. This can lead to the filling of the ultramicropores already at very low relative pressures of about $10^{-7} p/p_0$. To measure the filling of the micropores at such pressures, very long measuring times are required, since the diffusion and adsorption of nitrogen at these pressures is very slow. Micropores smaller than about 0.45 nm cannot be filled at all due to these kinetic restrictions. Additionally, the adsorption of individual nitrogen molecules in or in front of small pore entries can completely block the pores behind them, preventing them from being filled.^[187,232] An alternative adsorptive, which is particularly suitable for micropore analysis, is carbon dioxide at 273 K. Although carbon dioxide has a similar kinetic diameter as nitrogen and argon (0.33 nm compared

to 0.36 nm and 0.34 nm respectively), the analysis of pores with a diameter of only 0.4 nm is possible. This is due to the fact, carbon dioxide at 273 K has a high saturation vapor pressure of about 3.5 MPa, so the ultramicropores are filled at moderate absolute pressures (between 0.1 and 100 kPa). (For nitrogen at 77 K and argon at 87 K, the saturation vapor pressure is approximately at normal pressure, so that the relative pressure corresponds approximately to the absolute pressure). Due to the comparatively high temperature at which CO₂ adsorption is measured, diffusion is additionally accelerated. As a result, the equilibria are quickly adjusted and measurement times are short. However, due to the high saturation vapor pressure, the maximum possible relative pressure during a measurement is limited to $3 \cdot 10^{-2} p/p_0$ and thus the maximum determinable pore size to approximately 1 nm.^[187,232,259]

2.2 Powder X-ray diffraction (P-XRD)

X-ray diffraction is based on the scattering of X-rays at ordered structures on the atomic scale. A solid can be regarded as ordered if it consists of a repeating motif whose multiplication in the three spatial directions allows it to be completely described. The displacement of the motif, the so-called base of the solid, can be described by three vectors, the base vectors. If the vectors are arranged starting from the base, the result is a regular structure, the lattice whose smallest unit is called an elementary cell. To measure its X-ray diffraction, a solid body, crystal or powder, is irradiated from different angles with X-rays of a fixed wavelength. The radiation is scattered at the electron shell of an atom so that a spherical scattering wave emanates from this point. The superposition of these individual scattering waves determines the diffraction of the X-rays: If the path difference of two adjacent waves is an integer multiple of the wavelength, constructive interference occurs, which is observable as a reflection in the diffraction pattern. For the complete measurement of a sample, it is irradiated at every possible angle of incidence. The measurement of powders leads to X-ray powder diffraction patterns. Due to the limited size of the individual crystallites, the structure of the examined solid cannot be determined from these. Information can be obtained above all by comparison with diffraction pattern of reference materials. But even without these, a computational determination of the lattice parameters can be performed if the diffraction pattern is of good quality. Typically for carbons, reflections of the (002) and (101) diffractions can be

detected, corresponding to the stacking of graphitic layers and displacement of such, respectively.^[260]

2.3 Raman spectroscopy

Raman spectroscopy is a non-destructive characterization method for molecules and solids. It is used to observe vibrational, rotational and other low-frequency modes in a system. Using monochromatic light, usually from a laser in the visible, near infrared or near ultraviolet range, Raman spectroscopy relies on inelastic scattering of photons on the examined sample. Radiated photons excite the sample and puts it into a virtual energy state for a short time before the photon is emitted. The emitted photons will be detected and their energy shift reveals information about the vibrational energy of the molecule. For inelastic scattering, the emitted energy of the photon is lower (Stokes scattering) or higher (anti-Stokes scattering), than the absorbed energy. When the energy level remains, it is called elastic scattering. The magnitude of the Raman effect correlates with polarizability within the observed molecule, which is a measure of the shiftability of positive charge relative to negative charge in the molecule when an external electric field is applied. There must be a change in its electric polarizability with respect to the vibrational mode for a molecule to exhibit a Raman effect. The elastic scattering (Rayleigh scattering) reveals no information and is typically filtered. Raman spectroscopy can be used to investigate the degree of graphitization of porous carbons.^[261,262] For different carbons, like graphite, phonons of graphene layers are excited using Raman spectroscopy. The Raman shift reveals information about the hybridization of the carbon (sp , sp^2 or sp^3) or the degree of crystallization. For porous carbons, the degree of crystallization is rather low. There are two characteristic peaks for carbons. The peak around 1580 cm^{-1} is denoted as the G band. It describes an interplanar C-C vibration, which reflects the ordered graphitic lattice within a carbon structure.^[263] Due to the weak interaction between the graphitic layers, rotational disorder can occur leading to turbostratic carbons. This disorder is displayed at a Raman shift at 1350 cm^{-1} being denoted as D band, which reflects the degree of disorder within the carbon structure. Commonly, the intensity ratios of the D and G band is calculated to estimate the general order of the graphitic lattice of the porous carbons according to equation (16):^[264]

$$R = \frac{I_D}{I_G} \quad (16)$$

2.4 Electrochemical measurements

Cyclovoltammetry

Cyclovoltammetry (CV or triangle voltage method) is an analytical method for the characterization of electrochemical processes. The current that occurs at a particular voltage is measured. The three-electrode arrangement is commonly used for the measurement. The electrodes are the working electrode, reference electrode and counter electrode. The desired voltage V_0 is applied between the working electrode and the reference electrode. The reference electrode must be a non-polarizable electrode to measure the potential. The voltage at the working electrode changes. This is where the electrochemical reactions take place. When an electrochemical reaction takes place at the working electrode, the voltage changes as electrons are withdrawn or released by the electrode. The reference electrode detects this and a current is sent from the counter electrode to the working electrode to adjust the voltage V_i to set the potential V_0 again. The counter electrode is usually made of the same material as the working electrode. It is important for the reference electrode to adjust its potential quickly and remain constant. In cyclovoltammetry, a triangle voltage is applied over a certain period of time and is repeated cyclically in a certain scan rate (potential change per time).^[265] The CV of a EDLCs is described by a rectangular voltammogram with current proportional to capacitance and scan rate $v = dV/dt$.^[94] When a voltage is applied at a constant scan rate, a constant limiting current flows, which is caused by the charging of the electric double layer. Figure 28 a shows the CV of a symmetric two electrode EDLC with activated carbon as electrode material and EMImBF₄ as electrolyte. At a low scan rate, the CV shows slightly rounded corners, which are caused by the internal resistance R_{ESR} . Before the capacitive current is reached, the system has to overcome the internal resistance.^[95] At higher scan rates the effects of R_{ESR} become more pronounced owing to the higher currents, causing a rounding of corners after each direction switch. At the extreme, the CV will begin to resemble the diagonal line of pure resistance. Plateau capacitance – occurring where the current has stabilized to constant value decreases with increased scan rate, reflecting the effects of R_{ESR} . Another deviation of the CV curve can occur, which is not related to the occurrence of any Faradaic charge transfer

and has become known as the butterfly-shape of CVs and is related to electrochemical doping as seen in Figure 28 b, which shows a symmetric carbon EDLC with TEABF₄ in ACN as electrolyte in a three-electrode configuration. The term “butterfly” describes the symmetric increase in capacitance during charge and discharge for positive and negative polarization. The lower capacitance at low potentials results from the low space charge capacitance which is the capacitive component inside the electrode material and depends on the density of states of the electrode material or charge carriers. Especially in materials with a limited number of charge carriers when separation occurs between the heavily charged surface and the depleted bulk material, like amorphous activated carbons, the space charge capacitance is the limiting factor for the overall capacitance. It is assumed, that the charge carrier density increases with the potential, which results in an increase of capacitance at the vertex of the CV, and the decrease at low potentials correspondingly.^[14,266] Faradaic charge transfer processes will also lead to distortions of the rectangular CV shape. Redox processes that are not continuous with voltage can be revealed via CV as the curve of the investigate capacitor will show redox bumps at the respective voltage of the occurring redox process.^[267–269] This can be seen in Figure 28 c where the redox peaks are caused by the redox active surface species with 1 M H₂SO₄ as electrolyte. It is also possible to observe electrochemical degradation processes near the edge of the electrochemical stability window. As shown in Figure 28 d the current increases significantly which is due to the electrochemical degradation of the electrolyte, the electrode material, the current collector or the binder. Because these phenomena can be readily identified in the CV curves, cyclic voltammetry is also frequently used for the qualitative analysis of EDLCs.

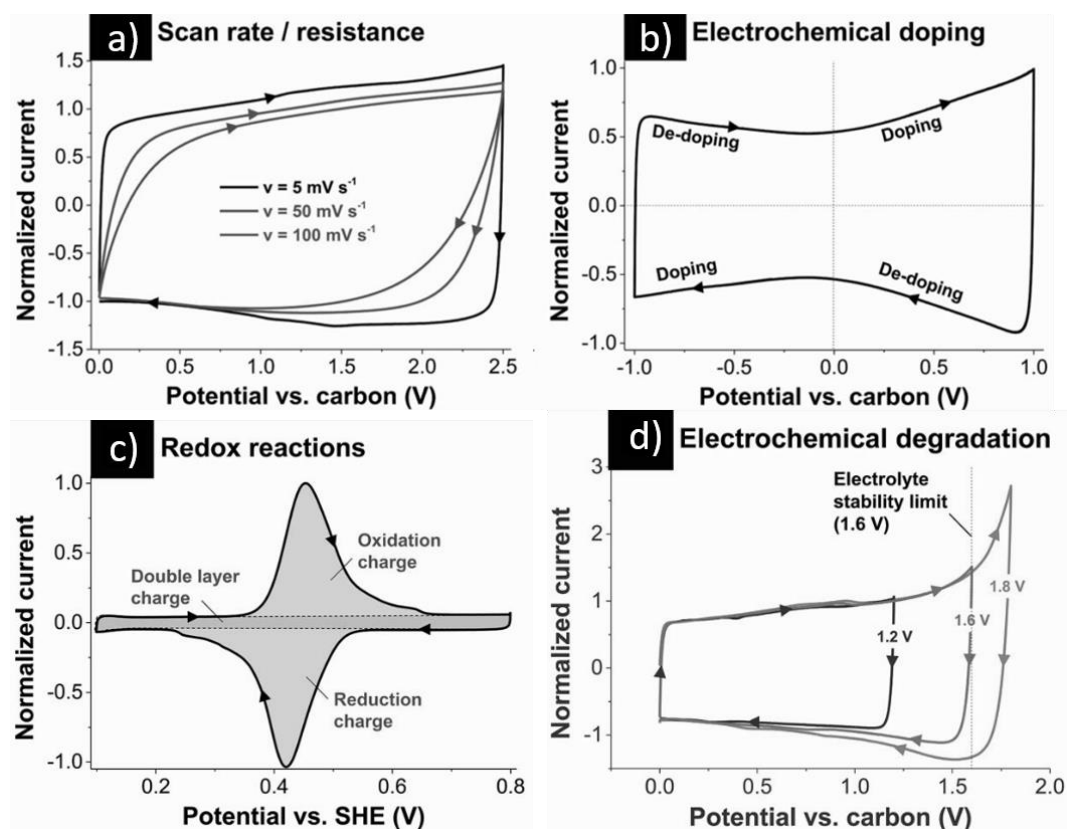


Figure 28: Common deviations from an ideal capacitor-like behavior in supercapacitors. a) Increased scan rate or higher material resistance increases the resistive response. b) Electrochemical doping results in the butterfly-shape of CVs. c) redox reactions will show as redox bumps at the respective voltage. d) electrochemical degradation of the electrolyte, current collector or the binder.^[270] Copyright 2014, Wiley-VCH Verlag GmbH & Co. KGaA. Reproduced with permission.

Charge discharge measurements

Another method for characterizing capacitors is galvanostatic charge/discharge (CDC) measurement. The capacitor is charged to a fixed voltage with a constant current. When the voltage is reached, the capacitor is discharged with the same current. Ideal capacitors in the CDC show a linear time/voltage curve at constant current and the capacitance is calculated from the slope. At the beginning of the discharge there is an IR voltage drop as shown in Figure 29. The linearity of the "voltage time" can be distorted by pseudocapacitance or saturation of the pores.^[271] The apparent magnitude of the IR drop is doubled at switching during cyclic CDC experiments compared to the voltage drop at the discharge experiment from a constant voltage as shown in Figure 29. The voltage drop upon switching to discharge

is twice as large because the true capacitor voltage will lag the applied voltage during charging owing to R_{ESR} .^[94]

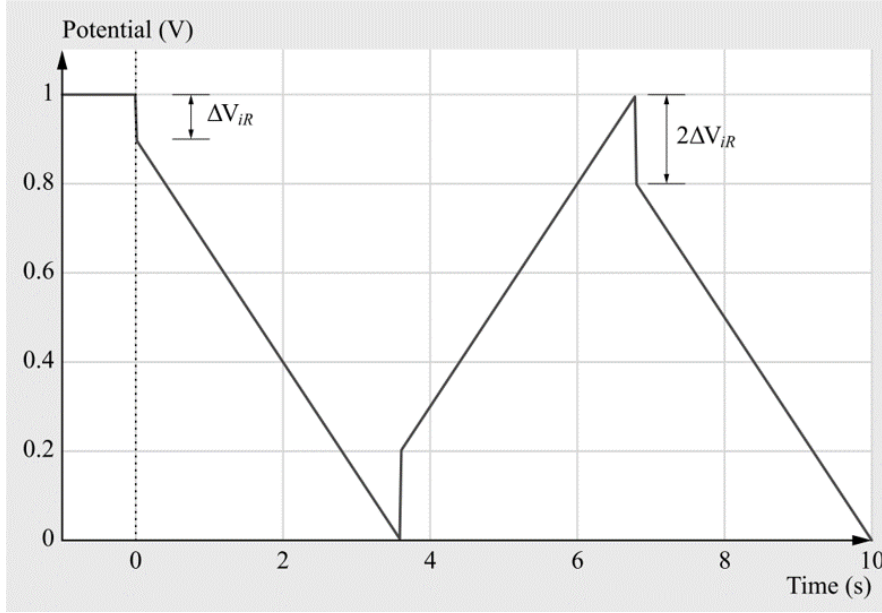


Figure 29: Profile of a CDC measurement of a drop from constant voltage (left) and a CDC cycle switch (right).^[94] Copyright 2017, Springer Berlin Heidelberg.

Electrochemical impedance spectroscopy

In the electrochemical impedance spectroscopy (EIS) a constant voltage is applied to the investigated system, which is superimposed by an alternating voltage in the order of a few millivolts. The measured variable is the current. The frequency of the alternating voltage is varied during the measurement. A typical measuring range extends over frequencies from 0.01 Hz to 1 MHz. The applied alternating voltage generates a phase-shifted alternating current. The low amplitude of the superimposed alternating voltage ensures that the system behaves pseudo-linearly. This means that the frequencies of the alternating current and the alternating voltage are identical. The sinusoidal alternating voltage $V(t)$ is described by equation (17) and the alternating current $I(t)$ phase-shifted by the angle ϕ by equation (18), where ω is the angular frequency and t the time.

$$V(t) = V_0 \sin(\omega t) \quad (17)$$

$$I(t) = I_0 \sin(\omega t + \phi) \quad (18)$$

With the Euler relation, it is possible to describe the alternating voltage and alternating current as complex units where j is the imaginary unit.

$$\underline{V}(t) = V_0 e^{j\omega t} \quad (19)$$

$$\underline{I}(t) = I_0 e^{j(\omega t + \phi)} \quad (20)$$

The frequency-dependent, complex impedance Z_w is the alternating current resistance and is described as the quotient of complex voltage and complex current, analogous to Ohm's law:

$$\underline{Z}(\omega) = \frac{\underline{V}(t)}{\underline{I}(t)} = |\underline{Z}(\omega)| \cdot e^{-j\phi} \quad (21)$$

The impedance is made up of a real part (Z_{Re}) and an imaginary part (Z_{Im}) and can be expressed by the following equation:

$$\underline{Z}(\omega) = Z_{Re} + j \cdot Z_{Im} \quad (22)$$

In the following, Z_{Re} will be referred to as Z' and Z_{Im} as Z'' . The real part of the impedance describes all processes, which lead to a real loss of energy, like Ohmic resistances. The imaginary part of the impedance describes resistive processes, which lead to a temporary energy loss, but will be restored afterwards, like capacitive and inductive processes. The capacitance can be calculated from the imaginary part of the resistance by the means of the following equation:

$$-Z'' = \frac{1}{\omega C} \quad (23)$$

The data of an impedance measurement can be displayed in a complex plane as a Nyquist diagram. The real part is plotted on the abscissa and the imaginary part on the ordinate. The amount of the complex impedance – also called impedance modulus – is called apparent resistance and corresponds to the vector length in the complex plane, and is calculated according to the Pythagorean Theorem:

$$|\underline{Z}(\omega)| = \sqrt{Z_{Re}^2 + Z_{Im}^2} \quad (24)$$

The phase angle ϕ is the angle between the pointer and the real axis in the complex plane and is calculated by the following equation:

$$\phi = \tan^{-1} \left(\frac{Z_{\text{Im}}}{Z_{\text{Re}}} \right) \quad (25)$$

A typical Nyquist plot is shown Figure 30 a. In the high frequency part of the impedance, induction behavior can be observed, caused by the test cell setup and connecting cables. The intersection of the impedance with the real impedance shows the equivalent serial resistance, which is described in section 1.4.1. It reflects the bulk resistance of the electrolyte, contact resistance of electrode material and current collector as well as intrinsic resistance of the carbon electrode. A semicircle in mid to higher frequency region up to 50 Hz, reflects the charge transfer resistance from faradaic charge transfer reactions and charge accumulation of electrolyte ions on the electrode surface.^[272] Faradaic charge transfers can be caused by impurities of carbon electrodes that lead to the decomposition of the electrolyte and narrow pores, which hinder the access of electrolyte ions on the electrode surface. In addition, the Warburg resistance, a short 45° segment at mid frequencies up to 5 Hz, is related to the diffusion resistance of the electrolyte ions within the pore network. To be more precise, surface diffusion of the adsorbed ions and diffusion within narrow pores might be responsible for the Warburg impedance.^[131] At low frequencies, a straight line with a large slope shows ideal double layer behavior. Whether the impedance has a straight line at low frequencies or not, can be determined with the phase angle. For perfect double layer, the phase angle is very close to -90° . The phase angle as a function of the frequency is called Bode plot and is shown in Figure 30 b. It is an illustrative representation of the results of the impedance measurement, since it represents a frequency dependence, which is often easier to interpret. Deviations from the ideal phase angle are mainly due to geometric aspects such as electrode porosity and electrode roughness, but also active site activation energy dispersion, which causes ohmic resistances, leading to a slope of the straight line at low frequencies of the impedance in the Nyquist plot.^[95]

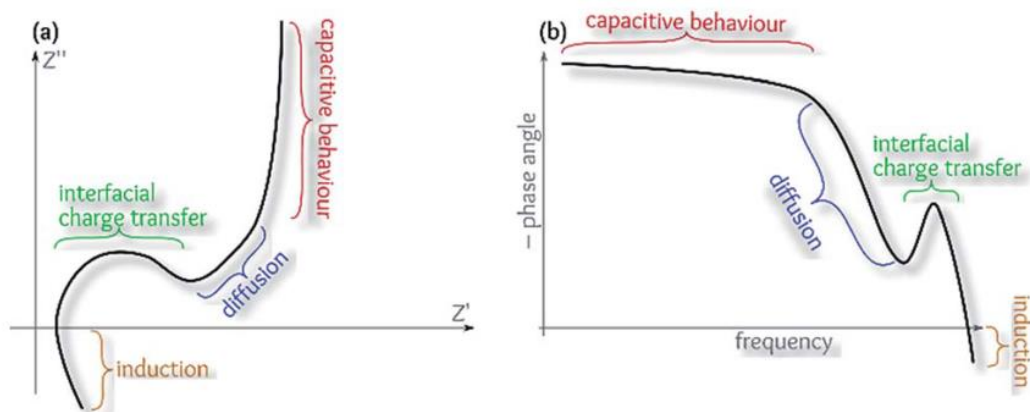


Figure 30: (a) Nyquist and (b) Bode plots for a schematic impedance model, valid for supercapacitors.^[131] Copyright 2018, Reproduced by permission of the Royal Society of Chemistry.

3 Motivation

While endeavoring to use renewable energies instead of finite fossil resources, various technical challenges must be overcome. Among other challenges, improved technologies for stationary and mobile energy storage must be developed. Electrochemical double-layer capacitors might play a major role for both applications in the future, but must be further optimized for this purpose.

Porous carbons in particular will play a decisive role, as they are still primarily used as electrode materials. They combine good thermal and chemical resistance, good electrical conductivity and low costs. However, there is also still room for improvement with regard to the design of the carbons. It is already clear that the specific surface plays an important role, but the pore structure of the carbon has proven to be just as important. They need to be optimized not only in terms of maximum capacitance, but also in terms of maintaining maximum power. Mesoporous carbons, in particular, have so far been considered optimal for this purpose, although their synthesis is not easily scalable and also is expensive.

For more than 10 years, many theories and conceived models have developed describing the capacitance's pore specific dependence. However, there is no model at present that can reliably simulate the capacitance of the carbon. In light of this, insights into the influence of the pore sizes on the capacitance could be clarified. Therefore, the aim of the work was to develop new synthesis routes for porous carbons in order to be able to control important properties such as pore size distribution and specific surface area. The approach was based on formaldehyde resins. Although these are well known, they have the advantage of synthetic scalability and low cost. Additionally, the semi-carbonization step after polymer synthesis and chemical activation was investigated in detail.

The material properties of the carbons should be determined extensively. In addition, the carbons as electrode materials for EDLCs were investigated by extensive electrochemical investigations. Subsequently, a new theoretical capacitor model should be developed to simulate the maximum capacitance of porous carbons. This should also provide new insights into the pore size dependent capacitance. In addition, the dependence of the retention of the capacitance on the pore sizes should be investigated on the basis of the data obtained from the new carbons.

Porous carbons with high specific surfaces are, however, of particular interest not only for use as electrode materials for electrical energy storage, but also as host materials for other energy carriers, such as hydrogen storage. Hydrogen is regarded as a clean energy source with great potential, but its transport and storage is extremely demanding from a technical perspective. Here, too, porous carbons have long been investigated as potential storage media, and in this field of application as well, knowledge about the influence of pore sizes on hydrogen storage capacity is desirable in order to optimize storage.

In this study, the aim was to gain a more precise insight into the pore size-dependent storage capacity, via a model to simulate the capacity on the basis of the sorption data.

4 Results and Discussion

In this work, different nanoporous carbons were synthesized and characterized, and formaldehyde resins were used as organic precursors. In the first part of the work, the syntheses of the carbon samples are presented. First, phenol-formaldehyde resins were investigated as organic precursor. Four synthesis parameters were varied: the amount of the activation reactant, the semi-carbonization temperature, the reactant composition and the activation temperature. Their respective influence on the material properties were investigated within the discussion. As a second series of samples, phenol-formaldehyde resins were cross-linked prior to carbonization, for further investigation of the influence of the precursor compound on the carbon properties. Here, too, phenol was combined with resorcinol as the reactant. The obtained carbon samples were characterized by scanning electron microscopy, X-ray powder diffraction, Raman spectroscopy, thermogravimetry and gas-physisorption. In particular, the results of gas physisorption were used as they provided detailed information on the porosity that has a central influence on electrochemical properties. Electrode materials were produced from the respective carbon samples, which were built into cells in a symmetrical two-electrode setup. Electrochemical investigations were carried out to investigate the applicability of the samples as EDLC electrode materials. Furthermore, the presented carbons were low cost, high surface area porous materials, which are also good candidates for hydrogen storage host materials. Therefore, hydrogen sorption measurements were carried out to determine the gravimetric hydrogen uptake capacity.

In the second part of the work, a new model was developed, based on the electrochemical measurements, to describe the dependence of the capacitance on the pore size, which emerged from existing models. Based on the results of gas physisorption, theoretical capacitances were calculated with the new model, whereby a refined model could be obtained in comparison with the experimentally determined values, which shows a structure-property relationship between capacitance and pore size. The same refining method was also applied to the gravimetric hydrogen uptake values, where the theoretical uptake values were average values in this case. Here, too, a structure-property relationship between maximum hydrogen uptake at 77 K and 1 bar and pore size could be established.

4.1 Synthesis and characterization of formaldehyde resin based carbons and their investigation as energy storage materials

In this entire chapter, the synthesis and investigation of all prepared phenol/formaldehyde and resorcinol/formaldehyde resins will be described. Furthermore their properties as electrode materials for ELDCs will be investigated. Additionally, their properties as storage materials for gaseous energy carrier will be investigated, namely hydrogen.

The general scheme of the synthesis of the formaldehyde based carbons is shown in Figure 31. The resins were carbonized (in this work semi-carbonized), and activated with KOH. From these synthesis parameters the following parameters were varied to investigate their respective influence on the properties of the resulting carbons: (1) the activation reactant, (2) semi-carbonization temperature, (3) activation temperature, (4) carbon precursor. In addition, (1) and (2) as well as (2) and (3) were varied in combination, to gain more information about the influence of the respective parameters.

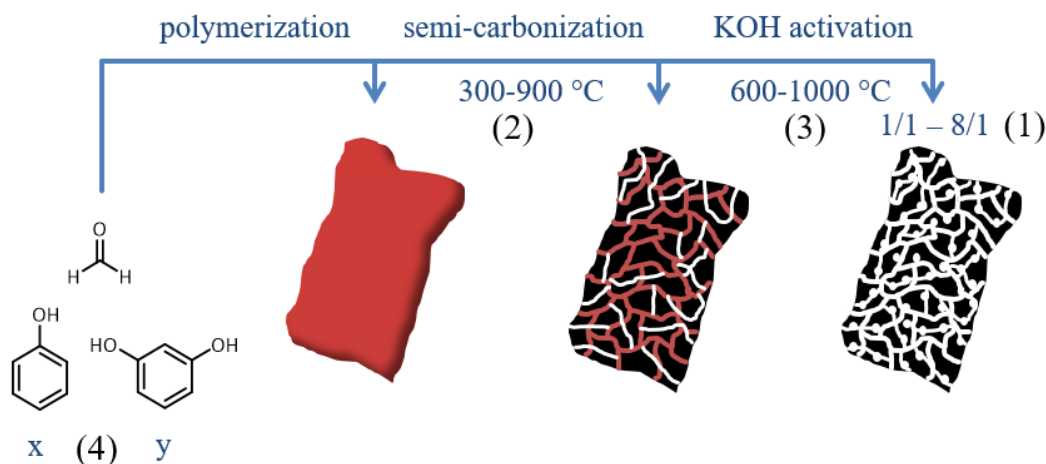


Figure 31: Synthesis scheme for the preparation of HSAC from PF- and RF-resins. Four parameters were varied, (1) the activation reactant, (2) the semi-carbonization temperature, (3) the activation temperature and (4) the carbon precursor.

Phenol and resorcinol were used as starting materials for polymerization with formaldehyde. In this section, the results of carbons based on phenol/formaldehyde (PF) resins are discussed. The PF resins, used as carbon precursor were polymerized under the same condition for all investigated carbons (see section 7.1).

Polymerization was carried out under acidic conditions, as the resulting polymer should have had greater resistance against chemical activation. Induced by the acidic medium, the polymerization was processed via a Novolac precursor before the red brown PF-resin, as shown in Figure 32, was obtained.

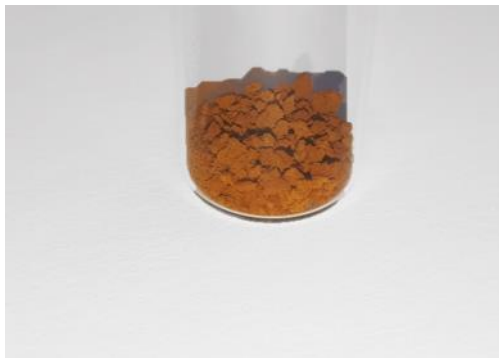


Figure 32: Phenol/formaldehyde-resin after polymerization under acidic condition.

4.1.1 Synthesis of PF-resin based carbons

Carbons are being obtained, when the PF-resins are carbonized under inert gas atmosphere like argon or nitrogen. To enlarge pore size and increase the specific pore volume and surface area of carbons, a chemical activation with KOH was performed. KOH was chosen as activation reactant because it is the most used and investigated activation reactant.^[65] The effectiveness of the KOH activation depends on the amount of activation reactant used and the activation temperature. Recently, it was observed, that the pre-carbonization temperature has a great effect on the chemical resistivity of the carbons.^[88,91,92] The carbonaceous framework of the porous carbon, becomes more rigid and resistive against chemical activation, with a higher carbonization temperature. That way, the chemical activation is supposed to be more effective if the carbonization temperature or semi-carbonization temperature is chosen lower. The synthesis scheme is shown in Figure 33. The acid catalyzed PF-resins were semi-carbonized at a temperature of 500 °C under argon atmosphere. We choose the term “semi-carbonization” to emphasize, the carbonization of the organic residues is not completed. The semi-carbonized samples were activated with different ratios of KOH and carbon at 900 °C under nitrogen atmosphere.

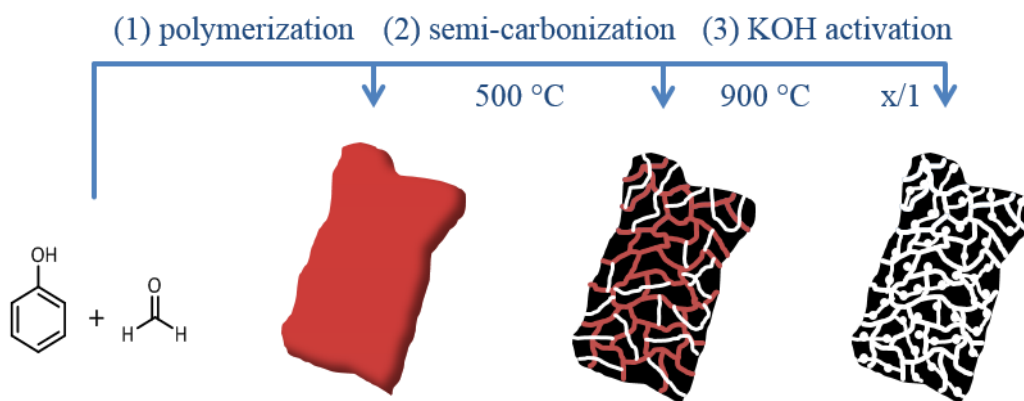


Figure 33: Synthesis scheme for the preparation of HSAC from PF resins. (1) polymerization of the PF resin under strong acidic conditions; (2) semi-carbonization of the PF resins at 500 °C under argon atmosphere; (3) chemical activation of the semi-carbonized carbons with different ratios of KOH and carbon at 900 °C under nitrogen atmosphere.

With the semi-carbonization temperature, activation temperature and the amount of KOH, three parameters are available, which influence the porosity of the carbons. Furthermore, the influence of the precursor composition was investigated. We used resorcinol and different ratios of phenol and resorcinol as reactants for the polymerization of the organic precursor. A detailed examination of the four parameters in combination, and the influence of the semi-carbonization temperature have not yet been carried out for acid-catalyzed PF-resins.

4.1.2 Influence of the activation reactant

Parts of the following chapter were published.^[273]

For our standard synthesis procedure we choose phenol formaldehyde resins as precursor, a semi-carbonization temperature of 500 °C, as mentioned in 4.1.1, a KOH/carbon ratio of 5 and an activation temperature of 900 °C. The sample was denoted as **C-500-5-T9**, with the first index being denoted to the semi-carbonization temperature, the second to the KOH/carbon ratio and the last to the activation temperature with the latter leaving out the last two zero digits. For better evaluation of the semi-carbonization temperature effect, two comparison samples were synthesized, with one having a semi-carbonization temperature of 900 °C and the other being semi-carbonized and carbonized without any activation reactant. These samples are denoted **C-900-5-T9**, and **C-500-0-T9**. To avoid misunderstandings, the term “semi-carbonization” is still used, although a heat treatment of 900 °C usually

results in fully carbonized carbons. Three more samples were synthesized with different KOH/carbon ratios of 1, 2.5 and 8, which are denoted as C-500-1-T9, C-500-2.5-T9 and C-500-8-T9 to evaluate the influence of the KOH ratio of the presented synthesis.

4.1.2.1 Characterization of carbons synthesized with different KOH/carbon ratios

The prepared samples were characterized by scanning electron microscopy (SEM) and the images are shown in Figure 34. The carbon samples C-500-1-T9 and C-500-2.5-T9 present a network structure which is composed of spherical carbon nanoparticles (Figure 34 a,b), similar to the control sample C-500-0-T9 (Figure 34 f). This particle morphology is typical of carbons, based on formaldehyde resins.^[274] The loose agglomeration of the spherical carbon nanoparticles leads to a formation of cavities within the network, which are 2-10 μm in diameter. The network structures of C-500-5-T9 and C-500-8-T9 possess the same cavities as C-500-0-T9, C-500-1-T9 and C-500-2.5-T9 as shown in Figure 34 c,d. However, a change in structure can be observed as the spherical particles agglomerated strongly, which is clearly caused by the increasing KOH/carbon ratio. Such an altering of the structure is unusual for carbons based on formaldehyde resins.^[275] Due to the low semi-carbonization temperature prior to the chemical activation, the network is less rigid, resulting to a stronger agglomeration of the spherical particles after the chemical activation with increasing KOH/carbon ratio. Figure 34 e shows the network of C-900-5-T9 is composed of loose agglomerated spherical particles, which form cavities in the network similar to C-500-0-T9, C-500-1-T9 and C-500-2.5-T9. The network withstood attrition by the KOH activation despite the high KOH/carbon ratio of 5. This is the effect of the higher semi-carbonization temperature, which led to a more rigid carbon network, and the preservation of the loose agglomerated spherical particles.

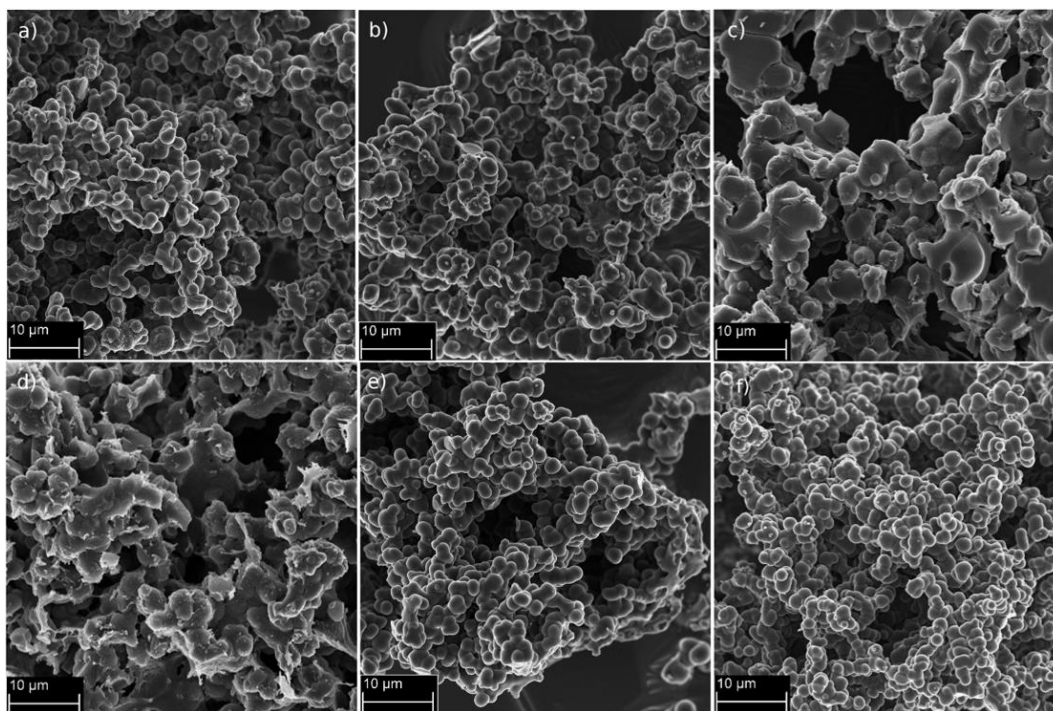


Figure 34: SEM images of the activated carbons. (a) C-500-1-T9, (b) C-500-2.5-T9, (c) C-500-5-T9, (d) C-500-8-T9, (e) C-900-5-T9 and (f) C-500-0-T9.

To investigate the composition of the carbon samples, powder X-ray diffraction (p-XRD) analysis was performed as shown in Figure 35. All p-XRD patterns show weak and extremely broad reflections at $44^\circ 2\theta$ corresponding to (101) diffraction pattern of a turbostratic carbon structure.^[260] The absence of (002) diffraction pattern, which would indicate the stacking of graphitic layers, for all carbon samples indicates a rotationally disordered structure of carbon layers, emphasizing the turbostratic carbon structure. The Raman spectra (Figure 36) show two broad peaks around 1320 cm^{-1} and 1585 cm^{-1} corresponding to the D (disordered carbon) and G-band (ordered graphitic lattice) respectively, which are typical for carbonaceous materials (see section 2.3). The calculated I_D/I_G ratios, which reflect the graphitic degree of the carbon materials, are 1.24, 1.07, 1.15, 1.16 and 1.25 for C-500-1-T9, C-500-2.5-T9, C-500-5-T9, C-500-8-T9 and C-900-5-T9, respectively. The intensity ratios show a rather low degree of graphitization for all samples, which are in a similar range. Results from p-XRD and Raman scattering indicate that the carbon samples are amorphous materials. This can be attributed to the relative low temperature treatment leading to a low degree of graphitization. For the formation and

parallel stacking of graphitic layer, temperatures of 2000 °C and higher are required. Additionally, the KOH activation lowers the degree of graphitization drastically, by increasing porosity and generating structural defects, as well as doping of oxygen leading to oxygen containing functional groups at the surface of the carbon materials.^[276,277] Nevertheless, the I_D/I_G ratios of C-500-1-T9 and C-900-5-T9 are slightly higher, compared to the other carbon samples, which so far cannot be reliably explained. In the case of C-500-1-T9, this can be attributed to the low ratio of KOH and carbon, possibly leads to a higher degree of oxygen containing functional groups, which then cause a displacement of the graphene layer stacking.^[278] As for C-900-5-T9, the activation may not be the cause of the generation of structural defects, but the KOH/carbon ration was still as high as 5 and the semi-carbonization temperature was not high enough to ensure the stacking of graphene layers, hence leading to a higher I_D/I_G ratio.

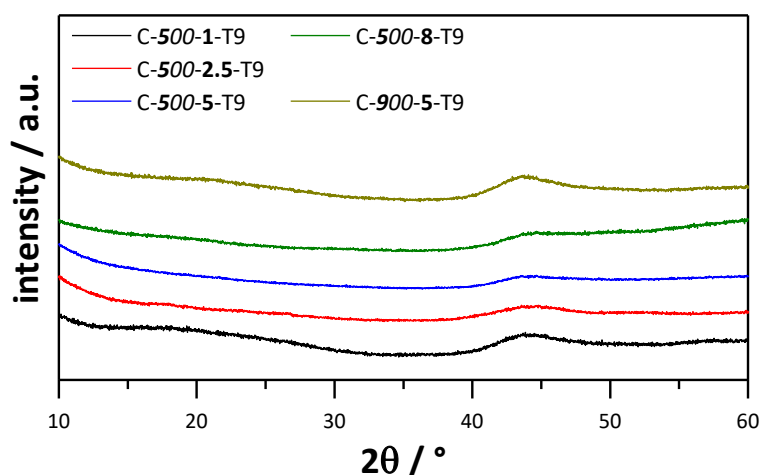


Figure 35: P-XRD patterns of the activated carbons.

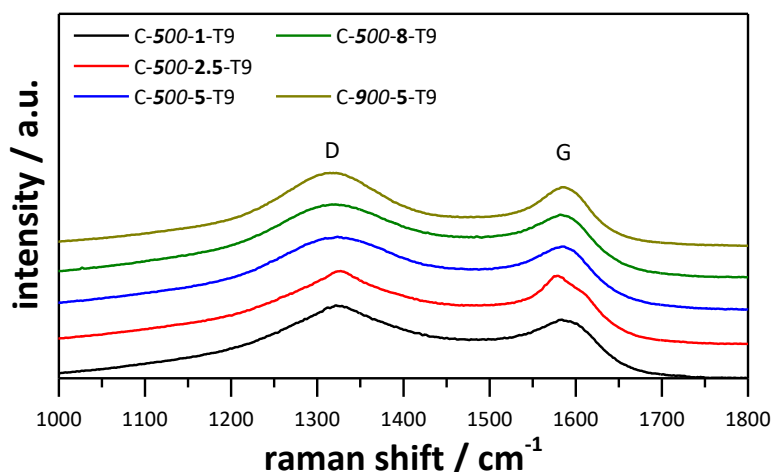


Figure 36: Raman spectra of the activated carbons.

The results of the thermogravimetry for all carbon samples are shown in Figure 37. The percentage mass loss during the burning process in air steam atmosphere is plotted against the temperature. All carbons show a complete burn off at a temperature of 630 °C without leaving any residual mass. This indicates the carbons are pure and free of any impurities like inorganic salts, which can remain after the chemical activation process. The burning process starts at temperatures of 450 °C (C-900-5-T9) to 500 °C (C-500-8-T9), is a typical range for carbons to combust.^[37] The variance in burning start temperatures for different materials is attributed to the different degree of porosity, which is investigated in the following section. Nevertheless, C-500-8-T9 and C-500-5-T9 are supposed to have the largest pores, hence the highest degree of porosity. This means that the carbons with a likely lower degree of porosity are starting to combust a lower temperatures. This effect would not have been expected, because a material with a higher porosity can give the combustion gas better access to the pore system and thus lead to a lower combustion temperature. It can therefore only be due to the fact that the materials activated with a lower KOH/carbon ratio have a higher content of oxygen functionalities, which already react with the carbon in the network at lower temperatures and thus lead to lower combustion temperatures. Oxygen atoms in a carbon network are active reaction sites during the KOH activation and will be likely removed during the process, along with carbon atoms. Eventually, carbons, which were activated with a higher KOH/carbon ratio, will possess a lower content of oxygen in their respective

carbon network, hence will have a higher thermal stability. The results from the thermogravimetry therefore show, that the content of oxygen atoms is likely more important for the thermal stability than the degree of porosity.

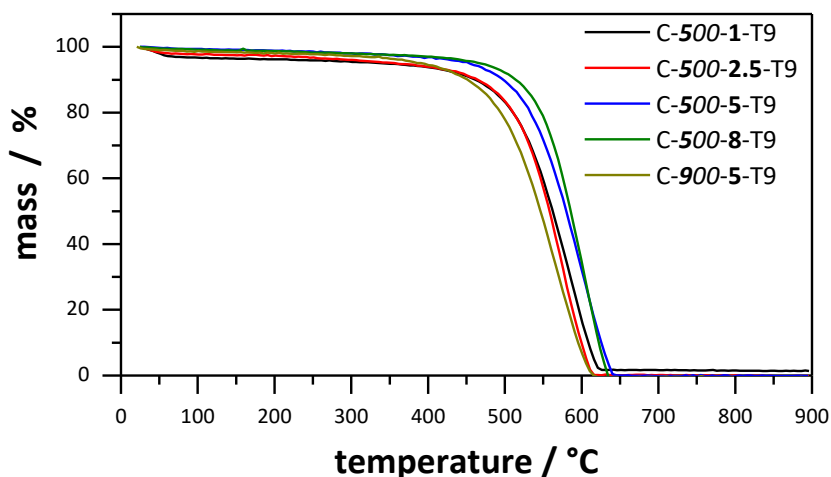


Figure 37: Results of the thermogravimetry of the activated carbons. The samples were heated to 900 °C in air steam with a flow rate of 50 mL·min⁻¹.

The prepared carbon samples were characterized with nitrogen physisorption (77 K), to investigate their porosity. The corresponding isotherms are shown in Figure 38 and the nitrogen physisorption derived data are summarized in Table 1. C-500-1-T9 and C-500-2.5-T9 show a typical type I isotherm, indicating carbon materials with predominantly micropores. The isotherms of C-500-5-T9 and C-500-8-T9 show a slope at relative pressures from 0.1 to 0.4 resulting from widening of pores and broad pore size distributions of large micropores and mesopores.^[7] The carbon sample C-900-5-T9 on the other hand shows a type I isotherm for microporous carbons, indicating that the KOH activation is less effective in generating larger pores, compared to C-500-5-T9. All prepared carbon samples have micropores from 0.62 to 1.10 nm originating from the carbonization process and additionally from the etching of carbon during the KOH activation, as shown in the pore size distribution calculated via DFT method (Figure 39). In addition to micropores, C-500-5-T9 and C-500-8-T9 also have mesopores up to 3.5 nm, while C-500-8-T9 has slightly larger pore sizes than C-500-5-T9. It is clear, that a higher

KOH/carbon ratio leads to an enlargement of the pores and a broader pore size distribution. C-900-5-T9, however, has significantly smaller pores than C-500-5-T9 despite the same KOH ratio for chemical activation. This shows the formation of a more rigid carbonaceous framework due to carbonization at 900 °C of the polymer precursor, prior to KOH activation.

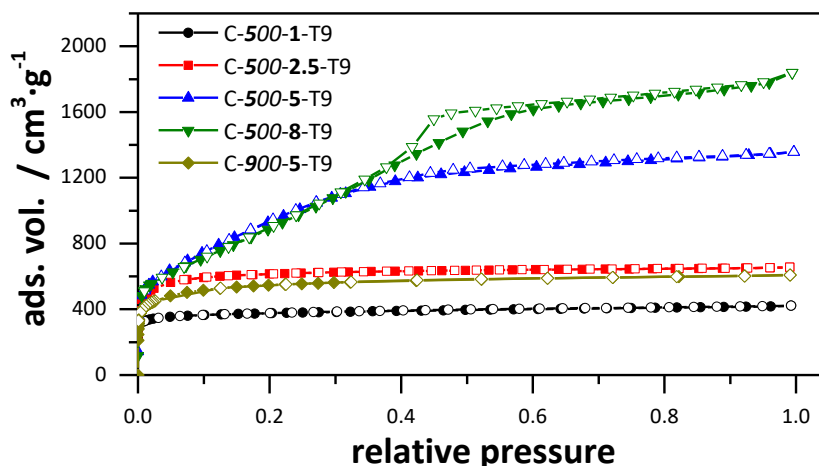


Figure 38: Nitrogen adsorption-desorption isotherms (77 K) of the carbon materials synthesized with different KOH/carbon ratios.

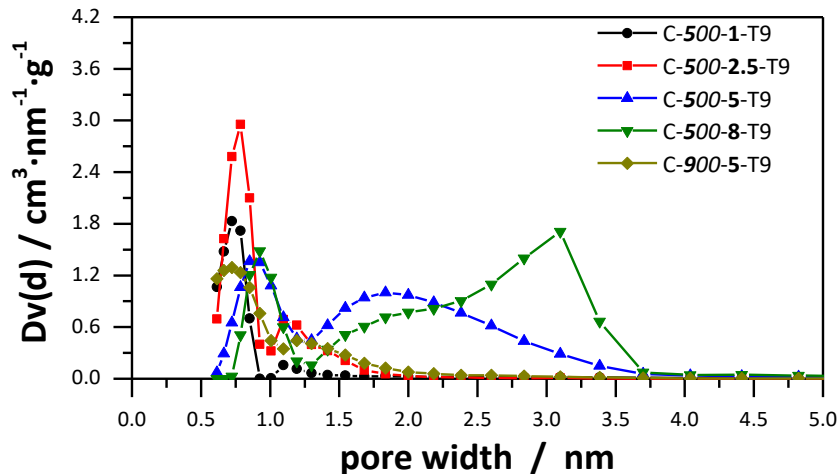


Figure 39: Pore size distributions of the carbon materials synthesized with different KOH/carbon ratios, calculated by the QSDFT method from nitrogen desorption branch assuming slit pores.

The prepared carbon samples possess high values for BET surface area ranging from 1473 to 3595 m²·g⁻¹. As mentioned in section 2.1, the BET method overestimates the surface area for microporous carbons with pore sizes larger than 0.9 nm.

As expected, the highest DFT surface area is $2551 \text{ m}^2 \cdot \text{g}^{-1}$ and significantly smaller than the corresponding BET surface area of the respective carbon sample C-500-8-T9, due to the strong gas adsorption of pores between 0.9 to 1.5 nm as described in chapter 2.1. Nevertheless, the results in Table 1 reveal the surface area directly depends on the KOH/carbon ratio with C-500-1-T9 having the smallest and C-500-8-T9 the highest specific surface area. A similar correlation is observable for the total pore volume. With an ultra-high pore volume of $2.62 \text{ cm}^3 \cdot \text{g}^{-1}$, C-500-8-T9 has the highest total pore volume among all carbon samples presented in this chapter, while C-500-1-T9 has the lowest total pore volume with $0.60 \text{ cm}^3 \cdot \text{g}^{-1}$. The micropore volume increases with the amount of KOH used for the chemical activation from 0.54 to $0.97 \text{ cm}^3 \cdot \text{g}^{-1}$ and then decreases to $0.86 \text{ cm}^3 \cdot \text{g}^{-1}$ with C-500-5-T9 having the highest micropore volume. The chemical activation predominantly, generates new micropores, but with a higher amount of chemical reactant, the newly formed micropores become large, and form small mesopores, lowering the micropore volume. The specific surface area, total pore volume and micropore volume of C-500-5-T9 are significantly larger than these of C-900-5-T9 as seen in Table 1. In fact, the material properties of C-900-5-T9 are similar to C-500-2.5-T9 despite the use of twice as much KOH. This emphasizes the greater effectiveness of the chemical activation combined with a semi-carbonization prior to the activation. C-500-0-T9 was only carbonized and is a purely microporous material with small pore size, surface area and pore volume. The corresponding isotherm and calculated pore size distribution of C-500-0-T9 is shown in Figure A.1.

Table 1: Nitrogen physisorption derived data of the carbon samples synthesized with different KOH/carbon ratios.

Sample	$S_{\text{BET}} /$ $\text{m}^2 \cdot \text{g}^{-1}$	$S_{\text{DFT}} /$ $\text{m}^2 \cdot \text{g}^{-1}$	$V_{\text{t}} /$ $\text{cm}^3 \cdot \text{g}^{-1}$	$V_{\text{mic}} /$ $\text{cm}^3 \cdot \text{g}^{-1}$
C-500-0-T9	483	574	0.19	0.18
C-500-1-T9	1473	1583	0.60	0.54
C-500-2.5-T9	2383	2108	0.93	0.91
C-500-5-T9	3537	2480	1.96	0.97
C-500-8-T9	3595	2551	2.62	0.86
C-900-5-T9	2068	1811	0.86	0.80

S_{DFT} (DFT surface area), V_{t} (total pore volume) and V_{mic} (micropore volume) obtained from QSDFT analysis. S_{BET} (BET surface area).

For further investigation of pores below 1.5 nm, carbon dioxide physisorption measurements were carried out. Figure 40 shows the adsorption-desorption isotherms of the carbon dioxide physisorption measurement at 273 K and the resulting pore size distribution using the NLDFT method for slit pores is shown in Figure 41. The isotherms of C-500-2.5-T9, C-500-5-T9, C-500-8-T9 and C-900-5-T9 show an almost linear correlation, which suggests a constant distribution of pore size. C-500-1-T9 shows a non-linear correlation of the isotherm, where the amount of adsorbed carbon dioxide is higher in the beginning for a relative pressure below a relative pressure of 0.007 compared to other samples, which indicates a higher distortion from a multimodal pore size distribution. The pore size distribution of carbon dioxide physisorption is only shown up to a pore size of 1 nm, as the vapor pressure of the adsorptive is too high for larger pores to provide accurate information.^[259] The pore size distributions show multimodal patterns for all carbon samples. This is due to the artifact, caused by the NLDFT method, which leads to zero minima at 0.4 and 0.7 nm.^[186,258] C-500-1-T9 has the highest amount of pores in the range of 0.35 and 0.4 to 0.7 nm. Using the lowest amount of KOH, small micropores were predominantly formed, increasing the amount of subnanometer ultramicropores. With increasing KOH/carbon ratio, the pore sizes increase, as a higher amount of activation reactant lead to the previously discussed pore enlargement. Pore sizes of C-900-5-T9 are comparatively small, due to the higher semi-

carbonization temperature, which hinders the effectiveness of the chemical activation.

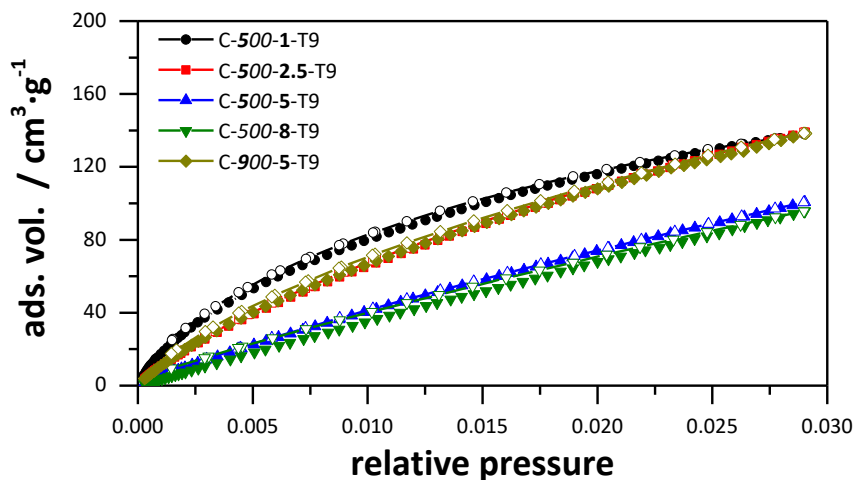


Figure 40: Carbon dioxide adsorption-desorption isotherms (273 K) of the carbon materials synthesized with different KOH/carbon ratios.

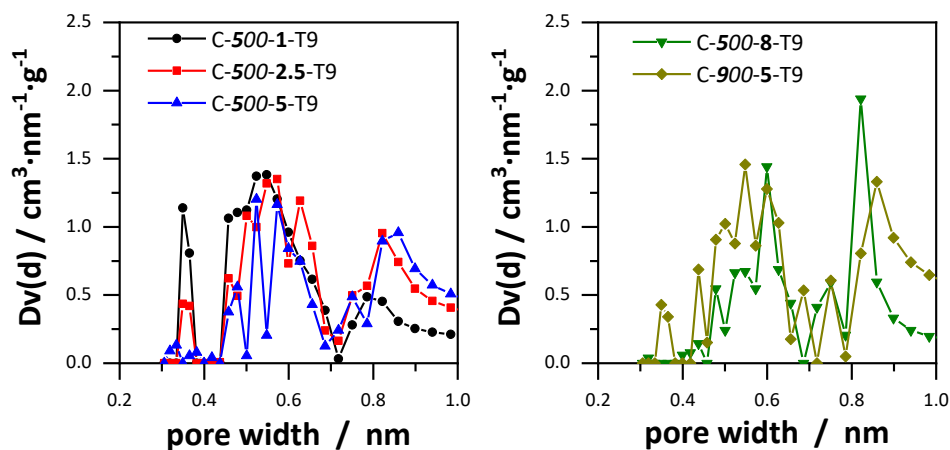


Figure 41: Pore size distributions of the carbon materials synthesized with different KOH/carbon ratios, calculated by the NLDFT method from carbon dioxide desorption branch assuming slit pores.

Regarding future applications of the carbon materials as EDLC electrode materials, the surface area is a key parameter. In this work, the carbons were investigated as electrode materials in EDLC with TEABF₄ in ACN as electrolytes and as solid hydrogen storage carriers. Figure 42 shows the cumulative specific surface area taken from the combined data of carbon dioxide and nitrogen physisorption. Larger than 10.7 nm no pore sizes were observed. In samples C-500-1-T9, C-500-2.5-T9 and C-900-5-T9, a large part of the surface area is generated by pores below 1 nm,

which is up to $1250 \text{ m}^2 \cdot \text{g}^{-1}$ and pores up to 0.6 nm provide a large part of the surface area for C-500-1-T9. Again, a higher KOH/carbon ratio leads to an enlargement of the pores, and a higher semi-carbonization temperature limits this effect. For C-500-5-T9 and C-500-8-T9, pores below 1 nm contribute less to the specific surface area. For C-500-5-T9, a large portion of the surface area is composed in pores between 1 and 2 nm, while in sample C-500-8-T9 more surface area is generated by pore sizes between 2 and 3 nm. This is due to the higher KOH/carbon ratio, as mentioned above. The combined cumulative pore volumes of the carbon samples (Figure 43) show larger pores generate a higher total pore volume, leading to C-500-8-T9 having the highest total pore volume of all carbon samples presented in this chapter.

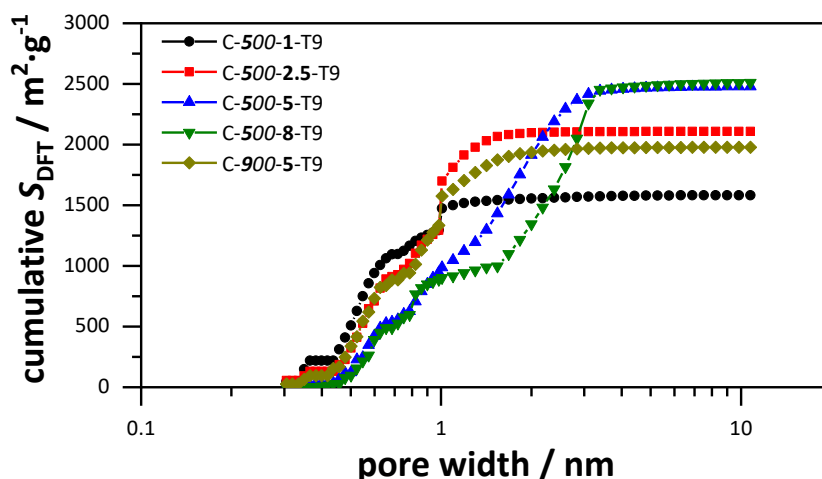


Figure 42: Combined cumulative surface area derived from carbon dioxide and nitrogen physisorption data of the carbon samples synthesized with different KOH/carbon ratios.

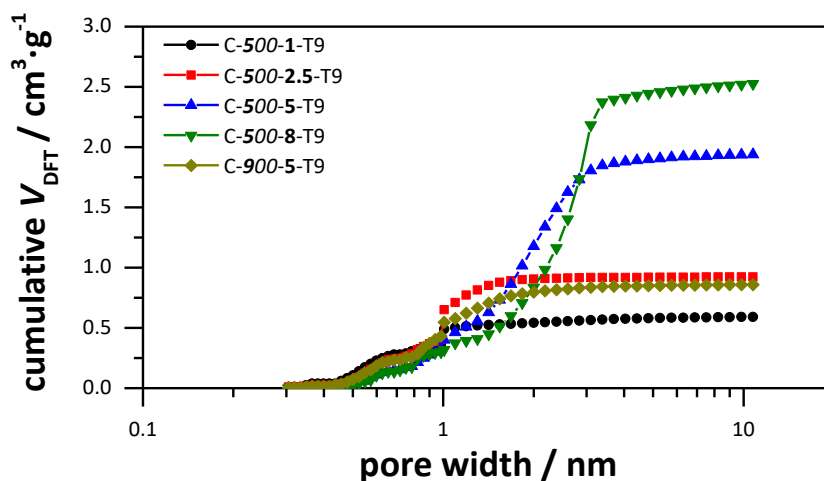


Figure 43: Combined cumulative pore volume derived from carbon dioxide and nitrogen physisorption data of the carbon samples synthesized with different KOH/carbon ratios.

4.1.2.2 Energy storage related properties of carbons synthesized with different KOH/carbon ratios

Electrochemical characterization

Representative for all investigated carbon materials in the entire work, SEM images were taken of all carbon samples discussed in this section. They have been coated on the aluminum foil mixed with PVDF binder and carbon black (8:1:1). The images are shown in Figure 44. For every carbon sample, particles with diameters of 5 to 40 μm are evenly distributed and of comparable size. Although cavities and voids between the particles are observable, the particles are agglomerated, which ensures electric conductivity. The PVDF binder is not observable, since the polymer chains are too small and the agglomerated strains of the PVDF are rarely observed.^[269,279] The carbon black conducting additive is evenly distributed on the carbon particles for all samples, which is supposed to enhance the particle-to-particle conductivity to a further extent.

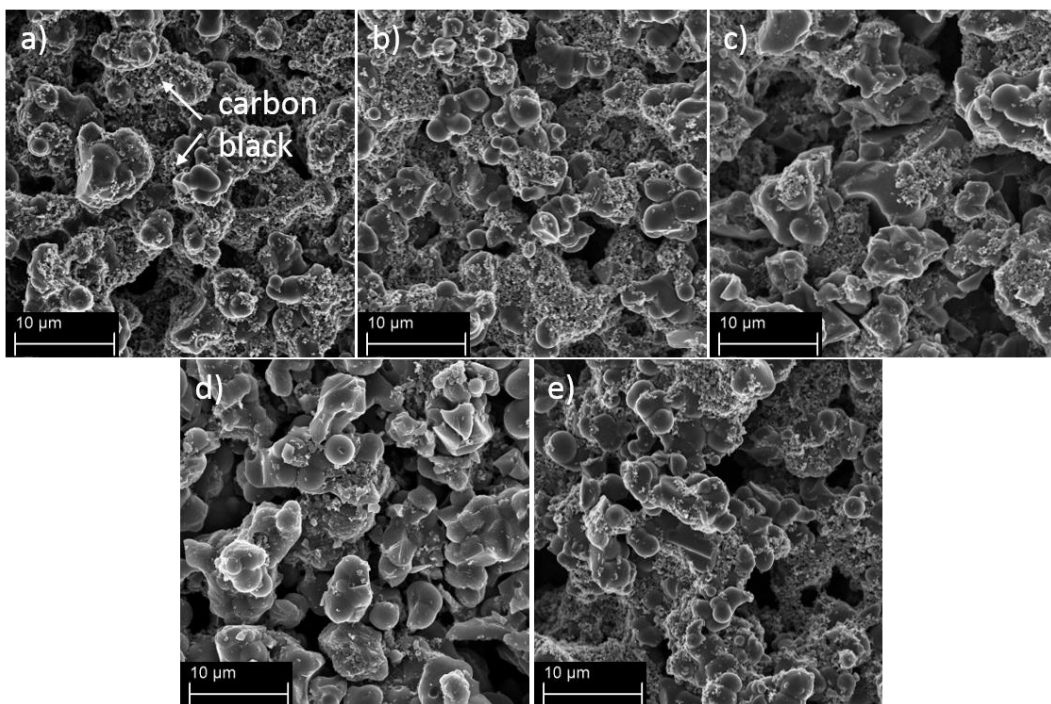


Figure 44: SEM images of the activated carbons samples mixed with PVDF-binder and carbon black, coated on an aluminum foil. (a) C-500-1-T9, (b) C-500-2.5-T9, (c) C-500-5-T9, (d) C-500-8-T9 and (f) C-900-5-T9.

The prepared symmetric EDLC were firstly characterized with cyclic voltammetry and the results are summarized in Table 2 on page 89. The CV of the carbons at a scan rate of $10 \text{ mV} \cdot \text{s}^{-1}$ show typical rectangular shapes, proving well developed electrochemical double layer capacitance properties (Figure 45). However, the CV curve of C-500-1-T9 shows a redox bump at 1.5 V and large distortions at the vertex of the discharge sweep. The redox bump can be ascribed to faradaic charge transfer reactions caused by impurities of the aluminum foil in the carbon material. These impurities cannot be avoided and are usually not visible in the CV as they are overlaid by the larger capacitive current. Charge transfer reactions caused by oxygen functional groups on the carbon surface with the solvent are another possibility. The redox bump and the strong vertex distortion become less significant at a scan rates of $20 \text{ mV} \cdot \text{s}^{-1}$ and disappear with further increasing scan rate. This indicates the observed processes are being diffusion-controlled. Since C-500-1-T9 has the highest content of small pores below 1 nm, an ion insertion is possible, requiring more energy for electrolyte ions to enter the pores and causing current increases at the vertex. With increasing scan rates, the ions are limited in entering the pores, due to diffusion limitations of the electrolyte ions.^[268,270] A small increase in capacitance

with increasing cell potential can be observed. This can be attributed to the non-metallic nature of carbon, where more charges can be accumulated as the density of states of charge carriers changes during increases of applied potential.^[268,270] As the scan rate increases, the CV curves of the carbon samples C-500-2.5-T9 and C-900-5-T9 are distorted, due to the greater effect of the R_{ESR} , as already mentioned in section 2.4. Another important factor, however, is the ability of the electrolyte ions to move in the pore network. If the diffusion of the ions is limited, the formation of the double layer is limited and delayed, leading to distortions of the CV curve, since the limiting current for charging the double layer is only reached with a delay. C-500-2.5-T9 and C-900-5-T9 have similar pore sizes, namely predominantly micropores below 2 nm. These pores are too small for electrolyte ions to provide a fast current response and hinder the double layer formation at high scan rates. Noticeably, the CV curves of C-500-5-T9 and C-500-8-T9 show only small distortions. Even at a very high scan rate of $2500 \text{ mV} \cdot \text{s}^{-1}$, the overall electrochemical performance is excellent showing a rectangular shape with only minor distortions. This indicates a very rapid current response on voltage reversal and ultra-fast ion-diffusion kinetic in the carbon frameworks. Besides a high surface area and pore volume, C-500-5-T9 and C-500-8-T9 contain a higher amount of mesopores contributing to the fast ion-diffusion within the carbon pore network, leading to high power retention.

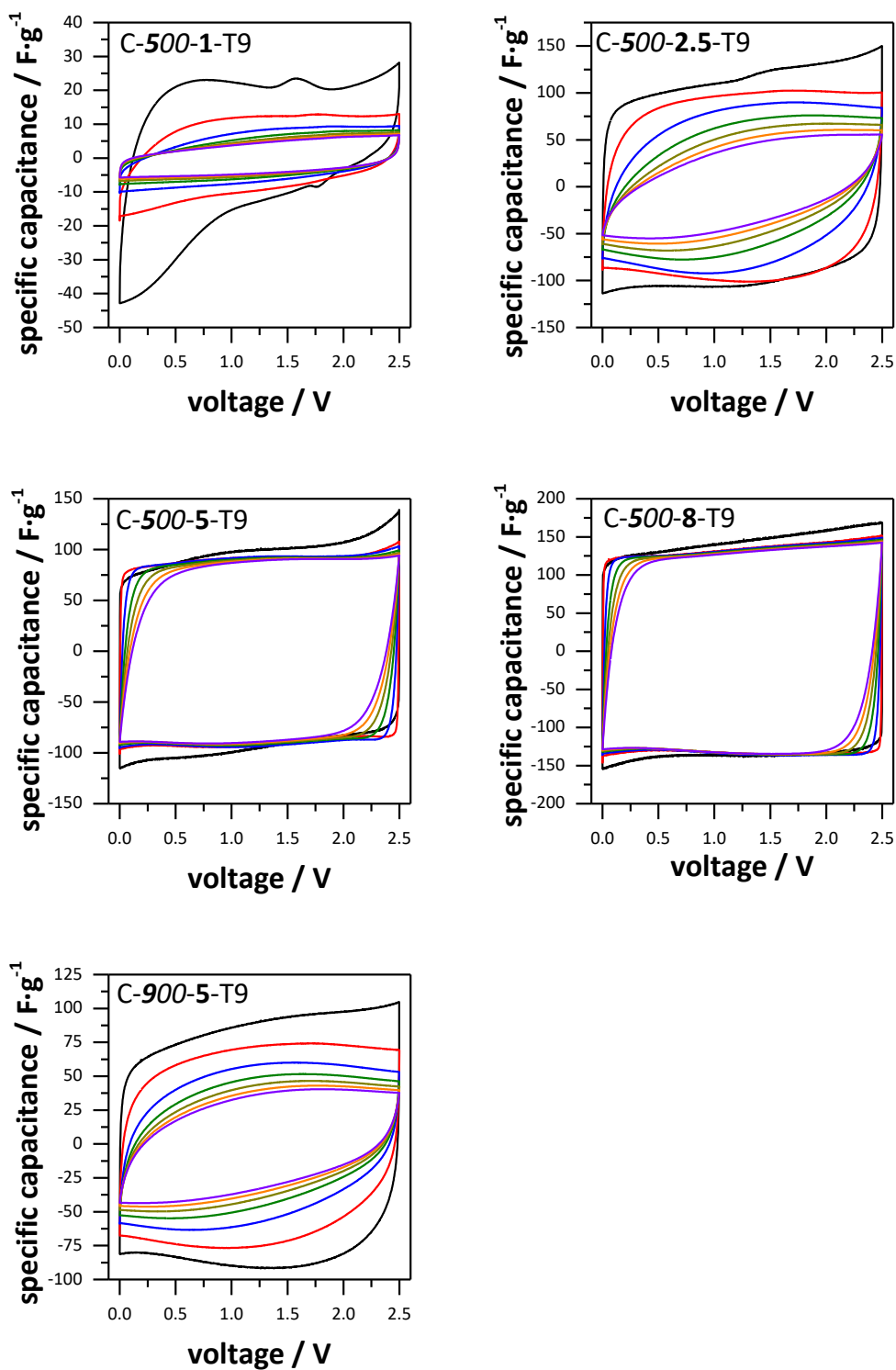


Figure 45: Cyclic voltammograms of the activated carbons synthesized with different KOH/carbon ratios at $10 \text{ mV}\cdot\text{s}^{-1}$ (black), $100 \text{ mV}\cdot\text{s}^{-1}$ (red), $500 \text{ mV}\cdot\text{s}^{-1}$ (blue), $1000 \text{ mV}\cdot\text{s}^{-1}$ (green), $1500 \text{ mV}\cdot\text{s}^{-1}$ (dark yellow), $2000 \text{ mV}\cdot\text{s}^{-1}$ (orange) and $2500 \text{ mV}\cdot\text{s}^{-1}$ (violet).

The electrochemical behavior was further investigated with galvanostatic charge/discharge tests, shown in Figure 46. For all current densities from 1 to

20 A·g⁻¹ the galvanostatic charge/discharge results from the activated carbon samples show symmetrical and linear shapes supporting the CV observations of the ideal double layer behavior. The discharge curve of C-500-1-T9 is slightly distorted, due to occurring processes, discussed above, namely the redox reactions of electrolyte and aluminum foil. The specific capacitance values for C-500-5-T9 and C-500-8-T9 stand out with values as high as 162.3 and 165.8 F·g⁻¹, calculated from galvanostatic discharge at 1 A·g⁻¹. The specific capacitance values compare very well with those of various state-of-the-art porous carbon materials used as electrode materials for capacitors with organic electrolytes.^[133,134,138,169,280–282] The capacitance values for C-500-2.5-T9 and C-900-5-T9 are lower, but still as high as 133.8 and 118.5 F·g⁻¹ respectively. Here, too, the discharge curves at a low current density are slightly distorted due to the possible ion insertion process, caused by the smaller pores. C-500-5-T9 and C-500-8-T9 have very high specific surface areas around 2500 m²·g⁻¹, which enables space for electrolyte ions to form an electric double layer. However, only the surface, which is accessible for the electrolyte ions, is of importance. Considering the sizes of the electrolyte ions (0.67 nm for TEA⁺, 0.45 nm for BF₄⁻), the accessible surface area S_{acc} for all activated carbons was calculated (Table 2). Pores larger than 0.66 nm generate the accessible surface area. It is important that both electrolyte ions can enter the pores of the respective electrode; otherwise, the cell capacitance in the symmetrical EDLC would be negligibly small.^[26,97,100,283] C-500-5-T9 and C-500-8-T9 have a similar high accessible surface area of 2000 m²·g⁻¹, resulting in the highest gravimetric capacitance values for all activated carbons discussed in this chapter. The micropore volume of C-500-5-T9 is higher than the micropore volume of C-500-8-T9. This could lead to a higher specific capacitance due to the possible increase of capacitance of micropores below 1 nm.^[152,153] However, the surface area generated by pores around 0.7 nm is nearly the same, as discussed above, resulting in similar capacitance values. The capacitance of C-500-2.5-T9 is higher than the capacitance of C-900-5-T9, despite the similar surface area and pore volume generated by pores around 0.7 nm, but the

accessible surface area of C-500-2.5-T9 is around $230 \text{ m}^2 \cdot \text{g}^{-1}$ larger, leading to a higher specific capacitance.

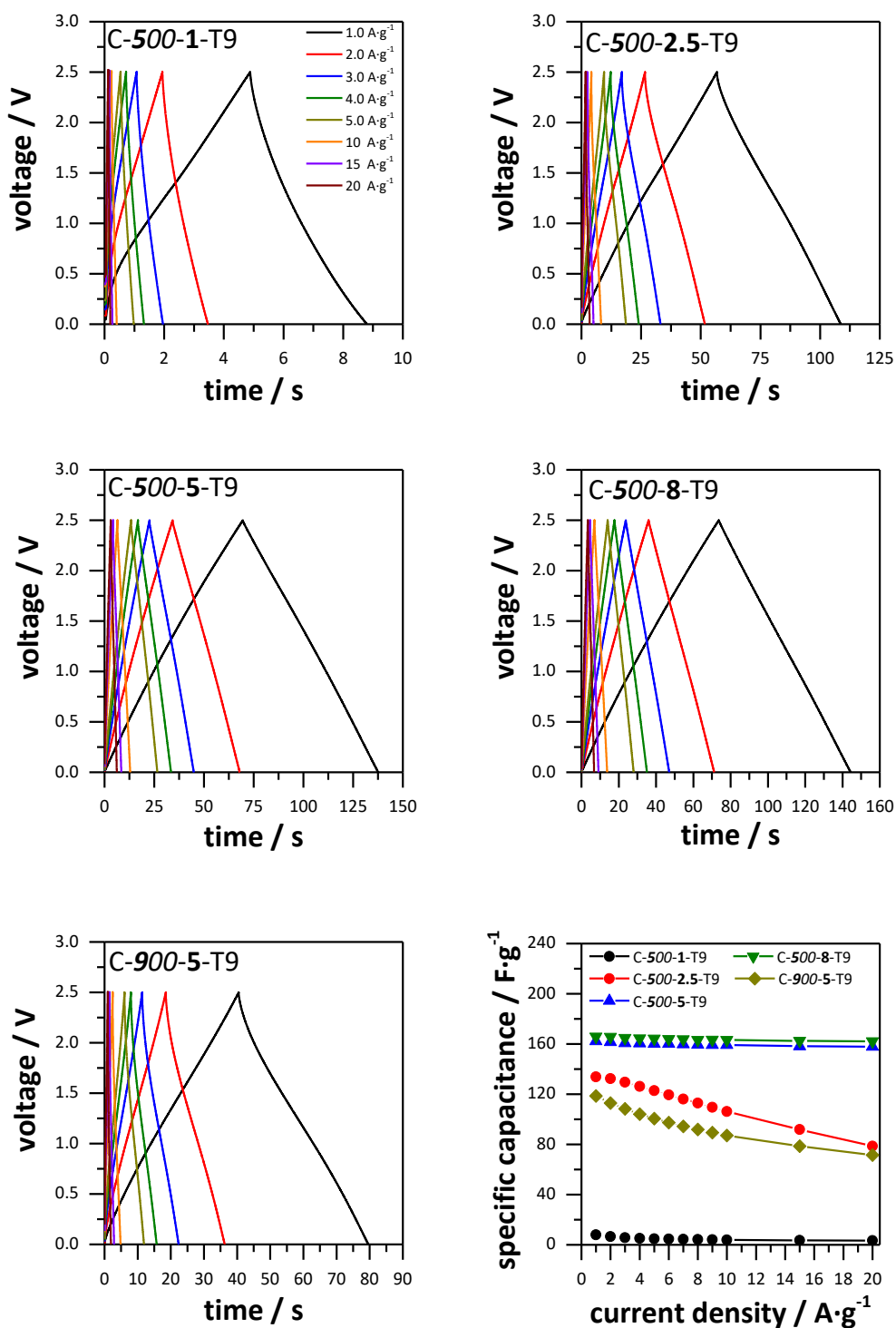


Figure 46: Galvanostatic discharge profiles of the activated carbon samples synthesized with different KOH/carbon ratios at different current densities and the specific capacitance as a function of discharge current density (bottom right).

While it is typical for EDLC to experience a significant deterioration of capacitance at higher current densities due to diffusion limitations of electrolyte ions, the loss of capacitance with respect to higher current densities for C-500-8-T9 is as small as 2.2 %, still having a capacitance of $162.1 \text{ F}\cdot\text{g}^{-1}$ at a high current density of $20 \text{ A}\cdot\text{g}^{-1}$. The same can be observed for C-500-5-T9 having a loss in capacitance of only 2.7 % and a high specific capacitance of $157.8 \text{ F}\cdot\text{g}^{-1}$ at a current density of $20 \text{ A}\cdot\text{g}^{-1}$. C-500-5-T9 and C-500-8-T9 have large micropores and small mesopores, in addition to ultramicropores. These not only serve as electrolyte reservoirs, but can also enable fast ion transport at high currents in the pore network. This clearly shows larger and ordered mesopores are not necessary for a good ion transport, even for high currents. Interconnected large micropores and small mesopores, generated by chemical activation are sufficient and the time-consuming and expensive syntheses of ordered mesoporous carbons via template methods is not necessary. The overall capacitive performance of C-500-1-T9 is rather poor due to small pores, low accessible surface area and pore volume.

So far in this chapter, a high accessible surface area is crucial for obtaining high capacitance values, while mesopores are important for fast ion transport in the pore network leading to high capacitance values even at high current densities.^[284] It is widely assumed, that high pore volumes can increase the capacitive behavior in terms of maximum capacitance and current response.^[281] While it is likely a high pore volume enhances the current response, the effect on the capacitance is rather unclear. In the narrow pore space, multilayer formation of the electric double layer is not proven, meaning that larger pores may create unused space, or a “dead volume” with no impact on the overall capacitance.

The surface area and pore volume normalized capacitance values were calculated for the activated carbon samples and are shown in Figure 47 and summarized in Table 3. Using the total surface area, the surface capacitance values for the carbon samples are almost the same, except for C-500-1-T9. This is rather surprising as it suggests each pore contributes a similar proportion to the surface capacitance. This is in contradiction with the previously observed increase in capacitance for pores below 1 nm. If the capacitance is normalized in dependence of the accessible surface area, the picture is clearly different. The surface capacitance ($C_{S>0.66}$) of C-500-2.5-T9 and C-900-5-T9 are significantly higher than those of C-500-5-T9 and C-

500-8-T9 (0.11 compared to $0.082 \text{ F}\cdot\text{m}^{-2}$), and since C-500-2.5-T9 and C-900-5-T9 also have smaller pores, this would in turn indicate a higher influence of smaller pores on the capacitance. Within the carbons discussed in this section, the dependence of volumetric capacitance (C_v) on the KOH/carbon ratio does not change when the capacitance is related to the accessible pore volume, compared to the total pore volume. C-500-2.5-T9 and C-900-5-T9 have the highest volumetric capacitance (around $180 \text{ F}\cdot\text{cm}^{-3}$) and C-500-8-T9 even has the lowest capacitance of the relevant samples ($66.4 \text{ F}\cdot\text{cm}^{-3}$). That means that the utilization of the pore volume regarding the capacitance is superior for the carbon samples with smaller pores, compared to the carbon samples with larger micropores or mesopores. This clearly shows the generated pore volume through mesopores promotes ion transport, but also leads to dead volume, which does not contribute to energy storage.

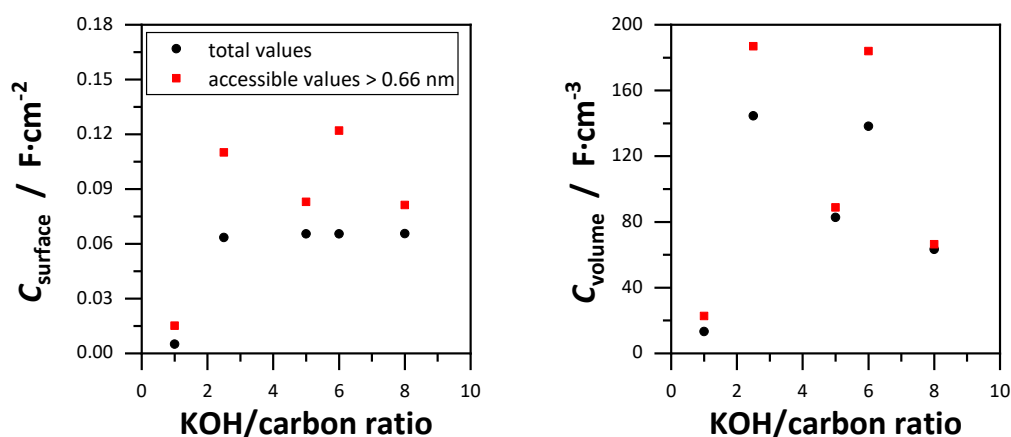


Figure 47: Surface area normalized capacitance as a function of the KOH/carbon ratio (left) and the pore volume normalized capacitance as a function of the KOH/carbon ratio (right). The sample C-900-5-T9 is placed at the ratio of 6.

Table 2: Electrochemical properties of the EDLC prepared from the activated carbons synthesized with different KOH/carbon ratios in 1 M TEABF₄/ACN.

Sample	$S_{\text{acc}} /$ $\text{m}^2 \cdot \text{g}^{-1}$	$V_{\text{acc}} /$ $\text{cm}^3 \cdot \text{g}^{-1}$	$C_{\text{CV}} /$ $\text{F} \cdot \text{g}^{-1}$	$C_{\text{DC}} /$ $\text{F} \cdot \text{g}^{-1}$
C-500-1-T9	522	0.35	17.6	7.9
C-500-2.5-T9	1216	0.71	110.5	133.8
C-500-5-T9	1954	1.83	141.2	162.3
C-500-8-T9	2039	2.50	155.7	165.8
C-900-5-T9	972	0.64	124.0	118.5

S_{acc} specific surface area for pores > 0.66 nm; V_{acc} pore volume for pores > 0.66 nm; C_{CV} calculated from $10 \text{ mV} \cdot \text{s}^{-1}$; C_{DC} calculated from $1 \text{ A} \cdot \text{g}^{-1}$.

Table 3: Surface- and volumetric capacitance values for activated carbons synthesized with different KOH/carbon ratios.

Sample	$C_{\text{S}} /$ $\text{F} \cdot \text{m}^{-2}$	$C_{\text{S}>0.66} /$ $\text{F} \cdot \text{cm}^{-2}$	$C_{\text{V}} /$ $\text{F} \cdot \text{cm}^{-3}$	$C_{\text{V}>0.66} /$ $\text{F} \cdot \text{cm}^{-3}$
C-500-1-T9	0.005	0.015	13.3	22.8
C-500-2.5-T9	0.063	0.11	144.5	186.8
C-500-5-T9	0.065	0.083	82.7	88.7
C-500-8-T9	0.066	0.081	63.3	66.4
C-900-5-T9	0.065	0.12	138.2	183.9

C_{S} , $C_{\text{S}>0.66}$ calculated from C_{DC} and the respective surface areas, obtained from the DFT results; C_{V} , $C_{\text{V}>0.66}$ calculated from C_{DC} and the respective pore volumes.

Electrochemical impedance spectroscopy (EIS) was carried out between 500 kHz and 10 mHz for further investigation of the prepared EDLC and are shown in Figure 48. In the Nyquist plot, the intersection of the real impedance shows the equivalent serial resistance (R_{ESR}) at high frequencies, which is discussed in detail in section 1.4.1. The R_{ESR} values for all investigated carbons are very low, indicating a sufficient intrinsic conductivity for electrochemical purpose.^[285] The activated carbon samples show either no significant semicircle or a short semicircle, like C-900-5-T9, indicating mainly electrochemical double layer energy storage for the prepared systems. The general visibility of the semicircle is due to either charge transfer reactions on the electrode surface, or to contact resistances, since these can also occur

in the medium frequency range.^[95] Warburg segments are of short length for all samples pointing to low diffusion resistance for electrolyte ions, when they enter the pore network. Regarding the frequency response of the phase angle, the angle should be close to -90° for low frequencies, for ideal capacitive behavior. However, the phase angle of ELDC devices are often smaller due to resistances, induced by the interaction of electrolyte ions and the surface of the carbon electrode material, even at low frequencies. The samples C-500-5-T9 and C-500-8-T9 show almost perfect double layer behavior with phase angles of -88.2° and -88.4° respectively. This is attributed to the mesopores which enhance electrolyte ion migration within the whole carbon framework. Interestingly the phase angles of the microporous C-500-2.5-T9 and C-900-5-T9 are -85.9° and -85.8° , respectively, indicating large micropores enhance electrolyte migration likewise at low frequencies. C-500-1-T9 shows rather poor capacitive behavior at low frequencies due to the small micropores, which prohibit resistance free migration within the pore network. It is therefore not possible, to determine the true maximum capacitance value for C-500-1-T9, because the diffusion resistance is still too large, even at low current densities.

The normalized real capacitance dependent on the frequency is plotted in Figure 48 bottom left. The real capacitance reflects the energy storage capacitance of the device or the electrode material. It is clear that with increasing frequency the capacitance decreases due to diffusion limitations of electrolyte ions. The resistance in narrow pores and the diffusion resistance of adsorbed ions in the double layer induce the diffusion resistance.^[131] While C-500-8-T9 shows superior characteristics by having almost the same capacitance at a relatively high frequency of 1 Hz, the capacitance of C-500-1-T9 already decreases at 10 mHz, and has never reached its maximum capacitance. From the imaginary resistance plotted against the frequency, the time relaxation constant τ_0 can be calculated by $\tau_0 = 1/f_0$ given by the maximum of the normalized imaginary resistance at the frequency f_0 . The imaginary capacitance reflects the capacitance loss at a given frequency, and the time relaxation constant reflects the discharge time of a capacitor in which the device energy efficiency is larger than 50 %. The time relaxation constants are > 100 , 1.19, 0.75, 0.29 and 1.50 s for C-500-1-T9, C-500-2.5-T9, C-500-5-T9, C-500-8-T9 and C-900-5-T9, respectively. All activated carbons, except for C-500-1-T9, have a very small time constant, while C-500-8-T9 outstands with a time constant as small as 0.26 s. This can be attributed to the larger mesopores, which grant fast diffusion

of electrolyte ions in the pore network at higher frequencies. For the series of carbon samples discussed in the present section, the time constant decreases with increasing pore volume. However, one should be careful with the interpretation of the time constant. Parameters such as the density of carbon also play a role, and this is not the same for all carbon samples. Nevertheless, the time constant for the samples presented here correlates relatively well with the pore volume and therefore with the pore size.

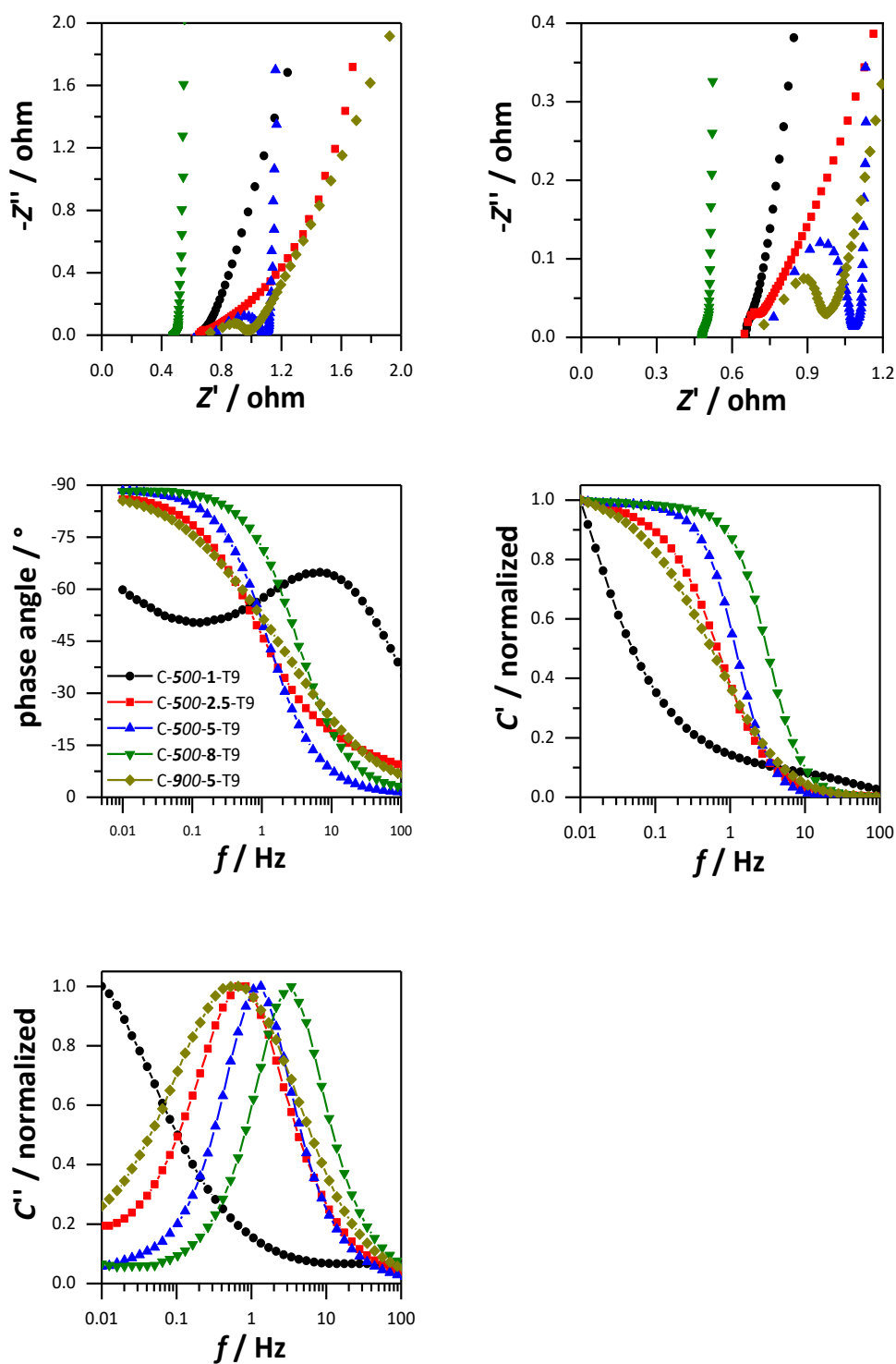


Figure 48: Nyquist plot of the activated carbons (top left and top right); frequency response of the phase angle (middle left), normalized real capacitance (middle right) and normalized imaginary capacitance (bottom left).

The long cycling life of supercapacitors is an important property and was tested representative for C-500-8-T9 with galvanostatic charge/discharge tests at $2 \text{ A} \cdot \text{g}^{-1}$.

Figure 49 shows the results from over 2750 cycles and C-500-8-T9 still exhibits 93 % of the initial capacitance indicating a good robustness of the material. The cycling stability of C-500-8-T9 is attributed to the double layer charge/discharge process in the electrode materials and to the mesopores content, which enables a low resistance diffusion and adsorption of electrolyte ions.^[286,287]

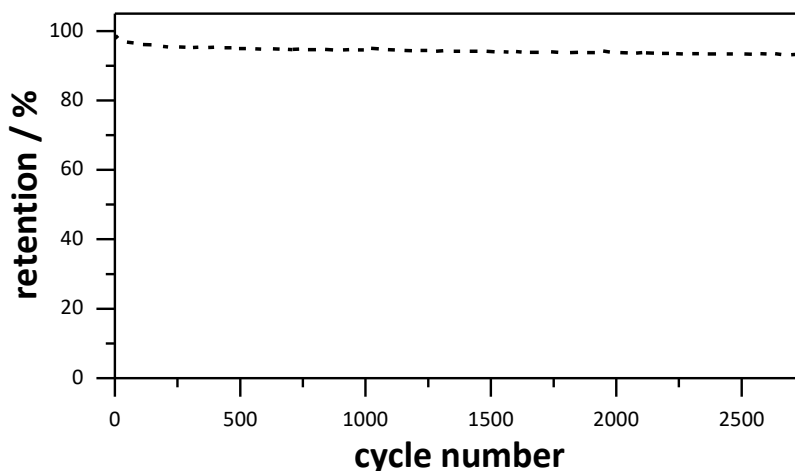


Figure 49: Cycling stability of C-500-8-T9 at a current density of $2 \text{ A} \cdot \text{g}^{-1}$.

The electrochemical performance of the activated carbons discussed in this chapter, depends heavily on the pore sizes, specific surface area and pore volume. A large accessible surface area is crucial for obtaining a large gravimetric specific capacitance. However, a higher micropore content is beneficial for the utilization of the electrode surface and the pore volume as mesopores create a “dead volume”. For adequate ion diffusion within the pore network, large micropores are necessary. Nevertheless, mesopores are required for a good retention of the specific capacitance with increasing current densities, since larger pores offer low resistance pathways within the carbon network.

Hydrogen storage

The hydrogen storage capacity of the activated carbons synthesized with different KOH/carbon ratios was investigated in the low pressure range of 0 to 1 bar at 77 K and the isotherms are shown in Figure 50. The values discussed in this chapter and in the entire work are based on a dry material basis. For all the activated carbon samples, the hydrogen uptake is reversible, with no hysteresis and no saturation is

attained in the 0 to 1 bar pressure range. Still, the low-pressure uptake is a strong indicator of the uptake capacity at higher pressure.^[217] While the hydrogen adsorption capacity at low pressures up to 0.1 bar mainly depends on the micropore sizes, the uptake at pressures up to 1 bar mainly depends on the surface area of the storage material. The surface area is also the most important factor for the uptake capacity at pressures up to 100 bar, which is why the uptake capacity at 1 bar is an indicator for the general adsorption capacity of a storage material.

The progression of the isotherms differ for the activated carbons at different pressure ranges. Up to a pressure range of 0.1 bar, sample C-500-1-T9 shows the highest uptake capacity of ca. 1.3 wt% followed by samples of C-500-2.5-T9 and C-900-5-T9. The uptake capacities of C-500-5-T9 and C-500-8-T9 are significantly lower, with C-500-8-T9 showing an uptake capacity of only 0.8 wt%. The hydrogen adsorption at these low pressure is dominated by the interaction of the adsorbed hydrogen and the pore wall of the carbon. For small micropores, the adsorption potentials of the pore walls overlap, which increases the adsorption potential of the hydrogen on the pore wall, as described in section 2.1. This results in an increased adsorption of hydrogen in these small micropores, since the surface of these small micropores is already completely occupied with hydrogen at the low pressure of 0.1 bar. A complete covering of the surface only takes place at higher pressures, because at lower pressures adsorbed hydrogen desorbs faster to provide a pressure equalization in the system. This is in accordance with the observations of the isotherm progressions in Figure 50. At a low pressure of 0.1 bar, the activated carbon samples with smaller pores show a significantly higher adsorption of hydrogen, while the activated carbon samples with a higher surface area show a higher hydrogen uptake capacity at pressures between 0.9 and 1 bar, namely C-500-5-T9, C-500-2.5-T9 and C-500-8-T9.

The hydrogen uptake capacity of C-500-5-T9 is the highest with 2.73 wt%, which is a high gravimetric uptake capacity for carbons based on synthetic polymers where the benchmark values where the benchmark values lie between 2.2 and 3.6 wt%.^[288,289] The uptake capacities of C-500-2.5-T9 and C-500-8-T9 are comparatively high with 2.70 and 2.66 wt% respectively. The uptake capacities of C-500-1-T9 and C-900-5-T9 are significantly lower with 2.30 and 2.49 wt% respec-

tively. It is clear, the high specific surface area of C-500-5-T9 is beneficial for obtaining the high uptake capacity of hydrogen, because more active adsorption sites for hydrogen are available on the carbon substrate. However, when the specific surface area dependency of the hydrogen uptake is considered (Figure 51) the maximum capacity seems to be saturated at surface areas exceeding $2000 \text{ m}^2 \cdot \text{g}^{-1}$. It becomes even clearer, when the specific surface area normalized hydrogen uptake is considered in relation to the KOH/carbon ratio (Figure 51). The normalized uptakes of C-500-1-T9 and C-900-5-T9 are the highest, while the values for C-500-2.5-T9, C-500-5-T9 and C-500-8-T9 decrease as the ratio increase. This clearly shows the contribution of the surface area to the hydrogen uptake capacity is not uniform and depends on other factors, such as pore size. This has also been observed for metal organic frameworks, which showed a differentiated influence of the surface area depending on the adsorbed amount of hydrogen.^[290] It has already been shown, that the small micropores, presumably lower than 1 nm, are important for the hydrogen uptake at pressures up to 0.1 bar, while the surface area becomes more predominant with higher pressures. Therefore, the utilization of the pore surface is more sophisticated von carbon samples with smaller micropores and lower surface areas, such as samples C-500-1-T9 and C-900-5-T9.

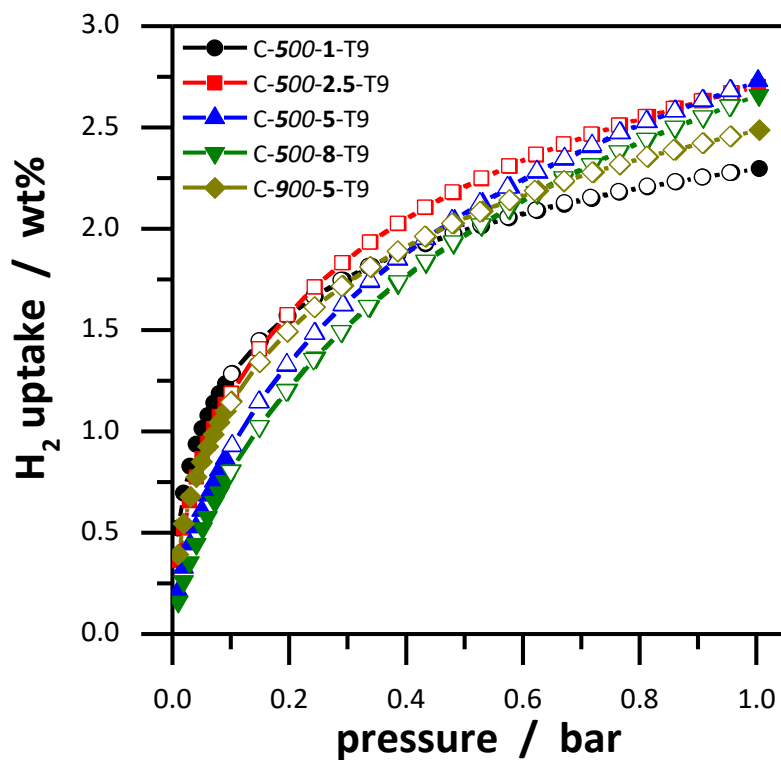


Figure 50: Gravimetric hydrogen storage capacity of different activated carbons at 77 K.

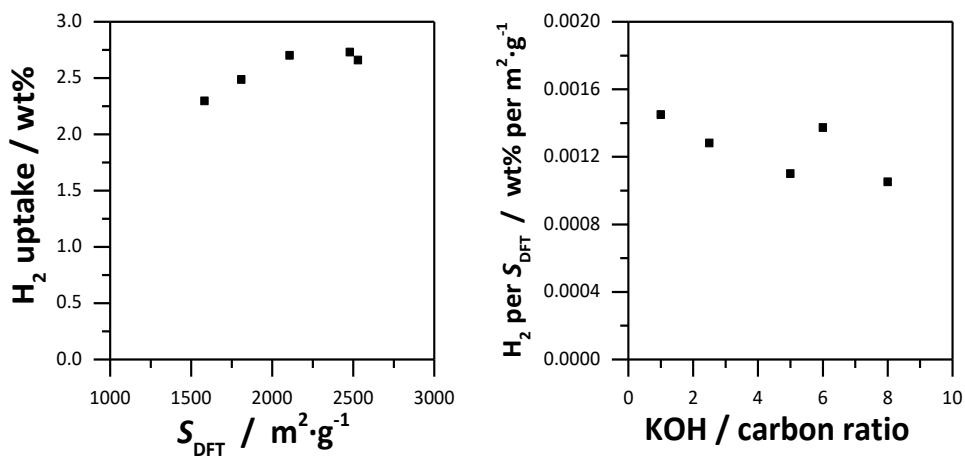


Figure 51: Gravimetric hydrogen uptake plotted against the specific DFT surface area of the activated carbons (left) and the specific surface area normalized uptake capacity plotted against the KOH/carbon ratio. The KOH/carbon ratio of C-900-5-T9 is denoted with 6.

A graphical summary of the carbon materials' properties of this chapter is shown in Figure 52. Regarding the influence of the activation reactant, a correlation between the KOH/carbon ratio and the pore size was observable, showing a larger amount of activation reactant leads to an enlargement of pores. At the same time, the specific surface area and total pore volume increase with a larger KOH/carbon ratio, although pores larger than 1 nm make up a majority of the surface area. The effectiveness of the chemical activation can be increased, by introducing a semi-carbonization step prior to the chemical activation. This way, the pre-carbonized material is less resistive against the chemical activation process, which leads to an enhanced porosity. Considering the carbon samples as possible ELDC electrode materials, the ion accessible surface area had to be taken into account. The gravimetric discharge capacitance clearly correlates with the accessible surface area. However, carbon materials with smaller pores, on average, showed a better utilization of the surface area and pore volume by the electrolyte ions. Similar correlations were observable regarding the gravimetric hydrogen uptake capacity. High specific surface areas lead to high gravimetric uptake capacities, but the capacity, normalized to the specific surface area, was superior for carbon materials with smaller surface areas and smaller pores. Therefore, pore sizes remain a key parameter, whose exact influence on the discussed applications require further evaluations.

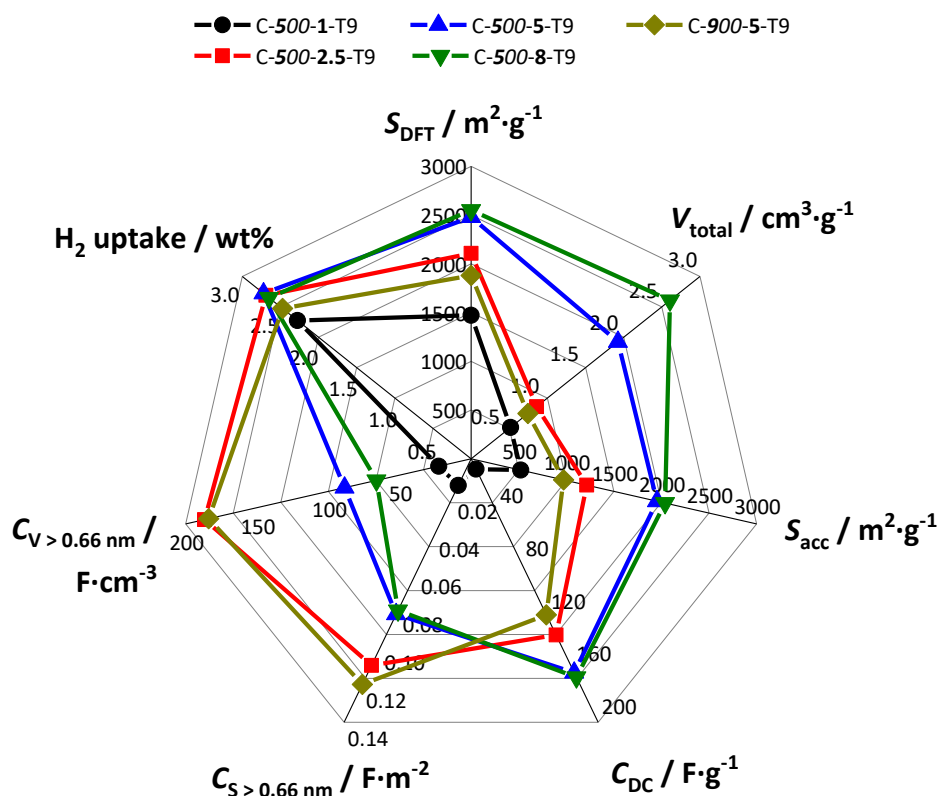


Figure 52: Graphical summary of the properties of the activated carbon samples, synthesized with different KOH/carbon ratios.

4.1.3 Influence of the semi-carbonization temperature

In this chapter, the influence of the semi-carbonization temperature on the properties of the activated carbon samples is investigated in more detail. The synthesis scheme is shown in Figure 53. The PF-resins were semi-carbonized at different temperatures, followed by a chemical activation with a KOH/carbon ratio of 5 at a temperature of 900 °C. The KOH/carbon ratio of 5 was set as the standard ratio for the synthesis procedure. It ensures a good and effective KOH activation, which is mandatory for obtaining larger micropores, small mesopores and high surface areas but still offers other synthesis parameters, like the semi-carbonization temperature or activation temperature the possibility to effect the structure of the resulting carbons. This is important, since it is the goal, to investigate the influence of the synthesis parameters on the structure and properties of the resulting activated carbons. Semi-carbonization temperatures of 300, 400, 600, 700 and 800 °C were chosen and the samples are denoted as C-300-5-T9, C-400-5-T9, C-600-5-T9, C-700-5-T9

and C-800-5-T9. The KOH/carbon ratio of 5 was maintained as standard, as the overall reaction was more controllable and to have only one parameter varied. In addition, the yield was very low at a KOH/carbon ratio of 8 (24 %), which significantly limits the applicability.

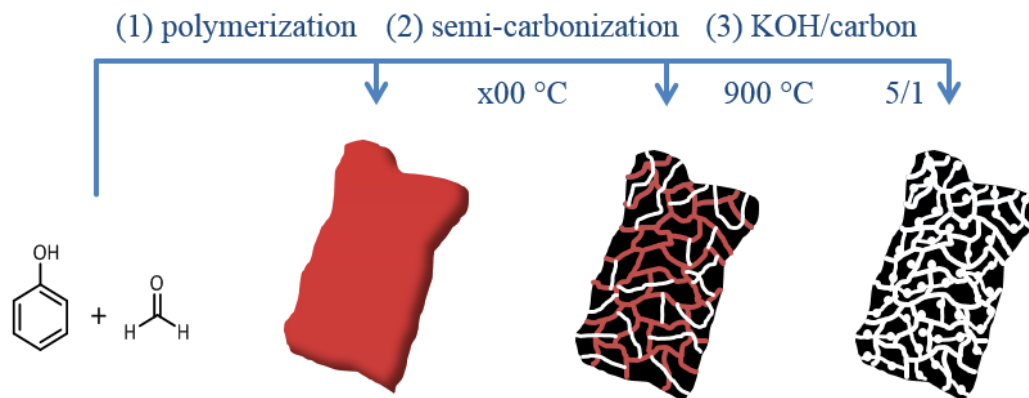


Figure 53: Synthesis scheme for the preparation of HSAC with different semi-carbonization temperatures. The PF resin (1) was semi-carbonized (2) with different temperatures followed by a chemical activation (3) with a KOH/carbon ratio of 5 at 900 °C.

4.1.3.1 Characterization of carbons synthesized at different semi-carbonization temperatures

The SEM images of the prepared activated carbons are shown in Figure 54. It is visible C-800-5-T9, C-700-5-T9 and C-600-5-T9 possess a network structure, composed of loose agglomerated spherical carbon nanoparticles. The network structure matches with the previously discussed structure of C-500-1-T9 and C-500-2.5-T9 (see section 4.1.2.1). The loose agglomeration of the spherical carbon nanoparticles leads to the same formation of cavities in the network, which are 2 to 20 μm in diameter. The network structures of C-400-5-T9 and C-300-5-T9 differ significantly from the other HSAC in this chapter. The carbon surface is smooth without agglomerated spherical carbon nanoparticles, while they still possess cavities within the network with similar diameters from 5 to 20 μm . The agglomeration of the particles occurred during the activation process. When PF-resins are semi-carbonized at lower temperatures, they become more susceptible towards the chemical activation in terms of chemical resistance. The reason is likely due to the higher content of heteroatoms, in this case oxygen, which weaken the otherwise chemical resistive carbon network, containing mainly carbon-carbon bonds. With a higher

semi-carbonization temperature treatment, more oxygen is removed from the carbon network by forming carbon dioxide or carbon monoxide, leaving behind holes, or pores and a network mainly consisting of carbon with stable carbon-carbon bonds. ^[91,273] The results are a stronger altering of the carbon structure, leading to a larger amount of pores and larger pores in general, as discussed in section 4.1.2. Apparently, this altering is also visible for macroscopic structure, as seen for samples C-400-5-T9 and C-300-5-T9 and to some extent for sample C-500-5-T9 where the agglomerated particles are slightly larger than for carbon samples C-500-1-T9 and C-500-2.5-T9. Due to the lower semi-carbonization temperature, more oxygen heteroatoms were present in the carbon networks. During the chemical activation, not only oxygen atoms were removed due to the simple heat treatment, but also likely due to the reaction with KOH or activation side products because they are active reaction sides during the KOH activation. At the same time, the carbon atoms were removed via chemical reactions with KOH. That way, a more bonds of the substrate structure were broken, more pores were created, which caused a collapse of the macroscopic structure. While a simple temperature treatment removes more oxygen atoms from the carbon network, the structural damage of the macroscopic structure is not very pronounced. This changes when many oxygen atoms are present during a chemical activation, as carbon atoms are removed from the network at the same time, severely damaging the macroscopic structure.

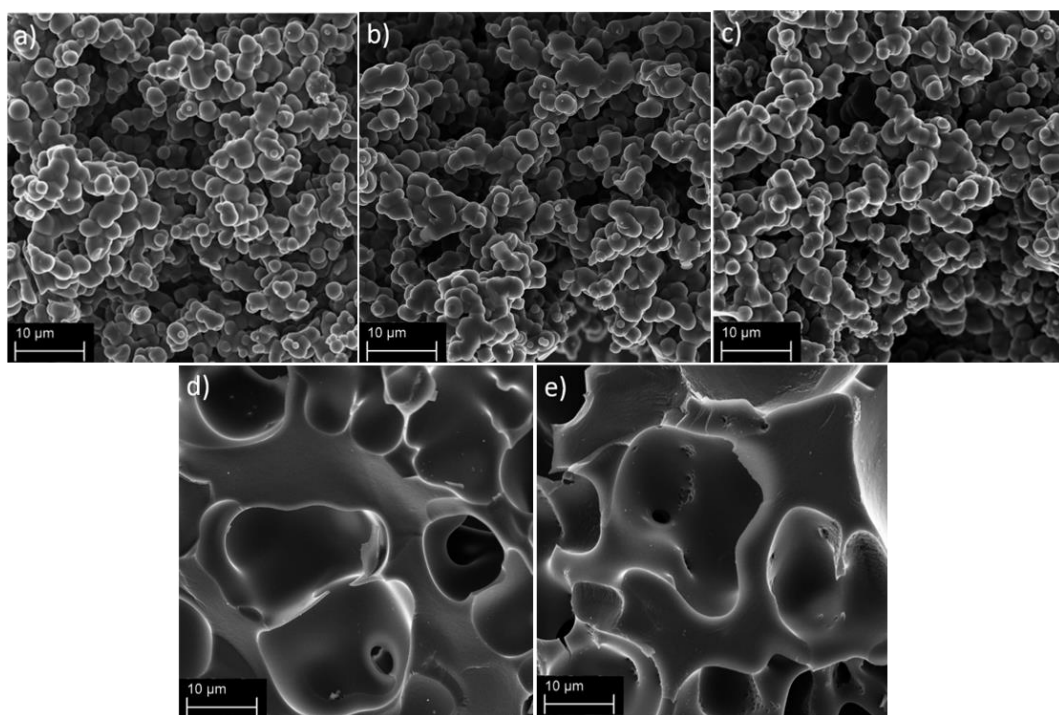


Figure 54: SEM images of the activated carbons. (a) C-800-5-T9, (b) C-700-5-T9, (c) C-600-5-T9, (d) C-400-5-T9 and (e) C-300-5-T9.

The p-XRD patterns of the carbon samples are shown in Figure A.2. Similar to the previously discussed carbon samples, all carbons show weak and extremely broad reflections at $44^\circ 2\theta$ corresponding to (101) diffractions of a turbostratic carbon structure. Only C-800-5-T9 shows a weak diffraction at $20^\circ 2\theta$ likely corresponding to stacked graphene layers. The semi-carbonization of 800°C was high enough to enable a stacking of graphene layers although only to a less extent. The Raman spectra are shown in Figure A.3. The calculated I_D/I_G ratios are 1.08, 1.15, 1.16, 1.22 and 1.26 for C-800-5-T9, C-700-5-T9, C-600-5-T9, C-400-5-T9 and C-300-5-T9 respectively. The intensity ratios are therefore increasing with decreasing semi-carbonization temperature indicating a lower degree of graphitization for the carbon samples, treated at a lower semi-carbonization temperature prior to the chemical activation. The low temperatures of 300 and 400°C were not high enough to enable a stacking of graphene layers, which was only slightly observable for sample C-800-5-T9. Results from p-XRD and Raman scattering indicate the carbon samples are amorphous materials. This can be attributed to the low semi-carbonization temperatures, especially for samples C-400-5-T9 and C-300-5-T9 and the chemical activation with a high KOH/carbon ratio of 5, which causes structural damage to the

carbon network as seen in section 4.1.2.^[65] The results of the thermogravimetry for all carbon samples are shown in Figure A.4. In general, all carbons show a complete burn off leaving no residual mass. This indicates pure carbons, which are free of any impurities like inorganic salts, which could remain after the chemical activation process. The starting combustion temperatures for C-800-5-T9, C-700-5-T9 and C-600-5-T9 are quite similar at approximately 550 °C, while the starting combustion temperatures of C-400-5-T9 and C-300-5-T9 are higher at 575 and 600 °C respectively. This means that porous carbon samples with a possibly higher degree of porosity in terms of larger pore sizes and higher surface area, seem to be more thermal stable. Similar results have been observed in the previous section 4.1.2.1. The reason is the lower content of oxygen atoms in the carbon networks of the samples, treated at a lower semi-carbonization temperature. With a lower semi-carbonization temperature, the carbon networks possess a higher content of oxygen, which are active reaction sites for KOH and therefore are the reason, for the less rigid character of the carbons toward the chemical activation. However, the results in a lower content of oxygen in the carbon network for the samples, treated at a lower semi-carbonization temperature and thus leading to a higher thermal stability.

The corresponding isotherms of the nitrogen physisorption measurements are shown in Figure 55 and the nitrogen physisorption derived data are summarized in Table 4. The samples C-800-5-T9, C-700-5-T9 and C-600-5-T9 show a typical type I isotherm, indicating carbon materials with predominantly micropores. C-400-5-T9 and C-300-5-T9 show a slope at relative pressures from 0.1 to 0.4 and additionally hysteresis loops. Both phenomena indicate the presence of large micropores and mesopores. It seems the pore size increases, with decreasing semi-carbonization temperature. The pore size distributions, calculated by the QSDFT method from the nitrogen desorption branch, shown in Figure 56, support this suggestion. All carbon samples possess micropores smaller than 1 nm originating from the carbonization process and the chemical removing of carbon atoms during the KOH activation. In addition to these small micropores, all carbons have larger pores, with C-400-5-T9 and C-300-5-T9 having additional mesopores up to 5 nm, while C-300-5-T9 has slightly larger pores than C-400-5-T9. It is clear, the semi-carbonization temperature is in direct correlation with the pore size. As confirmed from section

4.1.2.1 the pore sizes of the carbon materials increase with a decreasing semi-carbonization temperature while maintaining a constant KOH/carbon ratio and activation temperature. This confirms that the carbon framework does not show high chemical resistance after a low temperature treatment in the form of a low semi-carbonization temperature. It is suspected a larger content of organic residues remains after a low temperature carbonization treatment, namely oxygen, which offers active reaction sites for the chemical activation reactant.^[65] This way, a greater amount of pores is created and more importantly, existing pores are enlarged. All in all, a lower semi-carbonization temperature leads to an increase in pore size. However, the thermal stability is increased at the same time, due to the low content of oxygen for the final activated carbons.

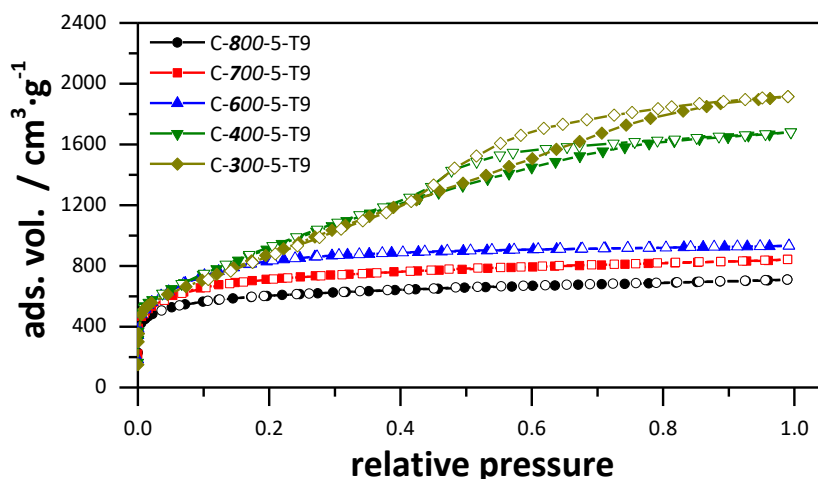


Figure 55: Nitrogen adsorption-desorption isotherms (77 K) of the carbon materials synthesized at different semi-carbonization temperatures.

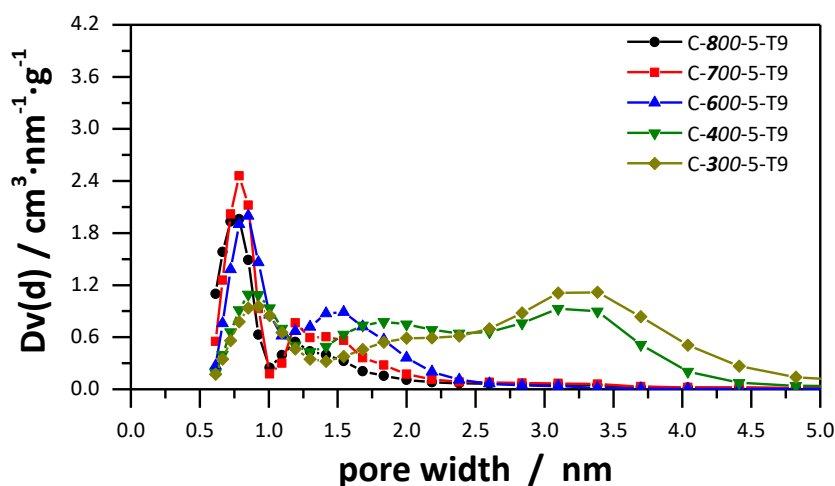


Figure 56: Pore size distributions of the carbon materials synthesized at different semi-carbonization temperatures, calculated by the QSDFT method from nitrogen desorption branch assuming slit pores.

The specific surface area depends on the semi-carbonization temperature as it increases with decreasing semi-carbonization temperatures in the range of 800 to 400 °C. Accordingly, C-400-5-T9 has the highest DFT surface area with $\sim 2600 \text{ m}^2 \cdot \text{g}^{-1}$. A low semi-carbonization temperature not only results in a pore enlargement, but also increases the amount of pores, which leads to high specific surface areas. With a higher semi-carbonization temperature, the carbon framework becomes more rigid and resistive against the chemical activation and the enlargement of pores is limited. The specific surface area of C-800-5-T9 is the lowest among the carbon samples discussed in this chapter, but still as high as $2045 \text{ m}^2 \cdot \text{g}^{-1}$. This can be attributed to the high KOH/carbon ratio, which ensures new micropores are formed during activation. A similar correlation is observable for the total pore volume. C-300-5-T9 has an ultra-high pore volume of $2.82 \text{ cm}^3 \cdot \text{g}^{-1}$ and the pore volume decreases with increasing semi-carbonization temperature in accordance with the decreasing pore sizes. The micropore volume increases with a decreasing semi-carbonization temperature up to 600 °C and then decreases again, with C-600-5-T9 having the highest micropores volume of $1.22 \text{ cm}^3 \cdot \text{g}^{-1}$. This may lead to the conclusions, that a lower semi-carbonization temperature increases the amount of small pores in general. However, micropores are pores with the range up to 2 nm and the pores become larger with a lower semi-carbonization temperature. The pores are just large micropores, on the edge of mesopores. The micropore volume

in dependence of the semi-carbonization temperature reflects the transition of the carbon materials from being mainly microporous (600 °C) to having additional mesopores (400 °C) as previously observed. The results so far, emphasize the observations and conclusions from section 4.1.2.1; the semi-carbonization temperature has a major influence on the formation of pores and their sizes, which then determines the surface area and pore volume.

Table 4: Nitrogen physisorption derived data of the carbon samples synthesized at different semi-carbonization temperatures.

Sample	$S_{\text{BET}} /$ $\text{m}^2 \cdot \text{g}^{-1}$	$S_{\text{DFT}} /$ $\text{m}^2 \cdot \text{g}^{-1}$	$V_{\text{t}} /$ $\text{cm}^3 \cdot \text{g}^{-1}$	$V_{\text{mic}} /$ $\text{cm}^3 \cdot \text{g}^{-1}$
C-800-5-T9	2259	2045	1.00	0.86
C-700-5-T9	2640	2220	1.20	1.02
C-600-5-T9	3045	2342	1.33	1.22
C-400-5-T9	3413	2606	2.45	1.00
C-300-5-T9	3367	2558	2.82	0.78

S_{DFT} (DFT surface area), V_{t} (total pore volume) and V_{mic} (micropore volume) obtained from QSDFT analysis. S_{BET} (BET surface area).

The micropore analysis was obtained from carbon dioxide physisorption measurements and the adsorption-desorption isotherms at 273 K are shown in Figure 57. All isotherms are reversible adsorption desorption behavior and show an almost linear correlation of adsorbed volume with increasing relative pressure except for the samples C-800-5-T9 and C-700-5-T9, which show a larger increase at relative pressures up to 0.004. This is due to the larger presence of small micropores with the size around 0.335 nm. For the other carbon samples, this indicates evenly distributed pores up to 1 nm in size. The pore size distribution calculated by the NLDFT method are shown in Figure 58. As described in the previous chapter the pore size distributions show multimodal pattern for all carbons due to the NLDFT artifact, which causes zero minima at 0.4 and 0.7 nm. Otherwise, the pore size distributions are similar for the carbon samples. There are minor differences in the intensities at certain pore sizes, but they are difficult to interpret, since the NLDFT method provides results streaked with smaller artifacts. The analysis of the cumulative surface area and pore volume is more sophisticated.^[188,189]

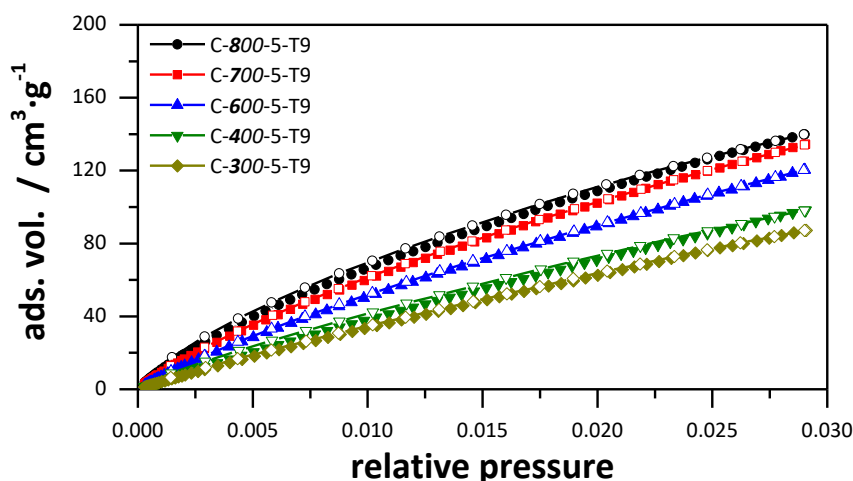


Figure 57: Carbon dioxide adsorption-desorption isotherms (273 K) of the carbon materials synthesized at different semi-carbonization temperatures.

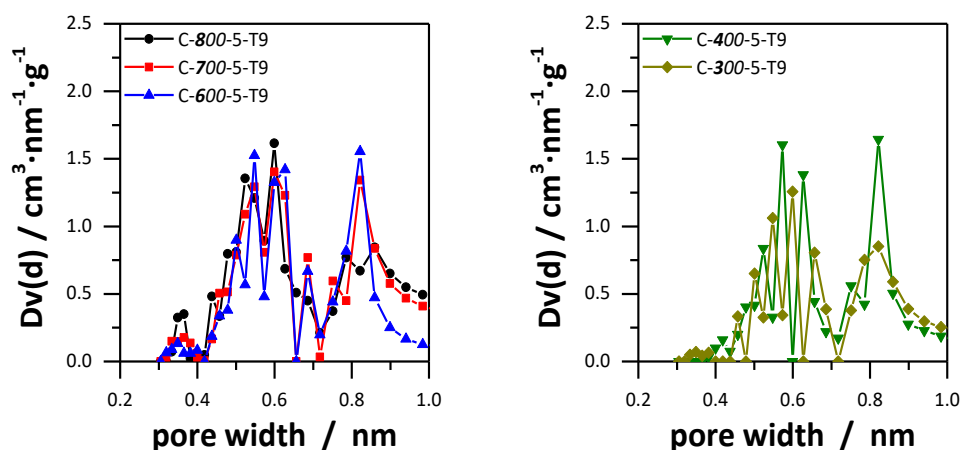


Figure 58: Pore size distributions of the carbon materials synthesized at different semi-carbonization temperatures, calculated by the NLDFT method from carbon dioxide desorption branch assuming slit pores.

The cumulative specific surface area of the combined data of carbon dioxide and nitrogen physisorption is shown in Figure 59. The proportion of the surface generated by pores smaller than 1 nm depends on the semi-carbonization temperature. The surface area provided by pores up to 1 nm is $1250 \text{ m}^2 \cdot \text{g}^{-1}$ for C-800-5-T9 and the surface area decreases with decreasing semi-carbonization temperature. The surface area, generated by pores up to 0.6 nm follows the same correlation. This

means, however, carbon samples synthesized at lower semi-carbonization temperatures, have larger accessible surface areas with respect to the electrolyte ions used for the electrochemical characterization. The critical pore size is the size of the BF_4^- ion with 0.67 nm and the accessible surface area describes the surface, promoted by pores larger than 0.67 nm. This means eventually, that the carbon samples, synthesized at lower semi-carbonization temperatures, not only possess a higher assessable surface area, but also likely a higher amount of pores between 0.67 and 1 nm, which are likely to be crucial for the electrochemical energy storage due to the partial or full removal of the solvent shell of electrolyte ions. The larger proportion of the total surface area for C-300-5-T9 and C-400-5-T9 compared to the other three carbon samples, is generated by pores between 1 and 3 nm. The cumulative pore volume for the activated carbon samples is shown in Figure 60 and confirms larger pores generate a higher total pore volume, leading to the ultra-high pore volume of C-300-5-T9.

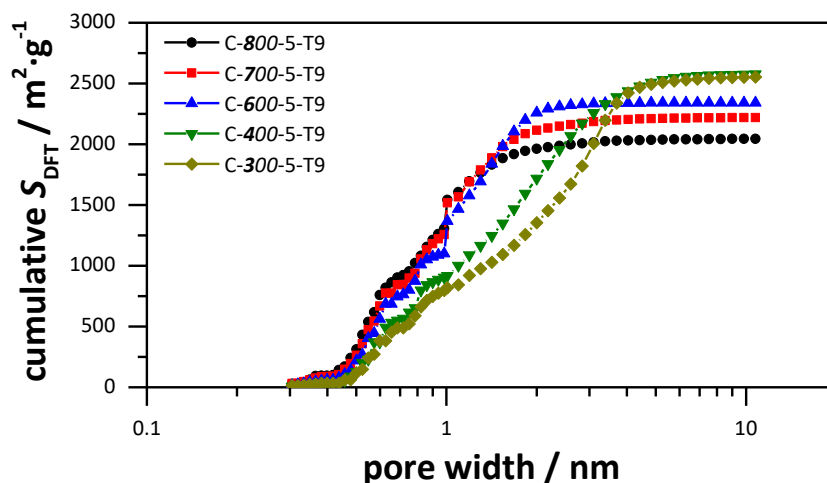


Figure 59: Combined cumulative surface area derived from carbon dioxide and nitrogen physisorption data of the carbon samples synthesized at different semi-carbonization temperatures.

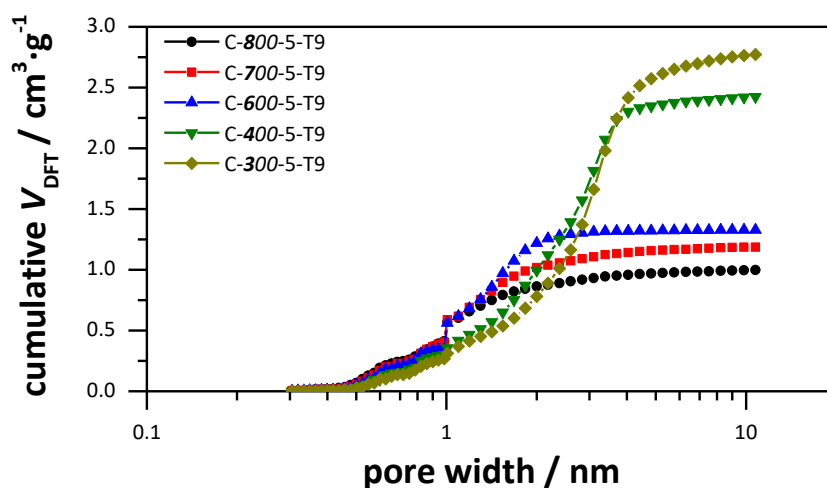


Figure 60: Combined cumulative pore volume derived from carbon dioxide and nitrogen physisorption data of the carbon samples synthesized at different semi-carbonization temperatures.

Including the results of the previous section 4.1.2, it becomes clear the semi-carbonization step is crucial in tailoring the porosity of the synthesized activated carbon material. With high semi-carbonization temperatures, the carbon framework is more resistive against the chemical activation and the pore generation and enlargement during the activation process is limited. Hence, the resulting carbons are predominantly microporous and have low pore volumes and surface areas. The total and accessible surface area can be tailored as shown in Figure 61. While the total surface area seems saturated at a semi-carbonization temperature of 400 °C, the accessible surface area is still increasing with decreasing semi-carbonization temperature. Whether or not the capacitance for EDLCs or the gravimetric hydrogen uptake capacity is pore size dependent, the surface area remains a key factor, as both applications need available activation sites for promoting high capacitance values and uptake capacities. A semi-carbonization temperature of 200 °C was not performed, since the burning process starts above 200 °C and a semi-carbonization is therefore not meaningful.

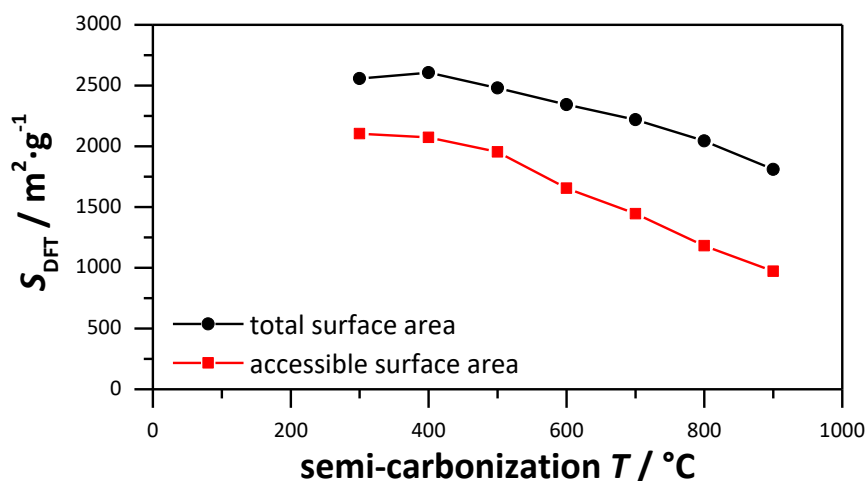


Figure 61: Total surface area and accessible surface area for pores > 0.66 nm of in dependence of the semi-carbonization temperature for carbon samples synthesized at different semi-carbonization temperatures.

4.1.3.2 Energy storage related properties of carbons synthesized at different semi-carbonization temperatures

Electrochemical characterization

Capacitance values for the carbon samples synthesized with different semi-carbonization temperatures were calculated and the results are summarized in Table 5. The CV of the carbons at a scan rate of $10 \text{ mV} \cdot \text{s}^{-1}$ show typical rectangular shapes which confirms well developed electrochemical double layer capacitance properties, as shown in Figure 62. Nevertheless, a small increase in capacitance with increasing cell voltage is observable for all carbons. This can be attributed to either the change in the density of states of charge carriers, or to leakage current caused by faradaic charge transfer side reactions of the electrolyte and the current collector. With increasing scan rate, the phenomenon becomes less significant or is no longer observable meaning the observed processes are diffusion controlled and the phenomenon is leakage current caused by side reactions. As mentioned in the previous section, the CV curves are distorted at a higher scan rate, due to the internal resistance and the diffusion resistance of the electrolyte ions in the pore network. Interestingly, the distortion of the CV curve changes continuously with the semi-carbonization temperature. The distortion is most pronounced for C-800-5-T9 and

decreases with decreasing semi-carbonization temperature. For C-300-5-T9 an almost perfect rectangular shape of the CV curve is observable, even at the highest scan rate of $2500 \text{ mV} \cdot \text{s}^{-1}$. The different CV curve distortions can be traced back to the diffusion resistance of the ions in the pore, which is reduced by large micropores and mesopores, as can be seen for C-300-5-T9.

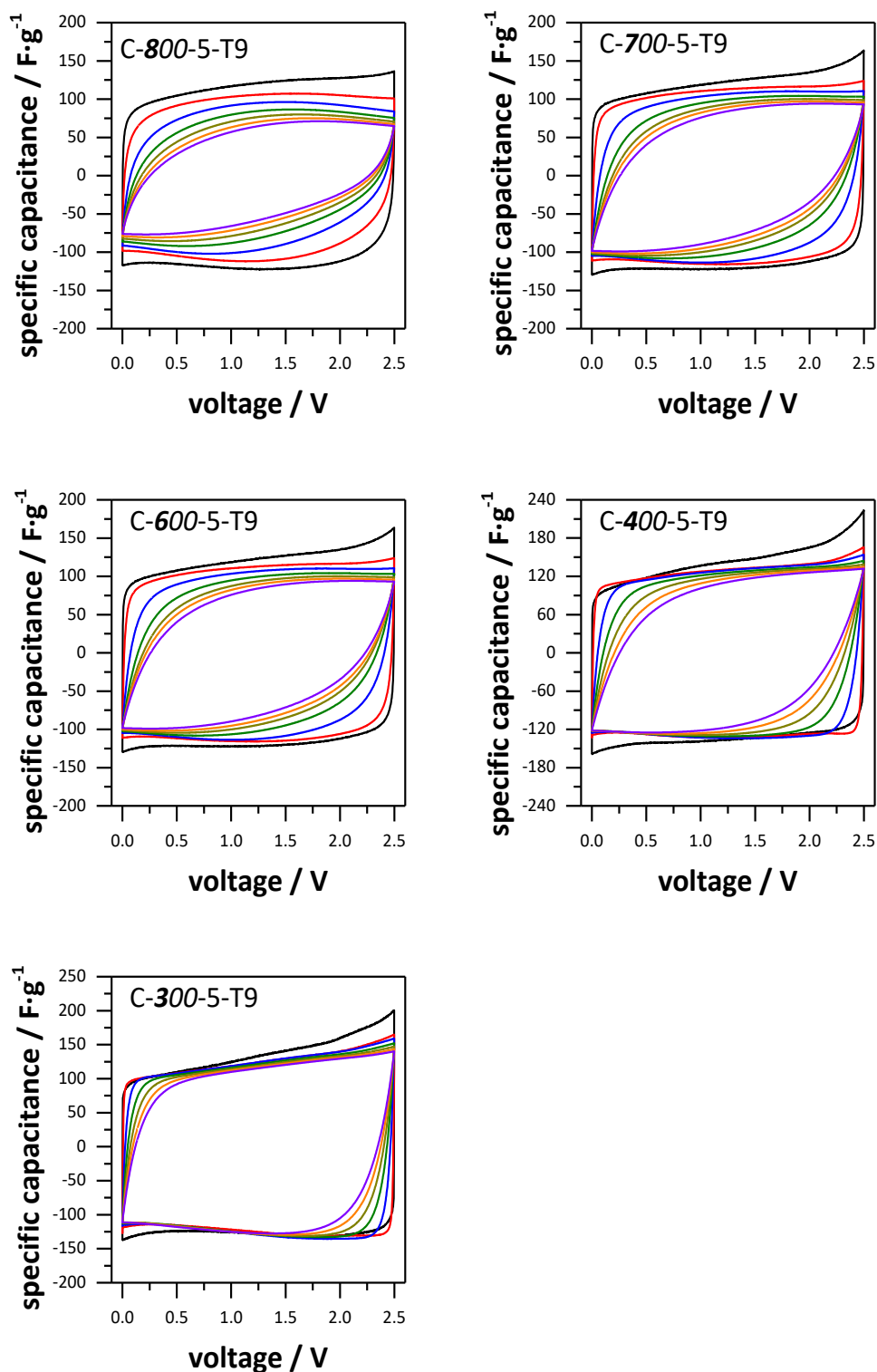


Figure 62: Cyclic voltammograms of the activated carbons synthesized at different semi carbonization temperatures at 10 $\text{mV}\cdot\text{s}^{-1}$ (black), 100 $\text{mV}\cdot\text{s}^{-1}$ (red), 500 $\text{mV}\cdot\text{s}^{-1}$ (blue), 1000 $\text{mV}\cdot\text{s}^{-1}$ (green), 1500 $\text{mV}\cdot\text{s}^{-1}$ (dark yellow), 2000 $\text{mV}\cdot\text{s}^{-1}$ (orange) and 2500 $\text{mV}\cdot\text{s}^{-1}$ (violet).

The results from the galvanostatic charge/discharge tests are displayed in Figure 63. All carbon samples show symmetrical and linear shapes indicating ideal double layer behavior, as suggested from the observations of the CV measurements. As the pores become larger with a lower semi-carbonization temperature, the accessible surface area increases correspondingly as shown in Figure 61. Therefore, it is no surprise the corresponding maximum capacitance at $1 \text{ A}\cdot\text{g}^{-1}$ increases with a decreasing semi-carbonization temperature in accordance to the accessible surface area. However, this only applies up to the semi-carbonization temperature of 400°C , which means C-400-5-T9 has the highest specific discharge capacitance with $157.4 \text{ F}\cdot\text{g}^{-1}$. This is rather surprising, since the maximum capacitance correlated quite well with the accessible surface area for all carbon samples discussed in the previous chapter. It has been suggested that pore enlargement, which leads to the higher specific and accessible surface area, results in a decrease of the average pore wall thickness in the highly porous activated carbons. Therefore, the electric field of the double layer and the corresponding charge density, no longer decay to zero within the pore wall, which would weaken the interaction of the ions with the pore wall on both sides.^[103,291] On the local scale of the samples, larger micropores and mesopores might contribute to the capacitance to a lesser extent. C-300-T9 has the lowest micropore volume, which is likely the reason for the comparatively low specific discharge capacitance of $143.3 \text{ F}\cdot\text{g}^{-1}$, despite having the highest accessible surface area of all carbon samples presented in this chapter. However, regarding the capacitance retention with respect to higher current densities, larger pores are beneficial. C-300-5-T9 and C-400-5-T9 have an outstanding capacitance retention of 98 and 97 % at a current density of $20 \text{ A}\cdot\text{g}^{-1}$, which is clearly attributed to the mesopores up to 4.5 nm, which enhance the ion diffusion into the pores and in the pore network. The capacitance retention decreases with increasing semi-carbonization temperature and decreasing pore sizes. Surprisingly, the capacitance retention for C-600-5-T9 is still as high as 93 % despite having predominantly micropores. It seems a high content of pores around 1.5 nm is sufficient for not only good ion accessibility of pores at high current densities, but also good ion diffusion within the pore network on the surface of the pore walls at high currents. This has not yet been observed frequently and shows large mesopores are not necessary, as it has been assumed.^[292,293] The capacitance retention for C-700-5-T9 and C-800-5-T9 decreases along with the decrease in pore size for both carbon materials.

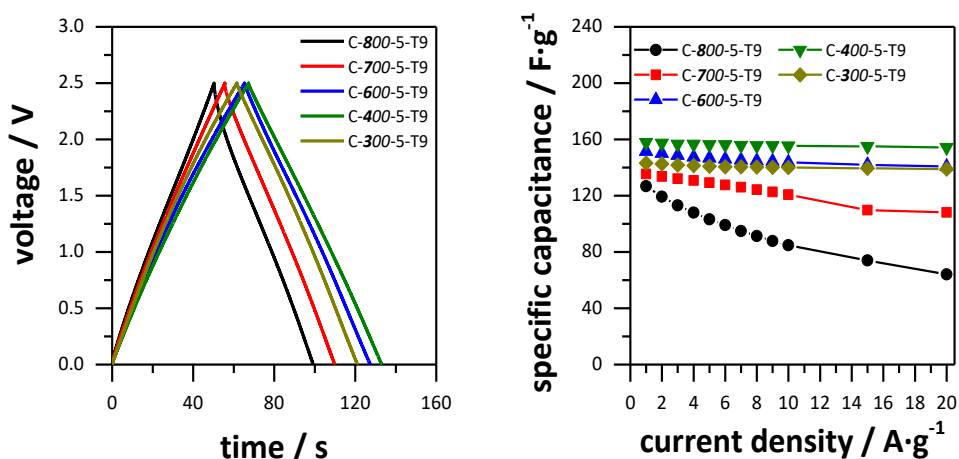


Figure 63: Discharge curve at 1 A·g⁻¹ for the carbon samples synthesized at different semi-carbonization temperatures (left) and the specific capacitance as a function of discharge current density (right).

Table 5: Electrochemical properties of the EDLC prepared from the activated carbons synthesized at different semi-carbonization temperatures in 1 M TEABF₄/ACN.

Sample	$S_{\text{acc}} /$ $\text{m}^2 \cdot \text{g}^{-1}$	$V_{\text{acc}} /$ $\text{cm}^3 \cdot \text{g}^{-1}$	$C_{\text{CV}} /$ $\text{F} \cdot \text{g}^{-1}$	$C_{\text{DC}} /$ $\text{F} \cdot \text{g}^{-1}$
C-800-5-T9	1181	0.79	112.5	126.7
C-700-5-T9	1445	1.00	116.3	135.4
C-600-5-T9	1656	1.15	128.5	151.5
C-400-5-T9	2074	2.31	133.4	157.4
C-300-5-T9	2104	2.72	126.4	143.3

S_{acc} specific surface area for pores > 0.66 nm; V_{acc} pore volume for pores > 0.66 nm; C_{CV} calculated from 10 mV·s⁻¹; C_{DC} calculated from 1 A·g⁻¹.

The specific DFT surface area and pore volume normalized capacitance values were calculated for the activated carbon samples. The capacitance values were normalized to the total surface area and pore volume (C_s and C_v) and to the accessible surface area and pore volume for pores larger than 0.66 nm ($C_{s>0.66}$ and $C_{v>0.66}$). The results are summarized in Table 6. Additionally, the surface capacitance values as a function of the semi-carbonization temperature are shown in Figure 64, including the carbon samples C-500-5-T9 and C-900-5-T9 from section 4.1.2.

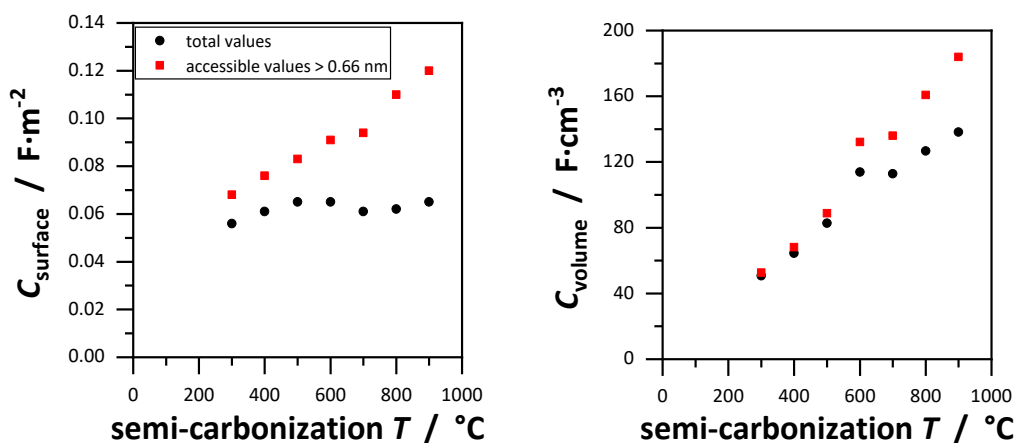


Figure 64: Surface area normalized capacitance (left) and pore volume normalized capacitance (right) as a function of carbon samples synthesized at different semi-carbonization temperatures, including carbon samples from section 4.1.2.

The C_s values are very similar for all samples and are in a range of 0.056 to 0.065 $\text{F} \cdot \text{m}^{-2}$. This confirms the observations from the previous chapter (4.1.3.2). There is apparently no pore size dependence of the surface capacitance, since both pure microporous (C-900-5-T9) and micro and mesoporous (C-300-5-T9) materials have similar capacitance values. However, this changes when the $C_{S>0.66}$ values are considered. A clear correlation is observable in which the surface capacitance increases with the semi-carbonization temperature. The $C_{S>0.66}$ values are not in a close range but differ significantly with 0.11 $\text{F} \cdot \text{cm}^{-2}$ for C-900-5-T9 compared to 0.068 $\text{F} \cdot \text{m}^{-2}$ for C-300-5-T9. This supports the previous observation that the gravimetric capacitance does not correlate linearly with the accessible surface area and indicates a pore size dependency of the capacitance. In this case, it would mean that smaller pores in the range of 0.66 to 1.2 nm contribute to the capacitance to a higher extent, compared to larger micropores and mesopores. A reduced pore wall thickness as described above is one possible reason. Another possibility would be the confined space in small micropores below 1 nm in size. The solvation shell of the electrolyte ions need to be adjusted, by either partial or full removal, so the ions are able to enter the pores. This might decrease the distance of the ions to the pore wall, hence reducing the double layer thickness. This results in an increase in capacitance, as can be seen from the classic Helmholtz equation. In any case, it seems clear that small pores provide a higher contribution to the capacitance, whether

through a specific increase in capacitance for electrolyte ions in small pores, a reduction in capacitance of larger pores or a combination of both. The volumetric capacitance increases with increasing semi-carbonization temperature, which is due to the smaller pore sizes of the carbon samples, semi-carbonized at higher temperatures. Again, micropores show a better utilization of the pore volume with respect to the capacitance, as larger micropores and mesopores may enhance the diffusion of electrolyte ions, but create “dead volume” and low volumetric capacitance values.

Table 6: Surface- and volumetric capacitance values for carbons, synthesized at different semi-carbonization temperatures.

Sample	$C_S /$ $F \cdot m^{-2}$	$C_{S>0.66} /$ $F \cdot cm^{-2}$	$C_V /$ $F \cdot cm^{-3}$	$C_{V>0.66} /$ $F \cdot cm^{-3}$
C-800-5-T9	0.062	0.11	126.7	160.8
C-700-5-T9	0.061	0.094	112.8	136.0
C-600-5-T9	0.065	0.091	113.9	132.2
C-400-5-T9	0.061	0.076	64.4	68.2
C-300-5-T9	0.056	0.068	50.8	52.7

C_S , $C_{S>0.66}$ calculated from C_{DC} and the respective surface areas, obtained from the DFT results; C_V , $C_{V>0.66}$ calculated from C_{DC} and the respective pore volumes.

The results from the PEIS are shown in Figure 65. The curve in the Nyquist diagram corresponds to the usual curve of ELDCs, with an abscissa intersection, a semicircle and a straight line at low frequencies. The R_{ESR} values are in a similar range and the semicircles are of short length. The curve of C-700-5-T9 is slightly shifted to higher resistance values, which can be ascribed to carbon sample-independent temperature fluctuations, impacting the bulk resistance of the electrolyte, having the greatest influence on the R_{ESR} . The specific in-pore diffusion resistance of carbon materials is not affected by that.^[294] The phase angles in the low frequency region for each carbon are similar, ranging from -85 to -88° . This shows ideal electrolyte ion migration for all carbons at low frequencies and therefore almost ideal capacitive behavior with little capacitance loss. This confirms the previous observations and emphasizes the ability of pores, even as small as 1.2 nm, to enhance the electrolyte ion diffusion on the surface and in the pores. The frequency response of the normalized real capacitance shows a plateau for all carbon samples at low frequencies and a

strong decay at mid frequencies. However, the plateau of C-800-5-T9 and C-700-5-T9 has a larger slope than the other carbon samples, which reflects a stronger decay of capacitance with increasing frequencies. This can be attributed to the smaller pore sizes, which hinder the diffusion of electrolyte ions. The electrode surface accessibility is therefore limited, which results in an earlier decrease in capacitance. This can be confirmed by the calculated time constants. The time relaxation constants are 1.52, 1.67, 0.75, 0.90 and 0.45 s for C-800-5-T9, C-700-5-T9, C-600-5-T9, C-400-5-T9 and C-300-5-T9, respectively. The time constants are obtained from the frequency response of the normalized imaginary resistance. The values are in a similar time range, revealing a capacitive behavior at fast charging and discharging times, even for carbons with smaller pores. However, a rough correlation of time constant and pore size can be found, as larger pores lead to smaller time constants as seen for C-300-5-T9. Larger pores, namely mesopores up to 4 nm, support the best diffusion behavior for the electrolyte ions.

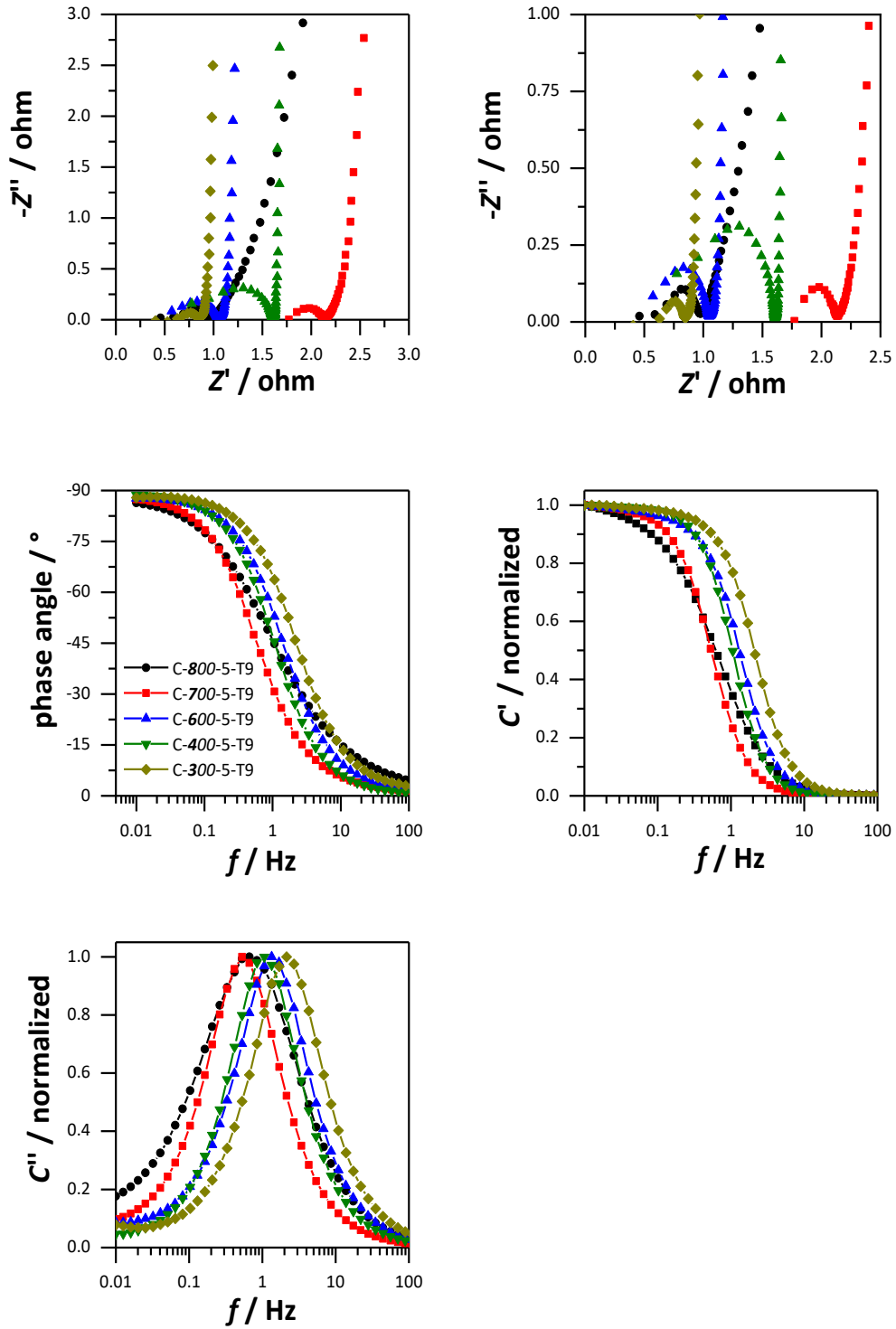


Figure 65: Nyquist plot of the activated carbons (top left and top right), frequency response of the phase angle (middle left), normalized real capacitance (middle left) and normalized imaginary capacitance (bottom left).

The electrochemical results in this chapter have clearly shown again that pore size has a large influence on capacitance. Although the accessible surface area is an

important factor for high capacitance values, especially gravimetric capacitance values, it is shown that the utilization of surfaces and volumes, generated by small pores is more effective than those generated by larger pores. Clearly larger pores are beneficial for ion diffusion in the pore network at higher currents, but pores as small as 1.5 nm seem to be sufficient to enable electrolyte ion diffusion within the pore network at low and high currents and frequencies.

Hydrogen storage

The isotherms of the hydrogen uptake capacity at 77 K for activated carbons synthesized at different semi-carbonization temperatures are shown in Figure 66. For all the activated carbon samples, the hydrogen uptake is reversible, with no hysteresis and no saturation attained in the 0 to 1 bar pressure range, which is expected.

At pressure range from 0 to 0.1 bar it can be seen that the carbon samples, synthesized at higher semi-carbonization temperatures show higher uptake capacities, which then decrease with decreasing semi-carbonization temperature. The difference is quite significant, as the uptake from sample C-800-5-T9 is as high as 1.2 wt% at 0.1 bar, compared to the lower hydrogen uptake from sample C-300-5-T9, which is 0.7 wt% at 0.1 bar. It clearly shows that more hydrogen is adsorbed in small micropores, so that the entire pore wall surface is occupied by hydrogen, which usually only occurs at higher pressures. This is due to the higher adsorption potential for hydrogen of the pore walls in small micropores, when the adsorption potentials of opposing pore walls overlap to increase the adsorption potential. Interestingly, samples C-700-5-T9 and C-600-5-T9 show a larger uptake capacity compared to C-400-5-T9 and C-300-5-T9, although the uptake capacity should be mainly dependent on the total surface area, which increases with decreasing semi-carbonization temperature.

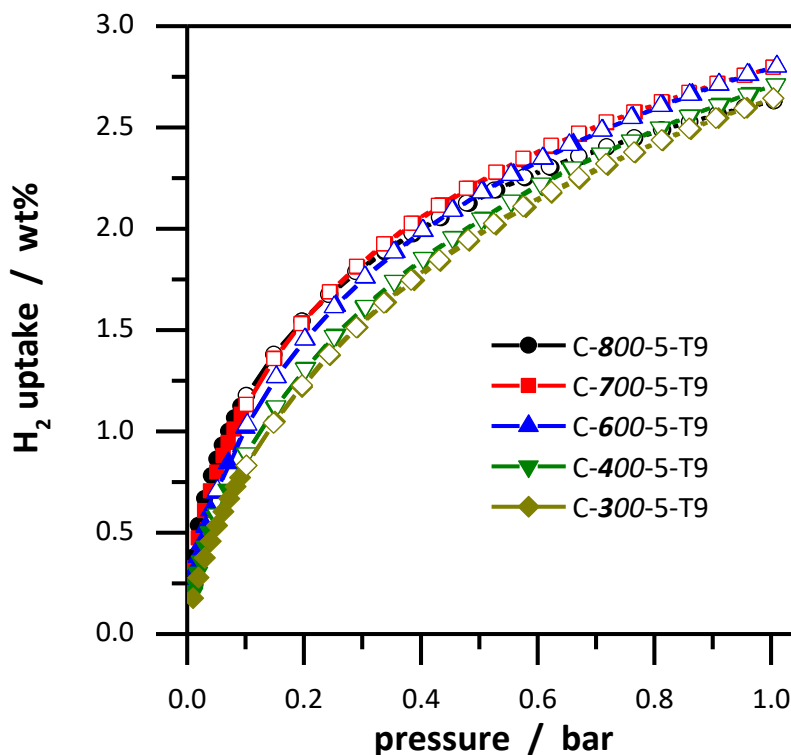


Figure 66: Gravimetric hydrogen storage capacity at 77 K of activated carbons, synthesized at different semi-carbonization temperatures.

The gravimetric hydrogen uptake capacities for the carbons samples at 1 bar are 2.63, 2.80, 2.80, 2.71 and 2.64 wt% for C-800-5-T9, C-700-5-T9, C-600-5-T9, C-400-5-T9 and C-300-5-T9 respectively. Since the specific surface area increases with decreasing semi-carbonization temperature, a similar behavior for the hydrogen uptake capacity is possible. This is not the case for the carbon samples in the present chapter, as C-600-5-T9 and C-700-5-T9 have the highest uptake capacities with 2.80 wt%. Considering the samples C-500-5-T9 and C-900-5-T9, no correlation is observable for the uptake capacity and the semi-carbonization temperature and therefore the surface area, as shown in Figure 67. After the peak uptake capacity is reached for temperatures of 700 and 600 °C, the capacity decreases again, despite the increasing specific surface area with lower semi-carbonization temperatures. It becomes clear the surface area is not the only factor for hydrogen uptake capacity. It is possible, the maximum capacity of C-300-5-T9 at higher pressures (100 bar) is significantly larger, when the entire surface area is saturated with adsorbate and the large free pore volume of sample C-300-5-T9 is involved in hydrogen storage.

However, considering the initial adsorption at low pressures, the pore size likely has a significant impact on the uptake capacity. Considering the specific surface area normalized uptake capacity, this fact is clarified once again as shown in Figure 67. With increasing semi-carbonization temperature, the normalized uptake capacity increases almost linearly, meaning a larger amount of small pores seems beneficial for the hydrogen uptake at low pressures. The reason for that could be the larger adsorption potentials of pore walls in micropores, due to the adsorption potential overlap, caused by the small wall-to-wall distance. This is a well-known phenomenon, not only observed for hydrogen in microporous carbons, but also for nitrogen and other adsorptive.^[7,206] A detailed investigation of the influence of the pore sizes from the synthesized carbons on the hydrogen uptake capacity will be given in section 4.3.

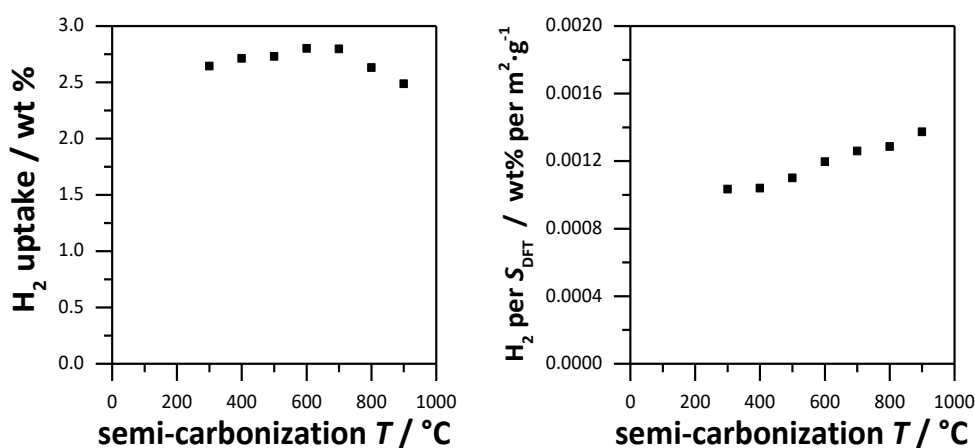


Figure 67: Gravimetric hydrogen uptake in dependence of the semi-carbonization temperature, including data of the samples from section 4.1.2 (left) and the specific surface area normalized uptake capacity in dependence of the semi-carbonization temperature (right).

The graphical summary of the carbon materials' properties of this chapter is shown in Figure 68 which displays key quantities from material characterization and energy related properties. The influence of the semi-carbonization temperature was investigated and a correlation between semi-carbonization temperature and the pore size was observable. Pores become smaller when the semi-carbonization temperature increases. At the same time, the specific surface area and total pore volume

increases with decreasing semi-carbonization temperature. If the PF resin is pre-carbonized at a lower temperature, more organic residues remain which increases the effectiveness of the chemical activation, since the activating process itself and the carbonization of the organic residues run simultaneously. While larger pores and higher accessible surface areas lead to high gravimetric capacitance values in EDLC setups, carbons with predominantly micropores showed a superior utilization of the surface area and the pore volume, by having larger surface and volumetric capacitance values. Similar correlations were observable regarding the hydrogen uptake capacity, although the total uptakes were similar for all discussed carbons in this chapter, despite the differences in the surface area. The uptake capacity, normalized by the specific surface area clearly showed, smaller pores are favorable, at least for the low-pressure uptake capacity. This is attributed to the higher adsorption potential of the pore walls in micropores.

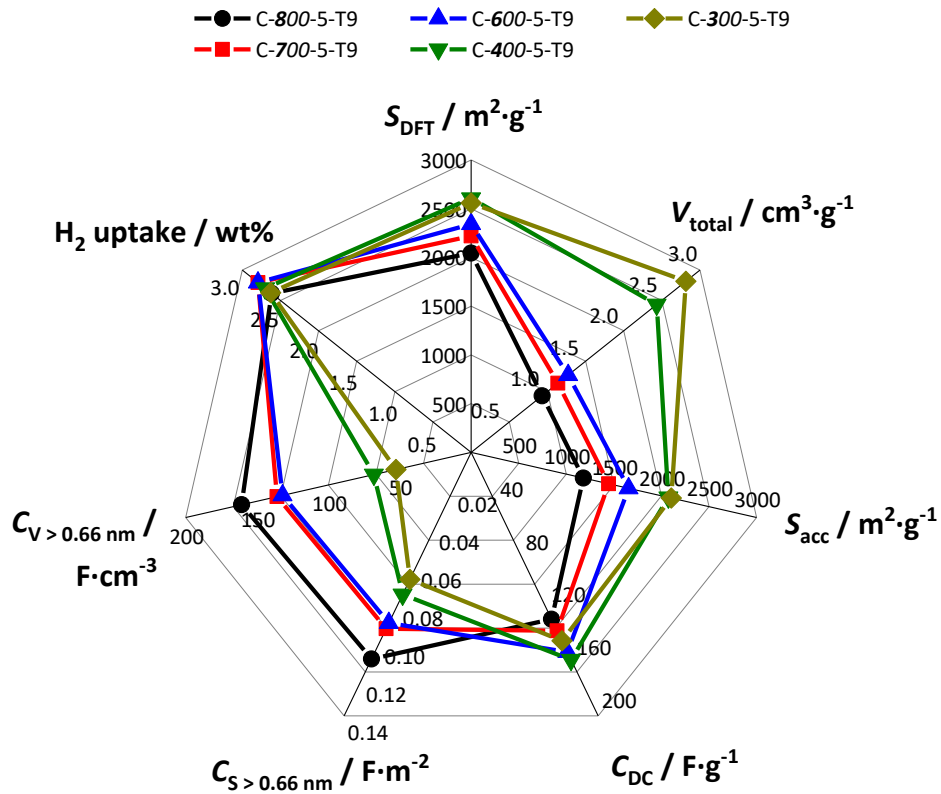


Figure 68: Graphical summary of the properties of the carbon samples, synthesized at different semi-carbonization temperatures.

4.1.4 Influence of the activation temperature

The influence of the activation temperature on the textural and structural properties of the activated carbons was investigated. The synthesis scheme is shown in Figure 69. The PF resins were semi-carbonized at 500 °C followed by a chemical activation with a KOH/carbon ratio of 5 at different activation temperatures. The semi-carbonization temperature of 500 °C was chosen as the standard temperature, as it offers the benefit of an effective activation, but the possibility remains for other synthesis parameters to reveal the influence on the porosity of the activated carbons. This is important, since it is the aim of this work to investigate the influence of the synthesis parameters on the activated carbon properties and not to optimize the parameters, because it remains to question, which carbon material properties are the optimum for the investigated applications. Activation temperatures of 1000, 800, 700 and 600 °C were chosen and the samples are denoted as C-500-5-T10, C-500-5-T8, C-500-5-T7 and C-500-5-T6.

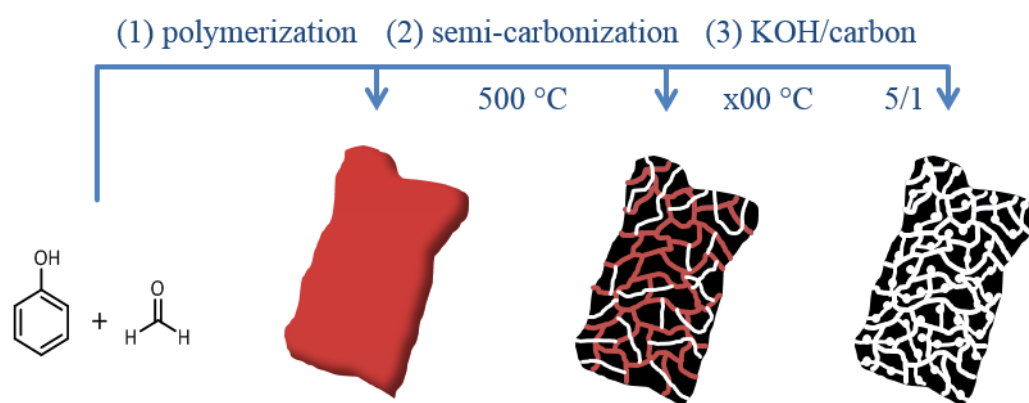


Figure 69: Synthesis scheme for the preparation of HSAC with different activation temperatures. The PF resin (1) was semi-carbonized (2) at 500 °C followed by a chemical activation (3) with a KOH/carbon ration of 5 at different activation temperatures.

4.1.4.1 Characterization of carbons synthesized at different activation temperatures

SEM images of the carbon samples were taken to study the carbon framework morphology. The SEM images are shown in Figure 70. The carbon framework structure is quite similar for all carbon samples synthesized at different activation temperatures. The frameworks consist of strongly agglomerated spherical particles, which

form cavities between 10 to 100 μm in diameter, where the agglomerate of C-500-5-T10 are slightly larger connate. In fact, the framework morphology is similar to C-500-5-T9, meaning higher and lower activation temperatures have a similar impact on the carbon structure. The KOH starts to react with carbon at 400 $^{\circ}\text{C}$ and is completely consumed around 600 $^{\circ}\text{C}$ by reacting with carbon to hydrogen and potassium carbonate. The carbonate itself can react at a temperature of 700 $^{\circ}\text{C}$ with carbon and decomposes to potassium oxide. At 800 $^{\circ}\text{C}$, the carbonate is completely consumed. The formed carbon dioxide can continue to react with carbon.^[65] Considering the morphology of the carbon framework, the main reaction of KOH and carbon between 400 and 600 $^{\circ}\text{C}$ has the highest influence. The side reactions of potassium carbonate and potassium oxide, starting at 600 $^{\circ}\text{C}$ and 800 $^{\circ}\text{C}$ respectively, likely influence the degree of graphitization and not on the carbon structure on the macroscopic scale, with the latter only to a small extent as the agglomerates of C-500-5-T10 are slightly more connate.

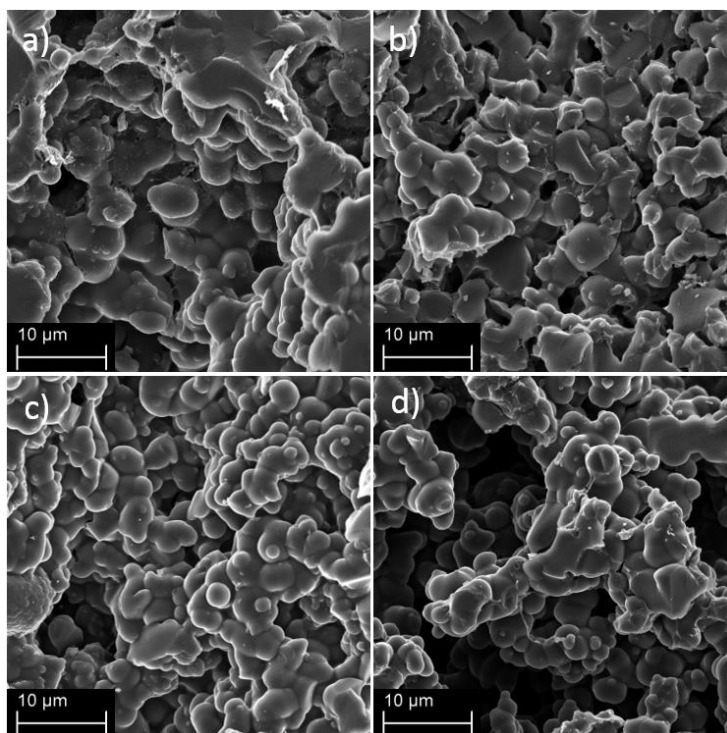


Figure 70: SEM images of the activated carbons with different activation temperatures. (a) C-500-5-T10, (b) C-500-5-T8, (c) C-500-5-T7 and (d) C-500-5-T6.

The p-XRD patterns of the activated carbon samples are shown in Figure A.5. All carbon samples show weak and broad reflections at 44 $^{\circ}$ 2theta corresponding to

(101) diffractions of a turbostratic carbon structure. Only C-500-5-T6 shows a weak diffraction at $22^\circ 2\theta$ corresponding to a beginning of stacked graphene layers. On one hand, a higher carbonization temperature should induce the stacking of graphene layers, leading to a higher degree of graphitization. On the other hand, the degree of chemical activation is enhanced with a higher activation temperature. The main reaction takes place at 600°C , but the formation of metallic potassium begins at 700°C . Metallic potassium is able to intercalate the graphene layers, which causes a structural deformation towards turbostratic carbon and therefore lowers the degree of graphitization.^[74] The intercalated potassium is removed during the washing step with water and ethanol at the end of the synthesis. This process occurred as well during the synthesis of the previously described activated carbons (sections 4.1.2 and 4.1.3) but their activation temperature was the same at 900°C , which is why the influence of the different reactions during the KOH activation was not taken into account, as they supposedly proceed at the same rate. The influence of the activation temperature on the degree of graphitization is supported by the results of the Raman spectra shown in Figure A.6 and the calculated I_D/I_G ratios. I_D/I_G ratios for the carbon samples are 1.17, 1.09, 1.04 and 1.02 for C-500-5-T10, C-500-5-T8, C-500-5-T7 and C-500-5-T6, respectively. The ratios for all carbon samples are generally low, indicating amorphous carbon materials, rather than graphitic carbons. However, the I_D/I_G ratio decreases with the activation temperature, meaning that a higher activation temperature leads to carbon materials with a lower degree of graphitization. Higher temperatures induce an enhanced formation of metallic potassium, which leads to structural deformation of the carbons through intercalation in the graphene layers. However, the intercalated potassium is removed during the washing, but the increased pore size, the spaced graphene layers, remains.

The thermogravimetry for all carbon samples is shown in Figure A.7. At a temperature of 650°C all carbons show a complete burn off with no residual mass, indicating the absence of impurities. Interestingly, the starting temperature of the burning process increases with the activation temperature, up to an activation temperature of 800°C . Sample C-500-5-T6 starts to combust at 375°C and for samples C-500-5-T7 and C-500-5-T8 is the start of the combustion observable at temperatures of 450 and 525°C respectively. The carbon sample C-500-5-T10, however, starts

to combust at the same temperature as sample C-500-5-T6. For the activated carbons in the previous sections, it was suggested, that the residual content of oxygen in the carbon framework possibly plays a major role, regarding the thermal stability. It is therefore likely, that a lower activation temperature, leads to activated carbons with a higher content of residual oxygen, since the KOH activation has its highest effectivity at higher temperatures, where all possible reactions are able to take place. Therefore, the thermal stability of the carbons increases with increasing activation temperature due to the lower content of oxygen in the carbon framework. Sample C-500-5-T10 has the lowest thermal stability, which can be ascribed to the higher degree of porosity, namely larger pores, and therefore higher accessibility to the air steam mixture.

The corresponding isotherms of the nitrogen physisorption measurements are shown in Figure 71 and the nitrogen physisorption derived data are summarized in Table 7. C-500-5-T7 and C-500-5-T6 show a type I isotherm, indicating these carbon samples have predominantly micropores. The corresponding isotherms of C-500-5-T10 and C-500-5-T8 show a slope at relative pressures from 0.1 to 0.4 and from 0.1 to 0.3 respectively, while the slope C-500-5-T10 occurs over a larger relative pressure range. This indicates the presence of larger pores compared to C-500-5-T7 and C-500-5-T6. The pore size distributions, calculated by the QSDFT method from the nitrogen desorption branch, shown in Figure 74, indicate a pore size dependency on the activation temperature. Besides micropores, C-500-5-T10 additionally possesses mesopores up to 4 nm and has the largest pore sizes among the carbon samples discussed in this chapter. The pore sizes become larger with increasing activation temperature, which can be attributed to additionally occurring side reactions, which increase the effectiveness of the chemical activation. As stated in the beginning of this section, at 700 °C potassium carbonate starts to react with carbon, or decomposes to potassium oxide, which consumes carbon from the framework as seen in in CE 13 and CE 14. Additionally, potassium can intercalate in graphene layers, which are then expanded. After the removal of potassium, the expansion is still present, and additional pores are created or existing pores are being enlarged. The pore size distributions of C-500-5-T7 and C-500-5-T6 are almost identical, because no significant side reactions take place, which could enlarge or create new pores. With increasing activation temperature, the side reactions will be promoted and with them the enlargement of pores. Additionally, carbon dioxide can

be reduced by carbon to carbon monoxide and the formation of metallic potassium is promoted as seen in CE 15 and CE 16. Both processes enhance the pore generation and enlargement of pores, leading to larger pores, as seen for sample C-500-5-T10.

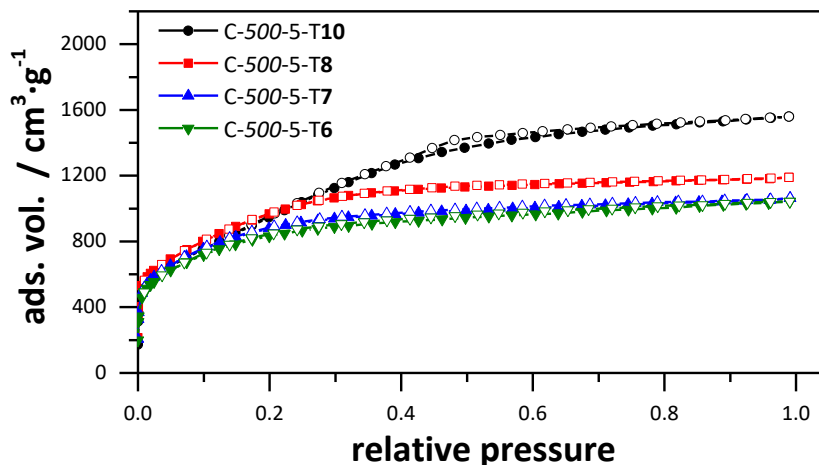


Figure 71: Nitrogen adsorption-desorption isotherms (77 K) of the carbon materials synthesized at different activation temperatures.

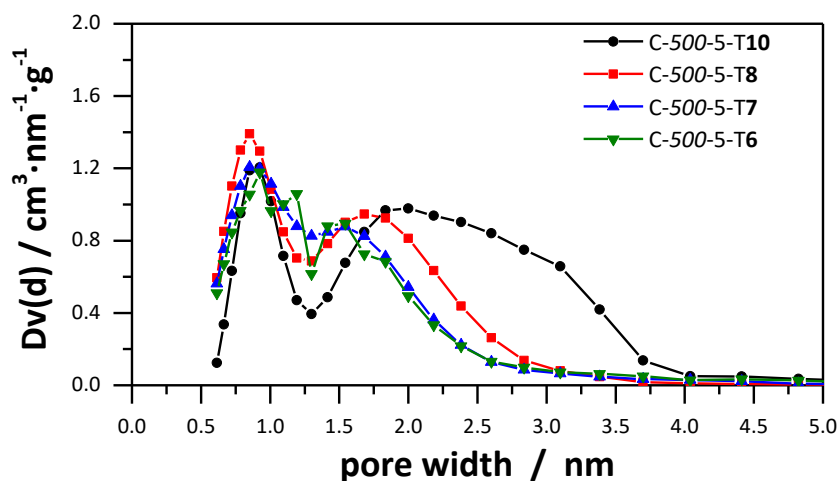


Figure 72: Pore size distribution of the carbon materials synthesized at different activation temperatures, calculated by the QSDFT method from nitrogen desorption branch assuming slit pores.

In principle, the specific surface area increases with the activation temperature, with carbon sample C-500-5-T8 having the highest specific surface area. However, the

differences are very small, as the surface areas of C-500-5-T9, C-500-5-T7 and C-500-5-T6 are still very high with 2480, 2335 and 2448 $\text{m}^2 \cdot \text{g}^{-1}$ respectively. The similar trend can be observed for the total pore volume, as the pore volume increases with the activation temperature, with C-500-5-T10 having the largest pore volume with 2.27 $\text{cm}^3 \cdot \text{g}^{-1}$. It is clear the chemical activation is effective, even at a lower temperature of 600 °C. Carbon materials with high surface areas and pore volumes can be obtained, as the KOH is already completely consumed at 600 °C, which is the main part of the chemical activation. A high degree of porosity is produced, which results in high surface areas and pore volumes. Nevertheless, the activation temperature affects the pore size, as seen above. The micropore volume increases with the activation temperature up to 800 °C and then decreases with an activation temperature of 900 and 1000 °C. The potassium carbonate formed during activation continues to react with the carbon, forming new micropores and enlarging existing pores. At higher temperatures, potassium intercalation further enlarges the pores as described above. In addition, more carbon dioxide is formed, which continues to react directly on the pore wall with carbon, which ultimately leads to a lower content of micropores and a more pronounced enlargement of the pores.

Table 7: Nitrogen physisorption derived data of the carbon samples synthesized at different activation temperatures.

Sample	$S_{\text{BET}} /$ $\text{m}^2 \cdot \text{g}^{-1}$	$S_{\text{DFT}} /$ $\text{m}^2 \cdot \text{g}^{-1}$	$V_{\text{t}} /$ $\text{cm}^3 \cdot \text{g}^{-1}$	$V_{\text{mic}} /$ $\text{cm}^3 \cdot \text{g}^{-1}$
C-500-5-T10	3686	2601	2.27	1.09
C-500-5-T8	3550	2660	1.71	1.35
C-500-5-T7	3199	2448	1.52	1.26
C-500-5-T6	3034	2335	1.51	1.20

S_{DFT} (DFT surface area), V_{t} (total pore volume) and V_{mic} (micropore volume) obtained from QSDFT analysis. S_{BET} (BET surface area).

Micropore sizes were further analyzed with carbon dioxide physisorption measurements and the adsorption-desorption isotherms at 273 K are shown in Figure 73. The isotherms are reversible for ad- and desorption and show an almost linear correlation with increasing relative pressure indicating evenly distributed pores up to 1 nm in size. The pore size distributions calculated by the NLDFT method are shown in Figure 74. The porosity of C-500-5-T7 and C-500-5-T6 is almost identical

and the pores have very similar sizes below 1 nm. C-500-5-T8 has the highest amount of pores between 0.8 and 0.9 nm, which is in accordance with the micropore volume. The amount of pores decreases again for C-500-5-T10 as the pores are being further enlarged.

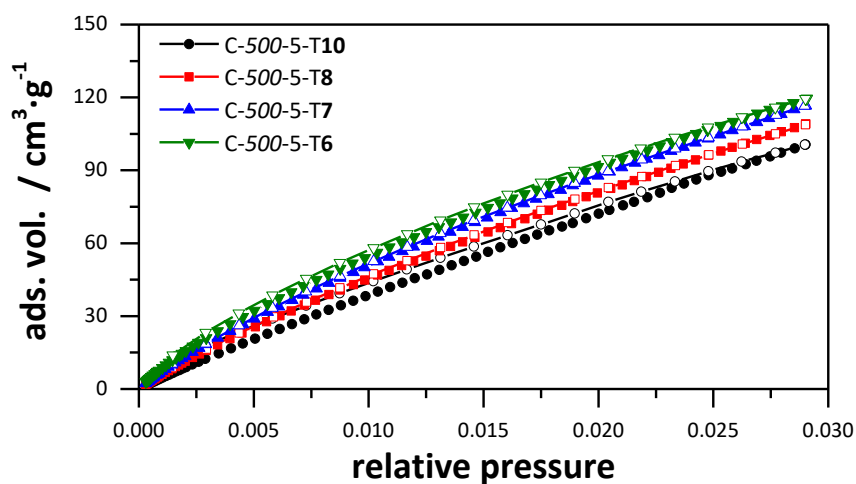


Figure 73: Carbon dioxide adsorption-desorption isotherms (273 K) of the carbon materials synthesized at different activation temperatures.

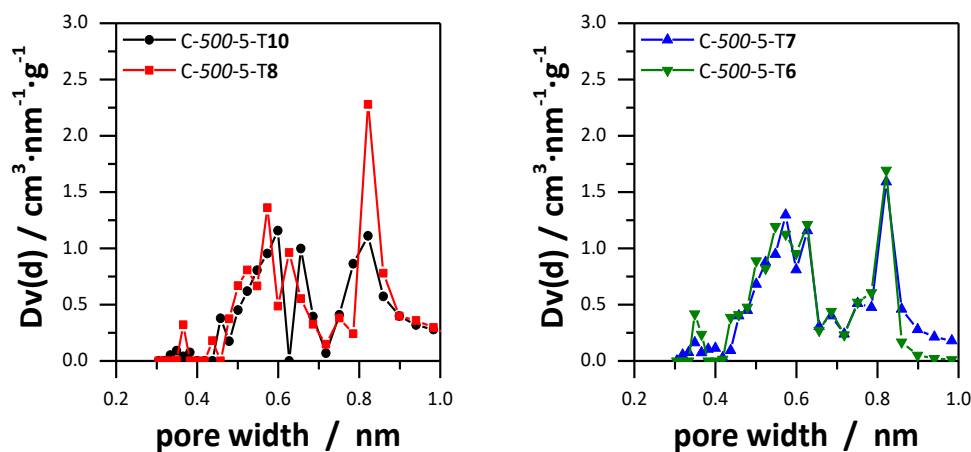


Figure 74: Pore size distribution of the carbon materials synthesized at different activation temperatures, calculated by the NLDFT method from carbon dioxide desorption assuming slit pores.

The combined cumulative surface area and pore volume for the carbon samples are shown in Figure 75 and Figure 76. The generated surface areas by pores with a size around 0.6 nm are of special interest for the electrochemical characterization. The sample, which has the largest surface area provided by pores smaller than 0.6 nm, is sample C-500-5-T6. In the following, the surface area decreases with increasing activation temperature. Surprisingly, the surface area provided by subnanometer pores is smaller for C-500-5-T7 although the overall porosity was almost identical with C-500-5-T6. This is probably due to the fact even more organic precursor residues are carbonized at 700 °C, which ultimately leads to an enlargement of pores. Furthermore, the potassium carbonate begins to react with carbon and decomposes to potassium oxide, which can also lead to an enlargement of ultramicropores. Nevertheless, pores below 1 nm contribute to surface areas of C-500-5-T6, C-500-5-T7 and C-500-5-T8 to a similar extent. Only for C-500-5-T10, were larger pores observable, leading the highest total pore volume for all carbon samples synthesized at different activation temperatures.

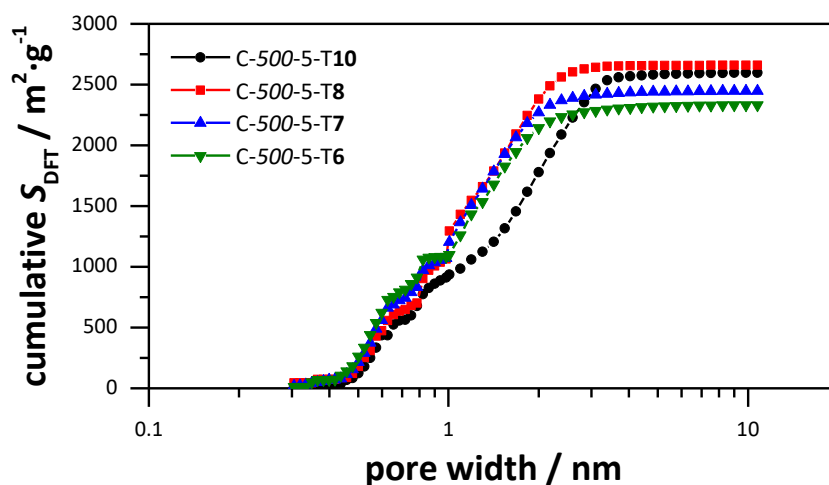


Figure 75: Combined cumulative surface area derived from carbon dioxide and nitrogen physisorption data of the carbon samples synthesized at different activation temperatures.

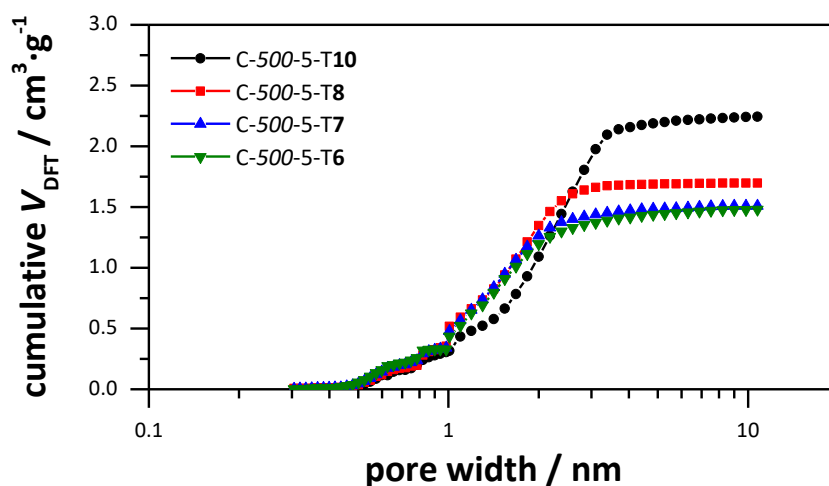


Figure 76: Combined cumulative pore volume derived from carbon dioxide and nitrogen physisorption data for carbon samples synthesized at different activation temperatures.

In principle, it became clear the influence of the activation temperature on the morphology of the carbons is insignificant, but does influence the graphitic degree and the porosity of the carbon framework. With increasing activation temperature, further side reactions take place which lead to structural defects in the arrangement of the graphene layer. Furthermore, new formation of micropores and enlargement of the micropores occurs. However, it should be noted, an activation temperature of 600 °C is sufficient to produce mainly microporous carbons with a high surface area and moderate pore volume. This suggests the reaction of KOH and carbon atoms from the framework is mainly responsible for the formation and enlargement of new pores. The activation temperature can be used additionally to accelerate the side reactions, which allow tailoring of pore sizes in a targeted manner.

4.1.4.2 Energy storage related properties of carbons synthesized at different activation temperatures

Electrochemical characterization

Capacitance values for the carbons, synthesized with different activation temperatures were calculated and the results are summarized in Table 8. The CV curves at various temperatures are shown in Figure 77.

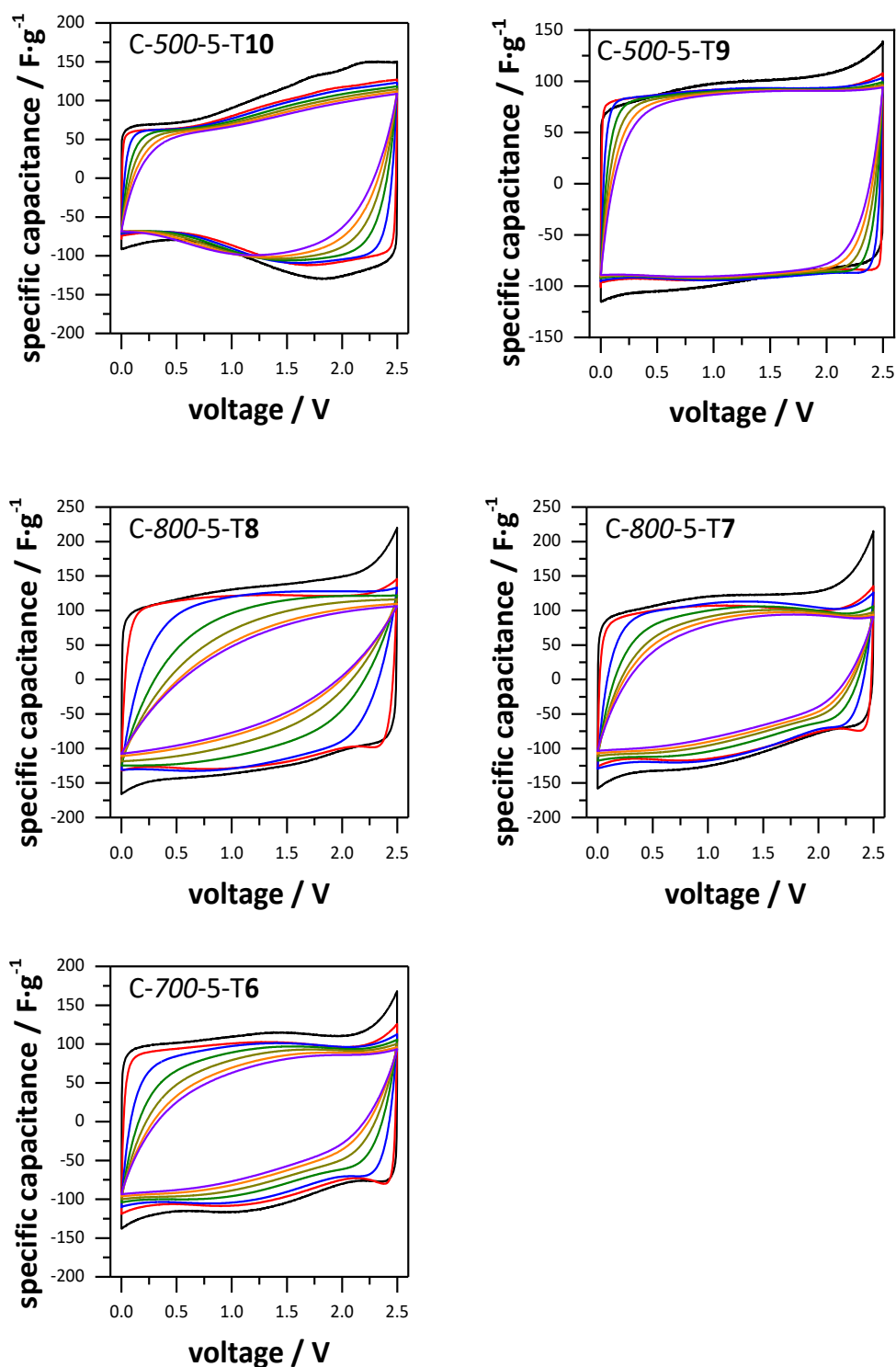


Figure 77: Cyclic voltammograms of the activated carbons synthesized at different activation temperatures at $10 \text{ mV}\cdot\text{s}^{-1}$ (black), $100 \text{ mV}\cdot\text{s}^{-1}$ (red), $500 \text{ mV}\cdot\text{s}^{-1}$ (blue), $1000 \text{ mV}\cdot\text{s}^{-1}$ (green), $1500 \text{ mV}\cdot\text{s}^{-1}$ (dark yellow), $2000 \text{ mV}\cdot\text{s}^{-1}$ (orange) and $2500 \text{ mV}\cdot\text{s}^{-1}$ (violet).

In general, all carbons samples show rectangular shapes of the CV curves, indicating a typical EDLC behavior. However, the capacitance increases with high cell

voltages for samples C-500-5-T9, C-500-5-T8, C-500-5-T7 and C-500-5-T6, while this effect is more pronounced for the last three carbon samples. This increase in capacitance disappears with increasing scan rate, which is why a faradaic charge transfer side reaction is the possible reason. As the content of oxygen in the carbon frameworks is supposed to be higher for the carbon samples, synthesized at lower activation temperatures, the cause of the increase in capacitance is likely caused by the degradation of the electrolyte, which is accelerated by the oxygen functionalities.^[295]

The CV curve of C-500-5-T10 differs from the CV curves of the other activated carbons, by showing a reversible slope during the discharge towards higher voltages. One possibility for this is voltage dependent faradaic charge transfer reactions, which would increase the current response during the charging process. However, this effect should become less significant with increasing scan rate, since faradaic charge transfer reactions are diffusion controlled, but the steeper slopes at higher voltages remain even at very high scan rate. Another explanation for the deviation may be attributed to electrochemical doping from oxygen groups within the carbon framework, although sample C-500-5-T10 is supposed to have the lowest content of these. Electrochemical doping can lead to a lower space charge capacitance, which is caused by a limited number of charge carriers when charge separation occurs between the heavily charged surface and the depleted bulk material.^[270] At low voltages, the density of states at the electrode/electrolyte interface is lower due to the doping, causing a low space charge capacitance and a corresponding voltage drop can be observed. Interestingly, none of the other samples show this effect. However, an increase in capacitance can be observed at a high cell voltage, which disappears again with increasing scan rate. This is very likely caused by the degradation of the electrolyte. It is possible that a high content of oxygen atoms in the carbon framework can accelerate the electrolyte degradation.^[295] Nevertheless, this effect can be minimized by performing statistical investigations at slightly higher currents via CDC measurements, in which the reaction can no longer take place because the reactions are diffusion controlled. It should be noted, the distortion of the CV curve of C-500-5-T10 with increasing scan rate, is less significant, compared to the other carbon samples. This can be attributed to the larger pores, which enable fast ion diffusion at the surface and in narrow pores of the carbon electrode.

The results from galvanostatic charge/discharge tests are shown in Figure 78. All CDC curves of the activated carbon samples show a triangular profile, indicating well developed EDLC behavior at $1 \text{ A}\cdot\text{g}^{-1}$. The gravimetric specific capacitance increases with the activation temperature and the accessible surface area, up to an activation temperature of 800°C , resulting in C-500-5-T8 having the highest specific capacitance of $164.1 \text{ F}\cdot\text{g}^{-1}$. The capacitance of C-500-5-T10 is significantly lower, despite having a similar accessible surface area as C-500-5-T8. Nevertheless, all carbons with different activation temperatures have a high capacitance value, which is attributed to the high accessible surface areas. All samples show a very good retention of capacitance at higher current densities. Larger pores favor this effect, which accounts for the good retention for samples C-500-5-T10 and C-500-5-T8, as these have small mesopores. However, samples C-500-5-T7 and C-500-5-T6 also show very good retentions, although they have a micropore content of more than 80 %. This indicates well-connected pores around 1.5 nm seem to favor the diffusion of electrolyte ions. This confirms once again, that a high activation temperature favors the generation of larger pores and higher surface areas, but a temperature of 600°C is sufficient to produce carbons with sufficiently large pores for a high capacitance and good capacitance retention.

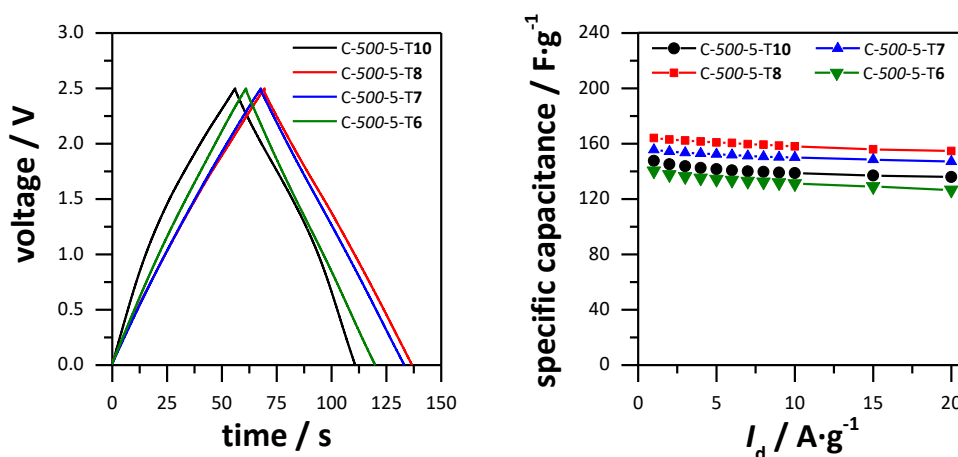


Figure 78: Discharge curve at $1 \text{ A}\cdot\text{g}^{-1}$ for the carbon samples synthesized at different activation temperatures (left) and the specific capacitance as a function of discharge current density (right).

Table 8: Electrochemical properties of the EDLC prepared from activated carbons synthesized at different activation temperatures in 1 M TEABF₄/ACN.

Sample	$S_{\text{acc}} /$ $\text{m}^2 \cdot \text{g}^{-1}$	$V_{\text{acc}} /$ $\text{cm}^3 \cdot \text{g}^{-1}$	$C_{\text{CV}} /$ $\text{F} \cdot \text{g}^{-1}$	$C_{\text{DC}} /$ $\text{F} \cdot \text{g}^{-1}$
C-500-5-T10	2077	2.15	118.2	147.6
C-500-5-T8	2045	1.56	125.3	164.1
C-500-5-T7	1760	1.34	108.9	155.7
C-500-5-T6	1581	1.31	103.8	140.3

S_{acc} specific surface area for pores > 0.66 nm; V_{acc} pore volume for pores > 0.66 nm; C_{CV} calculated from $10 \text{ mV} \cdot \text{s}^{-1}$; C_{DC} calculated from $1 \text{ A} \cdot \text{g}^{-1}$.

The specific DFT surface area and pore volume normalized capacitance values were calculated and the results are summarized in Table 9. For all carbon samples, the C_s values are very similar in a close range of 0.056 to $0.065 \text{ F} \cdot \text{m}^{-2}$. Therefore, the surface capacitance seems independent of the pore size, as already stated in the previous sections. However, a clear correlation is observable in which the surface capacitance ($C_{S>0.66}$) increases with a lower activation temperature. This is also in line with the results of the sections 4.1.2.2 and 4.1.3.2 already mentioned and discussed. Although there is a clear dependence of activation temperature and surface capacitance, the values are closer together, because C-500-5-T6 has smaller pores compared to C-500-5-T10, but still possesses a high surface area and pore volume which limits the surface capacitance. Nevertheless, it has been shown again that carbons with smaller pores have a higher surface capacitance, which suggests the surface can be used more effectively for charge storage.

With regard to volumetric capacitance, the tendencies of the values remain the same when comparing the accessible volumetric capacitance with the standard volumetric capacitance. In general, the volumetric capacitance increases with a decreasing activation temperature up to 700°C with sample C-500-5-T7 having the highest volumetric capacitance ($115.8 \text{ F} \cdot \text{cm}^{-3}$). Although sample C-500-5-T6 does not seem to fit into this correlation, its volumetric capacitance is the second highest with $107.0 \text{ F} \cdot \text{cm}^{-3}$ and therefore close to the capacitance of sample C-500-5-T7. The volumetric capacitance values for C-500-5-T6 and C-500-5-T7 are significantly lower. The pore sizes of samples C-500-5-T9 and C-500-5-T10 are in a similar range, as are the pore volumes. The volume is therefore used relatively well for

charge storage. The same is observable for C-500-5-T8 although the pores are larger, especially in the pore size range 1 to 2 nm. Therefore, these pores seem to provide a good utilization of the pore volume with respect to the capacitance. Nevertheless, the capacitance is lower, compared to carbon samples with smaller pores. Samples C-500-5-T9 and C-500-5-T10 have larger pores, especially above 2 nm, which are not able to provide a good utilization of the pore volume, as seen by the significantly lower capacitance values.

Table 9: Surface- and volumetric capacitance values for carbons synthesized at different activation temperatures.

Sample	$C_S /$ $F \cdot m^{-2}$	$C_{S>0.66} /$ $F \cdot cm^{-2}$	$C_V /$ $F \cdot cm^{-3}$	$C_{V>0.66} /$ $F \cdot cm^{-3}$
C-500-5-T10	0.056	0.071	65.0	68.5
C-500-5-T9	0.065	0.083	82.7	88.7
C-500-5-T8	0.060	0.078	93.2	102.0
C-500-5-T7	0.064	0.088	102.4	115.8
C-500-5-T6	0.060	0.089	93.2	107.0

C_S , $C_{S>0.66}$ calculated from C_{DC} and the respective surface areas, obtained from the DFT results; C_V , $C_{V>0.66}$ calculated from C_{DC} and the respective pore volumes.

Results from the PEIS tests are shown in Figure 79. The R_{ESR} values from the carbon samples, deduced from the intersection of the abscissa of the Nyquist plot, are in a similar range. However, the length of the semicircle varies with the activation temperature. The semicircle of samples C-500-5-T10 and C-500-5-T8 is short, while the semicircles of samples C-500-5-T7 and C-500-5-T6 are slightly longer. This means the surface resistance of the electrodes is higher. This resistance is often caused by charge transfer reactions at the electrode surface. At a lower activation temperature, it is possible the oxygen content in the activated carbon is higher, which in turn is an active site for charge transfer reactions. However, it should be noted, the contact pressure of the electrodes, as well as the electrolyte resistance and resistances caused by impurities can influence these processes, which complicates an interpretation of the length of the semicircle. The phase angles of the carbon samples are in a close range between -84.6 and -87.4° indicating an ideal electrolyte ion migration promoted by larger micropores and small mesopores. This is of little surprise, since all carbons showed excellent capacitance retention at high

current densities. The frequency response of the normalized real capacitance shows the plateau at low frequencies and a strong decay at mid frequencies. The time constants, calculated from the peak frequency of the frequency response of the imaginary resistance, are 0.37, 0.94, 1.50 and 1.19 s for C-500-5-T**10**, C-500-5-T**8**, C-500-5-T**7** and C-500-5-T**6**, respectively. The values are in a similar time range, emphasizing the good diffusion promotion of electrolyte ions, even for smaller pores around 1.5 nm. The time constant of C-500-5-T**10** stands out with a very short time, due to the larger pores between 2 and 3.5 nm.

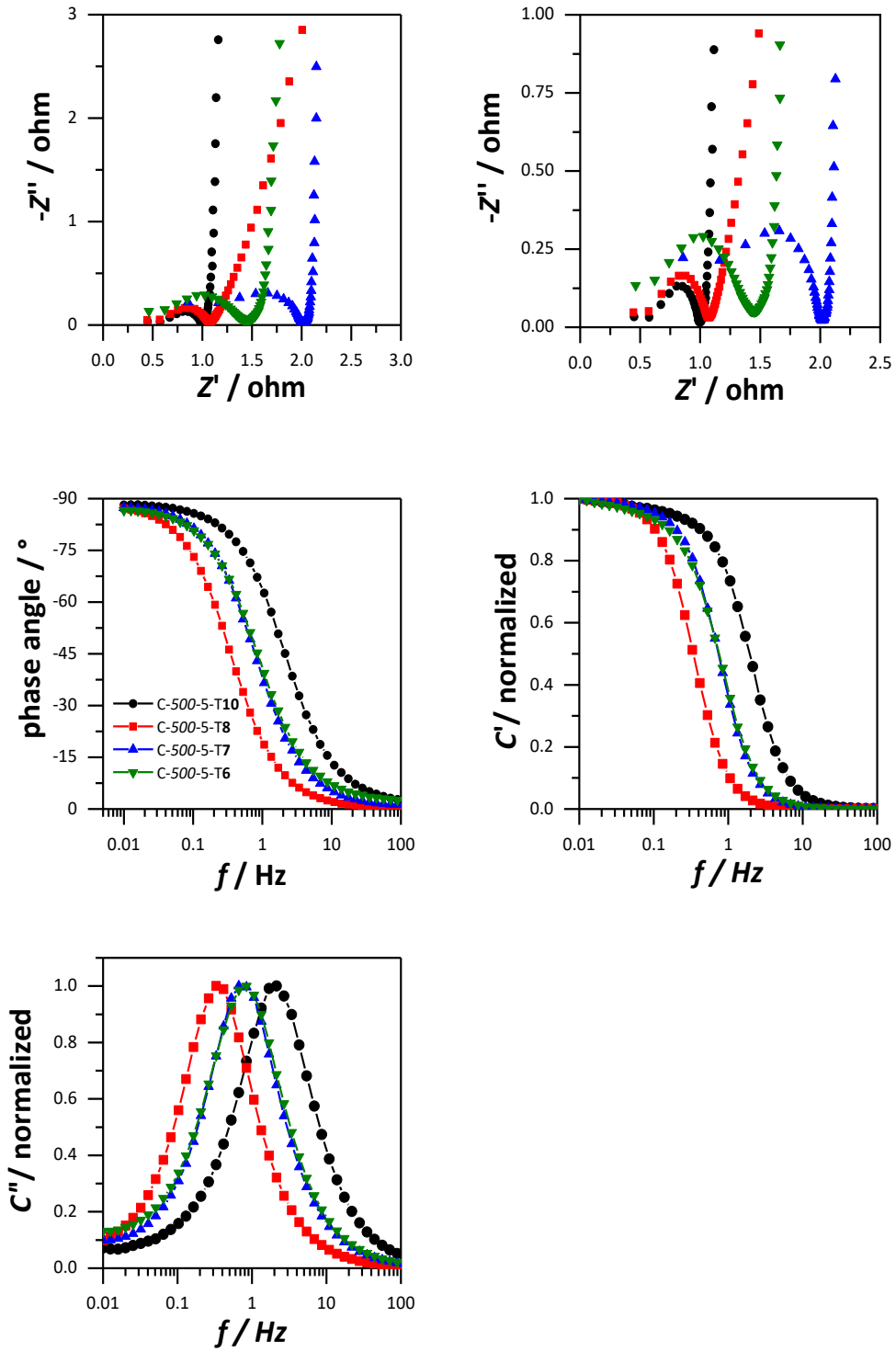


Figure 79: Nyquist plot of the activated carbons (top left and top right), frequency response of the phase angle (middle left), normalized real capacitance (middle right) and normalized imaginary capacitance (bottom left).

The impact of the pore size on capacitance values was emphasized in this chapter once again. Electrochemical utilization of carbons with smaller pores is higher compared to samples with larger pores, which became evident by considering the surface capacitance values. Moreover, it was possible to confirm small pores with the size of 1.5 nm seem to be sufficient to enable electrolyte ion diffusion within the pore network at low and high currents and frequencies, as the results from galvanostatic discharge and impedance spectroscopy.

Hydrogen storage

Isotherms of the hydrogen uptake capacity at 77 K for activated carbons with different activation temperatures are shown in Figure 80. As expected, the hydrogen uptake is reversible with no hysteresis and no saturation attained in the 0 to 1 bar pressure range, for all carbon samples.

In contrast to the carbon samples from sections 4.1.2.2 and 4.1.3.2, all activated carbon samples show a similar hydrogen uptake capacity in the pressure range of 0 to 0.1 bar. Since a difference in uptake capacities at 0.1 bar, would mean a difference in the amount and size of small micropores, it can be concluded that the small micropores are of similar size and abundance for all carbon samples, activated at different temperatures. This is in accordance with the observation from the carbon dioxide physisorption measurements, as seen in Figure 74. The hydrogen uptake capacities at 1 bar, which are mainly governed by the surface area, show different results.

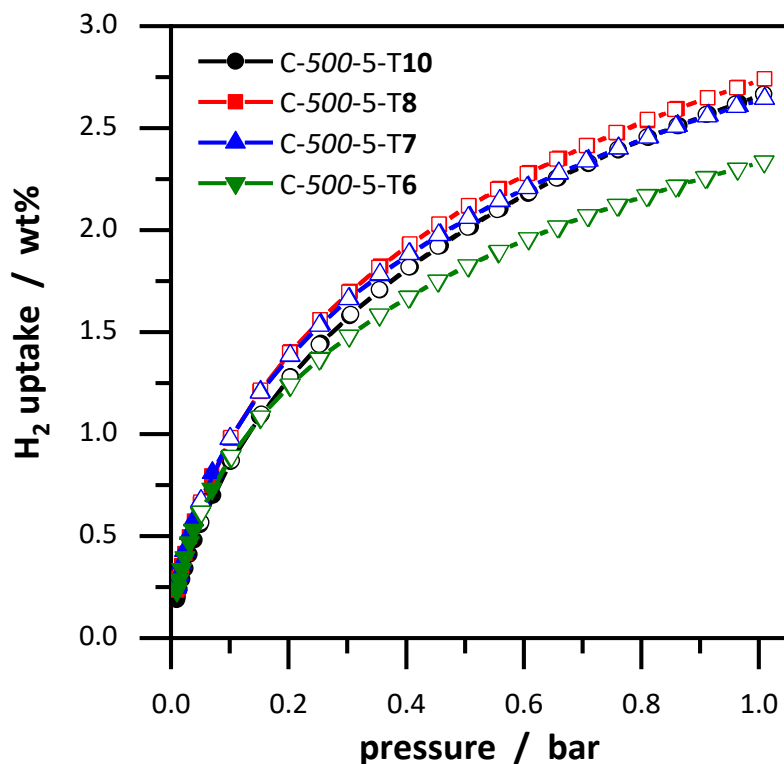


Figure 80: Gravimetric hydrogen storage capacity at 77 K of activated carbons synthesized at different activation temperatures.

The hydrogen uptake capacities for the carbon samples are 2.67, 2.74, 2.64 and 2.34 wt% for C-500-5-T10, C-500-5-T8, C-500-5-T7 and C-500-5-T6 respectively. The uptake capacity values are all in a similar range in accordance with their specific surface areas. Only the uptake capacity for C-500-5-T6 is considerably smaller, which is ascribed to the slightly smaller surface area, compared to the other carbon samples. Apart from C-500-5-T6, the uptake capacity is therefore essentially independent of the activation temperature as shown in Figure 81. For the normalized hydrogen uptake capacity, the values are almost independent from the activation temperature. This is not surprising since the surface areas do not differ very much from one other. And although the pore sizes depend on the activation temperature as they are becoming smaller with lower activation temperature, sample C-500-5-T6 still has a large proportion of pores above 1.5 nm. This suggests that for larger micropores, there is no significant overlap of adsorption potential, which increases the uptake capacity. For small micropores, the opposing pore wall distance is small enough, that the adsorption potentials of each wall overlap, which leads to

an increased adsorption of hydrogen at small pressures. This effect becomes less pronounced with increasing pore walls. Apparently, larger micropores above 1.5 nm, do not show a higher adsorption potential, for the activated carbons in this study, since the uptake capacity of C-500-5-T6 is as high as the other samples in the low pressure range and smaller at 1 bar, which is due to the lower surface area.

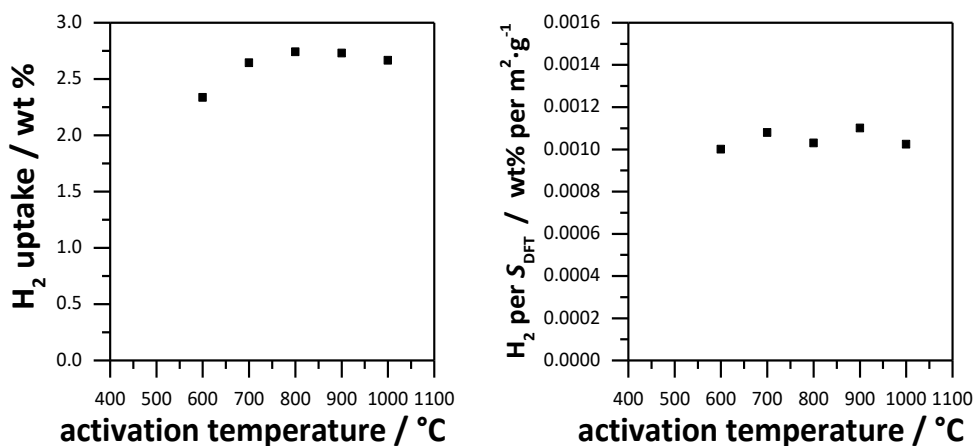


Figure 81: Gravimetric hydrogen uptake in dependence of the activation temperature, including data of the sample C-500-5-T9 (left) and the specific surface area normalized uptake capacity in dependence of the activation temperature (right).

The graphical summary of the carbon samples properties of this chapter is shown in Figure 82. The influence of the activation temperature on the porosity of the carbon materials was investigated, as well as their electrochemical properties and the gravimetric hydrogen uptake capacities. Generally, the pore sizes become larger with increasing activation temperature due to the additional side reactions with carbon. Nevertheless, the entire KOH is consumed at 600 °C leading to highly porous carbons with large micropores around 1.5 nm as well as high specific surface areas and pore volumes. At higher activation temperatures, the formed potassium carbonate and potassium oxide are able to consume additional carbon from the framework and enlarging the pores and the porosity in general. However, the effect is limited up to an activation temperature of 800 °C. Only at 1000 °C, carbon dioxide and carbon monoxide participate in the activation process in a larger extent along with the increased intercalation of potassium, which may create additional pores and enlarge existing ones. However, it must be noted, that higher activation temperatures may lead to an increase in porosity, but also reduces the yield. With regard

to the electrochemical performance, it was found that even larger micropores around 1.5 nm not only promote ion migration in the pore network at low currents and frequencies, but also at high currents. This was demonstrated by the good retention of capacitance and low time constant.

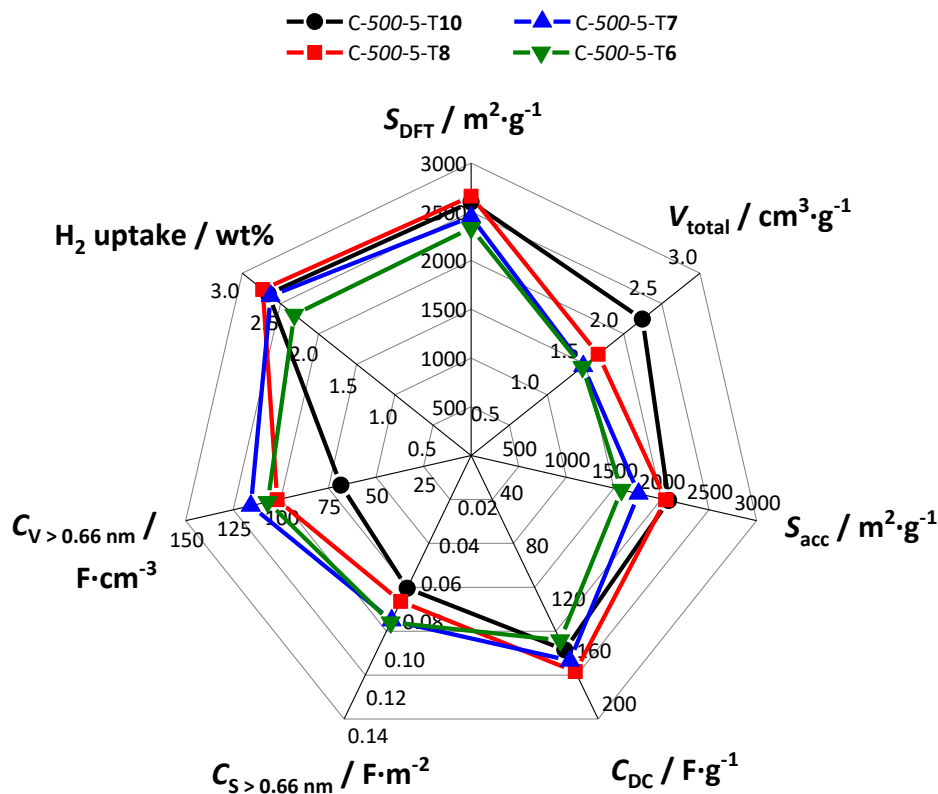


Figure 82: Graphical summary of the carbon sample properties, synthesized at different activation temperatures.

4.1.5 Combining low activation reactant and semi-carbonization

In this chapter the influence of the KOH amount and the semi-carbonization temperature will be further investigated and the effects of the synthesis parameters on the carbons will be extended. A lower KOH/carbon ratio than 5, namely 2.5, was selected and the semi-carbonization temperature was varied. It is to be expected, that the resulting carbons will have smaller pores, therefore smaller surface areas and pore volumes. However, obtaining carbons with predominantly micropores is

important to gain more precise information about the influence of pore sizes of carbons and the electrochemical performance. The work has shown so far, that the surface capacitance of activated carbons with smaller pores was higher and therefore a variety of carbons with smaller pores is mandatory. The semi-carbonization temperature was varied, as it is supposed to have a great influence on the porosity and therefore the importance of the semi-carbonization temperature will become clear. Semi-carbonization temperatures of 900, 800, 700, 600, 400 and 300 °C were chosen and the samples are denoted as C-900-2.5-T9, C-800-2.5-T9, C-700-2.5-T9, C-600-2.5-T9, C-400-2.5-T9 and C-300-2.5-T9 and the synthesis scheme is shown in Figure 83.

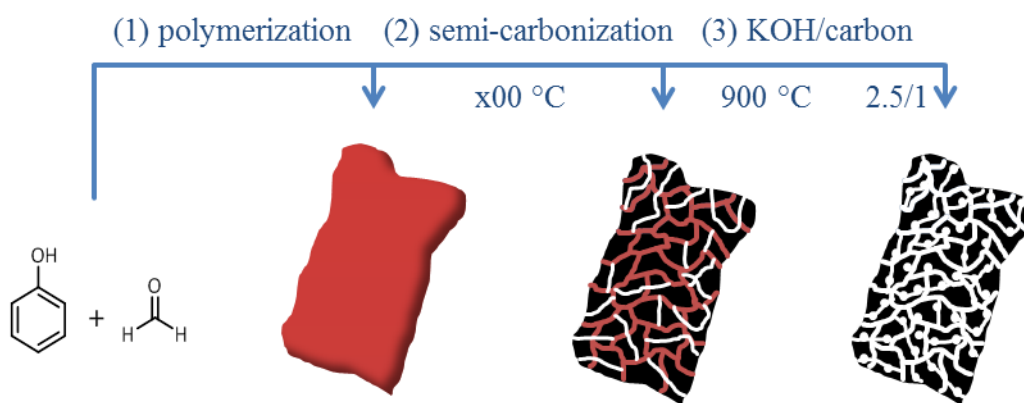


Figure 83: Synthesis scheme for the preparation of HSAC from PF resins. (1) polymerization of the PF resin under strong acidic conditions; (2) semi-carbonization of the PF resins at different temperatures under argon atmosphere; (3) chemical activation of the semi-carbonized carbons with a KOH/carbon ratio of 2.5 at 900 °C under nitrogen atmosphere.

4.1.5.1 *Characterization of carbons synthesized with a KOH/carbon ratio of 2.5 and different semi-carbonization temperatures*

SEM images of the carbons samples, shown in Figure 84, reveal that C-900-2.5-T9, C-800-2.5-T9, C-700-2.5-T9 and C-600-2.5-T9 possess a similar surface morphology as carbons synthesized at semi-carbonization temperatures of 600 °C and higher. Loose agglomeration of spherical particles form larger carbon particles and cavities, which are of similar diameter. The resistivity against chemical activation should be lower for C-400-2.5-T9 and C-300-2.5-T9 resulting in different network structures. In both cases, the spherical particles are merged, resulting in larger particles with smooth surfaces. Furthermore, cavities with a diameter of approximately

10 μm are also visible for the two materials. Therefore a sponge like structure can be derived, which can be explained by the high effectiveness of the chemical activation.

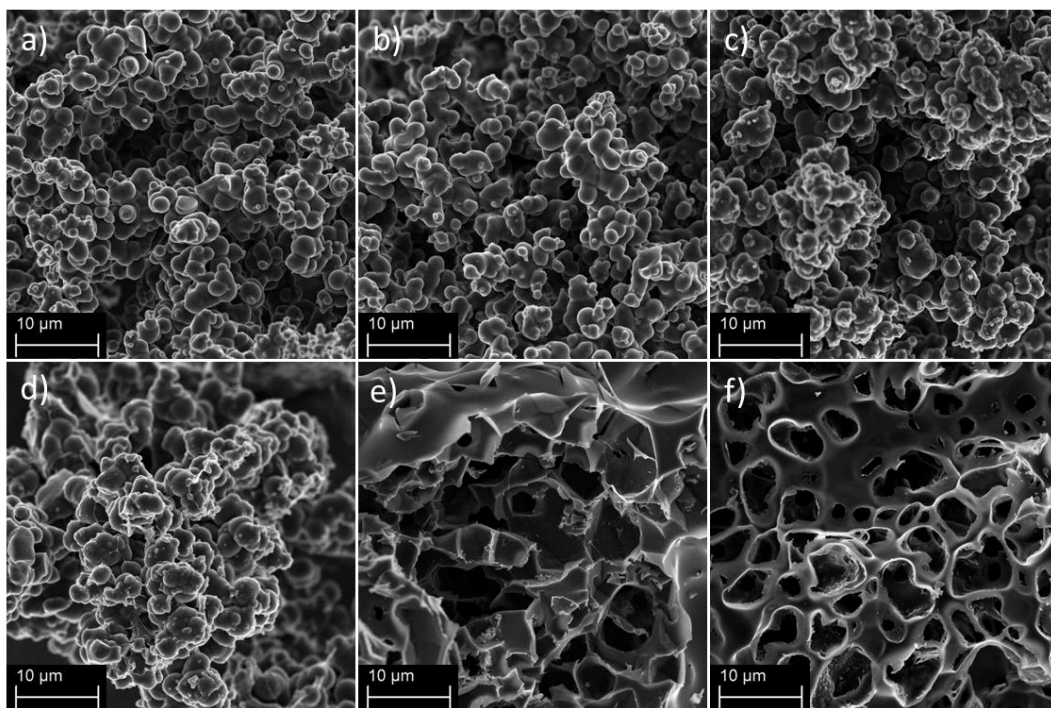


Figure 84: SEM images of (a) C-900-2.5-T9, (b) C-800-2.5-T9, (c) C-700-2.5-T9, (d) C-600-2.5-T9, (e) C-400-2.5-T9 and (f) C-300-2.5-T9.

P-XRD patterns of the carbon samples are shown in Figure A.8 and the Raman spectra are displayed in Figure A.9. All samples show weak and broad reflections at $44^\circ 2\theta$ and only C-900-2.5-T9 shows a weak reflection at $22^\circ 2\theta$, which is ascribed to stacked graphene layers indicating a slightly higher degree of graphitization. The I_D/I_G ratios from Raman spectroscopy are 1.06, 1.07, 1.07, 1.05, 1.03 and 1.04 for C-900-2.5-T9, C-800-2.5-T9, C-700-2.5-T9, C-600-2.5-T9, C-400-2.5-T9 and C-300-2.5-T9, respectively. The ratios are in a similar range and reflect a rather low degree of graphitization, but still higher as the carbon samples, activated with a higher ratio of KOH/carbon. The activation temperature was not high enough for a proper structuration of graphene layers to obtain a higher degree of graphitization. Nevertheless, the structural damage of the carbon framework was not as large due to the lower KOH/carbon ratio. This is shown by comparing these results with the I_D/I_G ratios of the carbon samples from section 4.1.3.1, where the semi-carbonization temperature was varied and the KOH/carbon ratio was kept at

5. The ratios were higher, between 1.15 and 1.26, indicating a lower degree of graphitization. This shows the degree of graphitization depends predominantly on the KOH/carbon ratio, where a higher ratio results in more structural defects because a larger amount of activation agent reacts with the carbon framework. Results of the thermogravimetry are shown in Figure A.10. All carbon samples burnt entirely at temperatures between 600 and 650 °C, showing no impurities and pure carbonaceous behavior. Interestingly, the temperature at which the combustion starts, shifts to higher temperatures with higher semi-carbonization temperatures. Presumably, the pore size decrease with increasing semi-carbonization temperature, which limits the diffusion of the combustion fluid within the pore network and, therefore, the combustion of the carbon is slightly delayed. However, the pore analysis still has to be carried out. Another possibility is the different content of oxygen in the carbon frameworks. As discussed before, a higher content of oxygen will weaken the thermal stability, hence leading to lower combustion temperatures. Carbon samples, synthesized at lower semi-carbonization temperatures presumably have a higher content of oxygen, which weakens the thermal stability.

Nitrogen adsorption-desorption isotherms (77 K) and the corresponding pore size distributions, calculated by the QSDFT method are shown in Figure 85 and Figure 86. All carbon materials show Type-I isotherms indicating samples with predominantly micropores. No significant impact from the semi-carbonization temperature on the pore size is observable from the pore size distribution. It can be concluded, a higher KOH/carbon ratio of at least 5 is required, to obtain carbons with large micropores and mesopores.

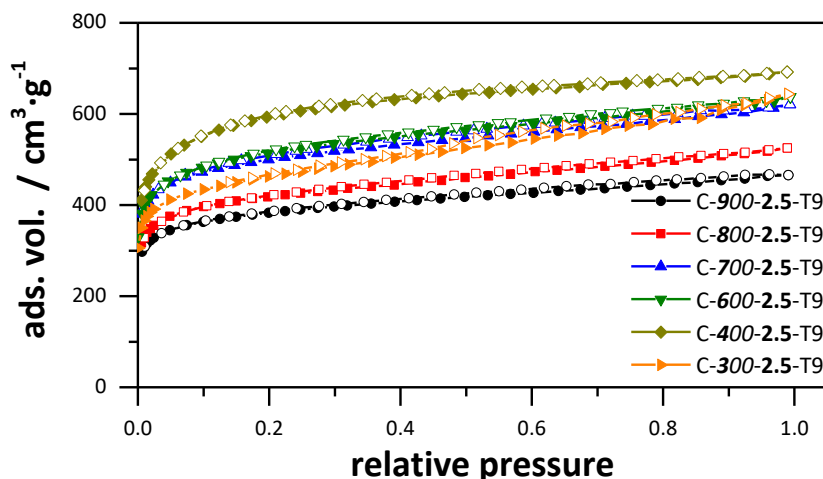


Figure 85: Nitrogen adsorption-desorption isotherms (77 K) of the carbon materials with different semi-carbonization temperatures and a KOH/carbon ratio of 2.5.

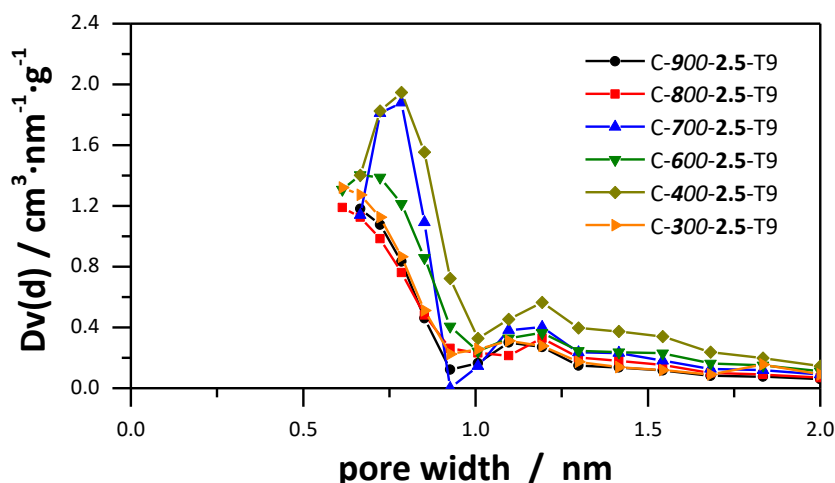


Figure 86: Pore size distributions of the carbons materials with different semi-carbonization temperatures and a KOH/carbon ratio of 2.5, calculated by the QSDFT method from nitrogen desorption branch.

Carbon dioxide adsorption-desorption isotherms (273 K) and the pore size distribution of the carbon samples are displayed in Figure 87 and Figure 88. All isotherms have a similar shape, and the pore size distributions reveal no major differences in micropore sizes of the carbons. Nevertheless, differences in porosity are visible, but only regarding the specific surface areas and pore volumes, which were calculated and summarized in Table 10. The DFT surface areas increase with decreasing semi-carbonization temperature, up to a temperature of 400 °C. This can be attributed to

the more effective chemical activation at carbons, with a less rigid carbon framework and presumably a higher content of oxygen. The same trend is observable for the total pore volume and the micropore volume meaning an increase of pore sizes regarding micropores and pore sizes in general, although difficult to obtain from the pore size distributions. So far, the observations from section 4.1.3.1 are confirmed, as a lower semi-carbonization temperature increases the effectiveness of the chemical activation, resulting in larger pores. This leads to higher pore volumes and possibly higher surface areas. The micropore volume increases with decreasing semi-carbonization temperature as the simultaneous occurring carbonization of organic residues and chemical activation results in the formation of new micropores. Interestingly, the surface area, total- and micropore volume for C-300-2.5-T9 are comparatively low regarding sample C-400-2.5-T9 and C-600-2.5-T9. Although the total pore volume is slightly lower, the content of mesopores is larger than the mesopore content of the other carbon samples. This indicates a relative pore enlargement caused by the low semi-carbonization temperature.

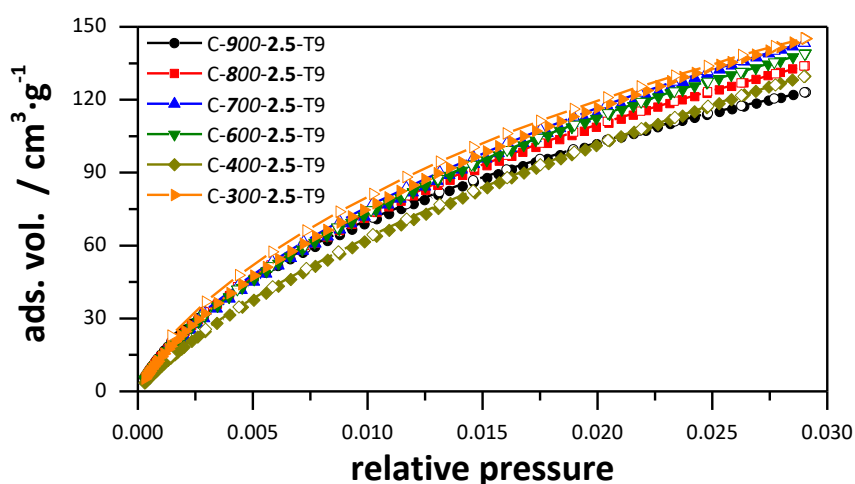


Figure 87: Carbon dioxide adsorption-desorption isotherms (273 K) of the carbon materials with different semi-carbonization temperatures and a KOH/carbon ratio of 2.5.

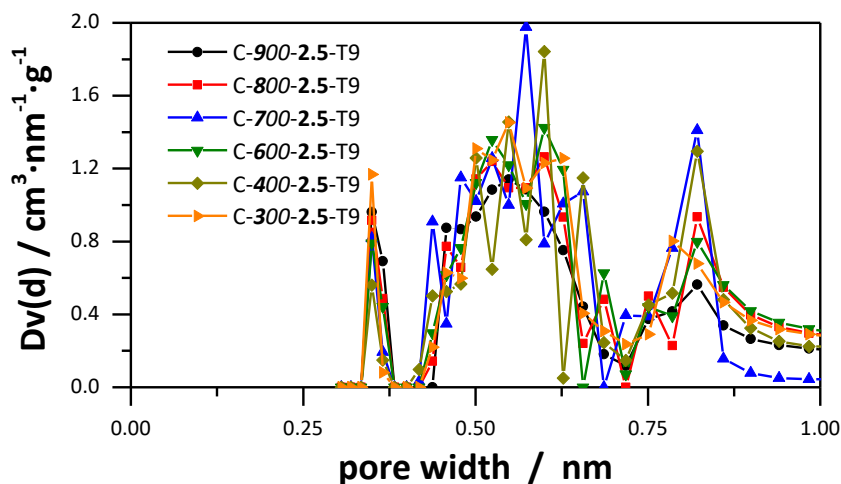


Figure 88: Pore size distributions of the carbon materials with different semi-carbonization temperatures and a KOH/carbon ratio of 2.5, calculated by the NLDFT method from carbon dioxide desorption branch.

More details are revealed by considering the combined cumulative surface area and combined cumulative pore volume, displayed in Figure 89 and Figure 90. The surface area provided by pores below 0.7 nm is approximately equal for all carbon samples and the surface area generated by pores below 1 nm differs only to a small extent. However, it becomes more evident, the lower semi-carbonization temperature leads to an enlargement of pores, which are particularly noticeable when considering the cumulative pore volumes in the range of 1 to 4 nm. Sample C-300-2.5-T9 is an exception, with a higher surface area and total pore volume than samples C-800-2.5-T9 and C-900-2.5-T9, but lower surface area and pore volume than samples C-400-2.5-T9, C-600-2.5-T9 and C-700-2.5-T9, thus having slightly smaller pores. On the other hand, a slightly pore enlargement is visible in Figure 90 as it shows a higher specific content of pore between 2 and 3 nm and a higher content of pores below 1 nm at the same time. The reason for the lower surface area and pore volumes are, that pores were enlarged, but the pores below 1 nm did not increase significantly. Therefore, the content of micropores in general is smaller, which eventually leads to a lower specific surface area.

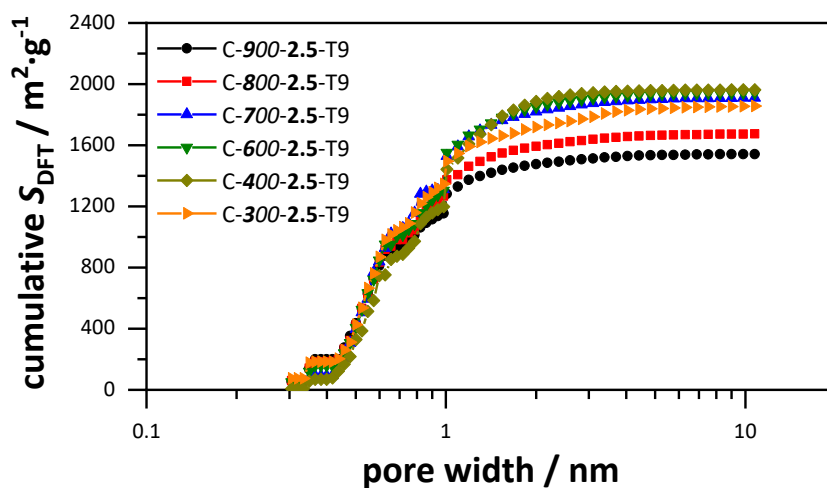


Figure 89: Combined cumulative surface area derived from carbon dioxide and nitrogen physisorption data of the carbon samples synthesized at different semi-carbonization temperatures and a KOH/carbon ratio of 2.5.

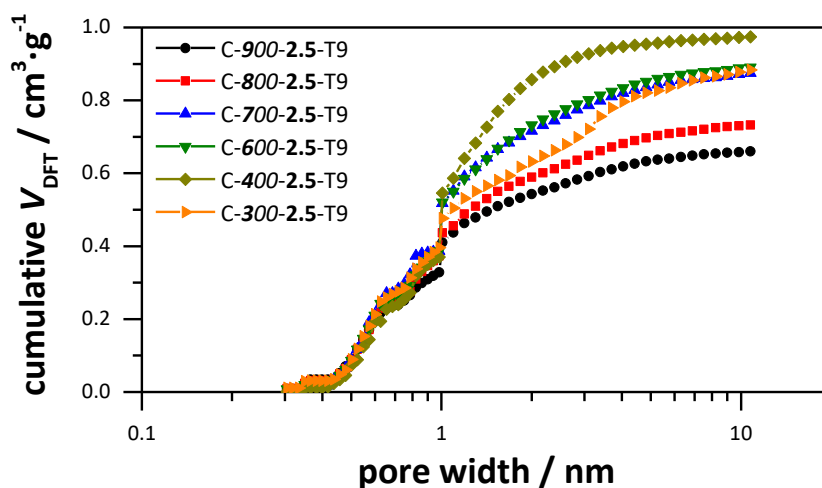


Figure 90: Combined cumulative pore volume derived from carbon dioxide and nitrogen physisorption data of carbon samples synthesized at different semi-carbonization temperatures and a KOH/carbon ratio of 2.5.

Table 10: Nitrogen physisorption derived data of the carbon samples synthesized at different semi-carbonization temperatures and a KOH/carbon ratio of 2.5.

Sample	$S_{\text{BET}} /$ $\text{m}^2 \cdot \text{g}^{-1}$	$S_{\text{DFT}} /$ $\text{m}^2 \cdot \text{g}^{-1}$	$V_{\text{t}} /$ $\text{cm}^3 \cdot \text{g}^{-1}$	$V_{\text{mic}} /$ $\text{cm}^3 \cdot \text{g}^{-1}$
C-900-2.5-T9	1449	1543	0.67	0.54
C-800-2.5-T9	1582	1675	0.75	0.59
C-700-2.5-T9	1892	1910	0.88	0.72
C-600-2.5-T9	1928	1945	0.90	0.73
C-400-2.5-T9	2205	1964	0.98	0.86
C-300-2.5-T9	1731	1860	0.92	0.63

S_{DFT} (DFT surface area), V_{t} (total pore volume) and V_{mic} (micropore volume) obtained from QSDFT analysis. S_{BET} (BET surface area).

In principle, conclusions from section 4.1.3 can be confirmed that a lower semi-carbonization temperature prior to the chemical activation leads to an enlargement of pores and thus also increases the surface area and pore volume of the carbons. However, it has also been shown that a KOH/carbon ratio of 2.5 is not sufficient to generate larger micropores or mesopores in the carbon samples. As already described in 4.1.2, a larger ratio of at least 5 is required.

4.1.5.2 Energy storage related properties of carbons synthesized with a KOH/carbon ratio of 2.5 and different semi-carbonization temperatures

Electrochemical characterization

Cyclic voltammograms of the activated carbons are shown in Figure 91. The CV curves of all samples show rectangular shapes indicating purely capacitive charge storage behavior. All CV curves are evenly distorted at the vertex potentials, caused by the R_{ESR} , and the distortion increases with higher scan rates due to kinetic diffusion resistances of electrolyte ions entering the pores. C-900-2.5-T9 differs with a significantly lower capacitance and strong current increases and curve distortions at 10 and 20 $\text{mV} \cdot \text{s}^{-1}$. Because of its disappearance with increasing scan rate, this is probably caused by charge transfer side reactions, or ion insertion. Since C-900-2.5-T9 has the smallest pores, it is possible the pore entering process of the ions is delayed during the charging, which causes a current increase. This process requires

energy, which limits the coulomb efficiency of the charge-discharge process at low scan rates.

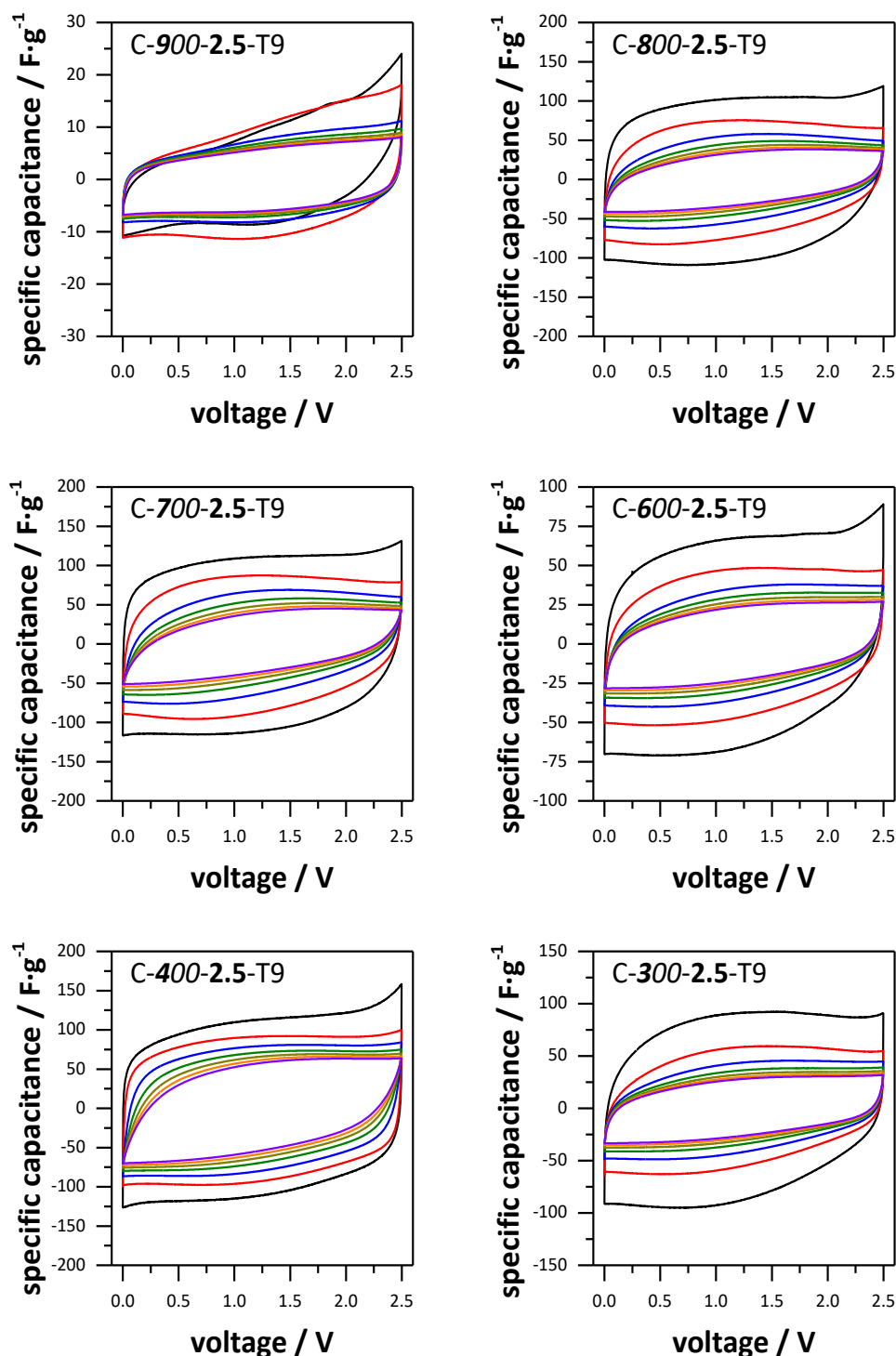


Figure 91: Cyclic voltammograms of the activated carbons synthesized at different semi-carbonization temperatures and a KOH/carbon ratio of 2.5 at 10 mV·s⁻¹ (black), 100 mV·s⁻¹ (red), 500 mV·s⁻¹ (blue), 1000 mV·s⁻¹ (green), 1500 mV·s⁻¹ (yellow), 2000 mV·s⁻¹ (orange) and 2500 mV·s⁻¹ (violet).

Results from galvanostatic charge-discharge tests are displayed in Figure 92 and the corresponding calculated discharge capacitance values are summarized in Table 11. Although, the semi-carbonization temperatures impact on the specific surface area is rather limited, as discussed in the previous section, the accessible surface areas show clear differences among the carbon samples. With decreasing semi-carbonization temperature, down to 400 °C, the accessible surface area increases, thus confirming the enlargement of pores due to the low resistivity against the chemical activation of the semi-carbonized carbons. The accessible surface area of C-300-2.5-T9, is comparatively low with $873 \text{ m}^2 \cdot \text{g}^{-1}$, which may be due pore enlargement without the amount of pores increasing significantly. This reduces the accessible surface area compared to C-400-2.5-T9. The specific capacitance correlates clearly with the accessible surface area, with the exception of sample C-300-2.5-T9. The accessible surface area of samples C-300-2.5-T9 and C-700-2.5-T9 is almost identical, but the capacitance differs by $20 \text{ F} \cdot \text{g}^{-1}$. The only significant difference between the two samples is the larger micropore volume and micropore surface area of sample C-700-2.5-T9. Thus, it can be concluded micropores provide a greater proportion of the capacitance, as already indicated in the previous sections. It is known from the previous sections that pore sizes of at least 1.5 nm are required in carbon materials to ensure ion transport in the pores at high current densities. Therefore, the retention of capacitance values at higher current densities is consequently low for all carbon samples. Since the sample C-400-2.5-T9 has larger pores than the other carbon materials, the retention is also the highest with 68 %. The capacitance of C-900-2.5-T9 is extremely low despite a theoretical achievable surface area of $626 \text{ m}^2 \cdot \text{g}^{-1}$. The pore sizes are probably too small, so that a low current induces diffusion resistances large enough, preventing access of the electrolyte ions to the electrode surface.

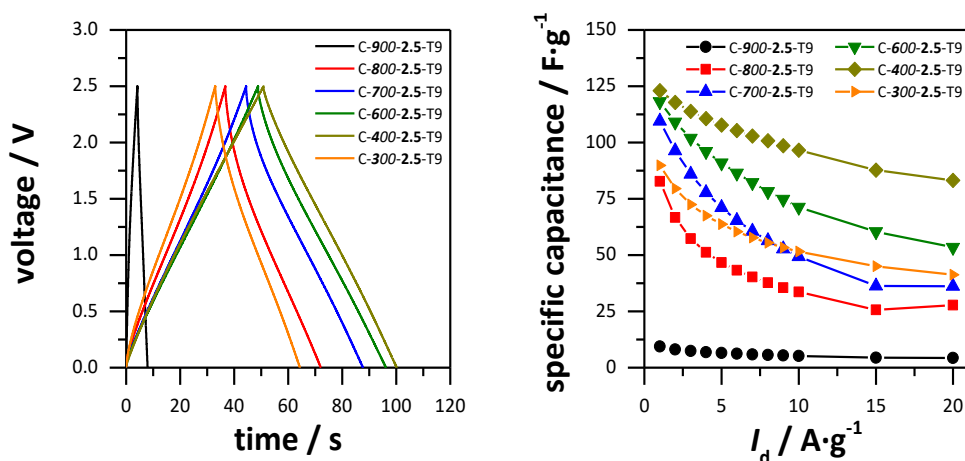


Figure 92: Discharge curve at 1 A·g⁻¹ for the carbon samples synthesized at different semi-carbonization temperatures and a KOH/carbon ratio of 2.5 (left) and the specific capacitance as a function of discharge current density (right).

Table 11: Electrochemical properties of the EDLC prepared from activated carbons synthesized at different semi-carbonization temperatures and a KOH/carbon ratio in 1 M TEABF₄/ACN.

Sample	$S_{\text{acc}} /$ $\text{m}^2 \cdot \text{g}^{-1}$	$V_{\text{acc}} /$ $\text{cm}^3 \cdot \text{g}^{-1}$	$C_{\text{CV}} /$ $\text{F} \cdot \text{g}^{-1}$	$C_{\text{DC}} /$ $\text{F} \cdot \text{g}^{-1}$
C-900-2.5-T9	626	0.45	8.5	9.4
C-800-2.5-T9	736	0.52	88.0	82.7
C-700-2.5-T9	888	0.64	98.5	109.5
C-600-2.5-T9	992	0.66	101.3	118.2
C-400-2.5-T9	1112	0.79	107.9	123.0
C-300-2.5-T9	874	0.60	75.4	87.9

S_{acc} specific surface area for pores > 0.66 nm; V_{acc} pore volume for pores > 0.66 nm; C_{CV} calculated from 10 mV·s⁻¹; C_{DC} calculated from 1 A·g⁻¹.

The surface normalized capacitance values and pore volume normalized capacitance values are shown in Figure 93 and are summarized in Table 12. Compared to the gravimetric capacitance values, the surface capacitance of the carbons are in similar ranges except for sample C-900-2.5-T9, which display an exceptional case of extremely low capacitance in general. This applies both to capacitances normalized to the total surface area and to the values normalized to the accessible surface area. There is only a slight tendency for the surface capacitance to increase with the

semi-carbonization temperature. This shows carbons with smaller pores use the surface more effectively for charge storage. However, the differences for these carbon samples are very small, as all materials are microporous and all have pores below 1.5 nm.

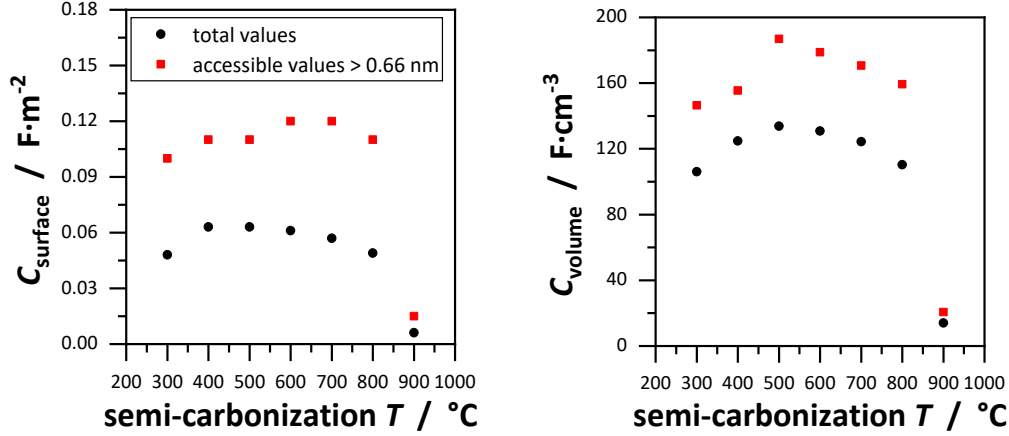


Figure 93: Surface area normalized capacitance (left) and pore volume normalized capacitance (right) as a function of the semi-carbonization temperature for carbons, synthesized at a KOH/carbon ratio of 2.5, including sample C-500-2.5-T9.

Table 12: Surface- and volumetric capacitance values for carbons synthesized at different semi-carbonization temperatures and a KOH/carbon ratio of 2.5.

Sample	C_s / F·m ⁻²	$C_{s>0.66}$ / F·cm ⁻²	C_v / F·cm ⁻³	$C_{v>0.66}$ / F·cm ⁻³
C-900-2.5-T9	0.0061	0.015	14.0	20.7
C-800-2.5-T9	0.049	0.11	110.3	159.3
C-700-2.5-T9	0.057	0.12	124.3	170.7
C-600-2.5-T9	0.061	0.12	130.8	178.8
C-400-2.5-T9	0.063	0.11	124.8	155.5
C-300-2.5-T9	0.048	0.10	106.1	146.5

C_s , $C_{s>0.66}$ calculated from C_{DC} and the respective surface areas, obtained from the DFT results; C_v , $C_{v>0.66}$ calculated from C_{DC} and the respective pore volumes.

The results of the PEIS measurements are displayed in Figure 94. Nyquist plots for all carbon samples show low R_{ESR} values and short semicircles with comparable length. The high frequency response for all test devices is therefore similar. The

phase angle at 10 mHz are -71.6 , -83.9 , -86.0 , -85.5 , -86.0 and -81.0 for C-**900-2.5-T9**, C-**800-2.5-T9**, C-**700-2.5-T9**, C-**600-2.5-T9**, C-**400-2.5-T9** and C-**300-2.5-T9**, respectively. With exception of sample **900-2.5-T9**, all materials are able to ensure ion transport without diffusion limitations at low frequencies. This is remarkable because larger pores have been assumed to be necessary for ions transport, even at low frequencies and currents. As for **900-2.5-T9**, the average pore sizes are too small to ensure resistance free ions transport, even at low frequencies and currents. Reevaluating the pore size distributions, pores below 1.2 nm are insufficient for enabling ion migration within the pore network. The frequency response of the normalized real capacitance further demonstrates the poor diffusion of electrolyte ions within the electrode material **900-2.5-T9**. Instead of a plateau in the low frequency region, a steep slope is observable indicating an instant loss of capacitance. Consequently, the time constant is higher than 100 s, deduced from the current response of the normalized imaginary capacitance. Interestingly, a maximum can be observed at a high frequency of 10 mHz. This can be attributed to charge transfer reactions, which are either caused by the electrolyte degradation at the surface of the electrode or by the reaction of the current collector with the electrolyte. Since the time constant for the observed phenomena is rather low (0.1 s) the cause is a reaction at the electrode surface, because the ions at the high frequency are unable to penetrate through the material to the current collector in large quantities. The other carbon samples show a plateau at high frequencies, followed by an exponential decay, resulting in frequency peaks at the currents' response of the normalized real capacitance. Another exception is sample C-**300-2.5-T9**, where the real capacitance decreases by a smaller slope, which is reflected in the imaginary capacitance by a very broad peak. Even at higher and lower frequencies around the peak, a relatively high capacitance loss is observable, which is attributed to the broader pore size distribution. Although, sample C-**300-2.5-T9** shows a slightly larger content of between 2 and 3 nm, the content of pores below 1 nm is higher as well, compared to the other carbon samples. These small micropores hinder the ion migration in the pore framework, which is also displayed by a larger time relaxation constant. The time constants for the carbon samples are 5.13, 3.02, 2.91, 1.25 and 2.30 s for C-**800-2.5-T9**, C-**700-2.5-T9**, C-**600-2.5-T9**, C-**400-2.5-T9** and C-**300-2.5-T9**, respectively. Therefore, the time relaxation constant decreases with decreasing semi-carbonization temperature except for sample C-**300-2.5-T9**. This

could be attributed to the decreasing average pore size, although the differences in pore size for the discussed carbon samples are minor.

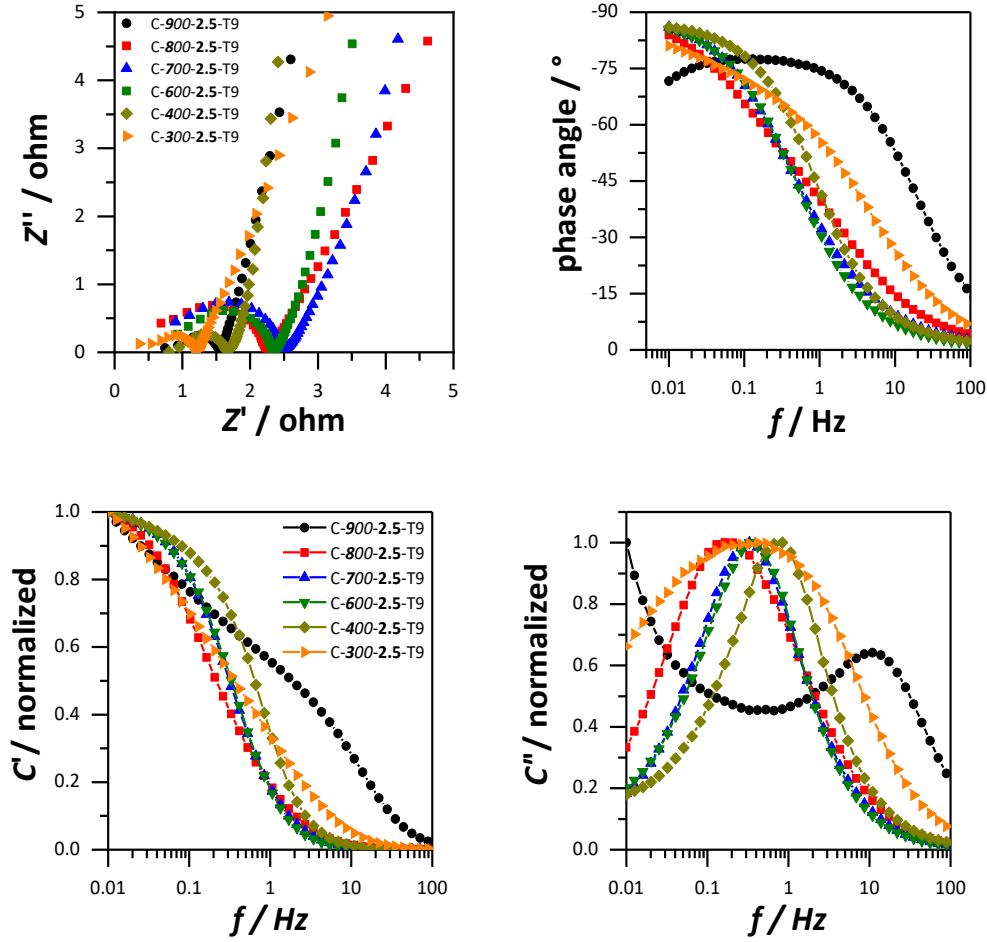


Figure 94: Nyquist plot of the activated carbons (top left), frequency response of the phase angle (top right), normalized real capacitance (bottom left) and normalized imaginary capacitance (bottom right).

The different pore sizes of the samples are difficult to assess and only minor assessable from the total surface area, total pore volume and micropore volume, but can be seen in the effects on the electrochemical properties. The accessible surface area shows a clear dependence on the semi-carbonization temperature, and is decisive for the gravimetric capacitance. None of the materials showed a good retention of capacitance at high currents and frequencies, which can be attributed to the small pores. The previous sections have shown a large content of pores larger than 1.5 nm are required for a sufficiently good capacitance retention. For a good migration of the ions within the carbon particles at low currents and frequencies, however, the

maximum pore size of 1.2 nm was sufficient. This is a clear indication the solvate shells of the electrolyte ions are distorted or partially removed, as no significant formation of the electrochemical double layer would otherwise be possible.

Hydrogen storage

The gravimetric hydrogen uptake isotherms at 77 K of the carbons are shown in Figure 95. Here, too, the isotherms are fully reversible and have not reached saturation. The activated carbon samples show similar hydrogen uptakes in the pressure range between 0 and 0.1 bar, which is dedicated to the similar sizes of the micropores. The uptakes at the pressure range at 1 bar, however, are different, which is due to the different surface areas.

The gravimetric uptake capacities are 2.10, 2.33, 2.51, 2.44, 2.67 and 2.43 wt% for **900-2.5-T9**, **C-800-2.5-T9**, **C-700-2.5-T9**, **C-600-2.5-T9**, **C-400-2.5-T9** and **C-300-2.5-T9** respectively. This means no clear trend is recognizable. **C-400-2.5-T9** has the highest uptake capacity, due to its high specific surface area, compared to the remaining samples. The capacity of **C-500-2.5-T9** is similarly high and the capacity generally decreases with increasing semi-carbonization temperature. This can be traced back to the smaller surface areas (Figure 96). The specific surface area normalized capacity varies for all discussed carbons around the same value. The capacity decreases marginally with increasing semi-carbonization temperature up to 500 °C, and then increases again. However, these values vary only slightly, as already mentioned. This gives the reason to assume, for microporous carbons, the pores contribute evenly to hydrogen adsorption at 77 K and 1 bar.

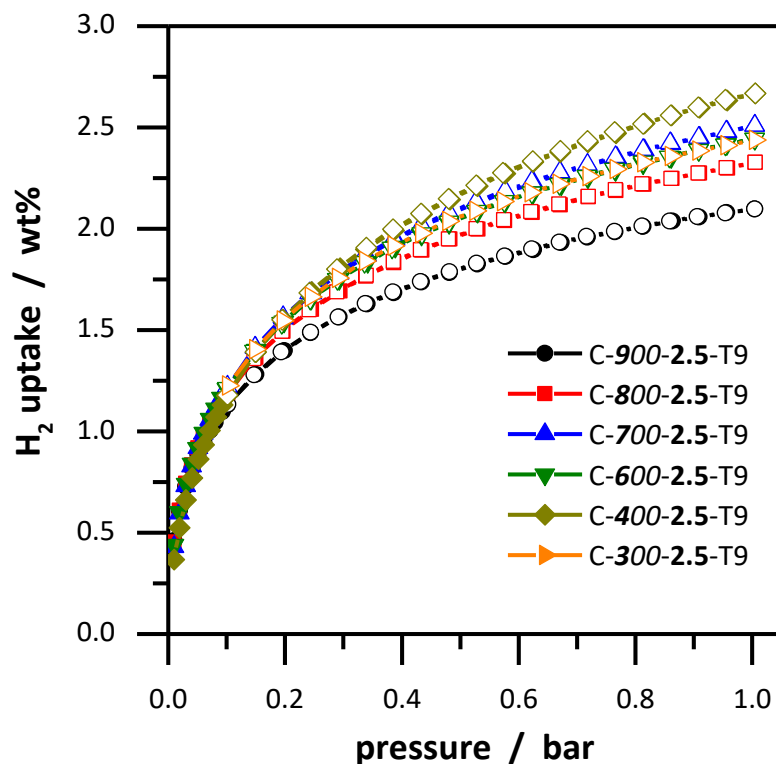


Figure 95: Gravimetric hydrogen storage capacity at 77 K of activated carbons, synthesized at different semi-carbonization temperatures and a KOH/carbon ratio of 2.5.

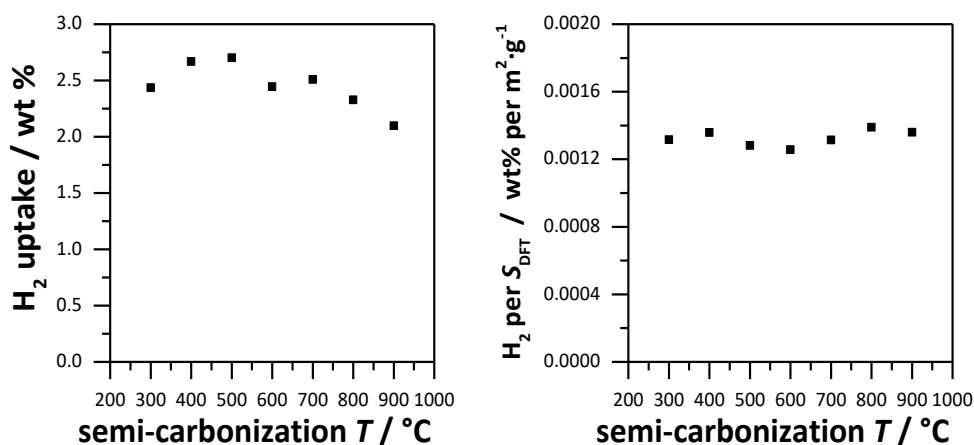


Figure 96: Gravimetric hydrogen uptake in dependence of the semi-carbonization temperature, including data of the sample C-2.5-500-T9 (left) and the specific surface area normalized uptake capacity in dependence of the semi-carbonization temperature (right). The KOH/carbon ratio was fixed at 2.5.

In this section, the conclusions from section 4.1.3 can be confirmed. The semi-carbonization temperature prior to the KOH activation influences the pore sizes and thus the surface areas and pore volumes. Due to the higher organic content in the carbon after a low temperature treatment, the material is more susceptible to the etching processes during the KOH activation. On average, the pores are enlarged as the semi-carbonization temperature decreases. However, due to the low KOH/carbon ratio, this effect is not pronounced, and the samples are all microporous with pores significantly smaller than 1.2 nm. Clearer differences can only be seen in the accessible surface area with regard to the electrolyte ion sizes. The gravimetric double layer capacitance is closely related to the accessible surface area, and no significant differences in of the pore surface utilization could be determined. Capacitance retention at higher currents was not particularly good for any sample, suggesting micropores between 1.0 and 1.2 nm are not large enough to allow ion diffusion. This seems reasonable as the TEA⁺ cation incl. solvent shell has a size of 1.3 nm and distortion or partial removal of this can only be operated with increased energy expenditure. This ultimately leads to a higher limitations of the diffusion kinetics, which ultimately leads to low capacitance values. At low currents and frequencies, the electrolyte ions are able to adsorb at the electrode surface, although nearly all samples in this section have few pores above 1.0 nm. This could be determined via PEIS. This means ions with distorted or partially removed solvent shell participate in the formation of the electrochemical double layer, which is in agreement with previous studies.^[296] Generally, the hydrogen uptake capacities increase along with a decreasing semi-carbonization temperature which is ascribed to the simultaneously increasing surface area.

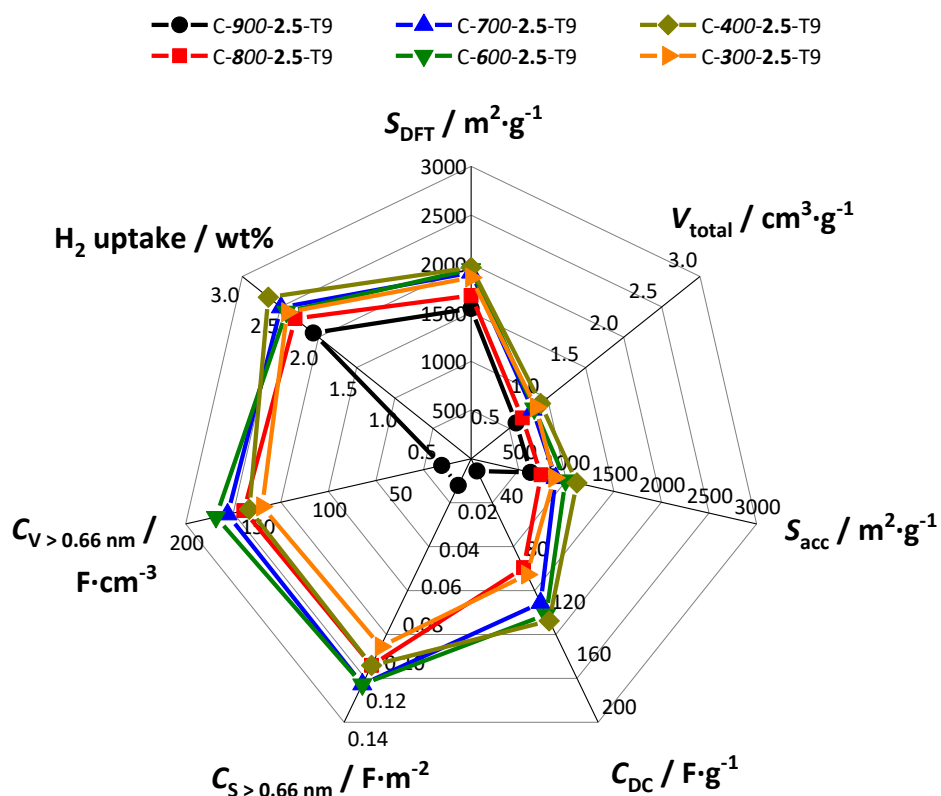
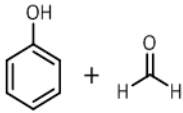


Figure 97: Graphical summary of the carbon sample properties, synthesized at different semi-carbonization temperatures and a KOH/carbon ratio of 2.5.

4.1.6 Influence of activation and semi-carbonization temperature

In order to illustrate the importance of the semi-carbonization on the porosity of the carbons, a high semi-carbonization temperature of 900 °C was selected in this section. Again, it is presumed, that the resulting carbons will have smaller pores and lower surface areas. Then again, carbons with tailored micropores are desired for certain applications, such as electrochemistry. To further confirm the influence of the activation temperature, temperature was varied between 600 and 1000 °C. Specifically activation temperatures of 1000, 800, 700 and 600 °C were chosen and the samples are denoted as C-900-5-T10, C-900-5-T8, C-900-5-T7 and C-900-5-T6. The KOH/carbon ratio was 5 and the synthesis scheme is shown in Figure 98.



4.1.6.1 Characterization of carbons synthesized at a semi-carbonization temperature of 900 °C and different activation temperatures

160

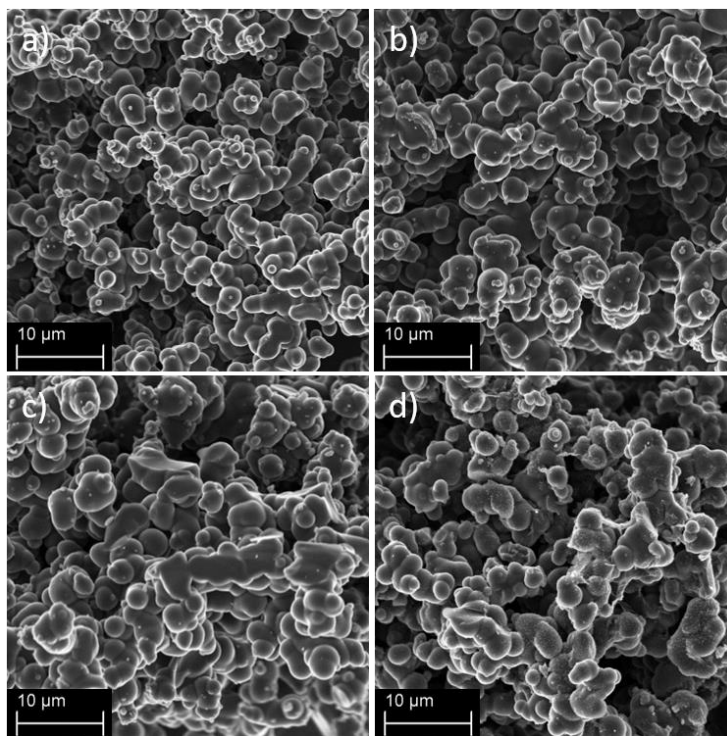


Figure 99: SEM images of (a) C-900-5-T10, (b) C-900-5-T8, (c) C-900-5-T7 and (d) C-900-5-T6.

P-XRD patterns and Raman spectra of the carbon samples are shown in Figure A.11 and Figure A.12 respectively. Broad (101) reflections are visible for all carbons at $44^\circ 2\theta$. Interesting, however, are the broad reflections around $21^\circ 2\theta$, which reflect the stacking of graphene layers. While C-900-5-T10 shows no reflection at $21^\circ 2\theta$, for the other samples the reflection becomes visible with decreasing activation temperature and increases in relative intensity at the same time. This indicates a higher degree of graphitization with decreasing activation temperature. The results of the Raman spectroscopy confirm this trend, recognizable by the I_D/I_G ratios. These are 1.16, 1.14, 1.11 and 1.08 for C-900-5-T10, C-900-5-T8, C-900-5-T7 and C-900-5-T6 respectively. These results agree with those from section 4.1.4. A higher activation temperature promotes the formation of thermodynamically preferred graphitic phases, but at the same time further etching reactions take place at higher temperatures, which leads to increased structural defects. Accordingly, all the carbons from this section are considered amorphous materials. Results from thermogravimetry are displayed in Figure A.13 and show that all carbon samples combust completely at a temperatures of 650°C . Noticeably, the combustion of C-900-5-T10 starts at lower temperature of 400°C , compared to the other samples, which can be ascribed

to the presumably higher porous character, which promotes the fluid diffusion within the samples, thus shifting the combustion to lower temperatures. The combustion of sample C-900-5-T6 starts at 500 °C and at 550 °C for samples C-900-5-T8 and C-900-5-T7 respectively. Sample C-900-5-T6 presumably has a higher content of oxygen due to the lower activation temperature.

Nitrogen physisorption adsorption-desorption isotherms and the corresponding pore size distribution, calculated by the QSDFT method, are shown in Figure 100 and Figure 101 respectively, and the results are summarized in Table 13. C-900-5-T8, C-900-5-T7 and C-900-5-T6 show Type-I isotherms for microporous carbons, and the isotherm of C-900-5-T10 shows a slope in the relative pressure range between 0.1 and 0.4, aligned with a small hysteresis, indicating the presence of mesopores. The pore size distributions confirm the presence of large micropores and mesopores for C-900-5-T10 up to 3.0 nm in size. Otherwise, it can be seen pore sizes become smaller with decreasing activation temperature. As in section 4.1.4, this can be attributed to the side reactions which lead to enlargements of the pores at higher temperatures. However, the pores of the materials are significantly smaller than the comparable samples from section 4.1.4 which were activated with a KOH/carbon ratio of 5, a semi-carbonization temperature of 500 °C and different activation temperatures. This is caused by the high semi-carbonization temperature, which increases the chemical stability of the carbon materials and thus limits the effectiveness of the KOH activation.

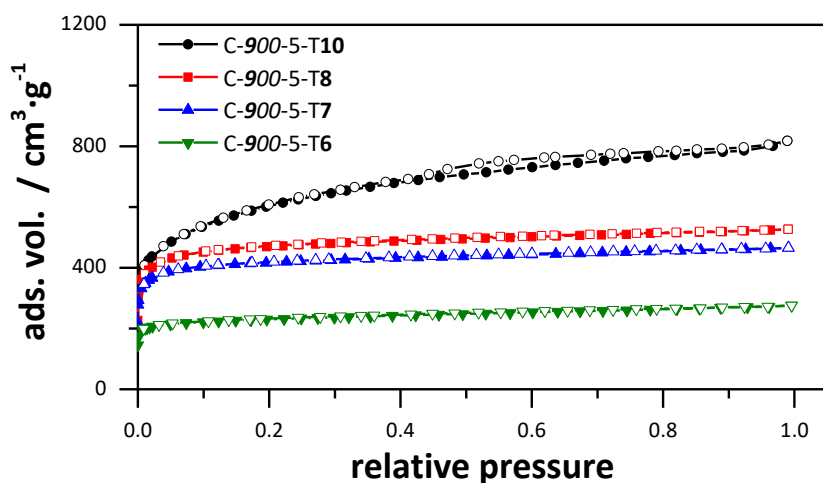


Figure 100: Nitrogen adsorption-desorption isotherms (77 K) of the carbon material with different activation temperatures and a semi-carbonization temperature of 900 °C.

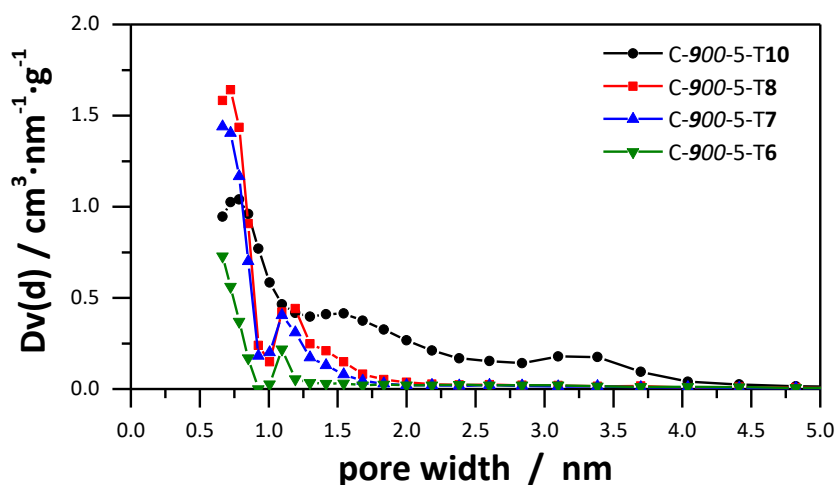


Figure 101: Pore size distributions of the carbon materials with different activation carbonization temperatures and a semi-carbonization temperature of 900 °C. Calculated from nitrogen physisorption with the QSDFT method, assuming slit pores from the desorption branch.

Carbon dioxide adsorption-desorption isotherms and the corresponding pore size distributions, calculated by the NLDFT method, and are shown in Figure 102 and Figure 103. Considering the pore widths of 0.4 to 0.8 nm, it is noticeable the pores also increase in size as the activation temperature increases. This is due to the higher

effectiveness of the chemical activation at higher temperatures where additional side reactions occur with the carbon framework.

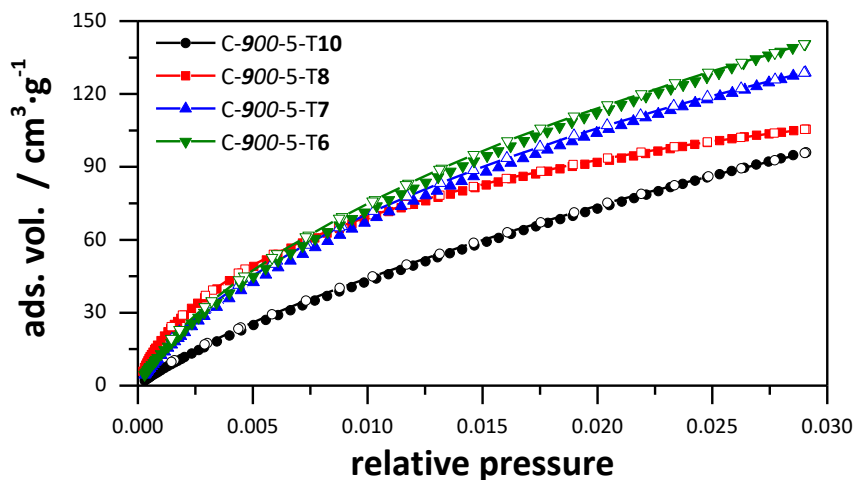


Figure 102: Carbon dioxide adsorption-desorption isotherms (273 K) of the carbon materials with different activation temperatures and a semi-carbonization temperature of 900 °C.

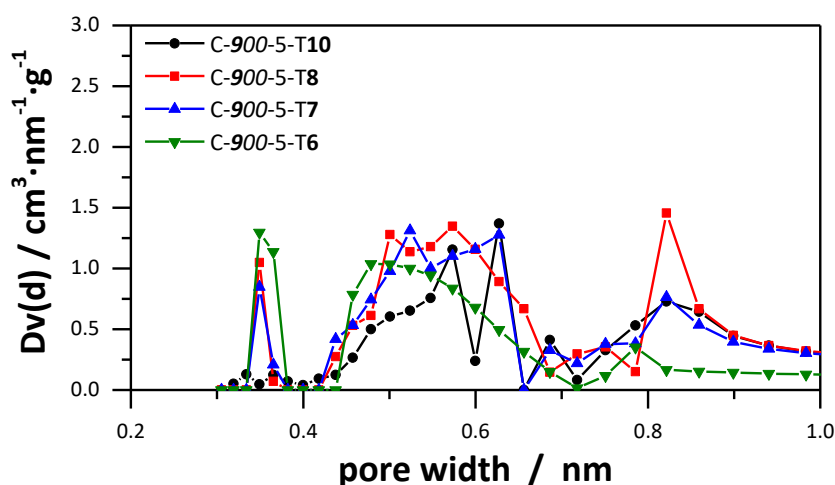


Figure 103: Pore size distributions of the carbon materials with different activation temperatures and a semi-carbonization temperature of 900 °C. Calculated from carbon dioxide physisorption with the NLDFT method assuming slit pores from the desorption branch.

The pore size dependent cumulative surface area and pore volume, deduced from nitrogen and carbon dioxide physisorption in combination shown in Figure 104 and

Figure 105. The specific surface area increases with increasing activation temperature, as the additional etching process not only enlarges existing pores but also generate additional pores. Since pores also become larger with the activation temperature, the pore volumes increase with increasing activation temperature accordingly. The surface area generated by pores up to 1 nm, generally increases with increasing activation temperature and is highest for sample **900-5-T8** with $1400 \text{ m}^2 \cdot \text{g}^{-1}$. For sample **C-900-5-T10**, however, it is significantly lower, which suggests the content of small micropores is considerably lower. It can be assumed the additional etching processes increase the size of all pores and decrease the frequency of small micropores below 1 nm. However, it is also possible the higher carbonization temperature causes smaller micropores to collapse due to carbon-oxygen bond breaks, which would reduce the number of small micropores. The same trend is observable regarding the accessible surface area for electrolyte ions.

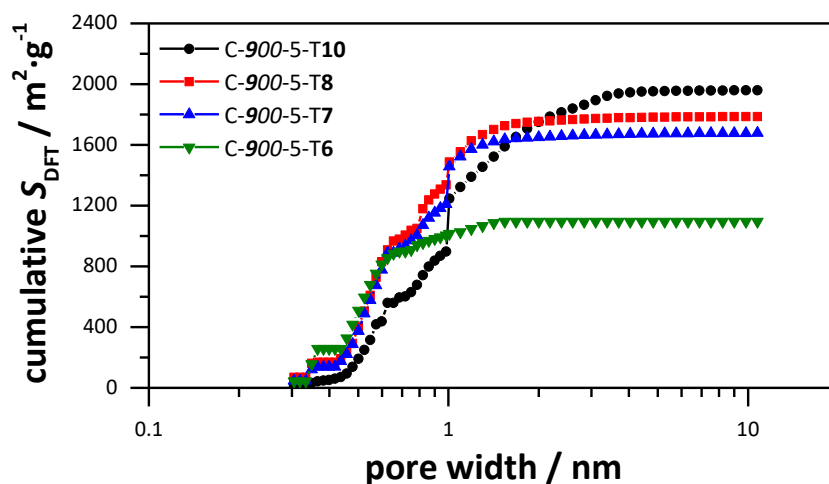


Figure 104: Combined cumulative surface area derived from carbon dioxide and nitrogen physisorption data of the carbon samples synthesized at different activation temperatures and a semi-carbonization temperature of 900 °C.

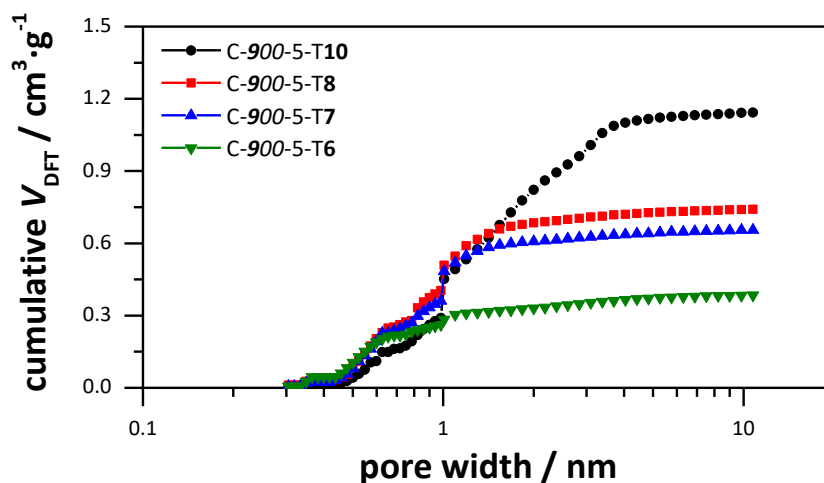


Figure 105: Combined cumulative pore volume derived from carbon dioxide and nitrogen physisorption data of carbon samples synthesized at different activation temperatures and a semi-carbonization temperature of 900 °C.

Table 13: Nitrogen physisorption derived data of the carbon samples synthesized at different activation temperatures and a semi-carbonization temperature of 900 °C.

Sample	$S_{\text{BET}} /$ $\text{m}^2 \cdot \text{g}^{-1}$	$S_{\text{DFT}} /$ $\text{m}^2 \cdot \text{g}^{-1}$	$V_{\text{t}} /$ $\text{cm}^3 \cdot \text{g}^{-1}$	$V_{\text{mic}} /$ $\text{cm}^3 \cdot \text{g}^{-1}$
C-900-5-T10	2169	1962	1.16	0.82
C-900-5-T8	1814	1786	0.75	0.69
C-900-5-T7	1620	1677	0.66	0.61
C-900-5-T6	892	1073	0.39	0.33

S_{DFT} (DFT surface area), V_{t} (total pore volume) and V_{mic} (micropore volume) obtained from QSDFT analysis. S_{BET} (BET surface area)

In general, the observations from section 4.1.4 could confirm the higher activation temperature enables additional etching processes and thus leads to carbons with larger pores, higher surface areas and higher pore volumes. At the same time a high semi-carbonization temperature limits these processes and leads to materials whose pore size and surface areas are comparatively small compared to materials synthesized at lower semi-carbonization temperatures.

4.1.6.2 Energy storage related properties of carbons synthesized at a semi-carbonization temperature of 900 °C and different activation temperatures

Electrochemical characterization

The results of the CV measurements are shown in Figure 106. Essentially, all CV curves show the expected rectangular shape, indicating capacitive double layer behavior. The curve of C-900-5-T10 shows no distortions even at very high scan rates of $2500 \text{ mV} \cdot \text{s}^{-1}$. The reason for this is the larger pore sizes up to 3.5 nm promote ion transport to and within the pores and minimize internal resistance. C-900-5-T8 and C-900-5-T7 show larger deviations of the CV curves, especially at the vertex of the potential change. This caused by diffusion resistance of the ions in the smaller pores and appears as deviations in the curve. A redox bump at 1.75 V is visible for C-900-5-T6, but only during the charging process, indicating a non-reversible faradaic charge transfer reaction. These are caused by electrolyte reactions on the electrode surface or on the current collector. The acetonitrile in particular can decompose at higher voltages via reaction with residual water.^[297–299] These side reactions almost always occur during EDLC charging processes and are often summarized under leakage current. These can only be detected in the CV of sample C-900-5-T6 because the capacitance of this sample is very small and therefore does not cover the leakage current.

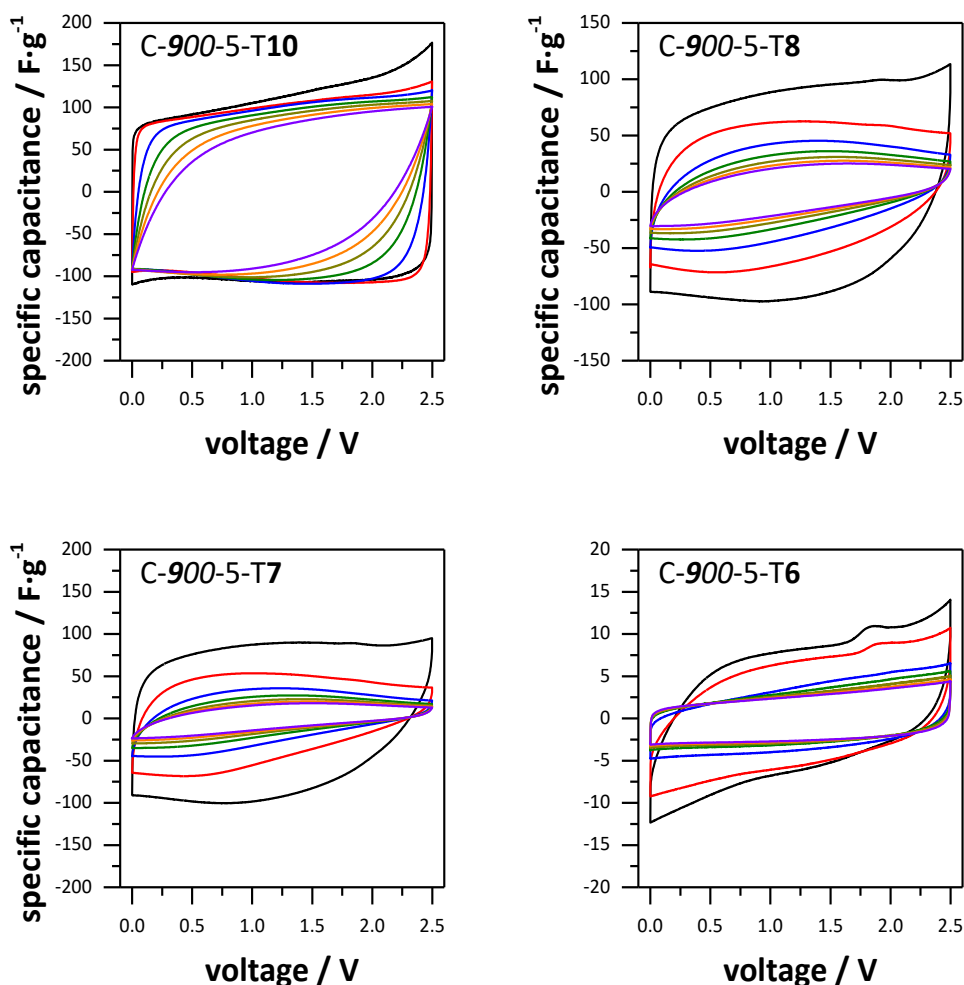


Figure 106: Cyclic voltammograms of the activated carbons synthesized at different activation temperatures and a semi-carbonization temperature of 900 °C at 10 $\text{mV}\cdot\text{s}^{-1}$ (black), 100 $\text{mV}\cdot\text{s}^{-1}$ (red), 500 $\text{mV}\cdot\text{s}^{-1}$ (blue), 1000 $\text{mV}\cdot\text{s}^{-1}$ (green), 1500 $\text{mV}\cdot\text{s}^{-1}$ (yellow), 2000 $\text{mV}\cdot\text{s}^{-1}$ (orange) and 2500 $\text{mV}\cdot\text{s}^{-1}$ (violet).

Results from charge discharge measurements are shown in Figure 107 and summarized in Table 14 with the electrolyte ion accessible surface area and pore volume. The discharge capacitance decreases with the activation temperature, which is consistent with the accessible surface area. C-900-5-T10 has the highest specific gravimetric capacitance and the gravimetric capacitance values of C-900-5-T8 and C-900-5-T7 are in a similar range, due to their similar accessible surface areas of C-900-5-T8 and C-900-5-T7. The specific surface area of C-900-5-T6 is very low due to its very small accessible surface area and narrow pores, which prohibit ion diffusion within the pores, even at low current densities. It can therefore be assumed the maximum capacitance of sample C-900-5-T6 is larger than $1.9 \text{ F}\cdot\text{g}^{-1}$, but not particularly high and not measurable due to the predominance of small pores under

1 nm in size. As expected, the capacitance retention of C-900-5-T10 is very good with 92.1 % due to its large micropores and additional mesopores up to 3.5 nm. This was expected, because the previous results showed pores with a size of 1.5 nm are sufficient to allow diffusion of the electrolyte ions, event at high currents. The capacitance retentions of C-900-5-T8 and C-900-5-T7 are significantly lower with less than 10 %, caused by the small pores smaller than 1.5 nm in size and the high content of pores smaller than 1 nm, which are not able to contribute the fast ion diffusion to and within the pores.

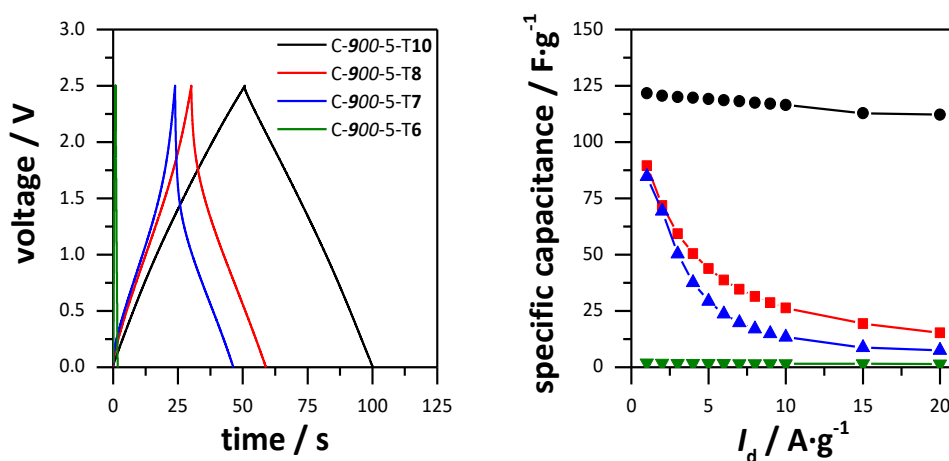


Figure 107: Discharge curve at 1 A·g⁻¹ for the carbon samples synthesized at different activation temperatures and a semi-carbonization temperature of 900 °C (left) and the specific capacitance as a function of discharge current density (right)

Table 14: Electrochemical properties of the EDLC prepared from activated carbons synthesized at different activation temperatures and a semi-carbonization temperature of 900 °C, in 1 M TEABF₄/ACN.

Sample	S_{acc} / $\text{m}^2 \cdot \text{g}^{-1}$	V_{acc} / $\text{cm}^3 \cdot \text{g}^{-1}$	C_{CV} / $\text{F} \cdot \text{g}^{-1}$	C_{DC} / $\text{F} \cdot \text{g}^{-1}$
C-900-5-T10	1403	1.01	102.6	121.7
C-900-5-T8	819	0.52	75.4	89.5
C-900-5-T7	789	0.43	71.8	84.8
C-900-5-T6	188	0.19	1.1	1.9

S_{acc} specific surface area for pores > 0.66 nm; V_{acc} pore volume for pores > 0.66 nm; C_{CV} calculated from 10 mV·s⁻¹; C_{DC} calculated from 1 A·g⁻¹.

The surface normalized capacitance values are shown in Figure 108 and are summarized in Table 15 including the values of sample C-900-5-T9. The capacitance values, normalized to the total DFT surface often show the slight tendency to increase with increasing activation temperature. This seems plausible, since the gravimetric capacitance of C-900-5-T10 is significantly larger than C-900-5-T8 with a difference of 30 F·g⁻¹. However, the surface capacitance values, normalized to the accessible surface area, reveal C-900-5-T10 has the lowest surface capacitance, compared to C-900-5-T9, C-900-5-T8 and C-900-5-T7, which have similar surface capacitance values. These observations are consistent with the previous results. Carbons with pores larger than 1.5 nm do not use the surface as effectively for energy storage as microporous carbons with a predominance of pores smaller than 1 nm. The same applies to the electrochemical use of the pore volume. The volumetric capacitance decreases with the activation temperature, as this leads to a reduction of the pores.

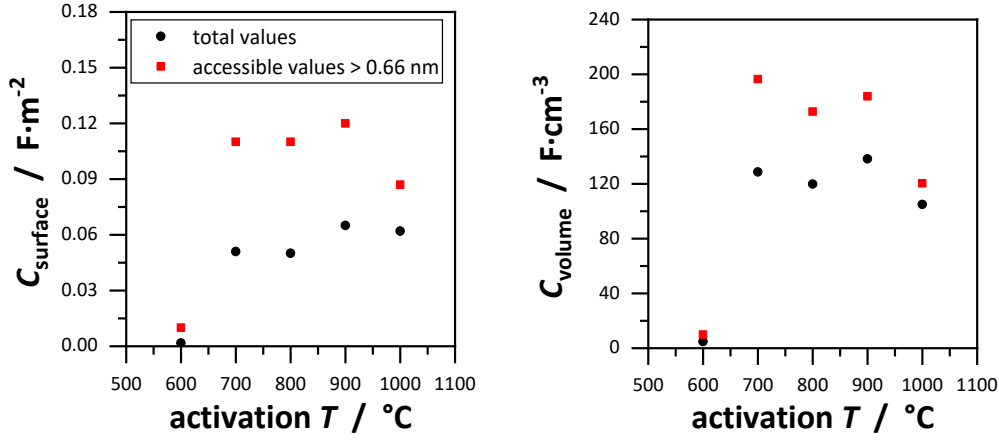


Figure 108: Surface area normalized capacitance (left) and the pore volume normalized capacitance (right) as a function of the activation temperature, including sample C-900-5-T9.

Table 15: Surface- and volumetric capacitance values for carbons synthesized at different activation temperatures and a semi-carbonization temperature of 900 °C.

Sample	$C_S /$ $\text{F} \cdot \text{m}^{-2}$	$C_{S>0.66} /$ $\text{F} \cdot \text{cm}^{-2}$	$C_V /$ $\text{F} \cdot \text{cm}^{-3}$	$C_{V>0.66} /$ $\text{F} \cdot \text{cm}^{-3}$
C-900-5-T10	0.062	0.087	104.9	120.3
C-900-5-T8	0.050	0.11	119.8	172.7
C-900-5-T7	0.051	0.11	128.6	196.4
C-900-5-T6	0.0017	0.010	4.7	9.9

C_S , $C_{S>0.66}$ calculated from C_{DC} and the respective surface areas, obtained from the DFT results; C_V , $C_{V>0.66}$ calculated from C_{DC} and the respective pore volumes.

Results from PEIS tests are shown in Figure 109. The Nyquist plots shows low resistance R_{ESR} values for all carbons and short semicircles caused by faradaic charge transfer reactions occurring at the electrode surface. Additionally, diffusion resistance of electrolyte ions entering the pores can cause ohmic resistances, as well as intrinsic resistances, caused by the R_{ESR} . The frequency response of the phase angle shows phase angles of -88.0 , -82.5 , -81.9 and -63.8° at 10 mHz for C-900-5-T10, C-900-5-T8, C-900-5-T7 and C-900-5-T6, respectively. Pore sizes up to 3.5 nm enable ion diffusion and resistance free double layer alignment of these at low frequencies, which is reflected by a phase angle close to -90° . The pore size distributions of samples C-900-5-T8 and C-900-5-T7 are very similar and show both materials are microporous, with pores smaller than 1.5 nm. Nevertheless, ions

can penetrate the pores and form double layers without resistance, which is confirmed by the phase angles. The pores of sample C-900-5-T6 are all smaller than 1 nm and most are even below 0.7 nm. This does not allow resistance-free diffusion of ions to and within the pores, even at low frequencies. However, it seems pore sizes above 0.7 nm allow a reasonably resistance-free formation of double layers. This means even pores accessible only to electrolyte ions with distorted or removed solvate shells contribute to the double layer capacitance without the contribution of larger resistances, at least at low frequencies and low currents.

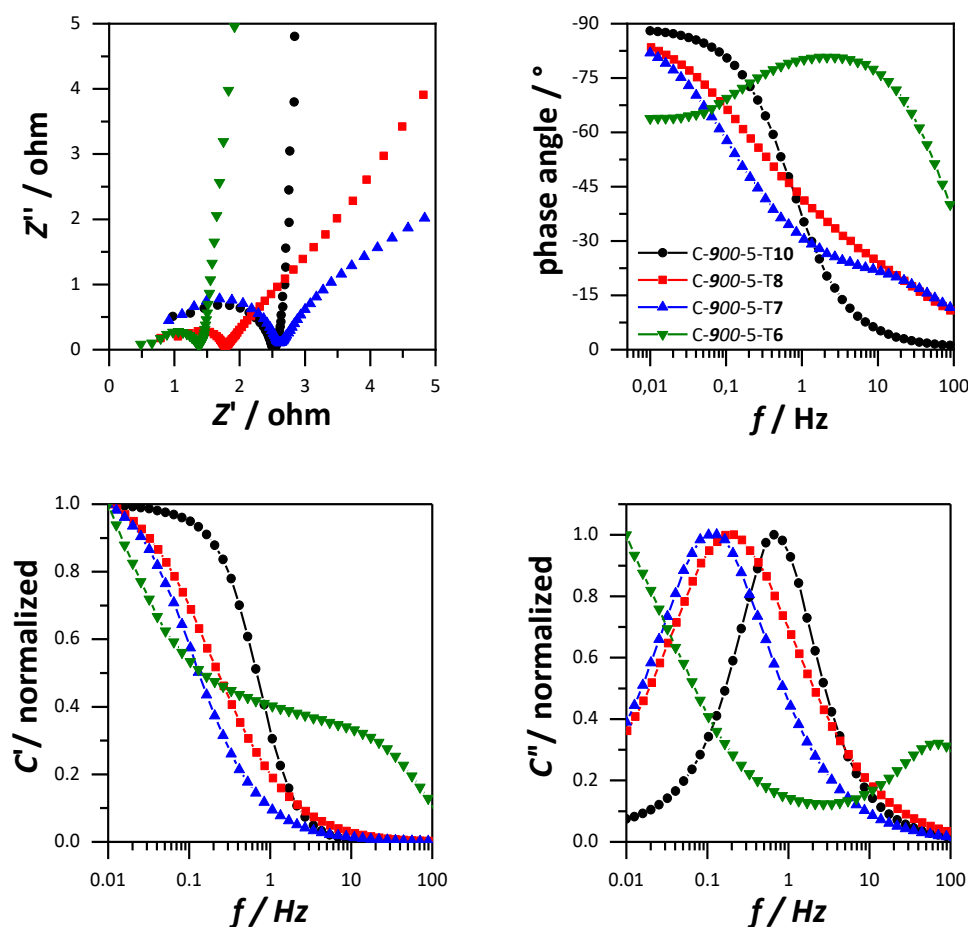


Figure 109: Nyquist plot of the activated carbons (top left), frequency response of the phase angle (top right), normalized real capacitance (bottom left) and normalized imaginary capacitance (bottom right).

The frequency response of the real capacitance shows the plateau at low frequency and an exponential decrease with higher frequencies, reflecting the capacitance loss caused by diffusion limitations of electrolyte ions in narrow pores. The peak frequency of the imaginary capacitance reflects the time relaxation constant which is

1.32, 4.58, 8.61 and > 100 s for C-900-5-T10, C-900-5-T8, C-900-5-T7 and C-900-5-T6, respectively. The influence of the pore sizes on the kinetics of electrochemistry can be clearly seen here again. The large micropores above 1.5 nm and mesopores up to 3.5 nm of sample C-900-5-T10 allow a loss-free charging and discharging process at high frequencies around 10 mHz, whereas for samples C-900-5-T8 and C-900-5-T7 this is only possible at significantly lower frequencies. The pores of sample C-900-5-T6, on the other hand, are too small to detect a loss of capacitance even at the lowest frequency. This can be explained by the fact a large amount of the pores are smaller than the desolvated TEA⁺ ion, which hinders diffusion even at low frequencies and currents.

In general, results from the previous chapters were confirmed, with the accessible surface area of the carbon samples being the dominating factor for the specific gravimetric capacitance. However, the utilization of the surface area and pore volume depends on the pore size, as both are being increased for samples with predominance or micropores under 1 nm. Regarding the kinetics, mass transport of ions is improved for the carbon sample, with pores larger than 1.5 nm, reflected by a good retention of capacitance at high currents and frequencies, as well as a low time relaxation constant. For samples with pore sizes up to 1.5 nm, the retention of capacitance is significantly lower, but the ion transport at low frequencies and currents is possible. However, a certain portion of pores must be larger than 0.7 nm, otherwise the maximum capacity cannot be reached.

Hydrogen storage

The gravimetric hydrogen uptake isotherms at 77 K of the carbons are shown in Figure 110, which are fully reversible and have not reached saturation. The uptake capacities up to 0.1 bar generally increase with the activation temperature from 1 wt% for sample C-900-5-T6 and 1.25 wt% for samples C-900-5-T7 and C-900-5-T8. This means, the carbons possess a higher amount of micropores especially below 1 nm, which lead to higher adsorption capacities. Sample C-900-5-T10, however, shows the lowest uptake capacity at 0.1 bar. Sample C-900-5-T10 shows a larger micropore content in general, but a lower content of pores, especially around 0.5 nm. Therefore, fewer pores which show the high adsorption potential of hydrogen, due to the overlap of opposing pore wall potentials. This also shows, that pores around 0.5 nm seem to show this effect more pronounced.

The gravimetric uptake capacities are 2.24, 2.44, 2.28 and 1.68 wt% for C-900-5-T10, C-900-5-T8, C-900-5-T7 and C-900-5-T6, respectively. Although the hydrogen uptake capacities increase with the activation temperature, no clear trend is recognizable, because the uptake capacity of C-900-5-T10 is lower than the capacity of C-900-5-T9. Generally, the increasing specific surface area is essential for the increasing uptake capacity. However, it can also be recognized here that the surface is not the only decisive factor. Figure 111 shows the uptake capacity and the specific surface area normalized uptake capacity in dependence of the activation temperature. It can be clearly seen, the use of the specific surface of the microporous sample C-900-5-T6 is significantly higher than that of material C-900-5-T10. This can only be attributed to the smaller pores, which have a higher adsorption potential and thus promote hydrogen adsorption of the carbon surface. Samples C-900-5-T7, C-900-5-T8 and C-900-5-T9 have similar uptakes per surface, as these also have very similar pore size distributions.

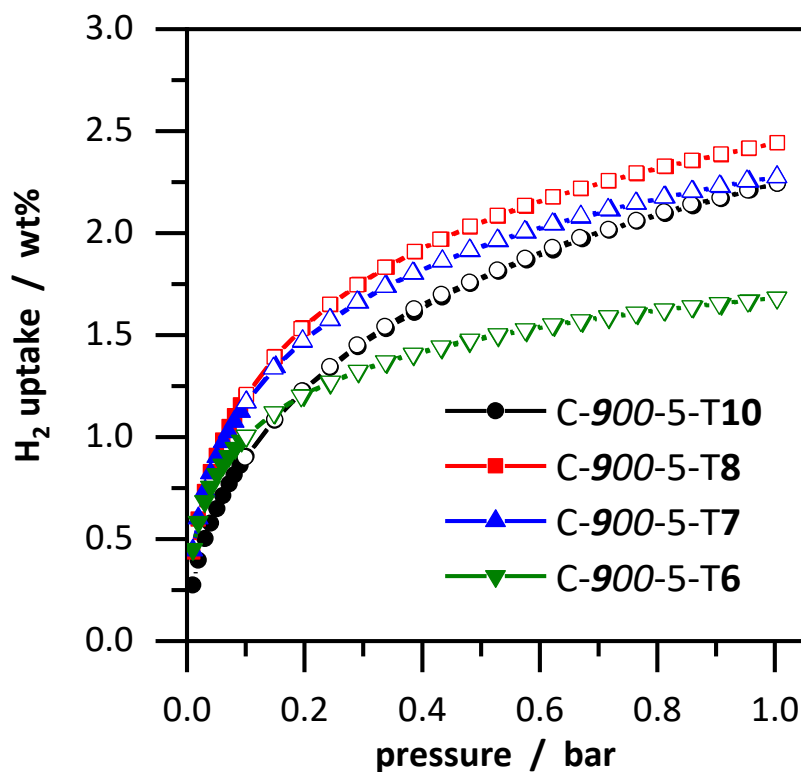


Figure 110: Gravimetric hydrogen storage capacity at 77 K of activated carbons synthesized at different activation temperatures and a semi-carbonization temperature of 900 °C and a KOH/carbon ratio of 5.

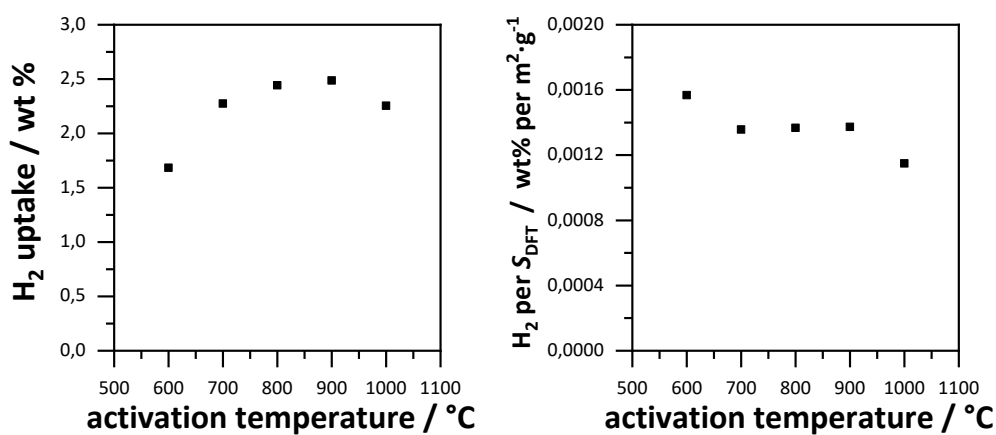


Figure 111: Gravimetric hydrogen uptake in dependence of the activation temperature, including data of the sample C-900-5-T9 (left) and the specific surface area normalized uptake capacity in dependence of the activation temperature (right). The KOH/carbon ratio was fixed at 5.

The results from section 4.1.4 were recognized in this section. A higher activation temperature causes a larger number of pores due to further side reactions during KOH activation, which leads to an increase in the specific surface area. At the same time, pores are also enlarged, leading to carbon materials with higher pore volumes. However, it has also become clear that due to the high semi-carbonization temperature, the effectiveness of KOH activation is limited, which can be seen in the low surfaces of maximum $1950 \text{ m}^2 \cdot \text{g}^{-1}$ and smaller pores in the carbons. With regard to electrochemical performance, it was confirmed in this section that pores smaller than 1.5 nm do not provide good retention of capacitance at high currents and frequencies. If the pores are mostly below 0.7 nm, which corresponds to the size of the naked TEA^+ ion, only low capacitances are detectable. However, it should be noted that samples C-900-5-T8 and C-900-5-T7 could reach their maximum capacitance at low frequencies and currents, although the pores had a maximum size of 1.5 nm. For both the electrical storage capacitance and the hydrogen uptake, microporous carbons showed a better usability of the carbon surface.

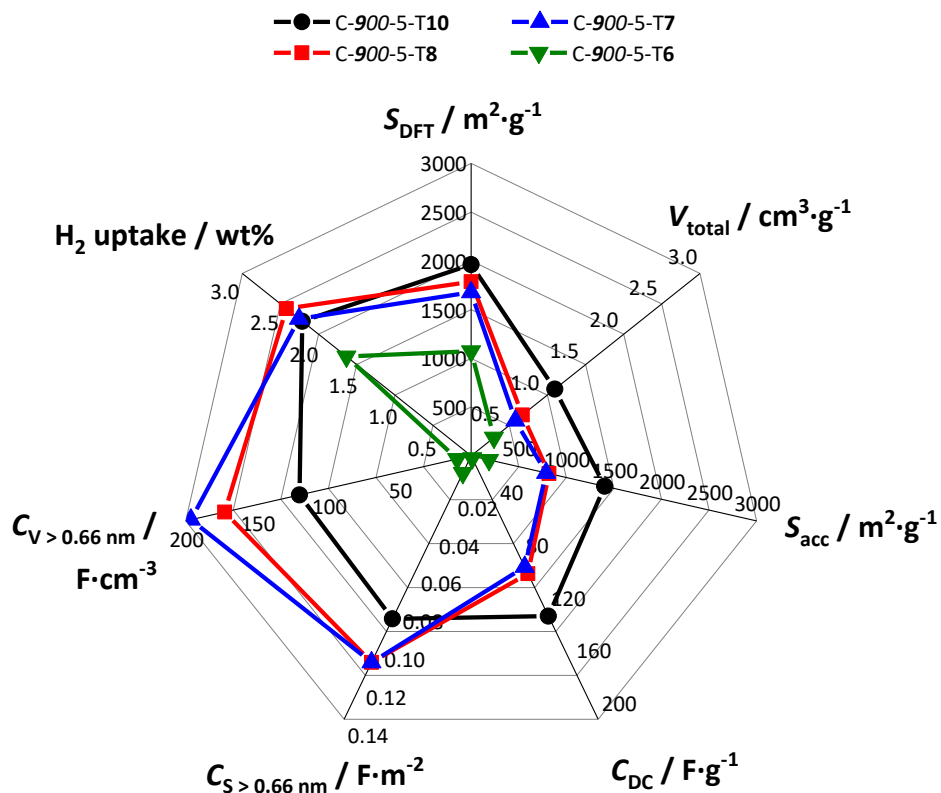


Figure 112: Graphical summary of the carbon sample properties synthesized at different activation temperatures and a semi-carbonization temperature of 900 °C, with a fixed KOH/carbon ratio of 5.

4.1.7 Influence of the carbon precursor

Since all reaction parameters and their effects on the structure and porosity of the carbons have now been investigated in detail, the influence of the precursor composition will be studied. For this purpose different ratios of phenol and resorcinol were used in polymer synthesis, and an additional pure resorcinol-formaldehyde resin was synthesized. The surface chemistry should be kept as similar as possible, which is the case with PF resins and RF resins. Phenol and resorcinol were used in the ratio 2/1, 1/1 and 1/2 and the samples are named C-PR-2/1, C-PR-1/1, C-PR-1/2 and C-RF. The ratio of formaldehyde and benzene alcohol remained the same. The synthesis scheme is shown in Figure 113 and shows the semi-carbonization temperature was 500 °C, the activation temperature 900 °C and the KOH/carbon ratio 5/1. This applies to all samples in this section.

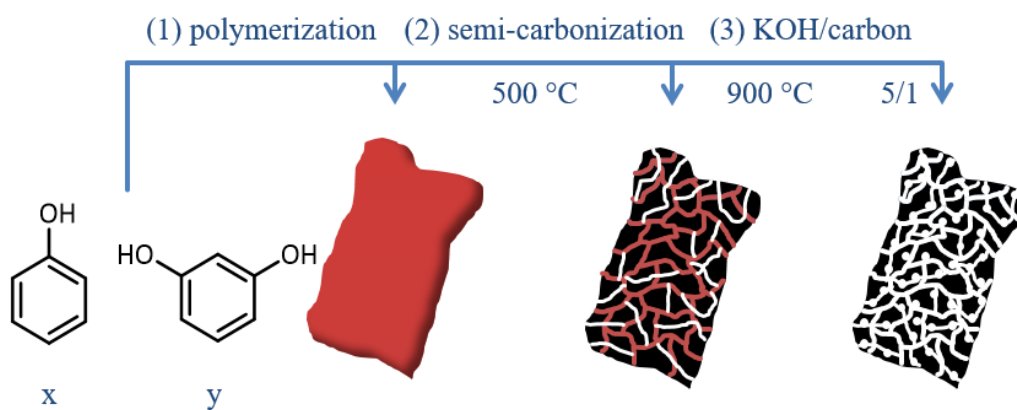


Figure 113: Synthesis scheme for the preparation of HSAC from formaldehyde resins with different ratios of phenol and resorcinol. (1) Polymerization of the formaldehyde resins under strong acidic conditions; (2), semi-carbonization of the formaldehyde resin at 500 °C under argon atmosphere; (3) chemical activation of the semi-carbonized carbons at 900 °C and a KOH/carbon ratio of 5 under nitrogen atmosphere.

4.1.7.1 Characterization of carbons synthesized from different formaldehyde resins

During the polymer synthesis it could be observed that with increasing resorcinol content the polymers became more swellable towards the solvent ethanol. This is a known phenomenon of resorcinol resins due to the higher number of hydroxyl groups and the higher degree of chain crosslinking.^[300] Images of the dry polymers are shown in Figure 114. Due to the high swellability of resorcinol resins, the material contracts during the drying process due to capillary forces.^[301] Therefore, the polymer no longer appears as a reddish brown powder, like the phenol-formaldehyde resin, but becomes darker and darker with increasing resorcinol content until the resorcinol resin appears as a hard black solid, as can be seen at sample C-**RF**. The contraction during drying can also affect the pore sizes. This is why it is assumed the phenol-resorcinol ratio influences the porosity of the obtained carbons.

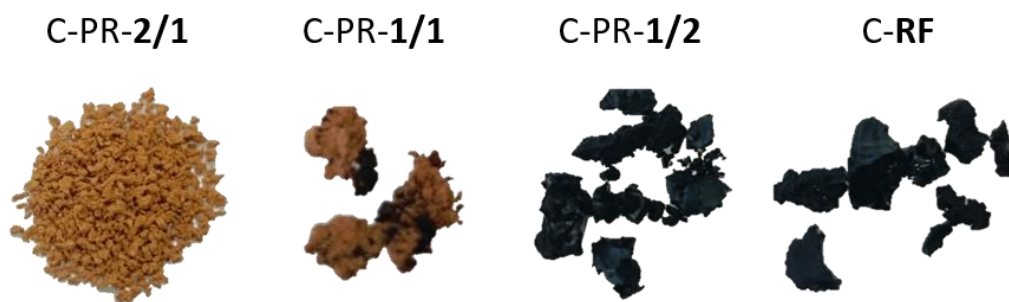


Figure 114: Images of the formaldehyde resins, polymerized with different ratios of phenol and resorcinol.

The macroscopic structure is investigated by SEM images of the carbons shown in Figure 115. The surface of sample C-PR-2/1 is smooth, in contrast to sample C-900-5-T9, which is based on a phenol-formaldehyde resin. There carbon surface is consisted of agglomerated spherical particles. Due to the higher proportion of oxygen functionalities on the carbon surface, increased carbon heteroatom bond cleavage occur during carbonization. This is why the surface structure is subjected to greater stress and the spherical particles are no longer visible. However, the cavities, which have a diameter of approx. 5 to 20 μm , are still visible. The surface of sample C-PR-1/1 is similar, except the cavities there have a much smaller diameter and are only a maximum of 10 μm in size. This trend continues from sample C-PR-1/2 with increasing resorcinol content in the precursor to sample C-RF, which is based on a pure resorcinol resin. For C-RF, only very small cavities in the range of 1 μm can be detected with a smooth surface structure. This is due to the increasing proportion of resorcinol in the precursor resin. The above-mentioned higher amount of hydroxyl groups increases the polarity of the polymer surface, and therefore increases the wettability of ethanol with the polymer surface. The ethanol accumulates in the cavities of the polymer and is removed during drying. This leads to a shrinkage process of the cavities, as the ethanol can only be removed if the adsorption forces on the surface and the capillary forces in the cavity spaces can be overcome. Eventually, a shrinkage of the cavities can be observed. This effect is more pronounced with a higher degree of ethanol wetting on the polymer surface.

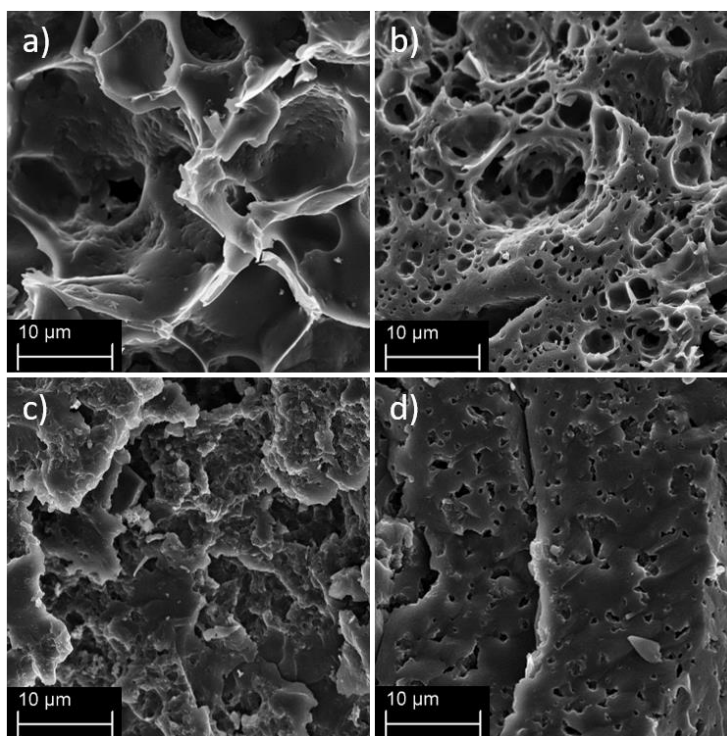


Figure 115: SEM images of (a) C-PR-2/1, (b) C-PR-1/1, (c) C-PR-1/2 and (d) C-RF.

P-XRD patterns of the activated carbons are shown in Figure A.14. For all samples the broad reflection at $44^\circ 2\theta$ is visible, but no reflection at $22^\circ 2\theta$ is visible. This shows the degree of graphitization of the samples must be very similar and it does not seem to depend on the precursor composition. The respective Raman spectra are shown in Figure A.15. The I_D/I_G ratios are 1.17, 1.09, 1.08 and 1.07 for C-PR-2/1, C-PR-1/1, C-PR-1/2 and C-RF, respectively. The ratios are in a very close range and only for sample C-PR-2/1 is a slightly higher ratio observable, indicating a slightly lower degree of graphitization. All in all, observations from Raman spectroscopy support the observations from the P-XRD patterns; the degree of graphitization seems mostly independent of the precursor composition. A different degree of graphitization could have been expected due to a possible stronger cross-linking of the polymer chains through the higher resorcinol content and through the more dense packing of these caused by contraction during the drying process. This is also indicated by the higher I_D/I_G ratio of sample C-PR-2/1. However, the degree of graphitization seems to be dominated by the semi-carbonization temperature and the activation conditions. This is not surprising since the graphitic arrangement of

carbon rings is a thermodynamically controlled process and therefore strongly temperature dependent. In addition, the activation conditions chosen for the carbons in this section have already been determined to be more structure-damaging, which can be deduced from section 4.1.2. These activation conditions therefore overcompensate a possible improved arrangement of graphite layers by a higher resorcinol content.

Results from thermogravimetry are shown in Figure 116. A complete combustion can also be detected for these carbon samples, meaning that all carbons are free of impurities. Interestingly, all the samples combust at the same temperature, around 500 °C, and all are also fully combusted around 650 °C. Furthermore, there are almost no differences in the combustion curve. Differences in combustion temperature are mainly caused by differences in porosity. This is a first indication that not only the degree of graphitization, but possibly also the porosity is independent of the precursor.

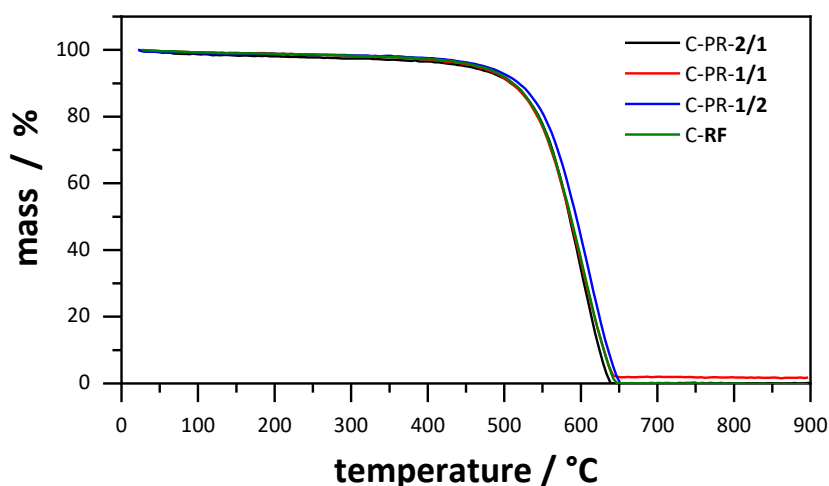


Figure 116: Results of the thermogravimetry of the activated carbons with different ratios of phenol and resorcinol for the resin precursor polymerization. The samples were heated to 900 °C in air steam with a flow rate of 50 mL·min⁻¹.

Nitrogen adsorption-desorption isotherms of the carbon samples are displayed in Figure 117 and the corresponding pore size distributions, calculated by the QSDFT method are shown in Figure 118. Noticeably that all four samples show an almost identical course of the isotherms and similar adsorption volumes. This is a clear indication the pore size distributions of the materials should also be identical. With

regard to the course of the isotherm, a slope in the relative pressure range from 0.1 to 0.4 can be observed, with a slightly pronounced hysteresis at higher relative pressures. This is an indication of microporous carbons, with additional mesopores. This is confirmed by the calculated pore size distribution. In addition to pores smaller than 1 nm, a further broad pore maximum at approx. 1.6 nm is visible. In addition, the materials have pores up to 4.0 nm, thus small mesopores. Furthermore, it is clear the pore size distributions of the four carbon samples are almost identical. This confirms the assumption the porosity, at least for pores above 1 nm, does not seem to depend on the polymer composition. This is a rather surprising conclusion. Since the affinity of the polymers to the solvent ethanol increased significantly with increasing resorcinol content, a noticeable shrinkage of the materials and their large cavities could also be observed after drying due to capillary effects. Accordingly, it could be assumed the small nanopores which are detectible with nitrogen physisorption could also be smaller on average. It seems, however, the porosity is generated exclusively by carbonization and activation and the formaldehyde resin composition has no influence. The reason for this is likely the non-porous character of the polymer resins. Although these have a certain macroscopic structure, as could be seen on the SEM images, there is no porosity in the range of micro- and mesopores. Therefore, the resorcinol content does not seem to influence the porosity. However, it could also have been assumed that a higher oxygen content, due to the greater number of hydroxyl groups in the polymer, could lead to an increase in porosity. In the carbonization process, heteroatoms are removed from the carbon network and leave voids or pores. This has also not been observed thus far. A detailed investigation of the micropores could lead to further findings.

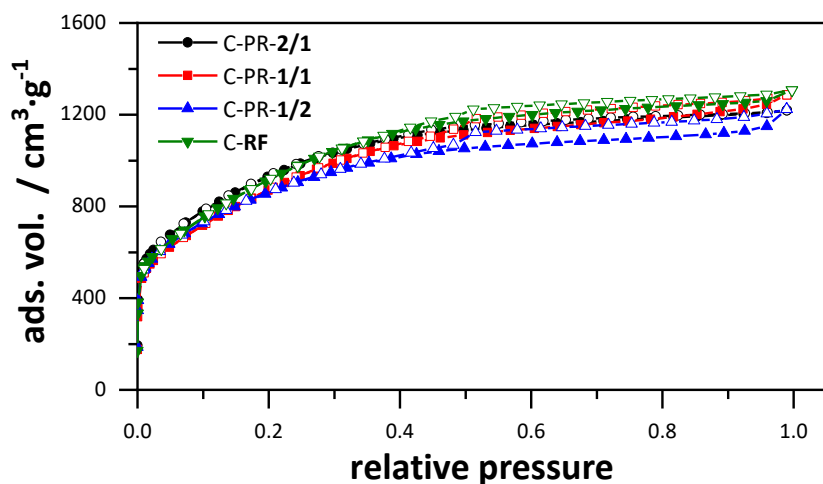


Figure 117: Nitrogen adsorption-desorption isotherms (77 K) of the carbon materials with different phenol/resorcinol ratios at the precursor polymerization.

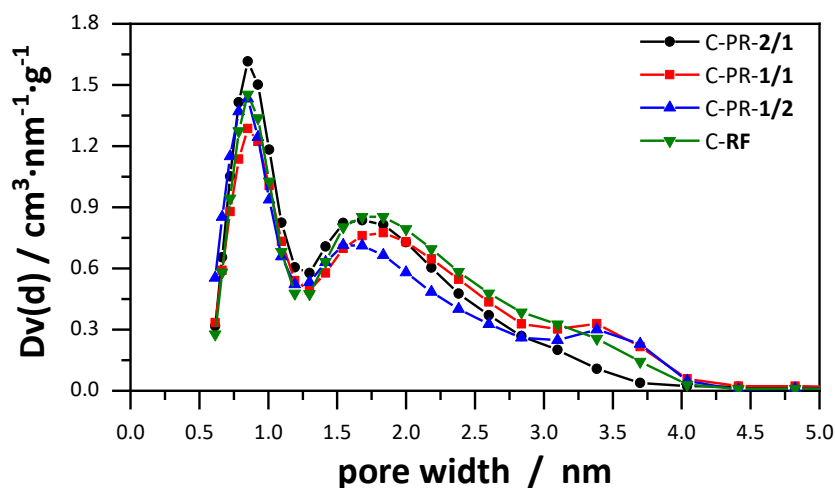


Figure 118: Pore size distributions of the carbon materials with different phenol/resorcinol ratios at the precursor polymerization, calculated by the QSDFT method from nitrogen desorption branch assuming slit pores.

Resulting data, derived from nitrogen physisorption measurements are summarized in Table 16. Unsurprisingly, the specific surface areas of all four carbon samples are similar with differences of only $150 \text{ m}^2 \cdot \text{g}^{-1}$. That is rather insignificant, considering the high surface areas larger than $2400 \text{ m}^2 \cdot \text{g}^{-1}$. The large surface areas originate from the low semi-carbonization temperature, which increases the effectiveness of the KOH activation, as extensively discussed in section 4.1.3. Additionally,

the large KOH/carbon ratio of 5 and the high activation temperature of 900 °C enhance pore generation and pore enlargement, resulting in high surface area porous carbons. The total pore volume and the micropores volume of the carbon materials are very similar as well, with differences of $0.13 \text{ cm}^3 \cdot \text{g}^{-1}$ and $0.16 \text{ cm}^3 \cdot \text{g}^{-1}$ among the samples, respectively. All in all, the porous derived data are nearly identical and very similar to C-500-5-T9, emphasizing the fact, that the porosity seems independent of the polymer precursor composition and is dominated by the semi-carbonization and activation conditions.

Table 16: Nitrogen physisorption derived data of the carbon samples with different phenol/resorcinol ratios at the precursor polymerization.

Sample	$S_{\text{BET}} /$ $\text{m}^2 \cdot \text{g}^{-1}$	$S_{\text{DFT}} /$ $\text{m}^2 \cdot \text{g}^{-1}$	$V_{\text{t}} /$ $\text{cm}^3 \cdot \text{g}^{-1}$	$V_{\text{mic}} /$ $\text{cm}^3 \cdot \text{g}^{-1}$
C-PR-2/1	3396	2574	1.75	1.26
C-PR-1/1	3208	2421	1.85	1.10
C-PR-1/2	3121	2477	1.75	1.13
C-RF	3387	2517	1.87	1.17

S_{DFT} (DFT surface area), V_{t} (total pore volume) and V_{mic} (micropore volume) obtained from QSDFT analysis. S_{BET} (BET surface area).

The influence of the polymer composition had no significant influence on the pore size distribution for pores above 1 nm, nor on the specific surface area and pore volume. CO₂ physisorption measurements provide information about the pores below 1 nm and the isotherms are shown in Figure 119, the calculated pore size distribution in Figure 120. As with nitrogen physisorption, the isothermal curve and adsorbed volumes of the CO₂ physisorption are almost identical for all four samples. The progression is quasi-linear, which should lead to an even pore size distribution. This was calculated according to the NLDFT method and is the same for all carbon materials. Pores below 0.6 nm can be detected and further pores at approx. 0.8 nm. Thus, even for micropores below 1 nm, no dependence of the polymer composition can be detected.

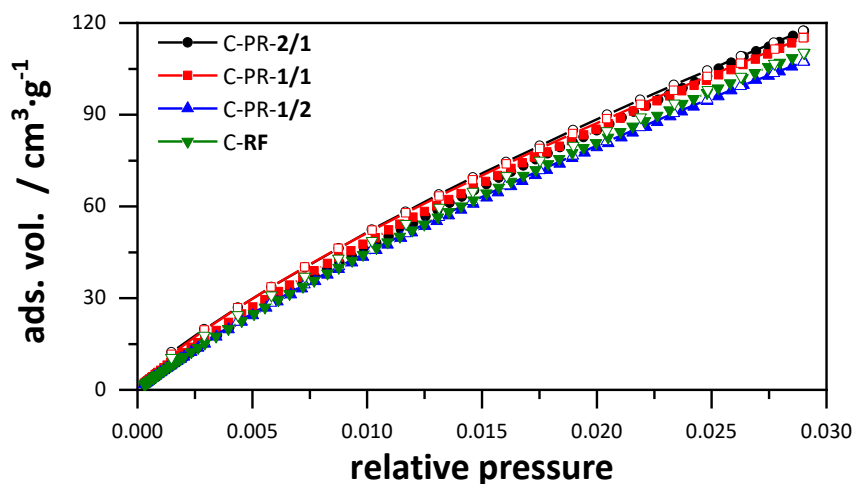


Figure 119: Carbon dioxide adsorption-desorption isotherms (273 K) of the carbon materials with different phenol/resorcinol ratios at the precursor polymerization.

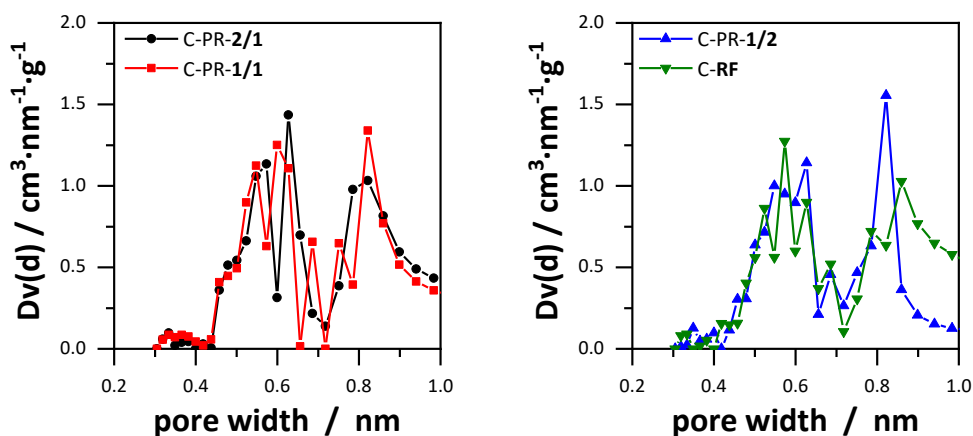


Figure 120: Pore size distributions of the carbon materials with different phenol/resorcinol ratios the precursor polymerization, calculated by the NLDFT method from carbon dioxide desorption branch assuming slit pores.

The combined cumulative surface area and pore volume for the carbon samples are shown in Figure 121 and Figure 122. Since the isotherms of nitrogen and carbon dioxide physisorption are almost identical for all carbons, the cumulative surface is also identical. Regarding the surface area, which is generated by pores up to 0.7 nm, the materials all have the same surface area. These pores are of particular interest for the double layer capacitance. Since the pore size distributions of the materials are identical, the curve of the cumulative pore volume is correspondingly similar.

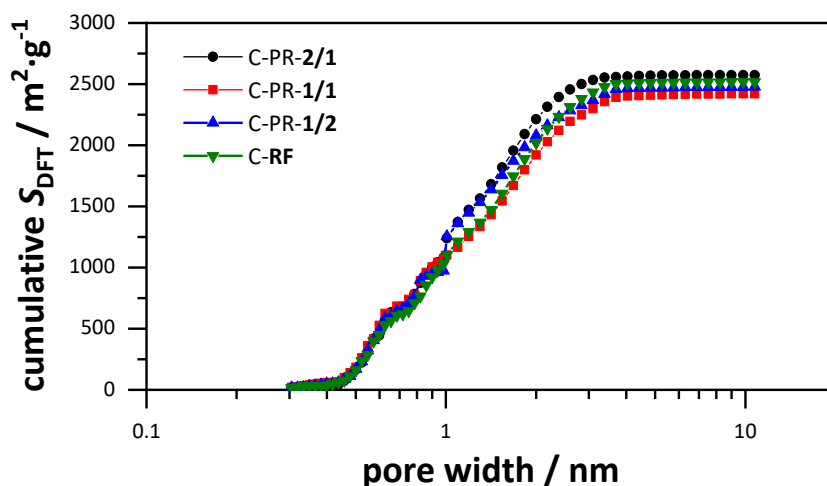


Figure 121: Combined cumulative surface area derived from carbon dioxide and nitrogen physisorption data of the carbon samples with different phenol/resorcinol ratios at the precursor polymerization.

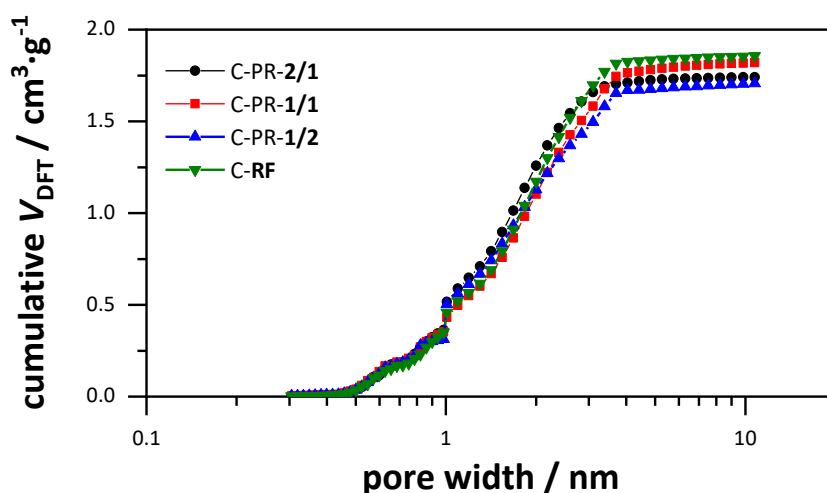


Figure 122: Combined cumulative pore volume derived from carbon dioxide and nitrogen physisorption data of the carbon samples with different phenol/resorcinol ratios at the precursor polymerization.

In this section the influence of the polymer composition, namely the resorcinol content, on the porosity of the carbon materials was investigated. It could be determined a higher resorcinol content, up to the pure resorcinol/formaldehyde resin, changes the macroscopic structure but has no influence on the porosity measured by gas physisorption. The porosity of the resulting carbons is independent of the precursor composition due to the non-porous character of the formaldehyde resins. This also

means porosity is determined exclusively by the carbonization and activation conditions. A possible influence of the oxygen functionalities can also be excluded. Pore size distribution and surface areas were almost identical to sample C-500-5-T9, which confirms the synthesis as reproducible, as well as the influence of semi-carbonization temperature and activation conditions.

4.1.7.2 Energy storage related properties of carbons synthesized from different formaldehyde resins

Electrochemical characterization

CV curves of the carbon samples, synthesized with different carbon precursors are shown in Figure 123. The curves of samples C-PR-2/1, C-PR-1/1, C-PR-1/2 and C-**RF** are almost identical and show a typical rectangular shape, indicating purely and well developed capacitive behavior. Additionally, the curves are barely distorted at $10 \text{ mV} \cdot \text{s}^{-1}$, even when the scan rates are increased. The reason for this is the presence of large micropores, which are larger than the solvated electrolyte ions, and mesopores up to 4.0 nm, which enable good electrolyte ion diffusion to and within the pores, even at higher scan rates. This keeps the effective resistance low even at higher currents. Since the porosity of the carbon materials C-PR-2/1, C-PR-1/1, C-PR-1/2 and C-**RF** is very similar, which is reflected in the same pore size distributions, specific surface areas and pore volumes, the CV curves show an almost identical profile. For all four carbon samples the CV curves show a current increase at the potential maxima. The current increase at the potential reversal points disappears at higher scan rates, which indicates a diffusion-controlled Faraday charge transfer. This is probably caused by the oxidation of the acetonitrile and the current collector. This is a well-known phenomenon, where aluminum is dissolved anodically in the electrolyte, with the accumulation of corrosion products on its surface.^[297,298] After a certain time, however, a passivation layer forms, so the observed current increase is probably not specific to the material.

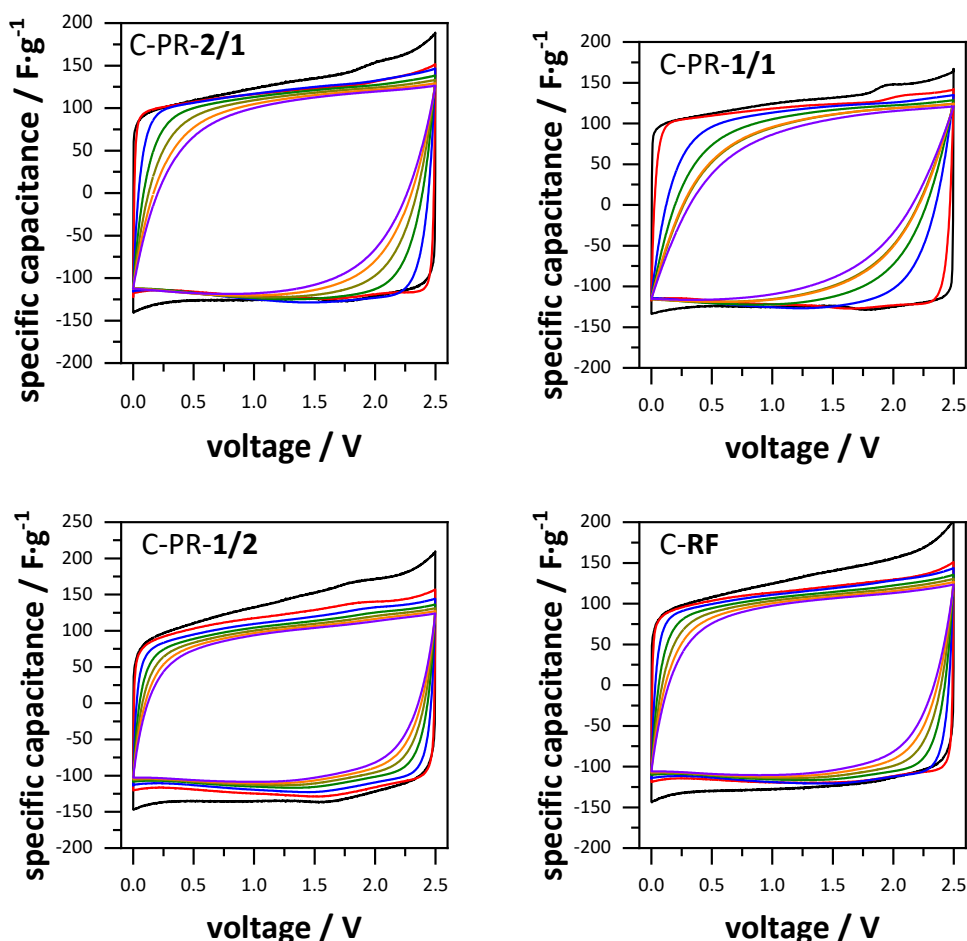


Figure 123: Cyclic voltammograms of the activated carbons synthesized with different phenol/resorcinol ratios at the precursor polymerization at $10 \text{ mV} \cdot \text{s}^{-1}$ (black), $100 \text{ mV} \cdot \text{s}^{-1}$ (red), $500 \text{ mV} \cdot \text{s}^{-1}$ (blue), $1000 \text{ mV} \cdot \text{s}^{-1}$ (green), $1500 \text{ mV} \cdot \text{s}^{-1}$ (dark yellow), $2000 \text{ mV} \cdot \text{s}^{-1}$ (orange) and $2500 \text{ mV} \cdot \text{s}^{-1}$ (violet).

Results from the galvanostatic discharge tests are shown in Figure 124 and the calculated capacitance values are summarized in Table 17. The discharge curves have a triangular shape, indicating a stable and reversible double layer charge storage behavior. Samples C-PR-2/1, C-PR-1/2 and C-RF also show very high specific capacitance values as electrode materials in EDLCs. The values are also relatively close for all three materials with capacitance values between 144 and $154 \text{ F} \cdot \text{g}^{-1}$. The main reason for this are the high accessible surface areas, which are about $1900 \text{ m}^2 \cdot \text{g}^{-1}$ for the materials and allow a high accumulation of electrolyte ions at the carbon surface. These samples also show correspondingly similar maximum capacitance values, because both the pore size and accessible surface area are ap-

proximately the same. Only the device that has sample C-PR-1/1 as electrode material, has a slightly lower maximum specific capacitance with $129.2 \text{ F}\cdot\text{g}^{-1}$. Capacity-reduced leakage currents caused by Faraday's side reaction can be excluded, since the galvanostatic discharge curves at $1 \text{ A}\cdot\text{g}^{-1}$ show no distortions, as is the case with the CV curves at the lowest scan rates. The only other noticeable feature is the slightly smaller accessible surface area of approx. $1800 \text{ m}^2\cdot\text{g}^{-1}$, which can lead to a reduction in capacitance. However, the difference of the accessible surface area of sample C-PR-1/1 compared to the other three samples is very small. The surface area, generated by pores up to 0.7 nm , which may lead to a higher capacitance, is similar for all four carbon samples. Only the surface area, provided by pores in the range of 1 to 2 nm is lower, compared to the other three carbon samples. It is possible, that the pores in this particular range, provide a differentiated capacitance, which ultimately results in a lower overall capacitance. This context will be further evaluated in section 4.2. The retention of the capacitance of all 4 discussed carbon samples is very good. All materials have large micropores above 1.5 nm and small mesopores up to 4 nm which allow ion transport in and to the pores even at high currents. This is consistent with the observations made in the previous sections.

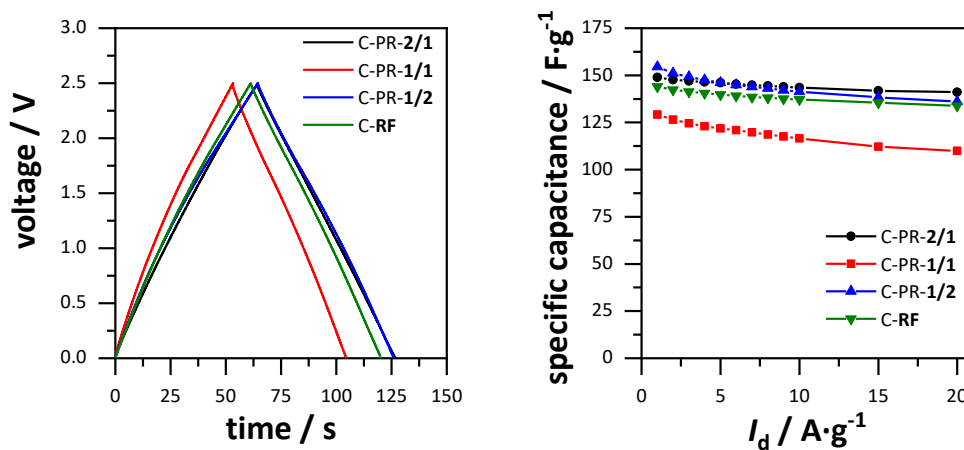


Figure 124: Discharge curve at $1 \text{ A}\cdot\text{g}^{-1}$ for the carbon samples with different phenol/resorcinol ratios at the precursor polymerization (left) and the specific capacitance as a function of discharge current density (right).

Table 17: Electrochemical properties of the EDLC prepared from activated carbons with different phenol/resorcinol ratios at the precursor polymerization, in 1 M TEABF₄/ACN.

Sample	$S_{\text{acc}} /$ $\text{m}^2 \cdot \text{g}^{-1}$	$V_{\text{acc}} /$ $\text{cm}^3 \cdot \text{g}^{-1}$	$C_{\text{CV}} /$ $\text{F} \cdot \text{g}^{-1}$	$C_{\text{DC}} /$ $\text{F} \cdot \text{g}^{-1}$
C-PR-2/1	1941	1.60	122.1	148.9
C-PR-1/1	1798	1.68	94.6	129.2
C-PR-1/2	1879	1.59	129.0	154.4
C-RF	1955	1.72	121.6	144.0

S_{acc} specific surface area for pores > 0.66 nm; V_{acc} pore volume for pores > 0.66 nm; C_{CV} calculated from $10 \text{ mV} \cdot \text{s}^{-1}$; C_{DC} calculated from $1 \text{ A} \cdot \text{g}^{-1}$.

The surface normalized capacitances are summarized in Table 18 and shown in Figure 125. In contrast to the gravimetric capacitance values, the surface normalized capacitance values for all four samples are in a similar range. This is also the case for the capacitances normalized according to the accessible surface. Accordingly, no dependence of the surface usability of the electrolyte ions on the resorcinol content in the polymer can be observed. The same applies to the volumetric capacitance values, even if the values of sample C-PR-1/1 are slightly lower.

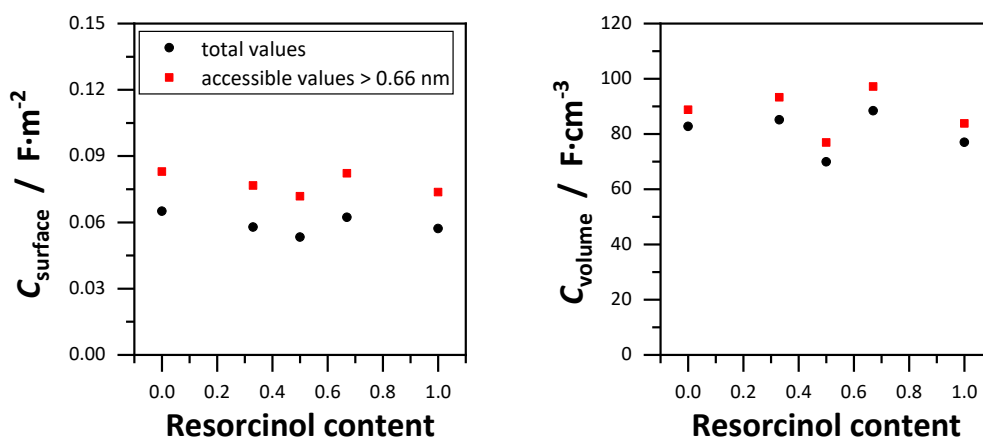


Figure 125: Surface area normalized capacitance (left) and pore volume normalized capacitance as a function of the resorcinol content used for the formaldehyde resins.

Table 18: Surface- and volumetric capacitance values for carbons synthesized from different polymer precursors with different phenol/resorcinol ratios at the precursor polymerization.

Sample	$C_S /$ $F \cdot m^{-2}$	$C_{S>0.66} /$ $F \cdot cm^{-2}$	$C_V /$ $F \cdot cm^{-3}$	$C_{V>0.66} /$ $F \cdot cm^{-3}$
C-PR-2/1	0.058	0.077	85.1	93.3
C-PR-1/1	0.053	0.072	69.9	76.9
C-PR-1/2	0.062	0.082	88.4	97.2
C-RF	0.057	0.074	77.0	83.8

C_S , $C_{S>0.66}$ calculated from C_{DC} and the respective surface areas, obtained from the DFT results; C_V , $C_{V>0.66}$ calculated from C_{DC} and the respective pore volumes.

Results from the PEIS are shown in Figure 126. The Nyquist plot reveals equally low R_{ESR} for all four carbon materials as well as short semicircles and short Warburg segments, indicating well-developed double layer formation leading to capacitive charge storage mechanisms for all prepared EDLCs using the carbon samples as electrode materials. The progression of the Nyquist plots is almost identical for all four samples, as the materials have a very similar porosity with respect to surface area and pore sizes. Accordingly, the frequency-dependent phase angle, real capacitance and imaginary capacitance are very similar for all four carbons. The phase angles are very low between -85.3 to -87.5° showing a good electrolyte ion diffusion at low frequencies, thus enabling the resistance free double layer capacitive charge storage. The mesopores up to 4 nm are certainly responsible for the good diffusion behavior. However, it has already been observed in the previous sections that micropores are sufficient for such a good diffusion behavior. Both are present for the four carbon materials. The real capacitance shows a typical frequency dependent curve. Up to approx. 1 mHz a plateau is present until the capacitance decreases exponentially due to the limited diffusion behavior of the electrolyte ions. The time constant was determined from the peak of the frequency response of the imaginary capacitance and is 0.25, 0.32, 0.37, 0.49 s for C-PR-2/1, C-PR-1/1, C-PR-1/2 and C-RF respectively. Not only, are the values all in a similar range, but also reveal very rapid ion diffusion within the pore network, event at high frequencies. This can be clearly attributed to the large micropores above 1.5 nm and the mesopores up to 4 nm.

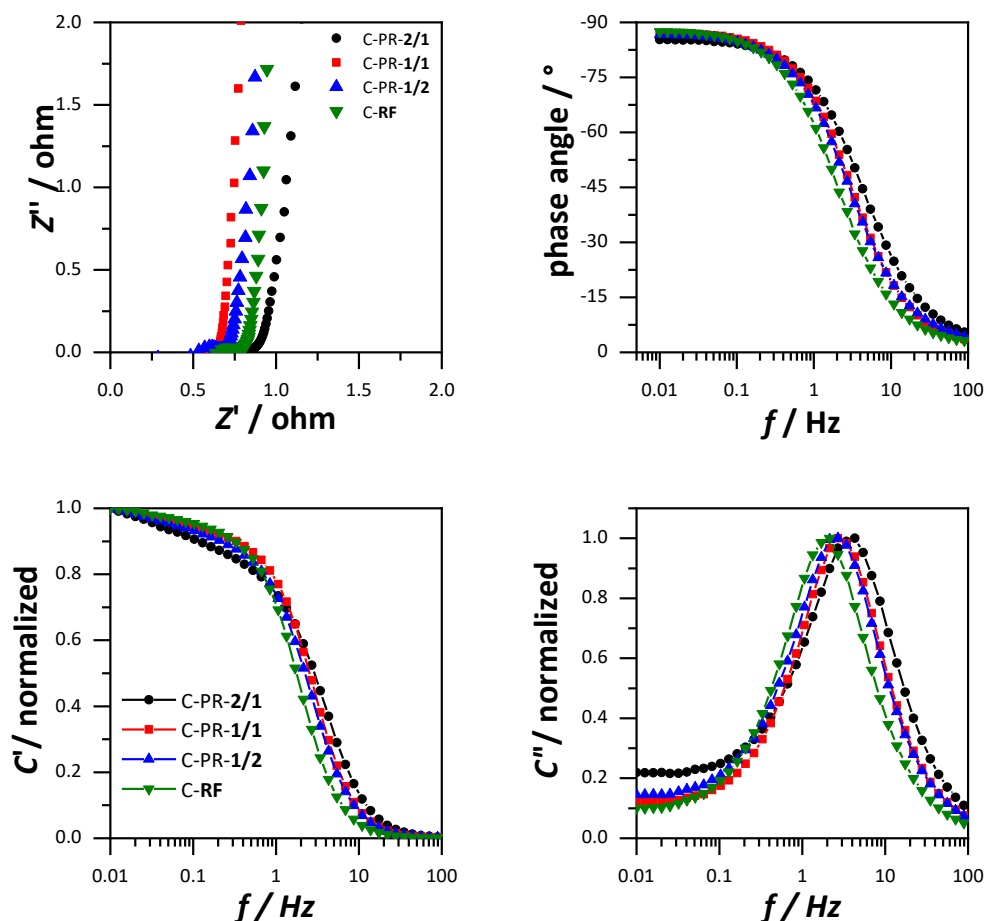


Figure 126: Nyquist plot of the activated carbons (top left), frequency response of the phase angle (top right), normalized real capacitance (bottom left) and normalized imaginary capacitance (bottom right).

Basically, the electrochemical characterization of the carbons, which were based on polymers with different resorcinol contents, showed the performance as EDLC materials is similar. This is due to the similar pore sizes, resulting in similar accessible surface areas. The diffusion behavior at higher currents is especially good for all four samples, as observed by the PEIS. The only exception was sample C-PR-1/1, since the capacitance was slightly lower compared to the other materials. The reason for this could be the lower accessible surface area for the electrolyte ions, although the surface area of sample C-PR-1/1 is only slightly smaller.

Hydrogen storage

Gravimetric hydrogen uptake isotherms at 77 K of the carbon samples are shown in Figure 127. As expected, the isotherms have the same course and are fully reversible and have not reached saturation due to the low uptake pressure. Previous sections have shown, the specific surface area, and supposedly, pores just below 1 nm are the key factors for a high hydrogen uptake capacity at 1 bar. Since all samples possess nearly the same surface area and have very similar pore size distributions, the uptake isotherms are identical and the capacities are between 2.70 and 2.76 wt% including sample C-500-5-T9. The uptake capacities are high and independent of the resorcinol content, which is expected, considering the porosity of the carbon samples.

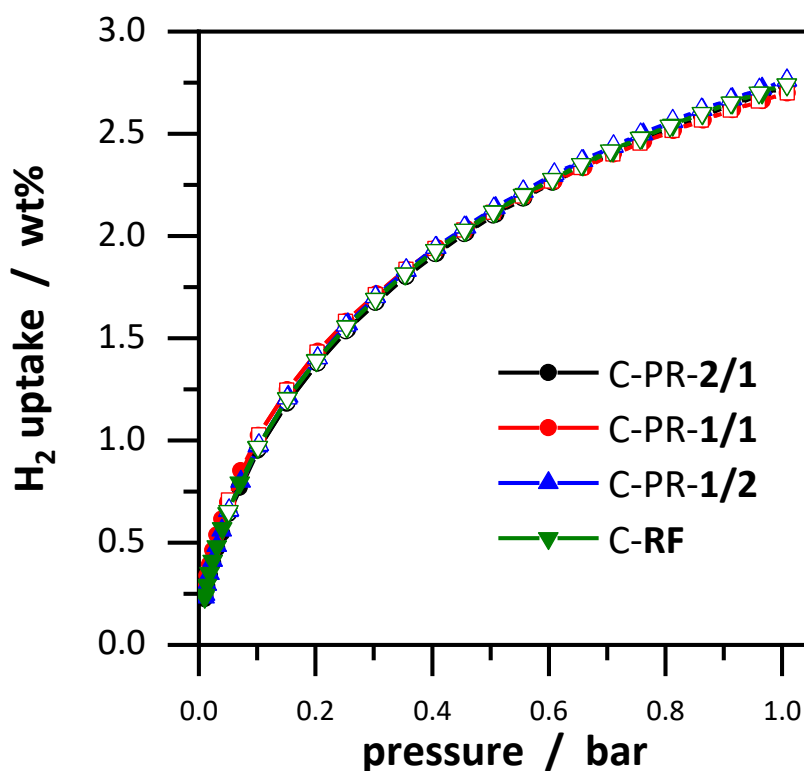


Figure 127: Gravimetric hydrogen storage capacity at 77 K of activated carbons, synthesized from different formaldehyde polymer precursors with different phenol/resorcinol ratios.

In this section the influence of the formaldehyde resin composition on the porosity of the carbons based on this resin is investigated and a graphical summary is shown

in Figure 128. It has been shown the porosity is independent of the phenol/resorcinol ratio used in polymer synthesis. The carbon samples have almost identical specific surfaces, pore sizes and pore volumes, suggesting the porosity of the formaldehyde resins is determined solely by the carbonization and activation conditions. Accordingly, the electrochemical properties and the gravimetric hydrogen uptake capacity were almost identical.

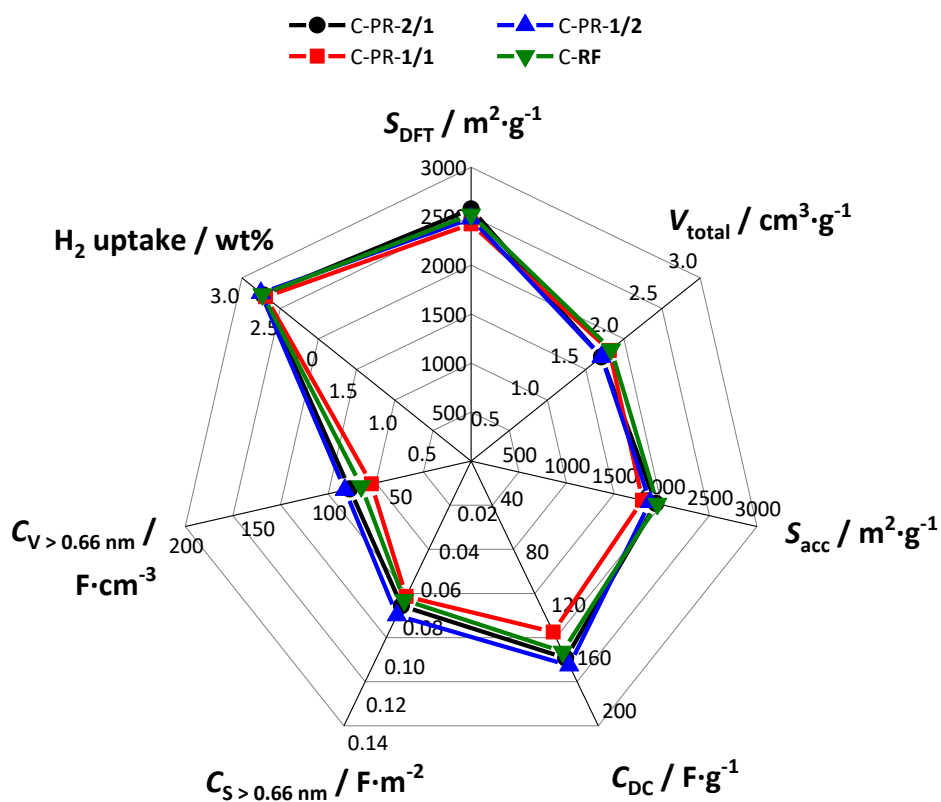


Figure 128: Graphical summary of the samples properties, synthesized from formaldehyde resins with different phenol/resorcinol ratios.

4.1.8 Cross-linking of formaldehyde resins via Friedel-Crafts alkylation

In the last section the composition of the formaldehyde resin was observed to have no further influence on the porosity of the subsequent carbons. In order to further investigate this point, a formaldehyde resin with different phenol/resorcinol ratios was synthesized again. This time, however, the polymerization time has been kept shorter so that only a few polymer chains can form. These were now further cross-linked by means of AlCl_3 and CCl_4 using Friedel-Crafts (FC) alkylation, whereby

the polymer structure was changed. Similar to section 4.1.7 phenol/resorcinol ratios of 2/1, 1/1 and 1/2 were chosen, as well as pure phenol and resorcinol formaldehyde resins respectively. The samples are named FC-**PF**, FC-PR-**2/1**, FC-PR-**1/1**, FC-PR-**1/2** and FC-**RF**. The ratio of formaldehyde and benzene alcohol remained the same. The synthesis scheme is shown in Figure 129 and shows the semi-carbonization temperature was 500 °C, the activation temperature 900 °C and the KOH/carbon ratio 5/1. This applies to all samples in this section.

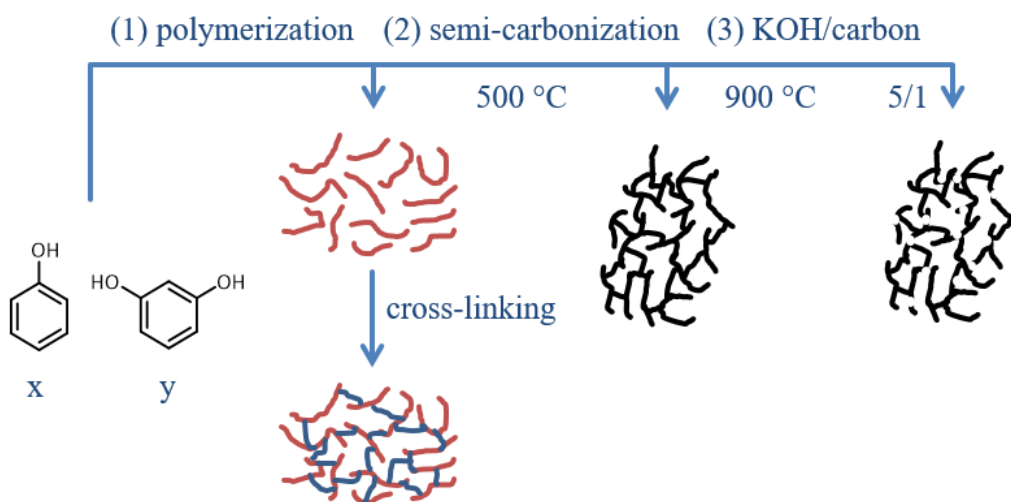


Figure 129: Synthesis scheme for the preparation of HSAC from FC cross-linked formaldehyde resins. (1) Polymerization of the formaldehyde resin chains under strong acidic conditions with different phenol/resorcinol ratios, followed by the FC cross-linking with CCl_4 ; (2) semi-carbonization of the cross-linked formaldehyde resin at 500 °C under argon atmosphere; (3) chemical activation of the semi-carbonized carbons at 900 °C and a KOH/carbon ratio of 5 under nitrogen atmosphere.

4.1.8.1 Characterization of carbons synthesized from FC cross-linked formaldehyde resins

SEM images of the carbons samples, prepared from FC cross-linked formaldehyde polymers with different phenol/resorcinol ratios are shown in Figure 130. In general, all five carbon samples have a similar macroscopic surface structure except for sample FC-**RF**. Sample FC-**PF**, for example, shows a rather rough particle surface with cavities in the particle having a diameter of 1-10 μm . Thus they differ from the macroscopic structure significantly from the standard samples such as C-500-5-T9, which consists of agglomerated spherical particles. This is due to the polymer synthesis, in which initially only shorter polymer chains are synthesized, and then cross-linked by FC-alkylation. The shorter length of the polymer chains is

due to the shorter reaction time. As the content of resorcinol increases, the general structure changes very slightly, as can be observed from samples PR-**2/1**, FC-PR-**1/1** and FC-PR-**1/2**. This is consistent with the conclusions of the previous section 4.1.7, where the formaldehyde resins with different resorcinol content had a similar structure. This suggests FC-cross-linking does not appear to have a significant effect on the structure and thus on polymerization. The reason for this is the increasing reactivity of resorcinol leading to a higher reaction rate with formaldehyde compared to phenol. As already described in section 1.3.4, the reactivity of the phenols increases with the number of hydroxyl groups, which complicates the control of the reaction. This means the polymerization of formaldehyde and resorcinol is too fast, so that the FC-cross-linking predominately occurs at the phenol parts only. This limits the influence of FC-cross-linking. However, it could be observed in section 4.1.7, the cavities became smaller with increasing resorcinol content, which was mainly due to the swellability of the polymer with the solvent ethanol. This swelling capability on the other hand is not given with CCl₄, which is why the cavities have not been influenced by it. Nevertheless, the SEM image of sample FC-**RF** shows the cavities are significantly smaller and in some cases smaller than 1 μm . At this point the higher reactivity of the resorcinol and the FC-cross-linking lead to a closer linkage of the polymer chains, which then leads to the corresponding network structure.

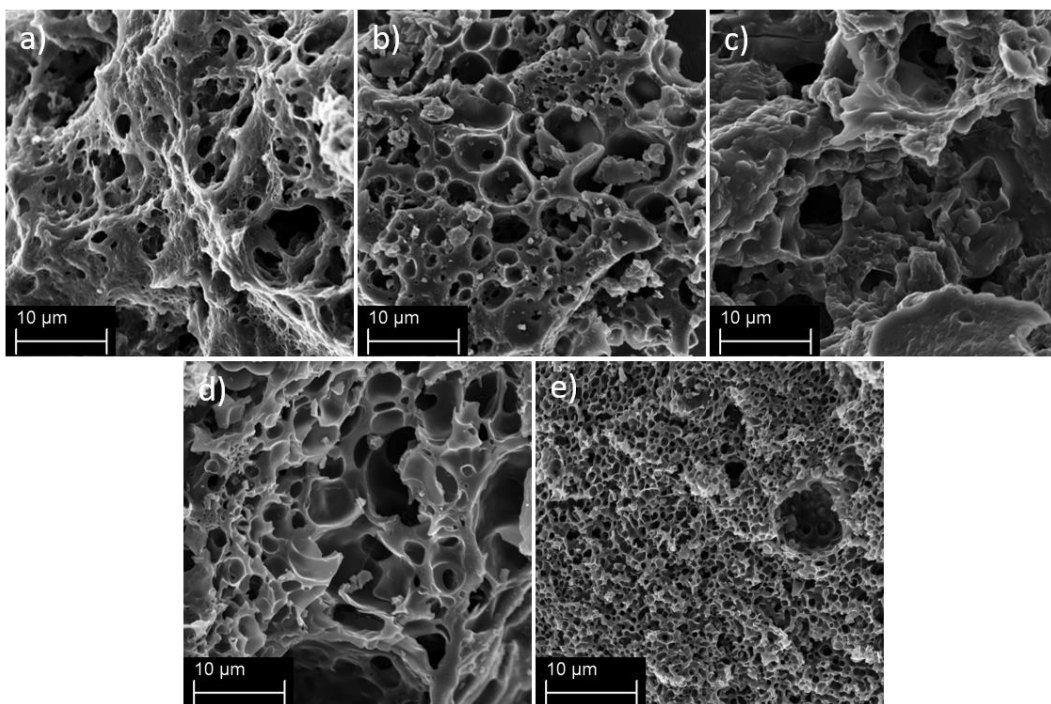


Figure 130: SEM images of (a) FC-**PF**, (b) FC-PR-**2/1**, (c) FC-PR-**1/1**, (d) FC-PR-**1/2** and (e) FC-**RF**.

P-XRD patterns of the carbon samples are shown in Figure A.16. All carbon patterns show weak and broad reflections at 44.0° 2θ corresponding to (101) diffractions of a turbostratic carbon structure. Similar to the carbon samples from the previous section 4.1.7, no diffraction is observable indicating a stacking of graphene layers for any material based on cross-linked formaldehyde polymers indicating a low degree of graphitization. The reason for that is the carbonization and activation conditions, as thoroughly described in section 4.1.3. Due to the low semi-carbonization temperature, the resulting carbon network is more susceptible to the chemical etching processes of KOH activation, whereby many structural defects lead to a lower degree of graphitization. Raman spectra of the activated carbons are presented in Figure A.17. The D- and G band are observable and the I_D/I_G ratios were calculated, which are 1.03, 1.12, 1.09, 1.04 and 1.07 for FC-**PF**, PR-**2/1**, FC-PR-**1/1**, FC-PR-**1/2** and FC-**RF** respectively. This confirms the low degree of graphitization for the carbon samples and shows all samples are structurally similar. The different resorcinol contents and the additional FC cross-linking of the polymers therefore have no influence on the degree of graphitization.

Nitrogen physisorption isotherms (77 K) of the carbon samples are shown in Figure 131 and the corresponding pore size distribution, calculated by the QSDFT method are shown in Figure 132. Similar to the carbon samples from section 4.1.7, all five carbon samples show a similar course of the isotherms and similar adsorption volumes. Therefore, the corresponding pore size distributions of the materials are supposed to be similar as well. All the isotherms possess a slope in the relative pressure range from 0.1 to 0.4 and slightly pronounced hysteresis at higher relative pressures. Therefore, microporous carbons with additional mesopores are expected. A small exception, however, is sample FC-**PF**. As can be seen on the right side of Figure 131, the isotherm on the adsorption branch closes at a relative pressure of approximately 0.5. This could indicate the cavitation phenomenon that occurs when a larger pore is located behind a smaller pore and is described in detail in section 7.2.1. The pore size distributions confirm all five carbon samples have micropores with a broad maximum at about 1.7 nm and additional mesopores up to 4.0 nm. Additionally, pores below 1 nm cannot be reliably evaluated by nitrogen physisorption. Also the pore size distributions of all samples are almost identical, as has already been assumed on the basis of the isothermic progressions. Only sample FC-**PF** shows a pore size maximum at 3.5 nm. However, this can also be an artifact which can be traced back to the cavitation effect.^[7] Furthermore, it is noticeable the pore size distributions of the carbons, which are based on FC-cross-linked formaldehyde resins, are not only very similar to each other, but also almost identical to the distributions of the carbons from section 4.1.7, which have been synthesized from non-cross-linked formaldehyde resins with different resorcinol contents. Minor exceptions might be samples C-PR-1/1 C-PR-1/2, which show slightly larger pores with the size of 2.5 to 3 nm. However, this difference in pore size is rather small and difficult to assign to the increasing resorcinol content, but rather difference in porosity caused by the synthesis procedure. This shows very clearly that not only the amount of resorcinol in the precursor has no influence on the porosity, but also the degree of cross-linking of the polymer chains has no further influence on the pore sizes. Although the formaldehyde resins differ relatively clearly in their physical properties, they have non-porous characteristics in common. Thus the formation and development of the pores depends exclusively on the carbonization and activation conditions and not on the nature of the formaldehyde precursor compounds. In order for the precursor compounds to have a significant influence on porosity, they

must already have a certain basic porosity, i.e. pores of different sizes. Otherwise, they only influence the surface morphology of the particles, as the SEM images have shown.

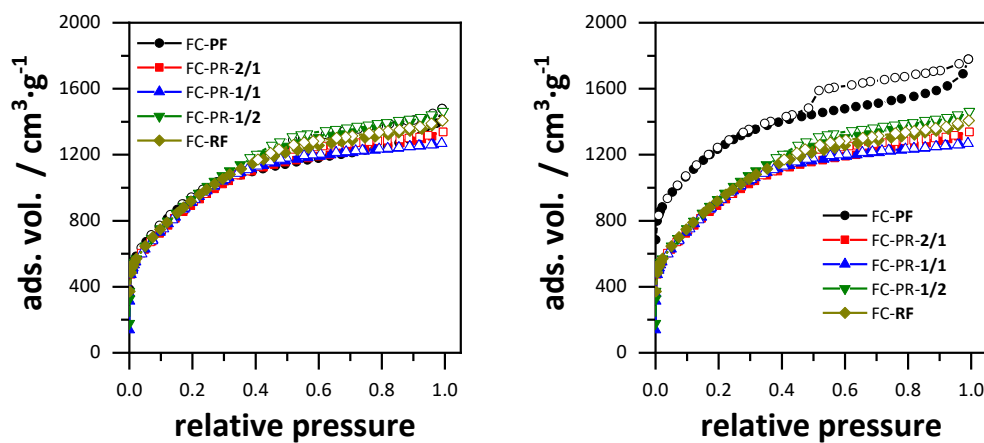


Figure 131: Nitrogen adsorption-desorption isotherms (77 K) of the carbon materials synthesized from FC-cross-linked formaldehyde resins and different phenol/resorcinol ratios (left), and the isotherms with sample FC-PF having a shift of $+300 \text{ cm}^3 \cdot \text{g}^{-1}$ (right).

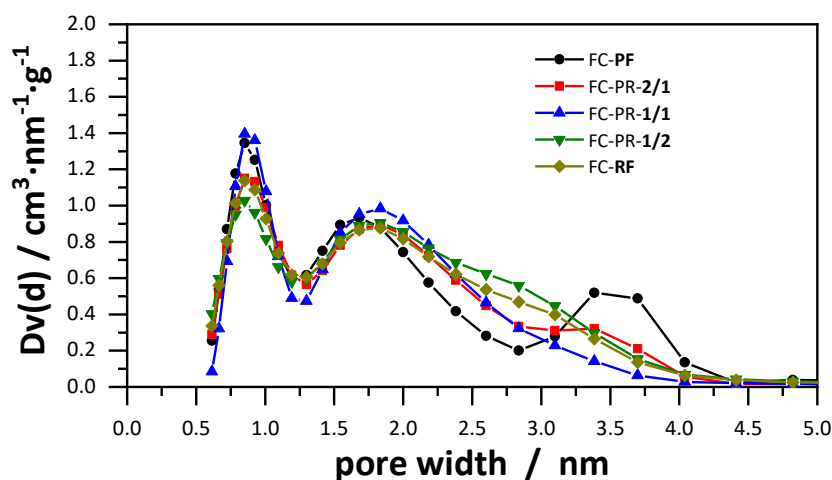


Figure 132: Pore size distributions of the carbon materials synthesized from FC-cross-linked formaldehyde resins and different phenol/resorcinol ratios, calculated by the QSDFT method from nitrogen desorption branch assuming slit pores.

The data, derived from nitrogen physisorption measurements are summarized in Table 19. The specific surfaces of the five carbons are all approximately the same size, with specific surface areas above $2400 \text{ m}^2 \cdot \text{g}^{-1}$ and a maximum difference in

surface of $160 \text{ m}^2 \cdot \text{g}^{-1}$. However, what is noticeable is sample C-PR-1/1 from section 4.1.7 and sample FC-PR-1/1, which both have the same resorcinol content in the precursor polymerization, have a very similar specific surface area and both samples have the lowest surface area in its sample row. The minimal influence of the resorcinol content on the porosity is reproducible and it can be shown that the FC-cross-linking of the formaldehyde resins has no effect on the porosity. The specific pore volumes of the carbons are also all in a similar range, but the difference between the largest pore volume ($2.12 \text{ cm}^3 \cdot \text{g}^{-1}$) and the smallest pore volume ($1.83 \text{ cm}^3 \cdot \text{g}^{-1}$) is more significant. This means the content of mesopores in sample FC-PR-1/1 is slightly lower compared to the other carbon materials. Apparently, a formaldehyde resin with a phenol/resorcinol ratio of 1/1 minimizes the effect of carbonization and activation. The micropore volumes, however, are in a similar range again, assuming the influence of the phenol/resorcinol ratio in the formaldehyde resins is minor due to their nonporous nature.

Table 19: Nitrogen physisorption derived data of the carbon samples synthesized from FC-cross-linked formaldehyde resins and different phenol/resorcinol ratios.

Sample	$S_{\text{BET}} /$ $\text{m}^2 \cdot \text{g}^{-1}$	$S_{\text{DFT}} /$ $\text{m}^2 \cdot \text{g}^{-1}$	$V_{\text{t}} /$ $\text{cm}^3 \cdot \text{g}^{-1}$	$V_{\text{mic}} /$ $\text{cm}^3 \cdot \text{g}^{-1}$
FC-PF	3455	2575	2.12	1.21
FC-PR-2/1	3356	2454	1.92	1.15
FC-PR-1/1	3438	2414	1.83	1.19
FC-PR-1/2	3499	2559	2.10	1.14
FC-RF	3452	2519	2.02	1.15

S_{DFT} (DFT surface area), V_{t} (total pore volume) and V_{mic} (micropore volume) obtained from QSDFT analysis. S_{BET} (BET surface area).

The FC-cross-linking of formaldehyde resins has shown only minor influence on the pore size distribution for pores above 1 nm. CO_2 physisorption measurement was used to determine whether the influence on pores below 1 nm was more significant. The corresponding isotherms are shown in Figure 133 with the calculated pore size distributions displayed in Figure 134. The progression of the isotherms and the adsorbed volumes from the CO_2 physisorption are almost identical for all five samples, again. The isotherms are quasi-linear, indicating even pore size distributions, only disturbed by the NLDFT artifacts. For all carbon materials, pores

below 0.7 nm are observable, as well as around and above 0.8 nm. The pore size distributions for all five samples are, all in all, very similar, except for FC-PR-1/1 and FC-RF which seem to have larger contents of pores between 0.8 and 1 nm. However, this difference to the other samples FC-PF, FC-PR-2/1 and FC-PR-1/2 is marginal and is more likely due to the carbonization and activation conditions.

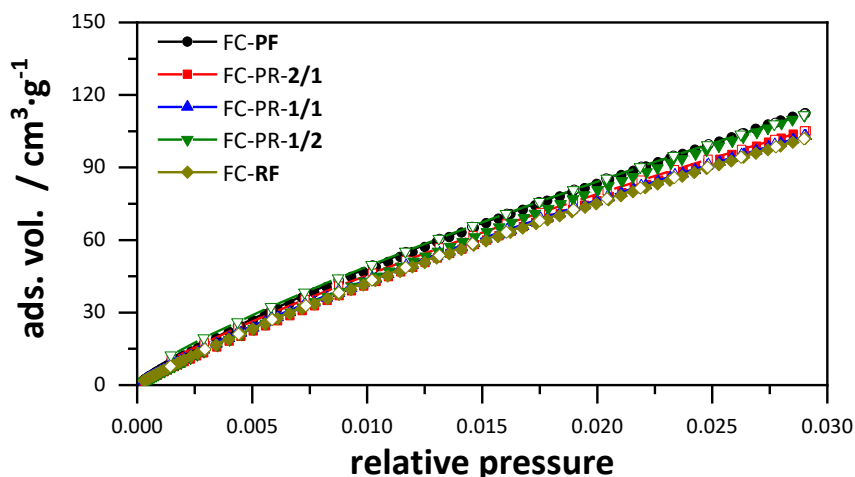


Figure 133: Carbon dioxide adsorption-desorption isotherms (273 K) of the carbon materials synthesized from FC-cross-linked formaldehyde resins with different phenol/resorcinol ratios assuming slit pores.

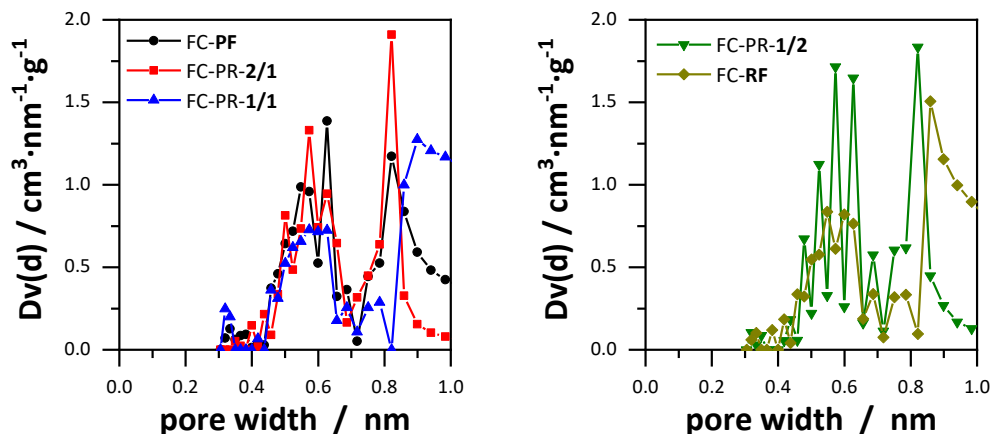


Figure 134: Pore size distributions of the carbon materials synthesized from FC-cross-linked formaldehyde resins with different phenol/resorcinol ratios, calculated by the NLDFIT method from carbon dioxide desorption branch assuming slit pores.

The combined cumulative surface area and pore volume for the carbons samples are shown in Figure 135 and Figure 136. As expected after evaluation the pore size

distributions from nitrogen and carbon dioxide separately, the curve of the cumulative surface area and pore volume are also almost identical. The surface area, generated by pores below 0.7 nm, as well as the corresponding pore volume are very similar for all five carbon materials. Only the surface area, generated by pores between 0.7 and 1 nm is slightly smaller for the samples FC-PR-1/1 and FC-**RF**, compared to the other three samples. This pore range is of particular interest as they are considered the smallest pores to be accessible to all electrolyte ions and may contribute more to capacitance than larger pores, due to confinement effects.

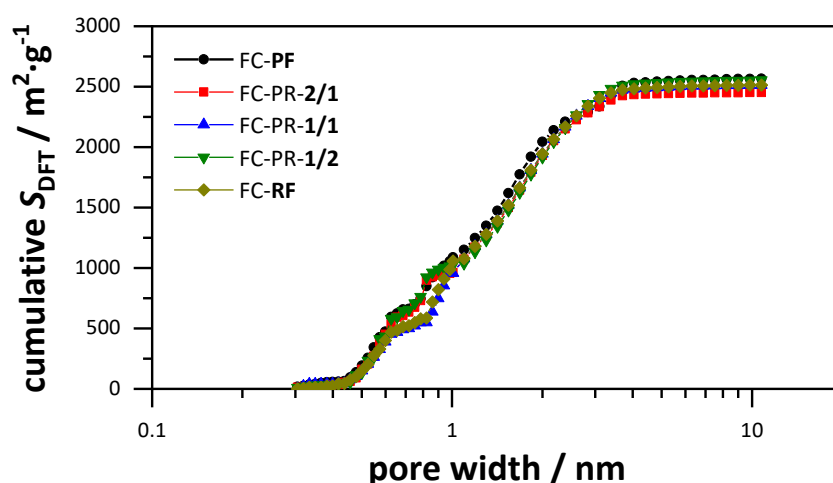


Figure 135: Combined cumulative surface area derived from carbon dioxide and nitrogen physisorption data of the carbon samples synthesized from FC-cross-linked formaldehyde resins with different phenol/resorcinol ratios.

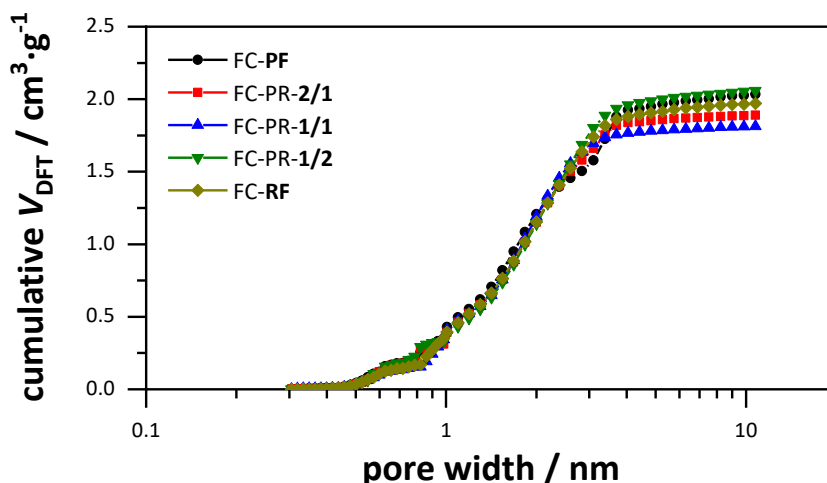


Figure 136: Combined cumulative pore volume derived from carbon dioxide and nitrogen physisorption data of the carbon samples synthesized from FC-cross-linked formaldehyde resins with different phenol/resorcinol ratios.

In this section it should be evaluated whether an additional cross-linking of the formaldehyde resins with different phenol/resorcinol contents has an influence on the porosity of the resulting porous carbons. In the previous section 4.1.7 it was already determined the phenol/resorcinol ratio has no influence on the subsequent porosity during the polymerization of the resins, with regard to the pore size distribution and specific surface area. The same could now be observed for the FC cross-linked formaldehyde resins. Again, a difference in surface morphology could be observed, but the influence on the porosity of the resulting carbon materials is minimal. Pore size distribution, specific surface area and thus the pore volumes were approximately the same for all samples. The reason for this is the resins lacking porosity of their own, whereby this is exclusively determined by the carbonization and activation conditions. Only the samples FC-PR-1/1 and FC-RF had slightly less cumulative surface area provided by pores in the range of 0.7 to 1 nm, which is also attributed to irregularities caused by the aggressive activation conditions.

4.1.8.2 Energy storage related properties of carbons synthesized from FC-cross-linked formaldehyde resins

Electrochemical characterization

CV curves of the carbon samples, synthesized from FC-cross-linked formaldehyde resins with different phenol/resorcinol contents are shown in Figure 137. In principle, all CV curves of the EDLC prepared from the carbon samples show a typical rectangular shape, indicating pure and well developed capacitive behavior. It is also noticeable that the CV curves of the samples are all very similar, especially in comparison to the change of the curve shape with increasing scan rates. Due to the current-related higher kinetics of the electrolyte ions, there is the often mentioned higher diffusion resistance of the ion migration in the carbon pores. For carbons, based on FC-cross-linked formaldehyde resins, none of the CV curves show any significant distortion at high scan rates, not even at a very high scan rate of $2500 \text{ mV} \cdot \text{s}^{-1}$. This shows the effect of the resistance only changes according to Ohm's law and an almost resistance-free ion transport in the carbon materials is ensured. A large part of the pores of the carbon samples have a size around 1.7 nm, which have already shown in the previous sections capability to ensure ion transport at high currents and frequencies. The additional mesopores up to 4 nm further enhance this effect. Since all samples have a very similar pore size distribution, the electro kinetic properties are similar as well.

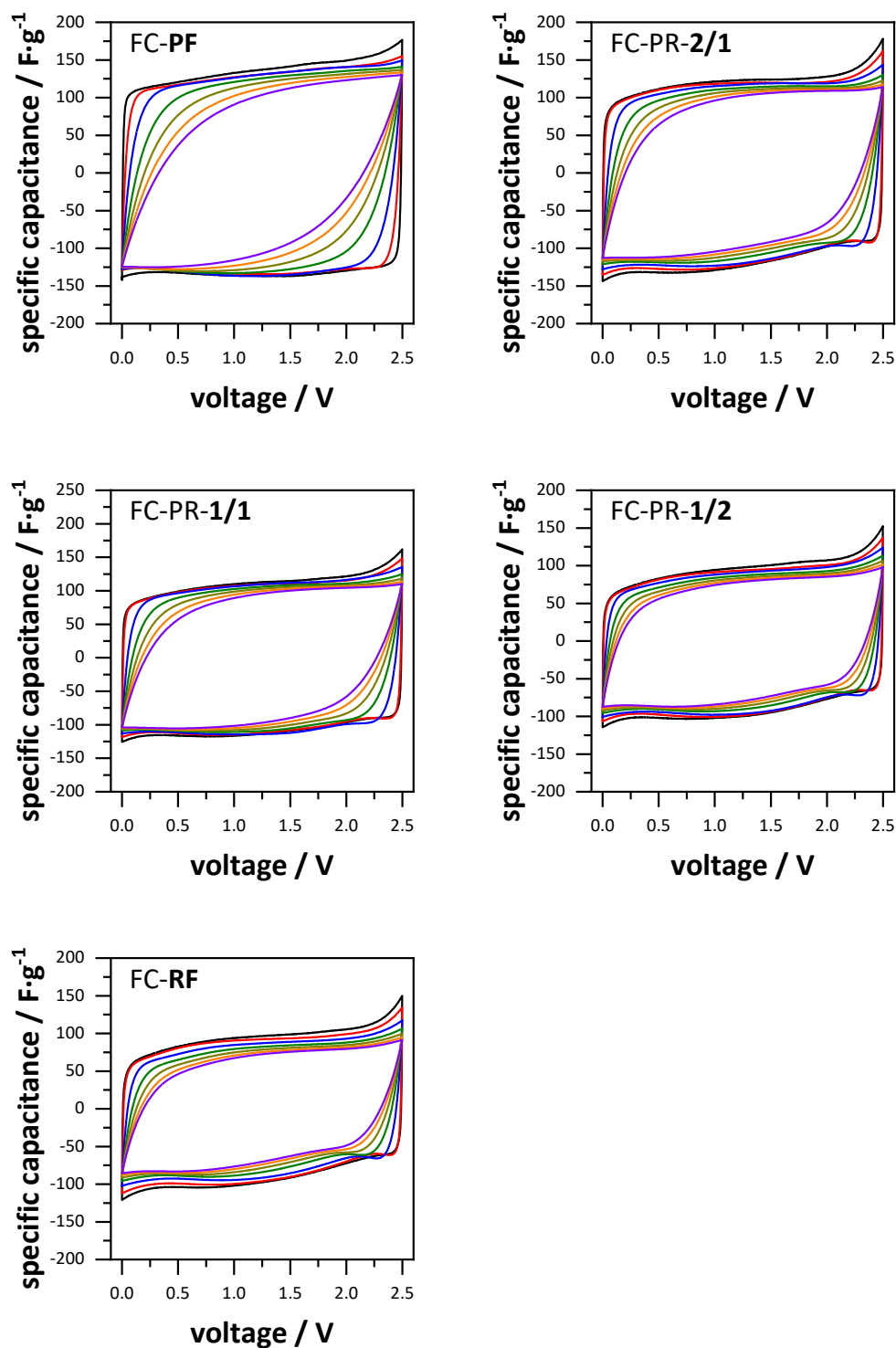


Figure 137: Cyclic voltammograms of the activated carbons synthesized from FC-cross-linked formaldehyde resins with different phenol/resorcinol ratios at $10 \text{ mV}\cdot\text{s}^{-1}$ (black), $100 \text{ mV}\cdot\text{s}^{-1}$ (red), $500 \text{ mV}\cdot\text{s}^{-1}$ (blue), $1000 \text{ mV}\cdot\text{s}^{-1}$ (green), $1500 \text{ mV}\cdot\text{s}^{-1}$ (dark yellow), $2000 \text{ mV}\cdot\text{s}^{-1}$ (orange) and $2500 \text{ mV}\cdot\text{s}^{-1}$ (violet).

Results from the galvanostatic charge/discharge tests are shown in Figure 138 and the calculated capacitance values, as well as, accessible surface area and pore volume are summarized in Table 20. The galvanostatic charge/discharge curves possess triangular shapes, indicating a stable and reversible double layer charge storage behavior. This applies to the charge/discharge curves of all five EDLCs with carbon samples as electrode materials. As initially expected due to the similar specific surfaces, all five samples have very similar specific capacitance values, which are in the range of $138.9 \text{ F}\cdot\text{g}^{-1}$ (FC-PR-2/1) and $148.5 \text{ F}\cdot\text{g}^{-1}$ (FC-PF), thus not even differing by $10 \text{ F}\cdot\text{g}^{-1}$. The decisive factor, however, is the accessible surface area, which is also in similar ranges for all five samples discussed in this section. Only sample FC-PR-2/1 with $1862 \text{ m}^2\cdot\text{g}^{-1}$ has a slightly lower accessible surface area than the other samples with 1950 to $2030 \text{ m}^2\cdot\text{g}^{-1}$. This also explains the slightly lower specific capacitance of sample FC-PR-2/1 due to the smaller accessible area for electrolyte ions. Capacitance retention is very good for all five carbon materials, with at least 93% capacitance retention (FC-PR-2/1) at a high current density of $20 \text{ A}\cdot\text{g}^{-1}$. This is primarily due to the sufficiently large pores, which allow even at high currents and frequencies, an almost resistance-free diffusion of electrolyte ions. The accessible pore volume is also relatively similar for all carbon samples, with a maximum difference of $0.25 \text{ cm}^3\cdot\text{g}^{-1}$. Therefore, the influence on the maximum capacitance and its retention is not significant.

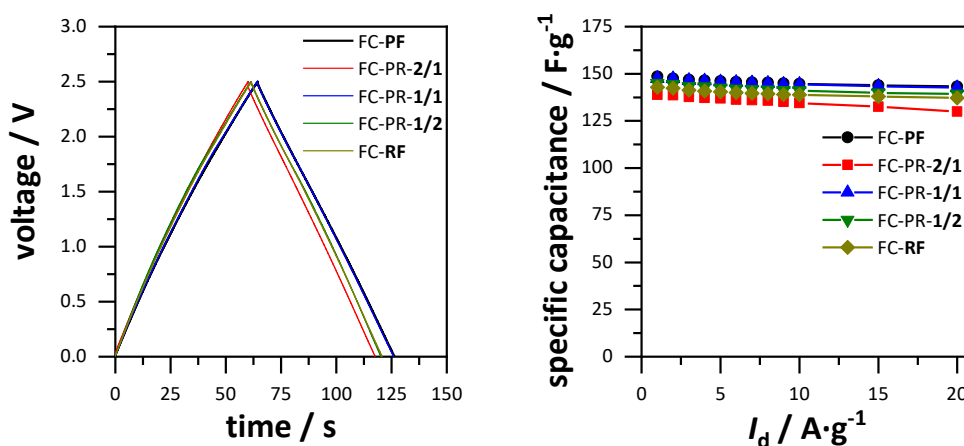


Figure 138: Discharge curve at $1 \text{ A}\cdot\text{g}^{-1}$ for the carbon samples synthesized from FC-cross-linked formaldehyde resins with different phenol/resorcinol ratios (left) and the specific capacitance as a function of discharge current density (right).

Table 20: Electrochemical properties of the EDLC prepared from activated carbons synthesized from FC-cross-linked formaldehyde resins with different phenol/resorcinol ratios at the precursor polymerization, in 1 M TEABF₄/ACN.

Sample	$S_{\text{acc}} /$ $\text{m}^2 \cdot \text{g}^{-1}$	$V_{\text{acc}} /$ $\text{cm}^3 \cdot \text{g}^{-1}$	$C_{\text{CV}} /$ $\text{F} \cdot \text{g}^{-1}$	$C_{\text{DC}} /$ $\text{F} \cdot \text{g}^{-1}$
FC-PF	1951	1.96	131.7	148.5
FC-PR-2/1	1862	1.77	121.9	138.9
FC-PR-1/1	1945	1.71	129.4	147.5
FC-PR-1/2	1963	1.94	132.3	144.9
FC-RF	2034	1.90	125.8	142.9

S_{acc} specific surface area for pores > 0.66 nm; V_{acc} pore volume for pores > 0.66 nm; C_{CV} calculated from $10 \text{ mV} \cdot \text{s}^{-1}$; C_{DC} calculated from $1 \text{ A} \cdot \text{g}^{-1}$.

The surface area normalized capacitance values are shown in Figure 139 and summarized in Table 21, along with the pore volume normalized capacitance values. Since both the capacitance values and the specific and accessible surface areas of the carbons are relatively similar, no trends can be observed for normalized capacitance values. Above all, the capacitances which have been normalized according to the accessible surface are very close to each other in the range from 0.070 to $0.076 \text{ F} \cdot \text{m}^{-2}$. This shows all pores have the same electrochemical utilization of the surface area. With regard to the volumetric capacitance values, normalized according to the accessible pore volume, sample **FC-PR-2/1** and **FC-PR-1/1** show the highest capacitance values with 94 and $86 \text{ F} \cdot \text{cm}^{-3}$, while sample **FC-PF**, **FC-PR-1/2** and **FC-RF** all have values around $75 \text{ F} \cdot \text{cm}^{-3}$. This is due to the relatively smaller pore volumes of samples **FC-PR-2/1** and **FC-PR-1/1**, which are generated by the smaller amounts of pores in the range of 3.5 to 4 nm. This indicates that while small mesopores allow improved diffusion of electrolyte ions, they do not further contribute to the electrochemical utilization of the electrode surface and thus generate dead volume.

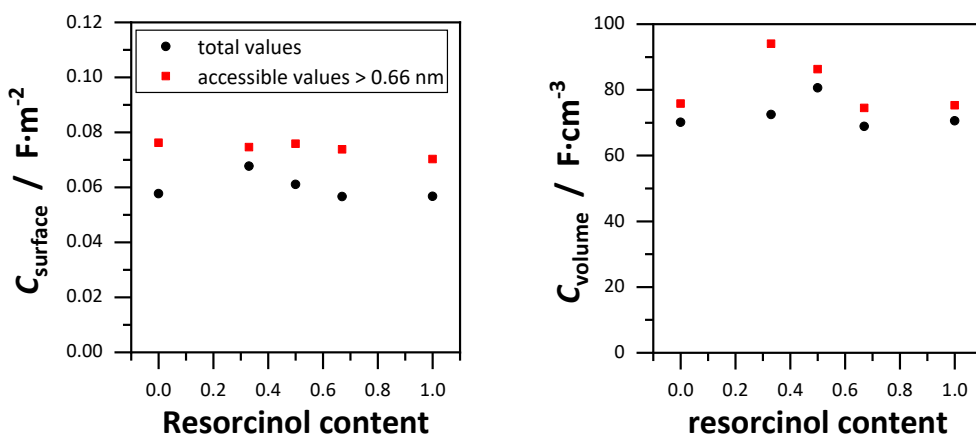


Figure 139: Surface area normalized capacitance as a function of the resorcinol content used for the FC-cross-linked formaldehyde resins.

Table 21: Surface- and volumetric capacitance values for carbons synthesized from FC-cross-linked formaldehyde resins with different phenol/resorcinol ratios.

Sample	$C_S /$ $\text{F} \cdot \text{m}^{-2}$	$C_{S>0.66} /$ $\text{F} \cdot \text{cm}^{-2}$	$C_V /$ $\text{F} \cdot \text{cm}^{-3}$	$C_{V>0.66} /$ $\text{F} \cdot \text{cm}^{-3}$
FC-PF	0.058	0.076	70.1	75.8
FC-PR-2/1	0.067	0.075	72.5	94.0
FC-PR-1/1	0.061	0.076	80.6	86.3
FC-PR-1/2	0.057	0.074	68.9	74.5
FC-RF	0.057	0.070	70.6	75.3

C_S , $C_{S>0.66}$ calculated from C_{DC} and the respective surface areas, obtained from the DFT results; C_V , $C_{V>0.66}$ calculated from C_{DC} and the respective pore volumes.

Results from the PEIS measurements are shown in Figure 140. The Nyquist plots reveal equally low R_{ESR} values for all five discussed carbon samples as well as short semicircles and almost negligible Warburg segments, indicating well-developed double layer formation for all prepared EDLCs using carbon samples as electrode materials. A closer look at the semicircles in the high frequency range shows the semicircles of samples FC-PR-1/1 and FC-RF are slightly longer and of sample FC-PF are only very weakly pronounced. This may be due to charge transfer reactions between the electrolyte and the electrode surface or the current collector. Although, a reaction with the current collector would be more probable, since chemical reactions of the solvent or electrolyte with the carbon electrode surface is unlikely.

However, it should also be noted that ohmic resistances, such as the electrolyte conductivity or contact resistances of the current collector and carbon electrode, also act on the RC element, which generates the semicircle, so a material-specific assignment of the semicircle length is difficult to obtain. The progressions of the low frequency range are very similar for all carbons, which can also be demonstrated with the phase angles from -87.5 to -88.6° , indicating an almost perfect double layer formation. This originates from the resistance free electrolyte ion diffusion enabled by the large micropores and small mesopores up to 4 nm, possessed by all five carbons, synthesized from FC-cross-linked formaldehyde resins with different phenol/resorcinol ratios. The current response of the real capacitance shows a plateau at low frequencies up to 0.2 Hz until the exponential decay of the storage capacity. This means every investigated EDLC, prepared from carbons based on FC-cross-linked formaldehyde resins can be completely discharged as fast as 5 s, without significant loss of capacitance. This is confirmed by the time relaxation constants, which have been determined from the peak of the frequency response of the imaginary capacitance. The time relaxation constants are 0.25, 0.79, 0.81, 0.49 and 0.77 s for FC-**PF**, FC-PR-**2/1**, FC-PR-**1/1**, FC-PR-**1/2** and FC-**RF** respectively. The time constants of all carbon samples are very low, indicating a well-developed and low-resistance ion diffusion to and within the pores. This depends above all on the size of the pores and it is now clear electrolyte ions are promoted not only by mesopores but also by large micropores from about 1.5 nm.

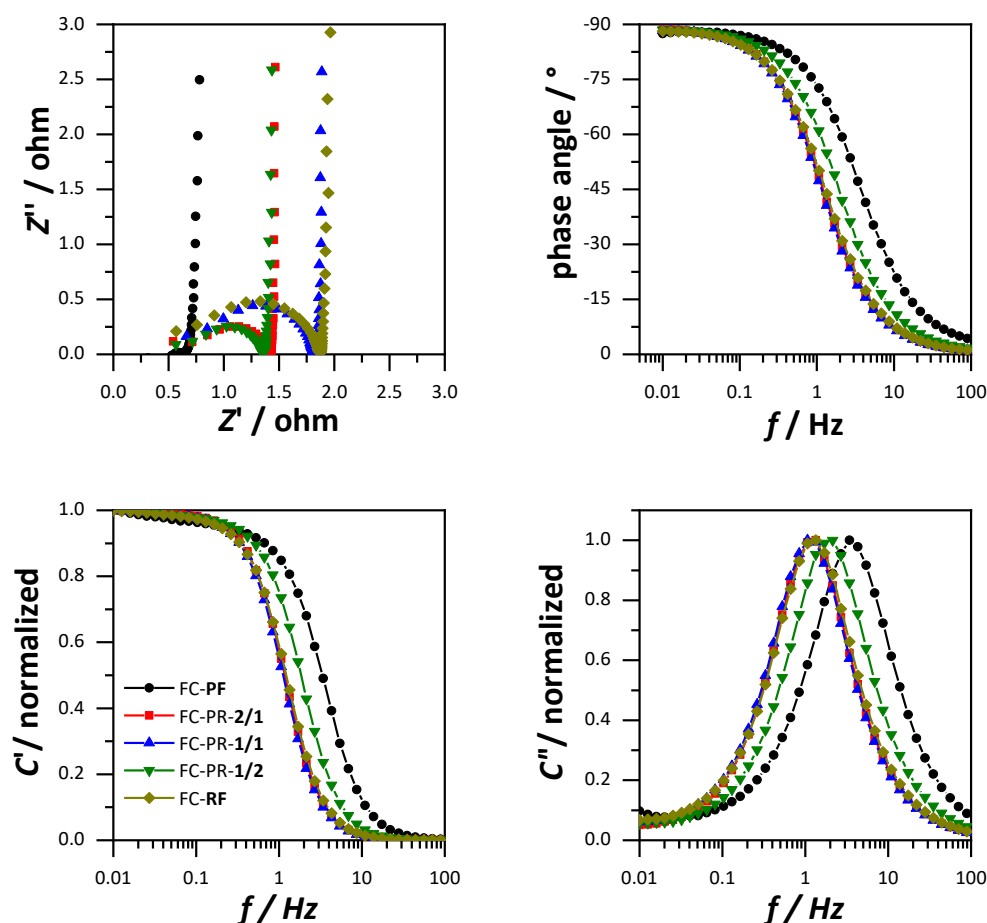


Figure 140: Nyquist plot of the activated carbons (top left), frequency response of the phase angle (top right), normalized real capacitance (bottom left) and normalized imaginary capacitance (bottom right).

As already observed in section 4.1.7, the carbons from this section show a very similar porosity. The pore size distributions are almost identical and the accessible specific surface areas are all very close to each other.

Hydrogen storage

Gravimetric hydrogen uptake isotherms of the carbons at 77 K are shown in Figure 141. The progressions of the isotherms are fully reversible and have not reached saturation, due to the low pressure range of the measurement. The uptake capacities are 2.89, 2.65, 2.58, 2.59 and 2.63 wt% for FC-**PF**, FC-PR-**2/1**, FC-PR-**1/1**, FC-PR-**1/2** and FC-**RF** respectively. All uptake capacities of the carbon materials are in a similar range, except for FC-**PF**. It was expected the samples would all have a very similar hydrogen uptake capacity, given the similarities in porosity. It is therefore

noticeable that sample FC-**PF** differs significantly. In addition, the uptake capacities of the other four samples are high, but still lower than the capacity of materials with similar porosity, like the previously presented C-500-5-T9 (2.73 wt%). The uptake capacity along with the specific surface area normalized uptake capacity of the carbon samples is shown in Figure 142. A direct influence of the resorcinol content seems unlikely at first, as shown in section 4.1.7.2. FC cross-linking can also be excluded as an influencing factor on the uptake capacity, since it has no effect on the porosity of the formaldehyde resins and thus has no influence on the porosity of the carbons. The influence of the surface can also be excluded, since the normalized capacities of the five samples are in the same ratio to each other as the non-normalized gravimetric uptake capacities. The influence of the total pore volume is also considered unlikely, since the pore volume of sample FC-PR-1/2 is almost as large as that of sample FC-**PF** (2.10 and 2.12 cm³·g⁻¹) and the respective hydrogen uptake capacities differ relatively strongly nevertheless. The micropore volume could have a greater influence here. It is the largest for sample FC-**PF**, although the micropore volume of sample FC-PR-1/1 is very similar (1.21 and 1.19 cm³·g⁻¹). Nevertheless, the higher content of micropores, is likely the reason for the high uptake of sample FC-**PF**, as micropores have a higher adsorption enthalpy. A more precise evaluation of the pore size dependent hydrogen uptake will be presented in section 4.3.

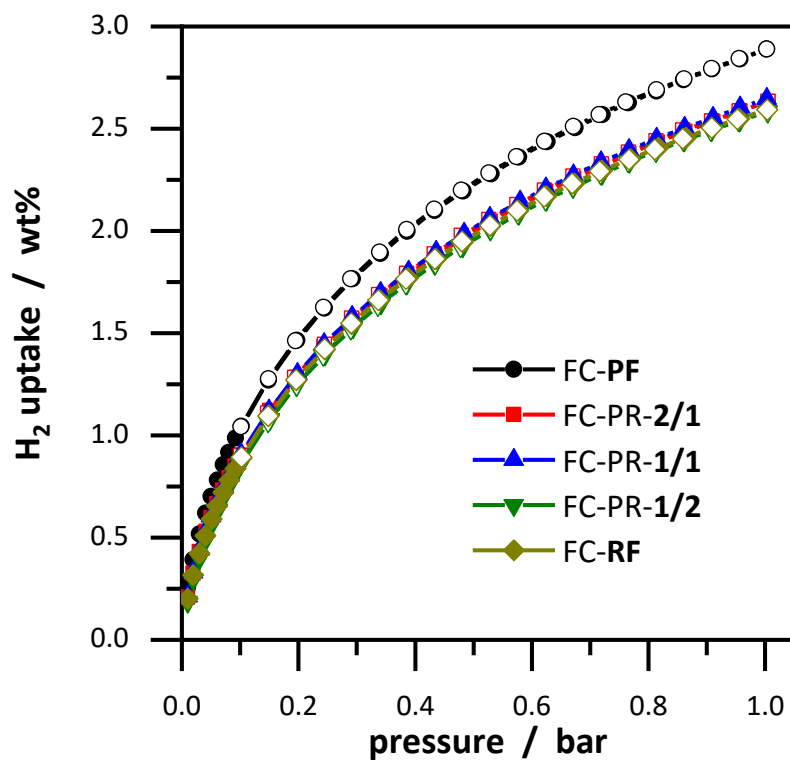


Figure 141: Gravimetric hydrogen storage capacity at 77 K of activated carbons, synthesized from FC-cross-linked formaldehyde resins with different phenol/resorcinol ratios.

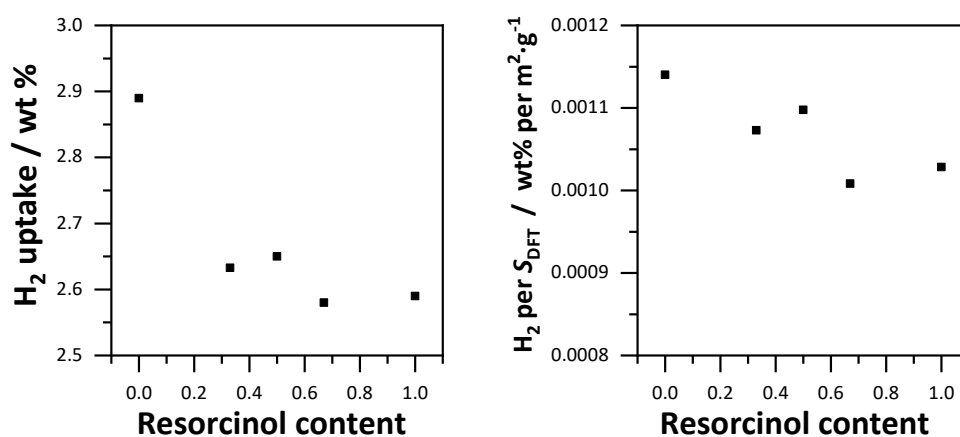


Figure 142: Gravimetric hydrogen uptake in dependence of the resorcinol content (left) and the specific surface area normalized uptake capacity in dependence of the resorcinol content (right).

In this section, a possible influence of the formaldehyde resin precursors should be further investigated by additionally cross-linking them by Friedel-Crafts alkylation. It has been shown that the resulting carbons differ in the surface morphology of the particles, but the porosity has barely been influenced. Therefore the energy related properties of all five carbon samples were similar, with the higher hydrogen uptake of sample FC-PF being the only exception.

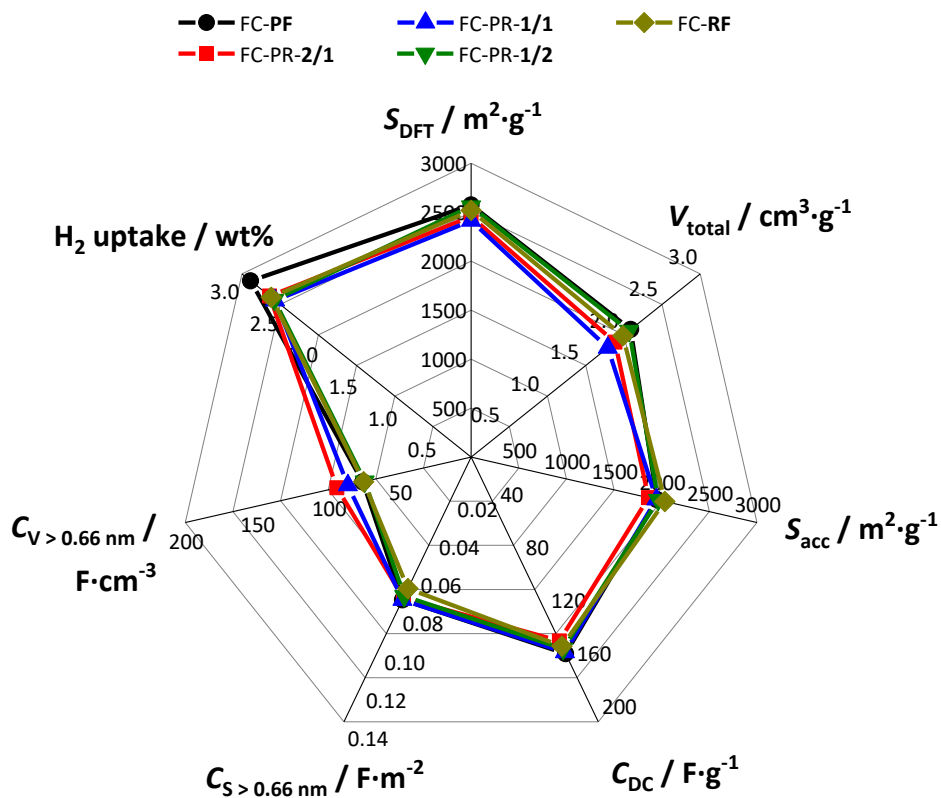


Figure 143: Graphical summary of the samples properties, synthesized from FC-cross-linked formaldehyde resins with different phenol/formaldehyde ratios.

The graphical summaries of the remaining activated carbon samples of the entire chapter 4.1 are shown in Figure 144.

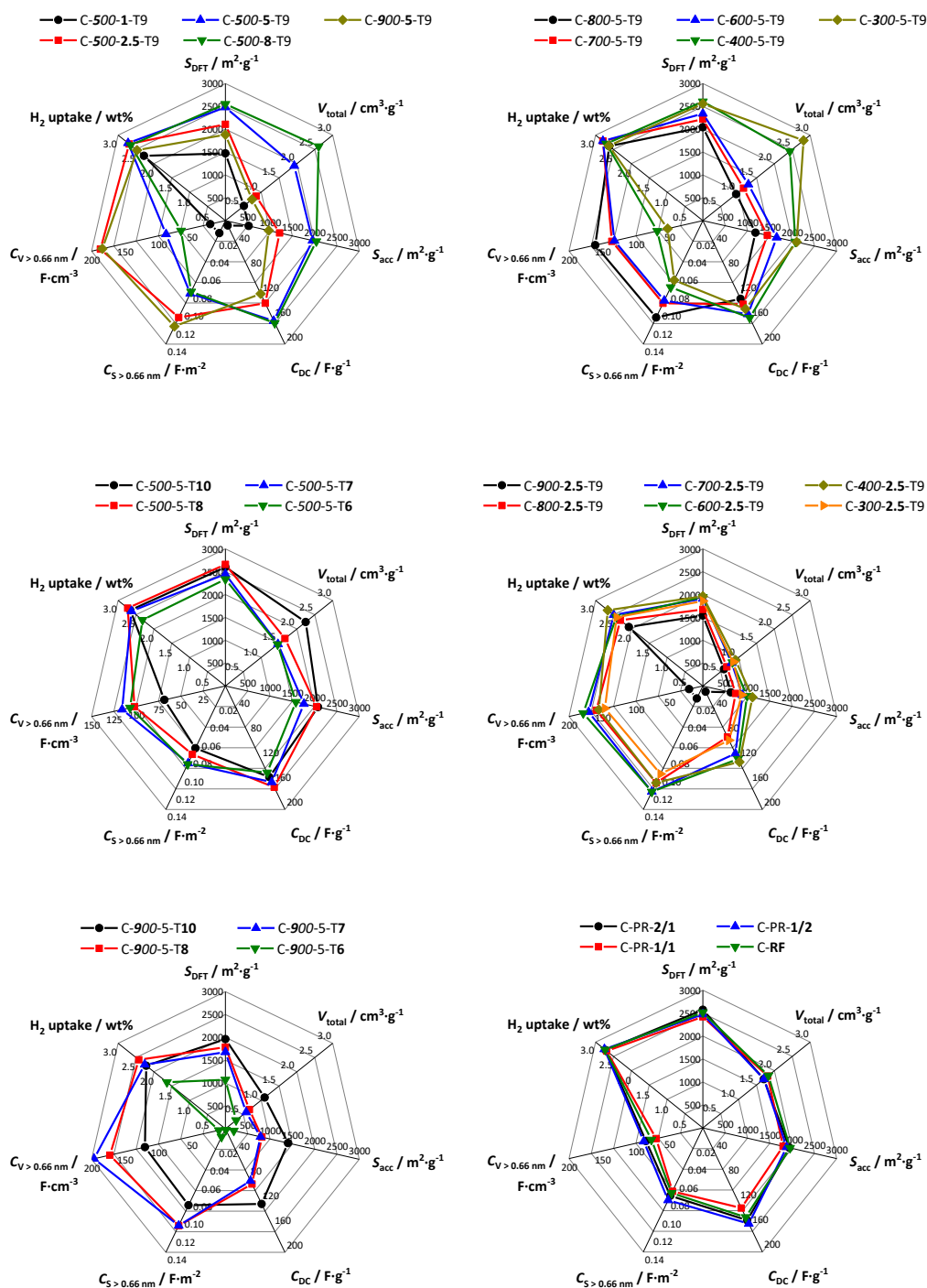


Figure 144: Graphical summaries of all activated carbon samples. Activated carbons, synthesized with different KOH/carbon ratios (top left), synthesized at different semi-carbonization temperatures (top right), synthesized at different activation temperatures (middle left), synthesized at different semi-carbonization temperatures and a KOH/carbon ratio of 2.5 (middle right), synthesized at different activation temperatures and a semi-carbonization temperature of 900 °C (bottom left) and synthesized with different phenol/resorcinol ratio at the formaldehyde resin polymerization (bottom right).

4.2 Influence of the pore size on capacitance

The results from chapter 5.1 have clearly shown, the surface areas of the carbons used as electrode materials in the EDLCs are of great importance. It has been clearly shown a high surface area accessible to electrolyte ion leads to a higher capacitance. By changing various synthesis parameters, it was possible to synthesize carbon with a high accessible surface area, which at the same time enabled good diffusion of the electrolyte ions to and within the pores due to their large micropores and small mesopores. By determining the surface capacitance, however, it was also possible to show the electrochemical utilization of the surface was not the same for all carbon samples. Microporous carbons tended to have a higher surface capacitance than microporous and mesoporous carbon materials. This suggests smaller pores around and below 1 nm seem to contribute more to the capacitance than correspondingly larger ones. This observation is in line with the results of the literature mentioned in section 1.4.4. In this chapter, it is now a matter of investigating the influence of pore sizes on capacitance in more detail and possibly providing a pore specific correlation of the capacitance contributions.

4.2.1 Mining the data

First, an effort is made to determine from the generated data pool of the previous sections whether new knowledge can be gained with regard to capacitance and pore size. In the previous sections, many carbons were synthesized and characterized in detail. In addition, they were electrochemically investigated and evaluated as electrode materials for EDLCs. Therefore, a lot of information is available in the data pool (Figure 143 and Figure 144). So far, however, the data have only been discussed in the narrow context of the synthesis parameters and not in a large context. It should be emphasized again that all carbons are considered the same in terms of surface chemistry. Although it is possible the carbons may have different oxygen contents in the respective network, this should have no effect on the capacitance in the organic electrolyte.^[109]

It is clear from chapter 4.1, the surface area or the accessible surface area is an important factor with regard to the maximum gravimetric specific capacitance. This is illustrated again in Figure 145, where the specific capacitance is shown as a dependency of the accessible surface area and the total pore volume of all carbon samples discussed in this entire work. From now on, the term all carbon samples

will refer to each discussed carbon material from the entire work in chapter 5.1. There is a clearly recognizable trend that the maximum gravimetric specific capacitance increases with increasing accessible surface area. This can be explained relatively clearly by the fact a higher accessible surface area is associated with a larger number of adsorbing electrolyte ions, which can accumulate on the surface to form the double layer and thus contribute to electrical energy storage. For the samples discussed here, there seems to be a limit between 630 and 730 $\text{m}^2 \cdot \text{g}^{-1}$, since the samples showed almost no capacitance if they exhibited less accessible surface and had at least 80 $\text{F} \cdot \text{g}^{-1}$ capacitance if they had more accessible surface. This shows the weakness of the data mining plots, as it is always necessary to look at each sample contextually.

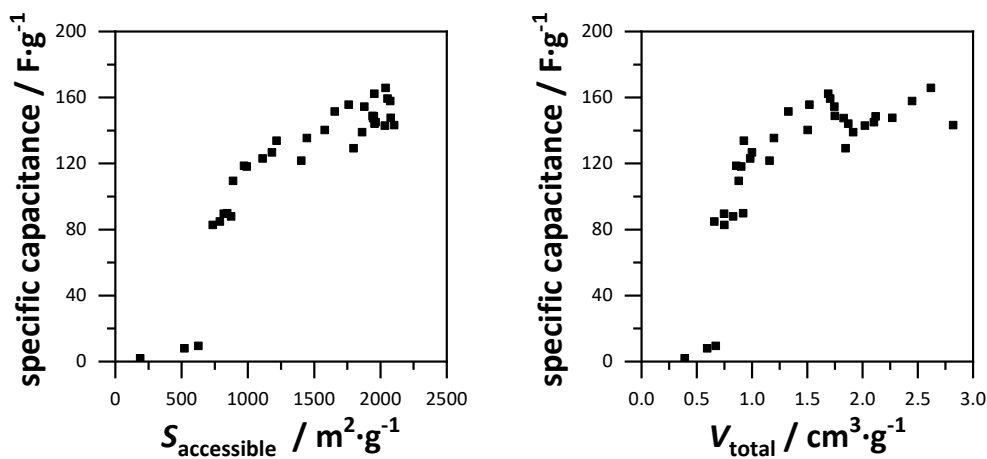


Figure 145: Specific capacitance, calculated from galvanostatic discharge at 1 $\text{A} \cdot \text{g}^{-1}$ in dependence of the accessible surface area (left) and the total pore volume (right) from every investigated carbon material of the entire work.

As already assumed in section 4.1.5, the pore size distributions are decisive, since it is not only about the pure number of accessible pores, but also about the pore connection. It was possible to establish that the pores were generally accessible, but so small that the kinetic diffusion resistance of the electrolyte ions was so high even at low currents and frequencies that the true maximum capacitance could never be achieved. Also, the general trend of increasing capacitance with increasing accessible surface area can only be considered as a general trend. Although the carbon sample with the highest capacitance (C-500-8-T9) has one of the highest accessible surface areas around 2000 $\text{m}^2 \cdot \text{g}^{-1}$, this does not apply to all materials. There is a wide range of materials with very high accessible surface areas between 1800 and

$2000 \text{ m}^2 \cdot \text{g}^{-1}$, but the maximum capacitance values of these materials vary greatly between 120 and $160 \text{ F} \cdot \text{g}^{-1}$. This observation cannot be explained solely in terms of the accessible surface. The dependence of the capacitance on the total pore volume is even more ambiguous than the dependence of the capacitance on the surface. It can also be seen here that materials with a pore volume above $1 \text{ cm}^3 \cdot \text{g}^{-1}$ tend to have a higher capacitance. However, for materials with pore volumes between 1 and $3 \text{ cm}^3 \cdot \text{g}^{-1}$ no clear trend can be observed. It is rather the opposite case that the capacitance values scatter very strongly between 120 and $160 \text{ F} \cdot \text{g}^{-1}$ there. Although it has been shown in chapter 4.1 that the pore volume basically correlates with the average pore size of carbons, the pore volume alone cannot be used to predict the distribution of the pores, as these are usually more complex. In addition, the plot provides no information about the electrochemical utilization of the surface, which is generated by different pore sizes.

In order to investigate the utilization of the carbon electrode surface in terms of highest possible contribution to the capacitance, it is mandatory to consider the surface capacitance, which is obtained by the normalization of the gravimetric specific capacitance by the total surface area or accessible surface area, as it has been elaborately shown in chapter 5.1 on several occasions. The surface capacitance of all carbon samples is shown as a function of the total pore volume in Figure 146, whereby the capacitance was calculated using the accessible surface area. With the exception of samples C-500-1-T9, C-900-5-T6 and C-900-2.5-T9, which show no noticeable capacitance values due to their small pore sizes, the clear trend can be observed that the surface capacitance is the highest for carbons with a low pore volume around $0.8 \text{ cm}^3 \cdot \text{g}^{-1}$, with values of up to $0.13 \text{ F} \cdot \text{m}^2$ and clearly decreases with increasing pore volume. The decrease in capacitance for carbon materials with increasing pore volume is significant and the carbon material with the lowest surface capacitance, which is only $0.068 \text{ F} \cdot \text{m}^{-2}$, is the carbon material with the highest pore volume (C-300-5-T9). Here, too, this is only a general trend, since the surface capacitances of carbon samples scatter with similar pore volumes. Since in the process of this work it was determined the total pore volumes basically correlate with the average pore size, it can again be assumed smaller pores have a higher surface capacitance. With smaller pores, meaning pores with the size from 0.7 to 1.0 nm . However, it becomes apparent very quickly this is only an assumption if the representation in Figure 146 is taken as a basis. As in chapter 4.1, each sample must be

evaluated individually in terms of pore size distribution and electrochemical properties in order to draw such conclusions. But even then, it becomes clear that only an estimation can be stated here, since a sample with a pore size distribution is attributed an exact surface capacitance. How each individual pore size contributes to the specific capacitance, cannot be stated. One possibility for closer analysis would be to calculate the ratios of some pore volumes of the different carbons and their dependence on the surface capacitance. Also in Figure 146 the surface capacitance is plotted against the pore volume ratio which is generated by pores above 1.30 nm and by pores in the range of 0.62 to 1.30 nm. These pore margins are chosen for two reasons. On the one hand, Chapter 5.1 has shown carbons, with predominantly micropores around 1 nm, have the largest surface capacitance. On the other hand, 1.30 nm is the limit at which both electrolyte ions can penetrate the pores with a complete solvate shell, thus reducing the effect of the confinement effect. Again, there is only a general trend that smaller volume ratios provide rather high surface capacitance values and these become smaller with increasing volume ratios. Whereby the ratios between 0.1 and 1 vary greatly and show no clear tendencies. Here it can also be assumed carbon materials with smaller volume ratios have a higher usability of the surface, meaning small pores contribute more to the capacitance. However, here too the problem remains that only pore ranges can be selected and no more precise statement can be provided about the individual pore sizes. In order to confirm the previous conclusions, a capacitance measure must be defined for a concrete pore size in order to concretize its influence.

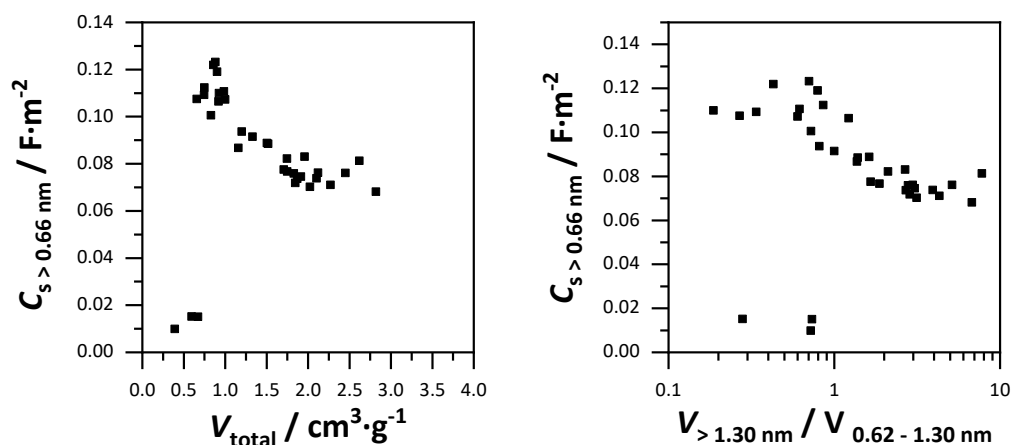


Figure 146: The surface capacitance, normalized by the respective accessible surface area in dependence of the total pore volume (left) and the surface capacitance in dependence of the pore volume ratio of the volume generated by pores $> 1.30 \text{ nm}$ and the volume generated by pores in the range of 0.62 to 1.30 nm (right).

In order to further specify the contribution of pores to capacitance, the literature did not often compare the pore range with the capacitance, but rather determined the volume-weighted average pore size of the individual carbon electrode materials.^[16,152,188–190,194,195] This is performed using the physisorption data. The DFT method delivers the cumulative pore volume as a function of pore size and the pore size is determined by which 50 % of the pore volume is reached. This is illustrated in Figure 147 using the sample C-500-5-T9 as an example. The volume-weighted average pore size was determined for all carbon samples and the surface capacitance was plotted as a function of the average pore size as seen in Figure 147. This now results in a concrete pore size relation to the capacitance, which was related to a relative abundance of the respective pore size in the corresponding carbon material. It is noticeable the progression of the surface capacitance with the volume-weighted average pore size is almost identical with the progression of the capacitance and the total pore volume. This confirms the observation that the pore volumes of the carbons of this work correlate relatively well with the pore sizes. Although it is clear larger pores generate relatively more pore volumes than the same number of smaller pores, this is taken into account in the volume weighting and cumulative application of the volume. Pore sizes between 0.9 and 0.8 nm show the largest surface capacitance values and thus also the best electrochemical utilization of the carbon electrode surface. However, it should be noted the capacitance values here also vary

between 0.10 and $0.13 \text{ F}\cdot\text{m}^{-2}$. As the pore size increases, the surface capacitance decreases, which seems to confirm the anomalous increase of the capacitance for pores below 1 nm . For carbon materials with an average pore size below 0.8 nm there is no significant capacitance, which can be attributed to there not being enough pores where the two electrolyte ions can penetrate, even in a desolvated state. Even if these results initially indicate pores below 1 nm provide a greater contribution to capacitance, this still cannot be related to concrete pore sizes. Although the volume-weighted average pore size gives a clearer reference, it is still only an average for each carbon and does not reflect the often multimodal character of the respective pore size distribution. Another approach for the evaluation of porosity and electrochemical data is therefore necessary.

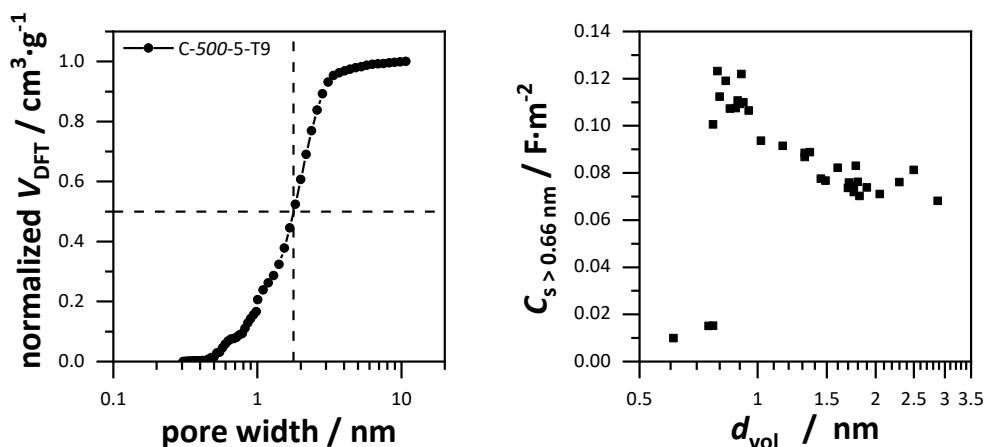


Figure 147: The normalized cumulative pore volume in dependence of the pore width from sample C-500-5-T9, as an example for the determination of the volume weighted average pore size (left) and the surface capacitance, normalized by the respective accessible surface area in dependence of the volume weighted average pore size (right).

Considering the relation of the accessible volumetric capacitance in dependence of the volume-weighted average pore size, a similar progress compared to the accessible surface area and the volume-weighted average pore size is evident as seen in Figure 148. Here, too, carbon samples with pore sizes between 0.8 and 0.9 nm show the highest volumetric capacitance values, while the volumetric capacitance steadily decreases with increasing volume-weighted pore size. This confirms earlier observations that carbons with smaller pores have more efficient utilization of pore volume in terms of capacitance than carbons with larger pores, indicating unused

or dead volumes. It should be noted again, however, that the capacitance values for carbons with pores in the range of 0.8 to 0.9 nm also vary significantly between 150 and 200 $\text{F} \cdot \text{cm}^{-3}$.

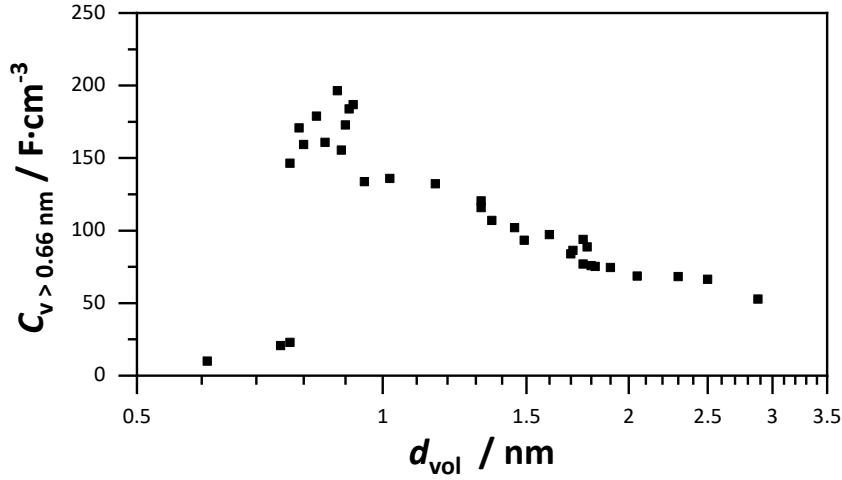


Figure 148: The volumetric capacitance, normalized by the respective accessible surface area in dependence of the volume weighted average pore size.

4.2.2 Simulation of capacitance using EDLC models

Parts of the following chapter were published.^[302]

Another approach to investigate the specific pore size dependence of the capacitance is the simulation of capacitance values of different porous electrode materials based on EDLC models. As described in section 1.4.4, Hsieh et al. used different capacitor models for micropores and mesopores, and simulated capacitance values of different porous carbons on the basis of the respective physisorption data.^[199] As displayed in Figure 149, the sandwich-type capacitor model was used for micropores and the double-cylinder capacitor model was used for mesopores in order to address the curvature of larger pores more accurately. Based on the model and the physisorption data of the carbon materials, capacitance values can be simulated using the following equation:

$$C_{\text{sim}} = \sum_{\text{micro}} \left(\frac{C}{S} \right) \cdot S_{\text{mic}} + \sum_{\text{meso}} \frac{\epsilon_r \epsilon_0}{b \ln \left(\frac{b}{b-d} \right)} \cdot S_{\text{me}} \quad (26)$$

where C_{sim} is the simulated capacitance, S_{mic} is the specific micropores surface area and S_{me} is the specific surface mesopores surface area.

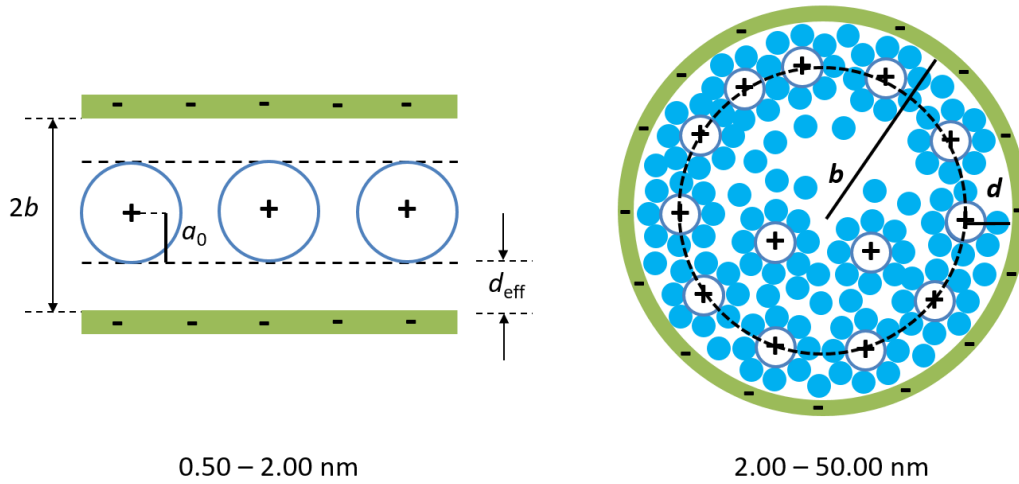


Figure 149: Capacitor models used by Hsieh et al. for the simulation of capacitance values from nanoporous carbons. The sandwich-type capacitor model for micropores (left) and the double-cylinder capacitor model for mesopores (right).

Another important assumption in the simulation of capacitance values was the assessment of the role of micropores. Hsieh et al. postulated, ultimately, each micropore provides the same contribution to the capacitance and thus no anomalous increase of capacitance for pores below 1 nm occurs. An important factor here is the consideration of relative permittivity. In small pores in the range from 0.7 to 2 nm it is assumed the relative permittivity is not constant. The permittivity is determined by the ability of the solvent molecules to conduct the electric field, which is strongly related to their local mobility. In a confined space, such as a small pore, this is greatly restricted, or possibly prevented. Under the assumption that the solvate shell of electrolyte ions can be completely removed, the permittivity is even changed independently of the solvent. Since Hsieh et al. have postulated a constant surface capacitance for the entire micropore range, according to equation (10) the relative permittivity must increase linearly with increasing pores so the conditions are fulfilled. This was a new step, since the concrete change of permittivity has not been considered very intensively thus far.^[11,194,195,198–200]

In the following, the approach of Hsieh et al. is investigated and the capacitance of different carbon samples of this work is simulated on the basis of the physisorption

data. First, surface capacitance values were postulated according to the model and then the cumulative gravimetric specific capacitance of the individual carbon materials were simulated according to the following equation:

$$C_{\text{sim}} = \sum \frac{C}{S}(L) \cdot (S_L - S_{L-1}) \quad (27)$$

where L is the pore width, S_L the pore size associated cumulative specific surface area and S_{L-1} the associated surface area of two consecutive pore sizes. The respective surface capacitance values were calculated using equation (4) for micropores and (26) for mesopores. Values for the relative permittivity ($\epsilon_0 = 9.73$) and the double layer thickness ($d = 1.015$ nm) were acquired from the literature under the consideration of the TEABF₄ concentration in acetonitrile.^[195] With regard to the surface capacitance, a literature-compliant progression was obtained as a function of the pore size, which is shown in Figure 150. The calculated surface capacitance in the pore range of 0.66 to 2.00 nm is $0.085 \text{ F} \cdot \text{m}^{-2}$, which is close to $0.094 \text{ F} \cdot \text{m}^{-2}$ predicted by Stoeckli and Centeno.^[190] The smaller surface capacitance values can be explained by the larger double layer thickness and smaller relative permittivity, caused by the 1 M concentration of the electrolyte. The smallest relevant pore size was determined to be 0.66 nm. It is assumed pores that are inaccessible for the bare TEA⁺ ion (0.67 nm) make no significant contribution to the capacitance. Although the BF₄⁻ ions can still reach these pores (0.45 nm), a larger electrode surface is only covered by electrosorption at the positive charged electrode. These small pores remain unoccupied at the negative electrode, which is why no capacitance is generated in the cell, since the two electrodes are connected in series as individual capacitors. While for the model of Hsieh et al. the capacitance for the micropores is constant, the pore size dependent progression of the surface capacitance for the mesopores shows the already known progression for double-cylinder capacitor. The capacitance is very low at 2 nm and then increases in a growth curve until it reaches the bulk capacitance at 50 nm. Explanations for that are given in literature, as it was originally assumed, that the capacitance is reduced in small pores due to steric restrictions and limited adsorption in small nanopores. Furthermore, it should be considered possible to have a simultaneously increased capacitance of pores in the range from 0.7 to 1.0 nm and reduced capacitance of pores from 2.0 nm onwards. The reason should be a possible pore saturation of electrolyte ions in pores from 2.0 nm.^[103]

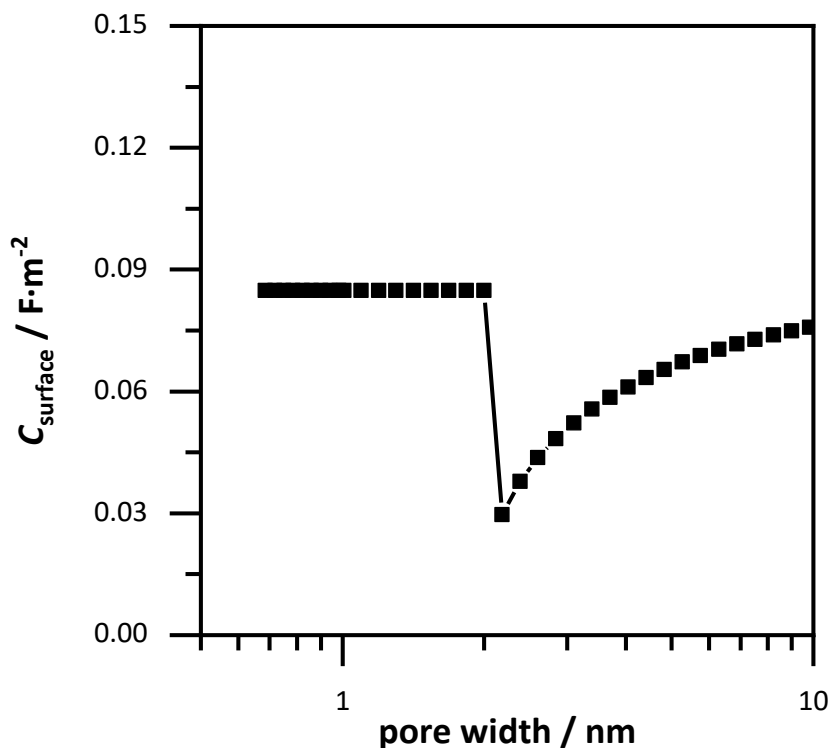


Figure 150: Surface area normalized capacitance dependent on the pore size for TEABF₄ in 1 M ACN, based on sandwich type capacitor for micropores and cylindrical capacitor model for mesopores.

The gravimetric capacitance values were simulated (C_{sim}) for the carbon samples from sections 4.1.2 and 4.1.3 and compared with the measured values (C_{meas}). The purpose was to verify whether the model could be used to determine the dependence of the surface capacitance on the pore size of the carbon material. These exact samples were used, as they range from pure microporous carbons to materials with additional mesopores up to 4.5 nm. The simulated gravimetric capacitance values for the carbon samples are displayed in Figure 151 and the corresponding values are listed in Table 22. Noteworthy, all simulated capacitance values were lower than the measured values, indicating a systematic error in the underlying assumption. Furthermore, the simulated values of the selected carbon samples deviate significantly from the measured values and the deviation of them for C-500-8-T9 is even as high as -31% . The inaccurate simulation of capacitance values can be attributed to three different reasons: (1) The assumption of a constant capacitance for subnanometer pores (< 2 nm) contradicts many observations and is too simplistic. The

confinement effect of electrolyte ions in pores below 1 nm has been observed on numerous occasions, as explained in detail in section 1.4.4. (2) Only two models were used to describe the pore ranges, which is insufficient for the complicated network structures of nanopores in carbons and confinement effects of electrolyte ions. (3) The pores were divided into ranges according to the definition of IUPAC and not into ranges that consider the ion sizes of the respective electrolyte ions. Therefore, a more sophisticated model needs to be developed, which considers the previous mentioned aspects.

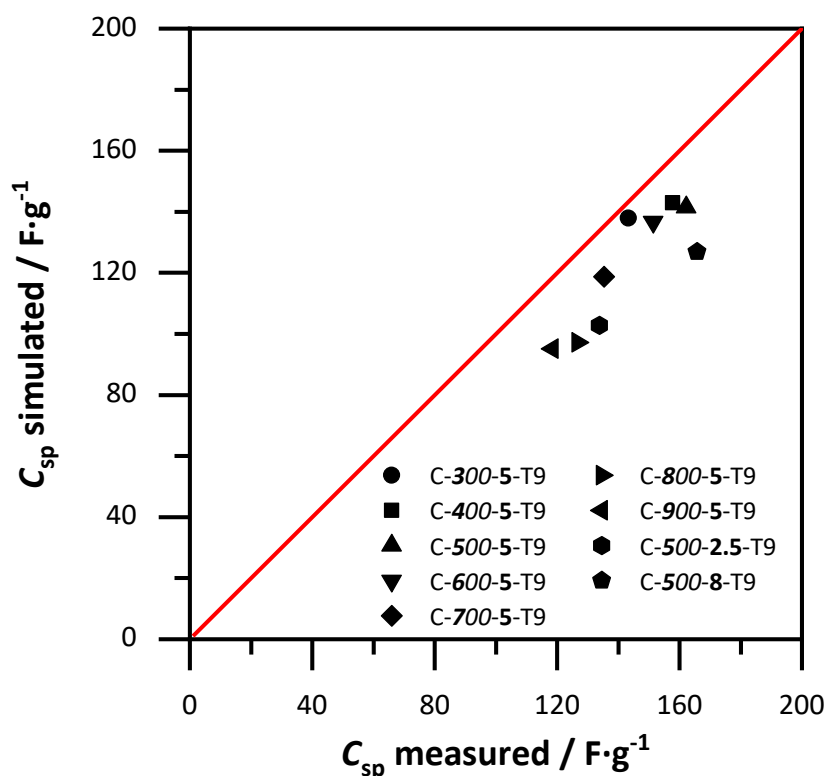


Figure 151: Comparison of simulated and measured gravimetric capacitance values of HSAC from section 5.1.2 and 5.1.3 for sandwich-type capacitor for micropores and cylindrical capacitor model for mesopores.

Table 22: Specific capacitance calculated from discharge tests of EDLC prepared from the carbon samples in 1 M TEABF₄/ACN and the simulated specific capacitance values based on the sandwich capacitor model for micropores and the double-cylinder capacitor model for mesopores.

	$C_{sp} / \text{F} \cdot \text{g}^{-1}$ measured	Sandwich + cylindrical model	
		$C_{sp} / \text{F} \cdot \text{g}^{-1}$ simulated	percentage deviation
C-300-5-T9	143.3	138.0	−4 %
C-400-5-T9	157.9	142.9	−11 %
C-500-5-T9	162.2	141.5	−14 %
C-600-5-T9	151.5	136.7	−11 %
C-700-5-T9	135.4	118.7	−14 %
C-800-5-T9	126.7	97.2	−30 %
C-900-5-T9	118.5	95.1	−25 %
C-500-2.5-T9	133.8	102.8	−30 %
C-500-8-T9	165.8	126.8	−31 %

4.2.2.1 Development of a new EDLC model

In order to overcome the shortcoming of the simplistic combination of sandwich-type capacitor for micropores and double-cylinder capacitor for mesopores, a more sophisticated combined model of these was developed. The pore sizes were divided into four different ranges, each of which was described with a capacitor model. The sandwich type, double-cylinder capacitor model and variations of both were used to obtain the enhanced sandwich double-cylinder capacitor model, or ESDCC model. For this combined model, the pore widths obtained from gas physisorption were divided into four ranges with each of them being described with a different capacitor model as shown in Figure 152. Again, only pores larger than 0.66 nm were considered, because the bare TEA⁺ ion penetrates pores smaller than its ion diameter only in a very limited extent and therefore do not contribute to the cell capacitance. The sandwich double layer capacitor model as shown in Figure 152 a is used for pores sized between 0.66 and 0.90 nm and the capacitance is calculated according to equation (10). Considering the size of the fully solvated ions (1.3 nm for TEA⁺ and 1.1 nm for BF₄[−] in acetonitrile), they need to be fully or partial desolvated to enter small pores between 0.66 and 0.90 nm. For larger pores in the range

of 0.90 and 1.83 nm, solvent molecules are able to enter the pore either free or in a solvation shell and become involved in the double layer formation. Therefore it is assumed the screening length of the double layer changes from the effective double-layer thickness d_{eff} (Figure 152 a) to the original double-layer thickness d . It is also assumed the model can still be described as a sandwich-type double layer capacitor, as shown in Figure 152 b. And the capacitance can be calculated according to equation (4) developed by Helmholtz, while the double-layer thickness is the pore radius of the carbon material. For pores larger than 1.83 nm, it is suspected the pore wall curvature has an influence on the double layer formation, which is best described with a cylindrical capacitor model as shown in Figure 152 c,d.

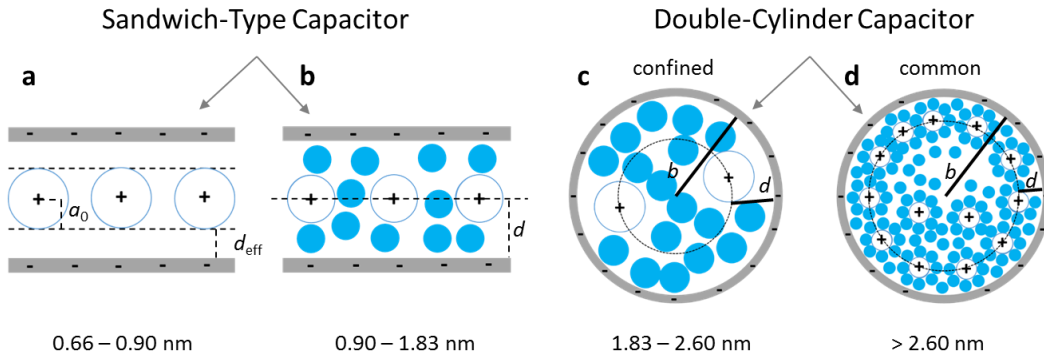


Figure 152: Scheme of the ESDCC model. (a) The sandwich double layer capacitor with d_{eff} and the average ion radius $a_0 = 0.278$ nm for pore diameters between 0.66–0.90 nm, (b) the sandwich double layer capacitor for pores with diameters in the range of 0.90–1.83 nm and the double layer thickness d equal to the pore radius, (c) the confined double-cylinder capacitor with restricted access for solvated ions and thinner double layer thickness $d = 0.820$ nm for pores with the radius b and a diameter between 1.83–2.60 nm and (d) the common double-cylinder capacitor model with the double layer thickness $d = 1.050$ nm for pores with the radius b and diameters larger than 2.60 nm.

Although the synthesized carbon materials in this work probably possess mostly slit shaped pores, regardless of the pores diameter, the curvature of pore walls for larger pores plays a significant role in the double layer formation.^[197,200] Since it is not possible for two or more fully solvated ions to enter pores between 1.83 and 2.60 nm, a restriction of the double layer formation is assumed, resulting in a smaller assumed double-layer thickness of 0.820 nm compared to 1.015 nm for the unrestricted double layer formation for pores larger than 2.60 nm. These values related to the double layer thickness are taken from the literature, whereby the first

refers to higher concentrated electrolyte systems and the latter refers to the electrolyte concentration from this work (1 M).^[194,199] Pores in the range of 1.83 and 2.60 nm are therefore described with a confined double-cylinder capacitor model as shown in Figure 152c. The solvate shells of the electro-adsorbed ions still have to be partially removed, which leads to the above-mentioned restrictions in the pore space. Pores larger than 2.60 nm can be described with the common electric double-cylinder capacitor model as shown in Figure 152d. For both ranges, the theoretical capacitance is calculated according to equation (7) for the electric double-cylinder capacitor model with the respective double-layer thickness d . This new combination of four models shown in Figure 152a-d can be referred to as ESDCC model.

For the relative permittivity, a pore size dependent progression is assumed, as described by Hsieh et al and shown in Figure 153.^[199] In their work they assumed the capacitance is constant for the entire micropores range, which results in a linear increase of the relative permittivity with increasing pore diameter. Two pore size ranges were considered: 0.45 to 2.60 nm and 2.60 to 10.7 nm. The space in the latter pore size range is still considered restricted, which is why a constant value of 9.73 is postulated. For the relative permittivity in the range of 0.45 and 2.60 nm, a pore size dependent progression is assumed. The initial value of the relative permittivity is assumed to be 1 at a pore width of 0.47 nm, at which the bare BF_4^- ion can enter the pore without a solvent molecule being involved in the double layer formation. The pore range of 0.47 to 0.67 nm is taken into account, although this only contributes to the cell capacitance to a negligible small extent. However, the acetonitrile molecules can already penetrate these pores and interact with electrolyte ions, both for the BF_4^- ion and for larger pores for the TEA^+ ion. Therefore, the pore size range from 0.47 to 0.67 nm must also be considered when considering the relative permittivity. All values for ion sizes, relative permittivity and double-layer thickness are taken from literature.^[194,199]

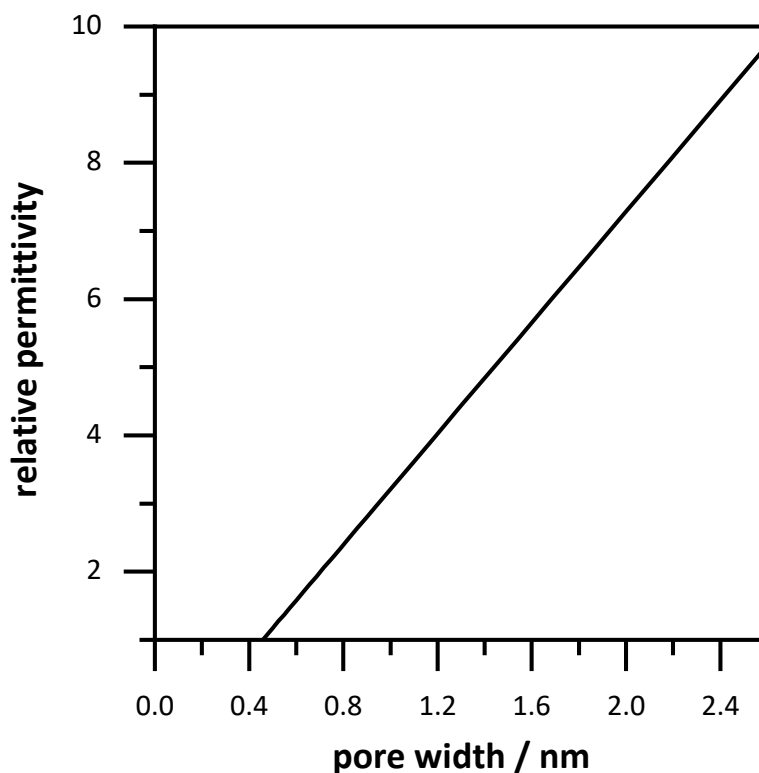


Figure 153: Assumed progression of the relative permittivity for TEABF₄ in 1 M ACN in the pore range of 0.47 to 2.60 nm. The values for the relative permittivity range from 1 to 9.73.

4.2.2.2 Applicability of the ESDCC model

A new combined capacitor model was developed, the ESDCC model, which is more sophisticated than the simplistic combination of the sandwich-type capacitor for the IUPAC defined micropore range and the double-cylinder capacitor model for the mesopores. The correlation of the normalized surface capacitance and pore size is displayed in Figure 154 and is more differentiated than before. Pores with a size of 0.66 nm provide the largest contribution to the surface area normalized capacitance and with increases in pore size, the capacitance decreases exponentially. Pores larger than 0.90 nm have significantly smaller surface capacitance values and differ to a smaller extent, except for the pores ranging in size from 1.83 to 2.6 nm.

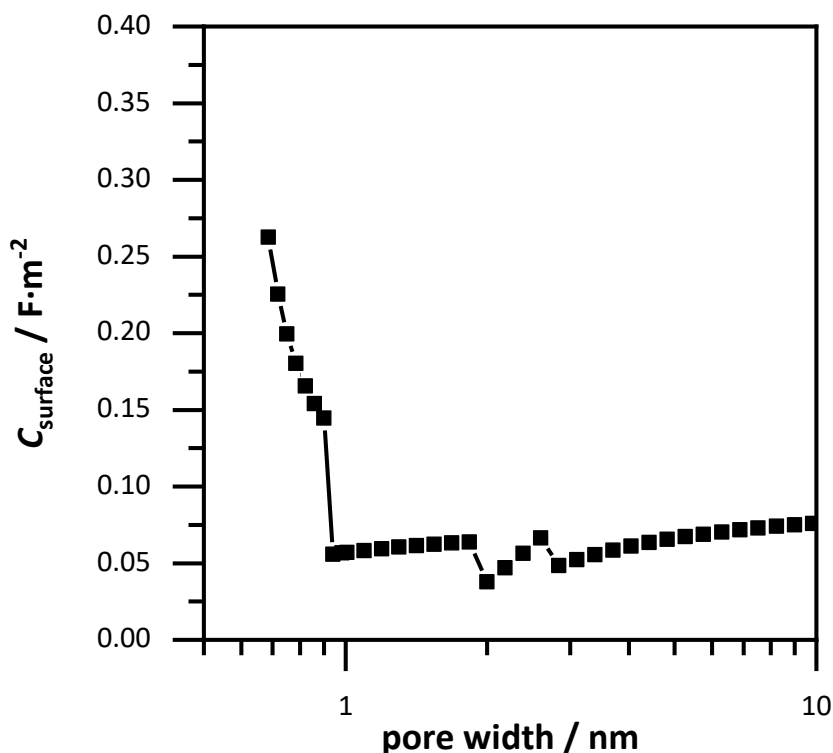


Figure 154: Surface area normalized capacitance dependent on the pore width, based on the ESDCC model in TEABF₄ in 1 M ACN. Values for $a_0 = 0.278$ nm and $d = 0.820$ nm were obtained from ref.^[199].

Comparing the simulated gravimetric capacitance values of the carbon samples employing the ESDCC model with the measured values, a better match can be observed as shown in Figure 155 and summarized in Table 23, compared to the previously investigated pore size-capacitance mode. With the exception of C-700-5-T9 and C-500-2.5-T9, all simulated values match with the measured values within a maximum deviation of 10 %. Considering the higher impact on the capacitance of subnanometer pores below 0.90 nm, the ESDCC model confirms the anomalous increase of capacitance for pores around 0.70 nm. It also reflects the more sophisticated classification of pore sizes depending on the electrolyte ions that are used, and the extension of capacitor modes is important for the determination of capacitance values of carbon materials with different pore sizes. However, the percentage deviation of the simulated values, compared to the measured values for C-700-5-T9 and C-500-2.5-T9 is still as high as -21 % and -23 % respectively. Although the ESDCC model is a more sophisticated approach to describe the influence of the

pore size on capacitance, the assumed pore geometries (slit-shaped pre and cylindrical pores) are rather simple considering the complex structure of activated carbons. As a result, some simulated values can deviate from the measured values for example samples C-700-5-T9 and C-500-2.5-T9, which shown significant deviations from their respective measured values.

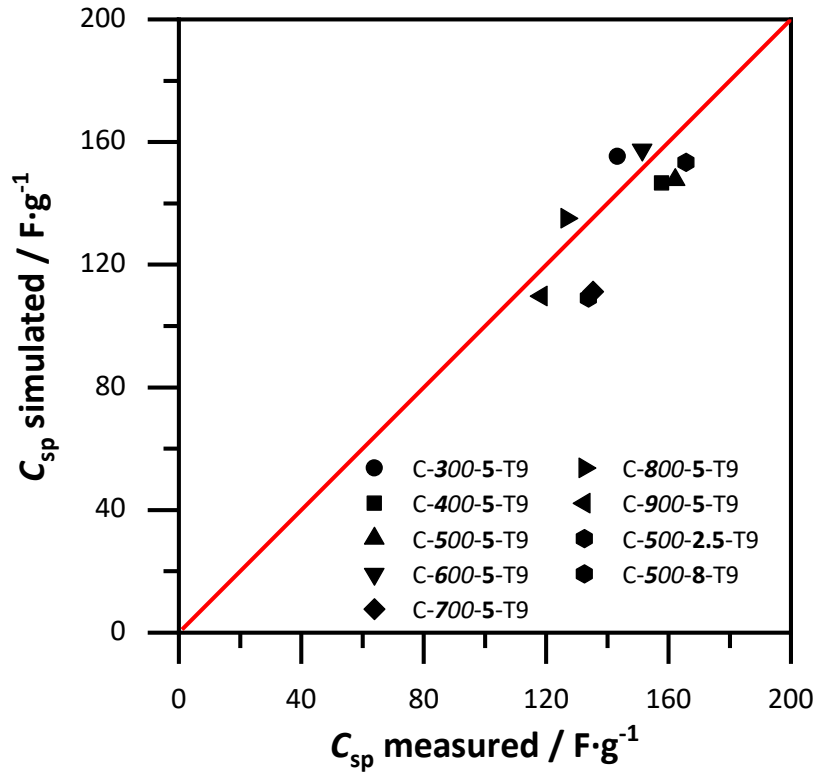


Figure 155: Comparison of simulated and measured gravimetric capacitance values for the ESDCC model.

Table 23: Specific capacitance calculated from discharge tests of EDLC prepared from the carbon samples in 1 M TEABF₄/ACN and the simulated specific capacitance values based on the ESDCC model.

	$C_{sp} / \text{F} \cdot \text{g}^{-1}$ measured	ESDCC	
		$C_{sp} / \text{F} \cdot \text{g}^{-1}$ simulated	percentage deviation
C-300-5-T9	143.3	155.3	+7 %
C-400-5-T9	157.9	146.6	−8 %
C-500-5-T9	162.2	147.7	−10 %
C-600-5-T9	151.5	157.5	+4 %
C-700-5-T9	135.4	111.2	−21 %
C-800-5-T9	126.7	135.0	+6 %
C-900-5-T9	118.5	109.8	−8 %
C-500-2.5-T9	133.8	109.1	−23 %
C-500-8-T9	165.8	153.4	−8 %

4.2.2.3 Modification of the ESDCC model

The ESDCC model provided a more reasonable relation of capacitance and pore width than the simplistic two-model combination of sandwich-type capacitor and double-cylinder capacitor. However, due to the complex pore structure of activated carbons, not all gravimetric capacitance values of the chosen carbon samples were adequately simulated. Therefore a modification of the ESDCC model was performed, to adapt the simulated gravimetric capacitance values to the experimentally measured values for all selected carbon materials. For this purpose, a factor modification of the capacitance values of each individual pore size was performed to minimize the average deviation (AD) of the overall measured and simulated capacitance values. To determine the factors, the nonlinear generalized reduced gradient (GRG) method was used to solve for the smallest possible average deviation of all selected carbon samples. The GRG method is a generalization of the reduced gradient method by allowing nonlinear constraints and arbitrary bound on the variables. The method is based on the Davidon-Fletcher-Powell algorithm.^[303] The average deviation was calculated by the following equation:

$$AD = \frac{1}{n} \sum_{i=1}^n \left| 100 - \frac{C_{\text{meas},i}}{C_{\text{sim},i}} \cdot 100 \right| \quad (28)$$

The modified ESDCC was developed using this method. All factors for the ESDCC model and theoretical surface area normalized capacitance values for the modified ESDCC model are listed in Table A1. It is worth mentioning the factor modification with the nonlinear GRG method only worked well for the ESDCC model. Neither the factor modification for the first discussed combined sandwich/double-cylinder capacitor model nor the a factor modification of a constant surface capacitance for all pore sizes provided satisfactory results in terms of a low average deviation and reasonable physical correlation of the pore size dependent values. As shown in Figure 156, the correlation of surface capacitance and pore size of the modified ESDCC model became more complex, but the simulated capacitance values are in agreement with the measured values, which is displayed in Figure 157 and summarized in Table 24. The highest deviation is as small as 7 % for C-500-5-T9 and the simulated capacitance values for C-300-5-T9, C-400-5-T9, C-600-5-T9, C-900-5-T9, C-500-2.5-T9 and C-800-5-T9 are even identical with the measured gravimetric capacitance values. This emphasizes the mathematical validity of the modified ESDCC model.

In the following text, the physical meaning of the correlation between surface capacitance and pore sizes will be discussed. As seen in Figure 156, pore sizes between 0.72 and 0.75 nm exhibit the largest values for the normalized capacitance, which indicates the strong influence of partially or fully desolvated ions on the capacitance of EDLCs as proposed in the theory of the anomalous increase of capacitance for subnanometer pores.^[152,153] The confined space in these pores results in a decrease of pore wall and electrolyte ions, which increases the strength of the electric field, thus increasing the capacitance or electrochemical utilization of the pore surface. With increasing pore sizes the surface capacitance decreases, which is in accordance to the sandwich capacitor model displayed in Figure 152 a. The pore spaces are less restricted and electrolyte ions with a more prominent solvate shell can penetrate the pore, increasing the distance to the pore wall, increasing the double layer thickness and thus reducing the capacitance. Interestingly, the surface area normalized capacitance slightly increases again for pores with the size of 0.90 nm and again for pores around 1.0 nm, though the capacitance of the former pore size

is larger than the surface capacitance of the latter. Electrolyte ions, which enter subnanometer ultramicropores contribute to the capacitance to a higher extent, but the amount of electrolyte ions, which can enter the pores is still limited, due to steric hindrance. This may change for 0.90 nm sized pores. Electrolyte ions can enter the pores without removing the entire solvent shell, which leads to an increase of surface capacitance, creating an improved electrochemical utilization of the electrode surface. For pores around 1 nm, BF_4^- ions can enter the pores almost fully solvated, which may result in a minor increase of the surface area normalized capacitance. For pores in the range of 1.0 to 1.3 nm, the surface capacitance decreases again. This can be explained with the sandwich capacitor model as shown in Figure 152 b. The electrolyte ion is centered between the pore walls, and with increasing pore size, the distance to the pore walls and thus the thickness of the double layer increases, resulting in a lower surface capacitance.

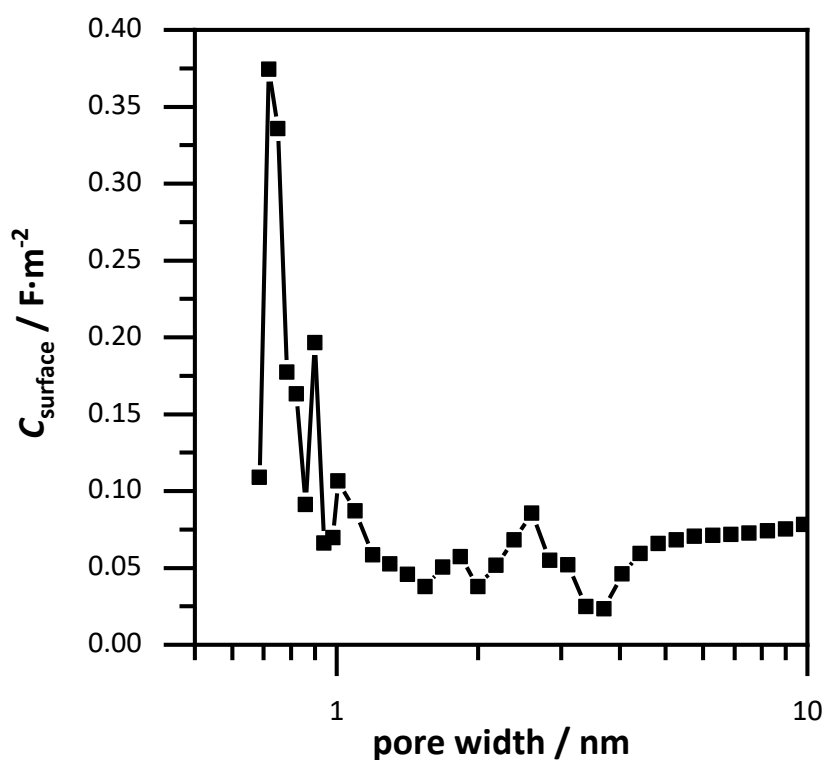


Figure 156: Surface area normalized capacitance dependent on the pore size, based on the modified ESDCC model in TEABF_4 in 1 M ACN.

Full accessibility of solvated TEA^+ ions towards pores ranging from 1.30 to 1.86 nm may be responsible for the slight increase of surface capacitance in the respecting pore size range. The double layer thickness remains, but the number of adsorbed electrolyte ions leads to the increase of surface capacitance or utilization of the electrode surface. A larger increase of capacitance is observed for pores ranging from 2.0 to 2.6 nm. This can be attributed to the fact that more solvated ions are able to enter the pores, which participate in the electric double layer formation for both ions. Additionally, a smaller thickness of double layer is assumed to the previously discussed confinement effect, displayed in Figure 152 c. Despite the coulomb repulsion of two equal polarized ions, it is assumed two ions of equal charge are able to enter pores between 2.3 and 2.6 nm at their respective electrodes. This then results in a smaller double layer thickness and leads to a higher normalized capacitance.

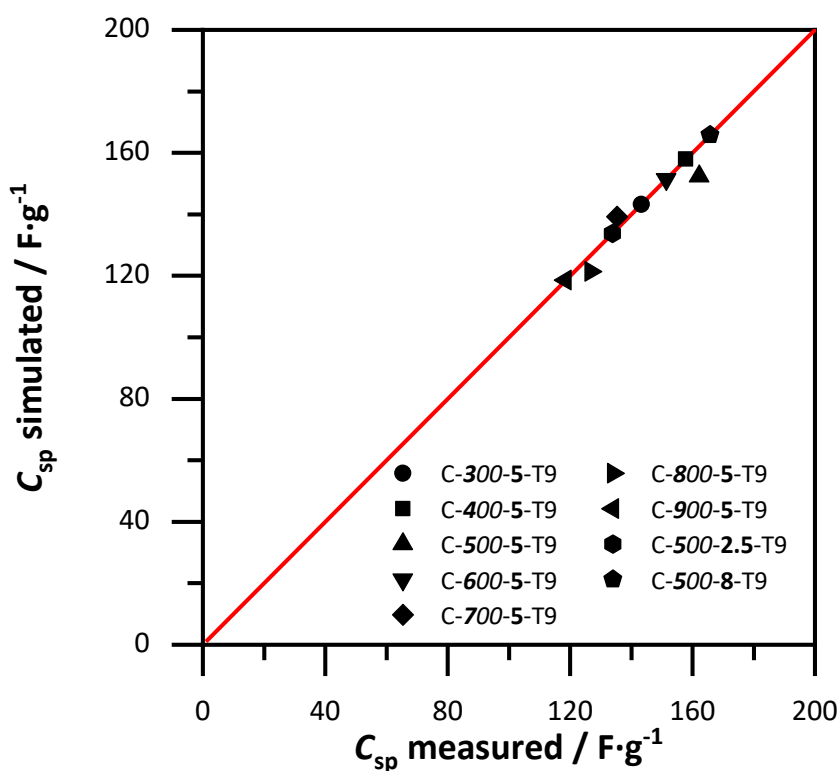


Figure 157: Comparison of simulated and measured gravimetric capacitance values for the selected carbon samples based on the modified ESDCC model.

Noteworthy, the surface capacitance decreases again and reaches an overall minimum for pore sizes between 3.4 and 3.7 nm. A destructive interference of the electric double layer from opposing pore walls may be the cause, as Jiang et al.^[304] and Feng et al.^[305], found an oscillatory behavior for capacitance with increases of the pore size. However, this has only been proven for ionic liquids and has yet to be validated for organic electrolytes. A confinement effect is a more likely the reason than an interference of electric double layers. For these pore sizes, a maximum of three fully – or partially desolvated ions are able to enter a pore at the same time due to steric hindrance caused by the pore geometry and Coulomb repulsion of the electrolyte ions. Therefore, the degree of adsorbed ions on the pore's surface is rather low similar to pores in the range of 1.8 to 2.6 nm (Figure 152 c). Nevertheless, compared to pore sizes of 1.8 to 2.6 nm, the double-layer thickness for pores between 3.4 and 3.7 nm is estimated to be thicker with 1.015 nm compared to 0.820 nm, which results in a lower surface capacitance for the considered pore sizes. The capacitance increases with pores larger than 3.7 nm and shows no significant deviations from the ESDCC model described in Figure 152. More solvated ions are able to enter the pores and occupy the pore surface, thus increasing the capacitance until confinement effects, and the influence of the pore wall curvature, becomes less significant.

Table 24: Specific capacitance calculated from discharge tests of EDLC prepared from the carbon samples in 1 M TEABF₄/ACN and the simulated specific capacitance values based on the modified ESDCC model.

	$C_{sp} / \text{F} \cdot \text{g}^{-1}$ measured	ESDCC modified	
		$C_{sp} / \text{F} \cdot \text{g}^{-1}$ simulated	percentage deviation
C-300-5-T9	143.3	143.3	± 0 %
C-400-5-T9	157.9	157.9	± 0 %
C-500-5-T9	162.2	152.2	-7 %
C-600-5-T9	151.5	151.5	± 0 %
C-700-5-T9	135.4	139.3	+3 %
C-800-5-T9	126.7	121.5	-4 %
C-900-5-T9	118.5	118.5	± 0 %
C-500-2.5-T9	133.8	133.8	± 0 %
C-500-8-T9	165.8	165.8	± 0 %

Having rationalized the pore-size dependent contribution to the overall capacitance in this way, the comparatively low specific capacitance of C-400-5-T9 and especially C-300-5-T9 can be explained, despite their large accessible surface area of $\sim 2000 \text{ m}^2 \cdot \text{g}^{-1}$. C-300-5-T9 and C-400-5-T9 have a larger amount of pores between 3.4 and 3.7 nm, which possess a low surface capacitance and therefore contribute to the overall capacitance to a very low extent. The capacitance values simulated with the modified ESDCC method matched, with good accuracy, the measured values of nine activated carbons with different pore sizes. It is therefore believed the gravimetric specific capacitance of various activated carbons can be simulated with the modified ESDCC model, on the basis of a thorough investigation of the respective porosity of the carbon samples.

The progression of the simulated cumulative gravimetric capacitance for the carbon samples activated with different KOH/carbon ratios is shown in Figure 158. It is noticeable at first that the simulated capacitance of sample C-500-1-T9 is significantly higher than the measured capacitance. This is caused by the fact that the

simulated capacitance assumes the maximum attainable capacitance and is compared with the corresponding maximum measured capacitance. This is the case for almost all materials at a low current density of $1 \text{ A} \cdot \text{g}^{-1}$, as could be confirmed in the respective impedance spectroscopy. However, sample C-500-1-T9 is an exception. The pores were so small that the diffusion resistance of the electrolyte ions in the narrow pore network was too high even at the low current density, so the true maximum capacitance could not be attained. Samples C-500-2.5-T9, C-500-5-T9, C-500-8-T9 and C-900-5-T9 show that half the capacitance of pores below 1 nm is generated. This is due to the fact that they show the highest electrochemical utilization of the carbon surface. Surprisingly, sample C-500-8-T9 has the highest capacitance up to 0.98 nm, although it may have the least surface area generated by pores in the 0.66 - 0.98 nm range. However, it is important to note sample C-500-8-T9 has a large surface area generated by pores between 0.79 and 0.82 nm, which provide the highest capacitance. This is the reason why sample C-500-8-T9 has the highest surface capacitance. The varying influence of different pore sizes becomes very clear, since the pores at 1 nm and from 1 to 3 nm of sample C-500-8-T9 provide almost the same cumulative capacitance, although the pore range from 1 to 3 nm generates $500 \text{ m}^2 \cdot \text{g}^{-1}$ more surface area. Sample C-500-2.5-T9 and C-900-5-T9 are mostly microporous and therefore these pores also provide the capacitance. The unusually large step around 1 nm is due to the transition from carbon dioxide physisorption to nitrogen physisorption.

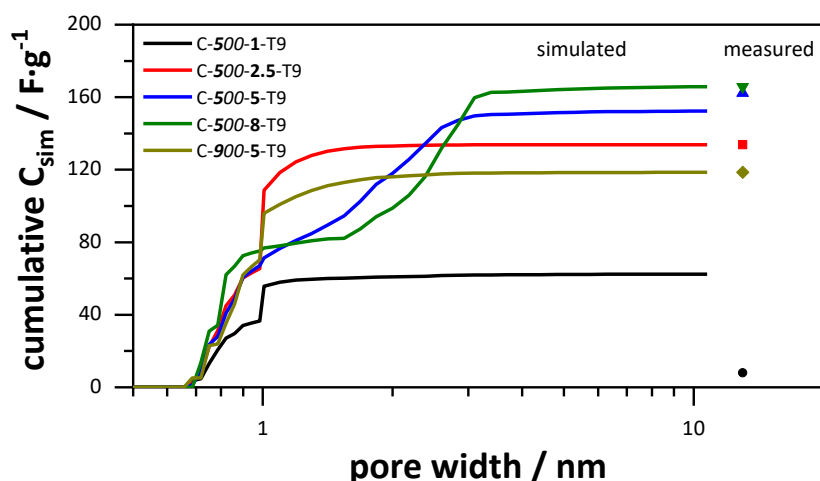


Figure 158: Simulated cumulative gravimetric capacitance in dependence of the pore width of the carbons, synthesized with different KOH/carbon ratios and their respective measured capacitance values in comparison.

The simulated cumulative gravimetric capacitance of the carbon samples synthesized at different semi-carbonization temperatures is shown in Figure 159. In general, it was determined the capacitance correlates with the accessible surface. Sample C-800-5-T9, C-700-5-T9 and C-600-5-T9 are mainly microporous and the capacitance is generated by pores down to 2 nm. Approximately half of the capacitance is generated by pores up to 0.98 nm, while a sharp rise in capacitance at 1 nm is again visible. Sample C-300-5-T9 barely differs from sample C-400-5-T9, except in sample C-300-5-T9 more surface is generated by pores between 2 and 4 nm. However, these have a lower surface capacitance, which is the reason why the gravimetric capacitance is not increased significantly. The decisive factor is that sample C-300-5-T9 has significantly less capacitance from pores down to 0.98 nm, is eventually important since the gravimetric capacitance is comparatively low, even though the material has a very high accessible specific surface area of over $2000 \text{ m}^2 \cdot \text{g}^{-1}$.

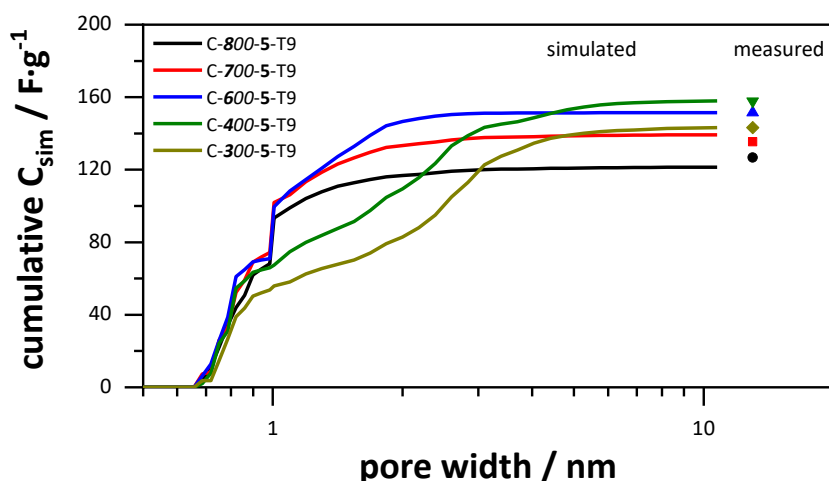


Figure 159: Simulated cumulative gravimetric capacitance in dependence of the pore width of the carbons, synthesized at different semi-carbonization temperatures and their respective measured capacitance values in comparison.

4.2.2.4 Applicability of the modified ESDCC model

As seen in section 4.2.2.3, the modified ESDCC model provided the possibility to simulate the gravimetric specific capacitance for various carbon samples that are in strong agreement with measured capacitance values and provided valuable information about the relation of surface capacitance and pore size at the same time. The model worked well for nine selected carbon materials and confirmed the surface area provided by pores around 0.8 nm is decisive for the overall gravimetric capacitance, as suggested by the modified ESDCC model. In this section, the ESDCC model is applied to the remaining carbon samples in order to verify the results from the previous section. In addition, the differentiated influence of the pores on the capacitance will be exemplified by the respective curves of the cumulative gravimetric capacitance. The results from the applicability of the modified ESDCC model are summarized in Table A.1.

The simulated capacitance data of the carbons, synthesized at different activation temperatures are displayed in Figure 160. To evaluate the modified ESDCC model, the percentage difference between the simulated capacitance values and the measured capacitance values was first considered. It turns out the modified ESDCC model can simulate all four values quite well, and the percentage deviation is only $\pm 5\%$ for all carbon samples. Additionally, the order of the maximum capacitance

of the four samples is correctly simulated and predicted. The progression of the cumulative capacitance values shows the samples C-500-5-T8, C-500-5-T7 and C-500-5-T6 generate significantly more capacitance by the pores around 0.8 nm, which is decisive for the high capacitances of sample C-500-5-T8 and C-500-5-T7. In addition, these two samples have a high capacitance through pores around 1 nm, which is caused by the increase of surface capacitance for pores around 1 nm. Sample C-500-5-T10 has on average larger pores, especially in the range of 1 to 3 nm, which also generate a large proportion of the capacitance. Since these pores have a lower surface capacitance compared to pores between 0.8 and 1 nm, this material has a comparatively low maximum capacitance compared to samples C-500-5-T8 and C-500-5-T7, which obtain a large part of their capacitance from pores up to 1.1 nm. The pores in the range of 1 to 3 nm are nevertheless an important factor. Although these have a comparatively lower surface capacitance, the respective surface is widely accessible and can be easily generated synthetically. In addition, the pores at 2.5 nm show a further maximum in surface capacitance, which is the reason why sample C-500-5-T10 exhibits a higher gravimetric capacitance than sample C-500-5-T6, which has fewer pores between 2 and 3 nm.

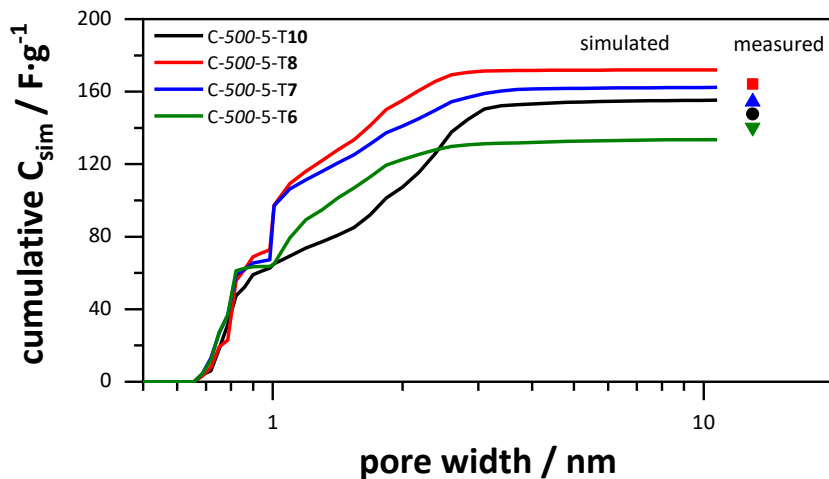


Figure 160: Simulated cumulative gravimetric capacitance in dependence of the pore width of the carbons, synthesized at different activation temperatures and their respective measured capacitance values in comparison.

The results from the capacitance simulation with the modified ESDCC model for the carbon materials, which were synthesized at different semi-carbonization tem-

peratures and a low KOH/carbon ratio of 2.5, are shown in Figure 161. It is immediately noticeable that the simulated capacitance of sample C-900-2.5-T9 is significantly higher than the measured capacitance. The reason for this is once again the measured capacitance at $1 \text{ A} \cdot \text{g}^{-1}$ is not the maximum achievable capacitance, as could be determined by impedance spectroscopy. Therefore, the modified ESDCC model cannot be used for comparison in this case. The simulated capacitance values of the other five samples, with the exception of sample C-600-2.5-T9, are in agreement with the measured values with a maximum difference of 7 %. Sample C-600-2.5-T9 shows a percentage deviation of -14 %, which is a higher difference than all other carbon samples, but the difference of the values is only $14.5 \text{ F} \cdot \text{g}^{-1}$. This can be explained, by the significantly lower capacitance values of this synthesis series compared to those of the other materials discussed in this work. Thus, similar differences in capacitance result in higher percentage differences. However, this only applies to this one sample in particular. The literature has also shown a deviation of 10 % is still within the scientifically acceptable scope in order to classify a model as reasonable.^[200] Thus, the maximum achievable capacitance values of this synthesis series can be accurately simulated with the modified ESDCC model. Nearly the entire capacitance of all carbon samples is generated by pores up to 0.98 nm and around 1 nm. Samples C-700-2.5-T9, C-600-2.5-T9 and C-400-2.5-T9 show the highest gravimetric capacitance, generated by pores down to 0.98 nm and also the highest capacitance generated by pores just above 1 nm. These three samples also have the highest capacitance values. The highest capacitance of the carbons is attributed to sample C-400-2.5-T9, because it also has pore sizes between 1 and 2 nm, which provide high surface capacitance values. Compared to samples with larger pores and surface areas, the capacitance values are sometimes 30 to $60 \text{ F} \cdot \text{g}^{-1}$ lower, which is still more than half of the capacitance (100 to $113 \text{ F} \cdot \text{g}^{-1}$ compared to 140 to $160 \text{ F} \cdot \text{g}^{-1}$). These are of course significant differences. However, it should be noted the accessible surface areas of the other carbon samples are sometimes more than twice as large (800 to $1000 \text{ m}^2 \cdot \text{g}^{-1}$ compared to $2000 \text{ m}^2 \cdot \text{g}^{-1}$) and the differences in capacitance are significantly smaller. The explanation for this can be found in the modified ESDCC model, which confirms pores around 0.8 nm provide a considerably higher surface capacitance than pores between 2 and 4 nm. The carbons of this synthesis series have a predominance of micropores due to the

small KOH/carbon ratio at activation and the partially high semi-carbonization temperatures.

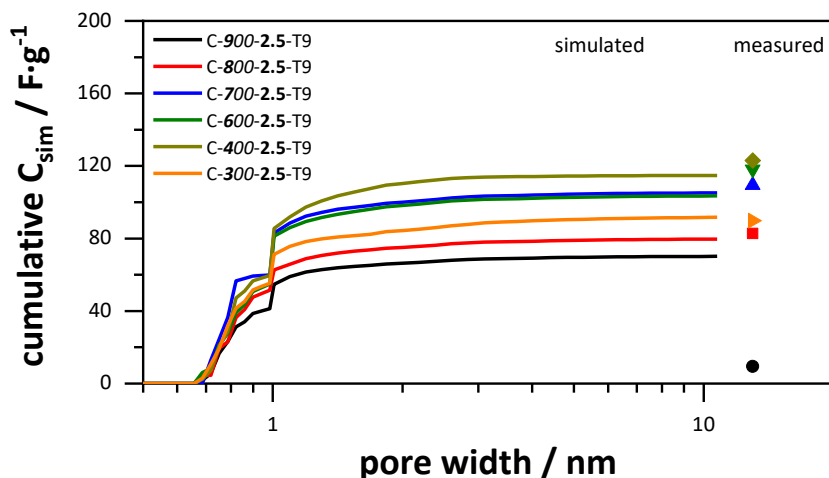


Figure 161: Simulated cumulative gravimetric capacitance in dependence of the pore width of the carbons, synthesized at different semi-carbonization temperatures and a KOH/carbon ratio of 2.5 and their respective measured capacitance values in comparison.

The cumulative simulated gravimetric capacitance values for the carbon samples, synthesized at a semi-carbonization temperature of 900 °C and different activation temperatures, are shown in Figure 162. The percentage deviation of the simulated and measured capacitance values are between 5 and 10 % and are therefore well within the scope, discussed previously. And even if the deviation of 10 % for sample C-900-5-T7 appears slightly higher, the difference of the capacitance values is only as small as 10 F·g⁻¹. Sample C-900-5-T6 can be considered an exception because the pores of the carbon material are so small, that, even at low frequencies and current densities, the diffusion resistance of the electrolyte ions is so high that the maximum achievable capacitance cannot be measured, which was confirmed via PEIS. Thus, this sample falls outside the evaluation criteria for the modified ESDCC model. Carbon sample C-900-5-T10 has the highest capacitance because the material has pores in the range of 1 to 3 nm, which can also contribute, in a larger extent, to the capacitance. This is especially the case for pores between 2 and 3 nm, which have a higher surface capacitance. Sample C-900-5-T7 and C-900-5-T6 have approximately the same capacitance, although sample C-900-5-T7 exhibits more capacitance for pores up to 0.98 nm. On the other hand, the pore content just

above 1 nm are slightly higher for sample C-900-5-T6, ultimately leading to a similar capacitance.

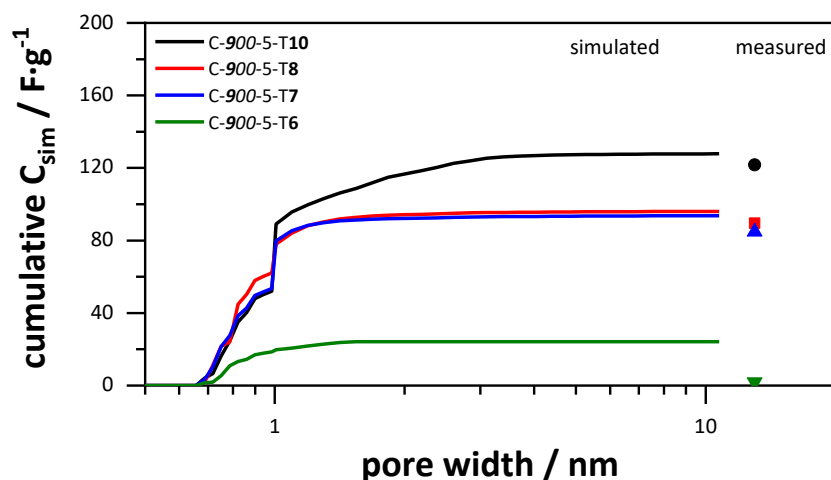


Figure 162: Simulated cumulative gravimetric capacitance in dependence of the pore width of the carbons, synthesized at different activation temperatures with a semi-carbonization temperature of 900 °C and their respective measured capacitance values in comparison.

The cumulative simulated capacitance progressions with the pore size of the carbon materials, synthesized from formaldehyde resins with different phenol/resorcinol ratios, are shown in Figure 163. Simulated and measured gravimetric capacitance values of the carbon samples are in agreement with percentage deviations between 5 and 10 %, which is within the scope of scientific tolerance. The porosity of the four carbon materials was relatively similar, thus the respective capacitance values did not differ significantly. The gravimetric capacitance, which is generated by pores up to 0.98 nm, is also nearly identical for all samples. Only the capacitance which is partly induced by the physisorption gas change, for pores around 1 nm, is higher for samples C-PR-2/1 and C-PR-1/2, which ultimately leads to a higher maximum capacitance. The pore size range between 0.98 and 1.01 nm is therefore also decisive, as these pores have a high surface capacitance and not only due to the fluid change of the sorption measurements.

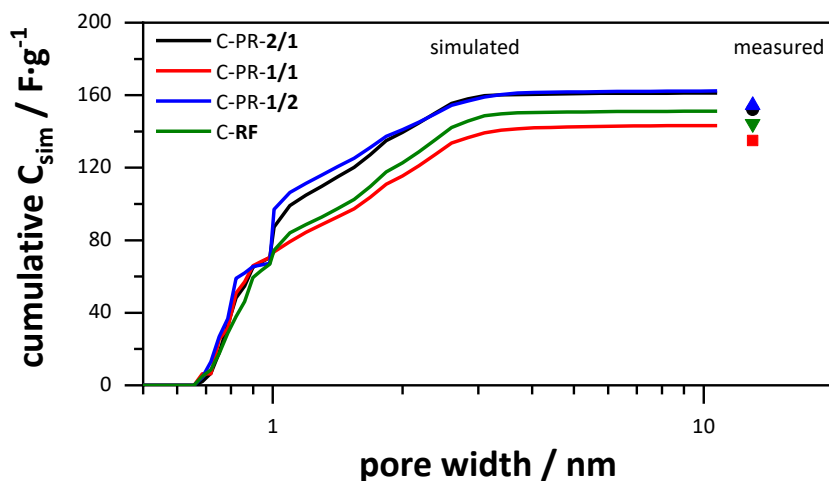


Figure 163: Simulated cumulative gravimetric capacitance in dependence of the pore width of the carbons, synthesized from formaldehyde resins with different phenol/resorcinol ratios and their respective measured capacitance values in comparison.

Lastly, the progression of the simulated cumulative gravimetric capacitance of the carbons samples, synthesized from FC-cross-linked formaldehyde resins with different phenol/resorcinol ratios are shown in Figure 164. Again, the porosity of the materials is very similar, and the maximum capacitance values are correspondingly similar, which is also reflected in the capacitance values simulated using the modified ESDCC model. In particular, the capacitance contribution of pores from 1.01 to 4 nm is the same for all five samples and is about $50 \text{ F} \cdot \text{g}^{-1}$. The capacitance contribution for pores up to 0.98 nm is also very similar for all samples, but the progression in the pore range of 0.66 to 0.98 nm is very different. Samples FC-PR-2/1 and FC-PR-1/2 have already generated a high capacitance up to 0.8 nm, explained by the high surface capacitance of these pores. For samples FC-PR-1/1 and FC-RF, however, the capacitance is rather generated by pores between 0.83 and 0.98 nm. For sample FC-PF the capacitance is provided very uniformly in the mentioned pore range. A straightforward explanation for this is not easy to provide, as these progressions do not show an exact trend towards the phenol/resorcinol ratio. It could still be assumed a higher resorcinol content in the formaldehyde resin leads to fewer pores being present up to 0.8 nm, which means these pores provide a correspondingly small capacitance contribution. However, this cannot be clearly proven, because this could not be achieved with either the previous carbon samples without FC cross-linking of the formaldehyde resins. It is therefore rather due to

differences in porosity that occurred during the synthesis itself, such as different argon gas flows during semi-carbonization.

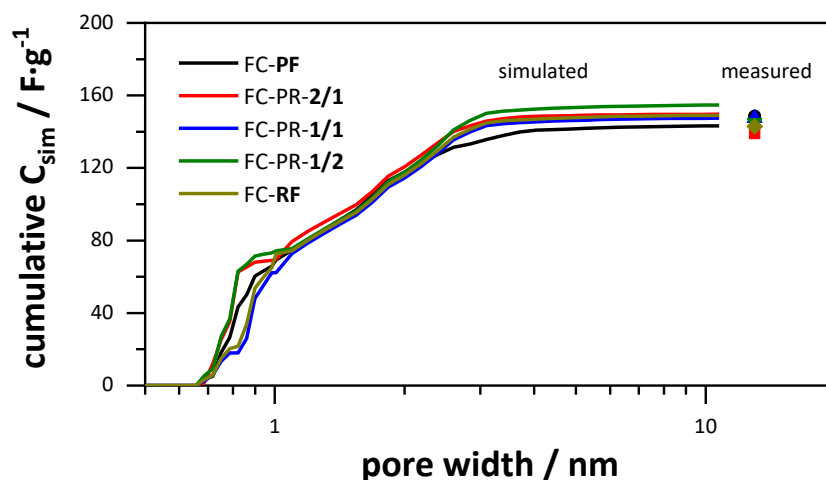


Figure 164: Simulated cumulative gravimetric capacitance in dependence of the pore width of the carbons, synthesized from FC-cross-linked formaldehyde resins with different phenol/resorcinol ratios and their respective measured capacitance values in comparison.

Understanding the influence of pore sizes of carbon electrode materials on the capacitance of EDLCs is desirable, since the amount of stored energy should be as large as possible. Therefore, a new combined model was developed, based on sandwich-type capacitors for micropores and double-cylinder capacitors for mesopores, respectively, which includes confinement effects and is named ESDCC model. Factors for the capacitance values of each pore size were optimized with the nonlinear GRG method to obtain a refined relation of pore sizes and capacitance, which were validated by comparing simulated capacitance values with experimentally measured capacitance values. The agreement of simulated capacitance values with the measured capacitance values was very good for 30 samples, with a maximum percentage deviation of 10 % and a maximum capacitance difference of $13.5 \text{ F} \cdot \text{g}^{-1}$, as shown in Figure 165.

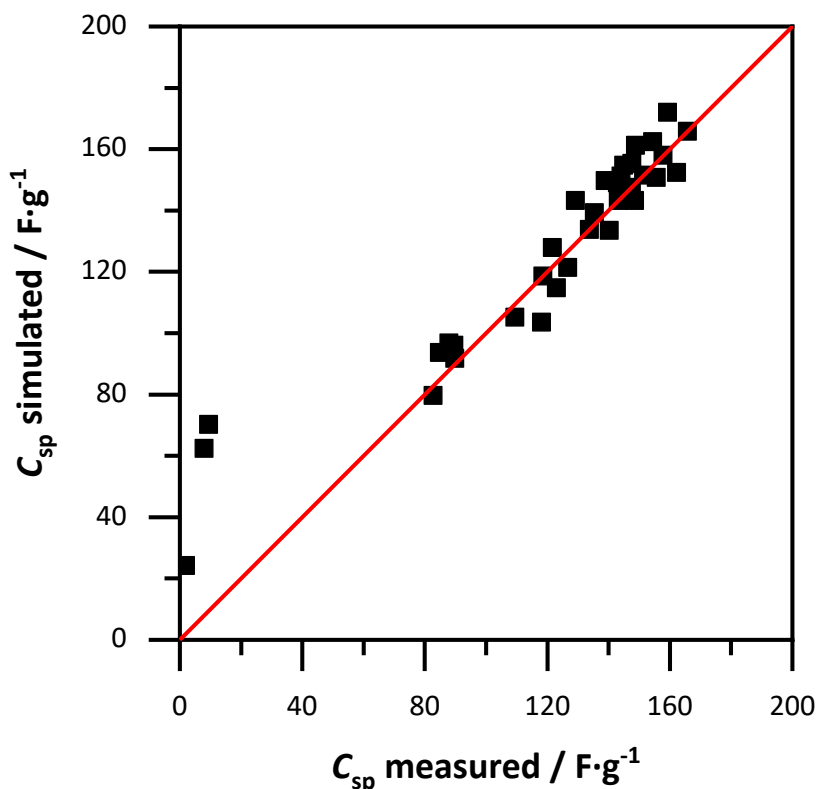


Figure 165: Comparison of simulated and measured gravimetric capacitance values for every carbon sample from the entire work, based on the modified ESDC model.

New insights could be obtained by the representation of the pore size dependent surface capacitance, based on the modified ESDCC model. The results show that pores below 1 nm provided the largest surface capacitance, especially pores between 0.74 and 0.90 nm, confirming the effect of an anomalous increase of capacitance for pores with the size of bare TEA^+ ions, while pores between 3.4 and 3.7 nm provide the lowest surface capacitance. This is supported by the fact the surface capacitance decreases with increasing pore volume of the carbon samples. However, the accessible surface area remains a key factor regarding the capacitance. Although specific surface area and average pore sizes are not linearly dependent on each other, it has been observed that synthesis parameters leading to carbons with high specific surface areas also lead to larger pores. Therefore, maximizing the capacitance is difficult, as an increase in specific surface area is associated with simultaneous enlargement of pore sizes, which neutralize their effects on the capacitance. Thus, the capacitance decreases which is demonstrated with carbon materials

C-300-5-T9 and C-400-5-T9 for example. With the new developed modified ESDCC model, it is possible to simulate the gravimetric capacitance values for activated carbon materials on the basis of physisorption derived data from carbon dioxide and nitrogen in combination. The model is applicable for EDLCs with TEABF₄ in acetonitrile. However, it can be expected, the factor modification approach of the ESDCC model can also be applied to other carbon/electrolyte systems for the optimization of EDLCs with regard to energy performance for the following reasons: (1) the modified ESDCC model was developed for and applied to various carbons with different range of pore sizes. The capacitance of both purely microporous carbons as well as carbons with additional mesopores up to 5 nm, was adequately simulated. (2) it was possible to assign a physical meaning to any feature of capacitance dependency on pore size, with the ion size being an important factor. The basic assumptions of the ESDCC model can be applied to other electrolyte systems. (3) the pore size dependence of the relative permittivity was also considered in the ESDCC model, which is an important factor on the capacitance and can be adjusted to other solvents.

4.2.3 Influence of pore size on capacitance retention

The most important factor for a functioning and usable EDLC device is certainly the energy it should provide, and this should be identified as the most important benchmark criteria. However, it is also very important that the advantages of the capacitor, fast storage and release of the energy, should be given at any power rate. This is actually the most decisive characteristic with which supercapacitors differ from batteries in terms of application. An electrode material for supercapacitors should therefore not only be designed in such a way that it can store as much energy as possible, but it must also enable its rapid storage and release. In concrete terms, this means the ions must be able to move as freely as possible in the EDLC setup system and in the pore system and must also deliver their full capacitance independently of the applied current. Galvanostatic charge/discharge measurements provide an indication of whether potential carbon materials, used as electrode materials for supercapacitors, meet these requirements. More precisely, it is about the retention of the capacitance calculated from the lowest current density at $1 \text{ A} \cdot \text{g}^{-1}$ versus the capacitance calculated from the highest current density at $20 \text{ A} \cdot \text{g}^{-1}$. If a

test cell with a carbon sample can hold the capacitance well over the entire current density range, then a possible EDLC device, with the same material as electrode, can also deliver constant energy over a larger power range. Performance evaluations of industrial capacitors were used, in order to find an evaluation for sufficient retention of the capacitance. The durability of capacitors is defined by the device's ability to deliver less than 80% of the original maximum capacitance or energy.^[271] From this point on, the capacitor is considered to be exhausted. With regard to the retention of the capacitance in the CDC measurements, this criteria cannot be evaluated in the same sense, but it should serve as an orientation from now on in order to have an evaluation benchmark. A retention of 80 % or higher is therefore considered suitable to be a potential electrode material.

It is relatively clear the pore size also has an impact in this case. The diffusion resistance of the electrolyte ions to and in the pores is determined by the size, since small pores and a small distance between the ion and the pore wall lead to an increased electrostatic interaction, which reduces the diffusion and mobility of the ions. In addition, an increased frictional resistance is to be expected in smaller pores and thus in confined spaces. The smallest critical pore size, however, has not yet been clarified. In many studies and review articles, mesopores, are considered to be large enough to allow a resistance-free diffusion behavior, which then enables loss-free energy storage and release over a large current range or over a large range of discharge times.^[113,115,306,307] However, some studies, including this one, show that mesopores are not absolutely necessary in order for a carbon electrode material to deliver the full capacitance even at high currents and frequencies.^[273,292] Many samples of this work, such as sample C-600-5-T9, have pores up to 3 nm, but the second maximum is only 1.5 nm. Therefore, the aim of this section is to generate new knowledge regarding the pore size dependent retention of the capacitance.

An approach as in the previous section would be desirable if it were possible to attribute a retention value to each specific pore size. One could then compare exactly which pore has the optimal size, as it has a specific value for surface capacitance and a specific value for capacitance retention. However, it is not possible to follow the same approach in section 4.2.2.3, since the retention cannot be calculated on the basis of pore sizes since it is too complex. Because the capacitance retention of a specific pore size does not depend on the size itself, but also on the frequency

of the size. The surface chemistry may influence the diffusion of electrolyte ions in pores as well.^[308] However, the organic residues in carbons are low in general and the influence of the surface chemistry on the retention of capacitance at different currents is still unclear. Therefore, the surface chemistry is neglected regarding this discussion. Consequently, no simulated retention can be compared with the measured retention and no useful conclusions can be deduced. Another difficulty can be seen in Figure 166, which shows the retention as a function of the total pore volume of each carbon sample. This seems to be a reasonable approach, since the average pore sizes of each sample correlate relatively well with the respective total pore volumes for the carbon materials of this work, which accordingly have also higher surface areas. The figure very clearly shows the retention of the capacitance increases with increasing pore volumes and for carbon samples with a pore volume above $1.1 \text{ cm}^3 \cdot \text{g}^{-1}$, a retention of the capacitance of more than 80 % is provided. This indicates materials with larger pores also show a higher retention of capacitance at higher currents which would be a confirmation of the stated theory so far. Along with the correlation of pore size and total pore volume in this work, larger pore volumes are usually associated with larger pores, since the latter generate more pore volume compared to smaller pores. The surface areas connects pore size and pore volume, but cannot provide further insights into the retention, since carbons of this work with larger pores, usually process higher surface areas.

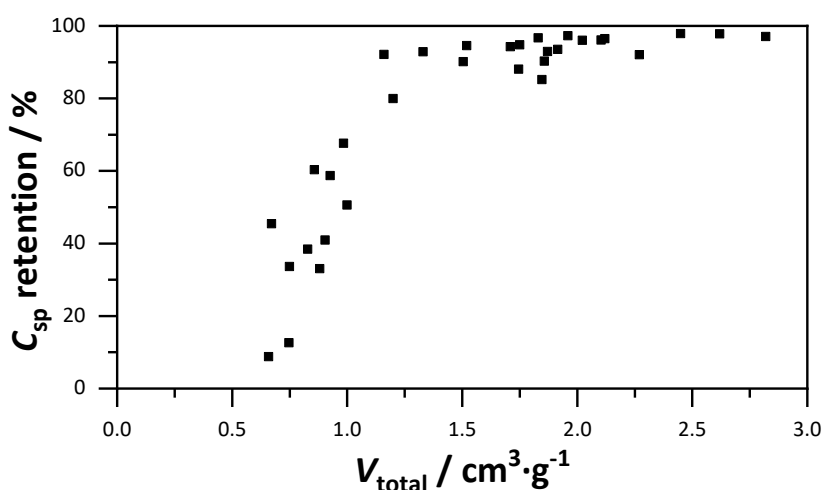


Figure 166: Capacitance retention from galvanostatic discharge measurement in dependence of the total pore volume for all carbon samples of the entire work.

It should be noted again the generation of the total pore volume is not only about the size of the pores but also about the abundance of the respective size, which is also implied in the term pore size distribution. Thus, the retention of capacitance is to be investigated in relation to a parameter which also depends on the frequency of certain pore sizes. Figure 167 shows the retention of the capacitance as a function of the micropore volume content. It can be seen carbon materials with a lower content of micropores show a superior retention of capacitance at high current densities, more precisely at a content of about 75 % or lower. This seems comprehensible in so far as pores above 2 nm certainly favor electrolyte ion mobility, and a low content of micropores does not only mean larger pores are present, but that they are also present with sufficient abundance.

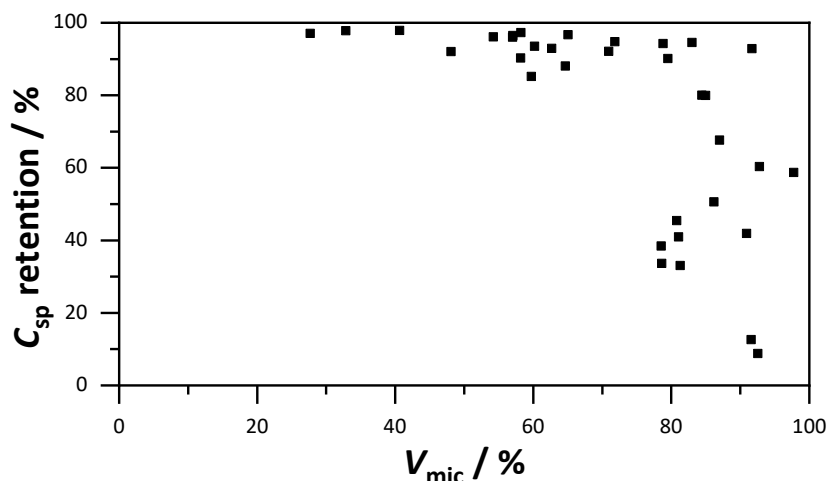


Figure 167: Capacitance retention from galvanostatic discharge measurements in dependence of the micropore volume content for all carbon samples of the entire work.

However, there was no clear trend for carbons with a micropore volume content of 80 to 95 %. Carbon samples with such a high micropore volume content show a high retention of capacitance, but a significantly larger part of these materials show a significantly lower retention. This allows for the conclusion that samples with micropore majorities can certainly enable a high ion diffusion, but it also means the critical pore size is also in the micropores range. This is also confirmed by the assumptions from previous sections, where carbon samples showed excellent retention, although they are mainly microporous. However, the figure and the conclusions mentioned, also show the difficulty of investigating the problem in this way.

With this representation there are components which cannot be considered. For example, the micropore volume content of two samples can be approximately the same, but the samples can have significantly different pore size distributions as the pores can still be divided into large micropores between 1.5 and 2.0 nm and small micropores below 1 nm. Such factors are difficult to achieve even with similar plots. Of course, the surface area needs to be considered, as it connects pore sizes and pore volumes. It can be seen in Figure 168 the dependence of the capacitance retention on the accessible surface area, that a high surface area of $1400 \text{ m}^2 \cdot \text{g}^{-1}$ seems to grant a high capacitance retention of 80 %. However, a high surface area also implies that certain pore sizes, in general smaller pores, are abundant in a higher frequency, whereas a specific pore size dependence cannot be derived from the pore volume and the surface area respectively.

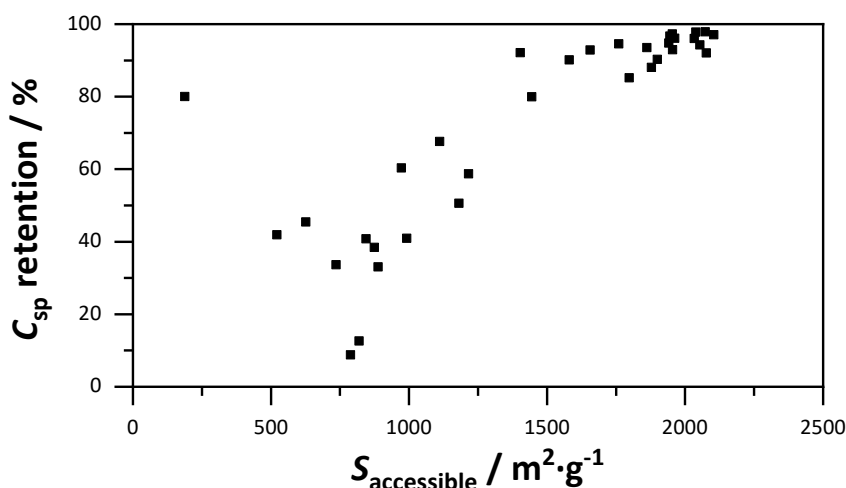


Figure 168: Capacitance retention from galvanostatic discharge measurements in dependence of the specific surface area, provided by pores larger than 0.66 nm for all carbon samples of the entire work.

A simulation, as in section 4.2.2, is also not possible, since the pore-specific retention depends on its abundance and the abundance of similarly large pores, which would lead to a very complex simulation model. Therefore, a compromise solution is sought since it is now known that the critical pore size is in the range of the larger micropores, but also depends on the frequency of these larger micropores.

The pore size distributions of three different samples were evaluated more precisely, as can be seen in Figure 169. The carbon samples were explicitly selected. Sample C-700-5-T9 was selected because it has a capacitance retention of exactly 80 % and represents the transition of the sufficiently large pores very well. Sample C-400-2.5-T9 was also selected, as this is the material with a capacitance retention of 68 % which has the next value closest to 80 %. Finally, results from sample C-600-5-T9 were used, which has a high retention of 93 % and at the same time has the highest micropore volume content and is therefore well suited for determining the pore size transition. As already mentioned, the pore size distribution, which was combined respectively from carbon dioxide and nitrogen, can also be used to determine the minimum pore sizes, which enables a good retention of the capacitance. Similar to the consideration of capacitance values, only pores larger than 0.66 nm are considered to be relevant, since TEA⁺ ions cannot penetrate the pores. All three carbon samples show pore sizes between 0.8 and 0.9 nm, whereby these are all present to the same extent in all three materials. Therefore, it cannot be assumed that the pores in this size range are decisive for the retention of capacitance at high currents. Sample C-600-5-T9 has pore sizes up to 2.5 nm with a broad maximum of approximately 1.5 nm. This could also be observed for other samples with similarly good capacitance retentions, which is the reason why a sufficient pore size of 1.5 nm could be assumed in the progress of this work. A minimum size of 1.5 nm seems comprehensible as both fully solvated BF₄⁻ ions and TEA⁺ ions are large enough to cover the surfaces of these pores. The BF₄⁻ ions with solvate shell in acetonitrile are 1.1 nm and TEA⁺ ions 1.3 nm large. However, since the pore space would still be confined even for fully solvated ions, it is still not expected that pore sizes from 1.3 nm could be sufficient. Nevertheless, it is still not clear whether this is actually the critical pore size and in what amount it must be present in relation to the total pore size distribution. The pore size distributions of samples C-700-5-T9 and C-400-2.5-T9 are very similar. Both have pore sizes up to 2.0 nm and larger contents of pores between 1.2 and 1.5 nm. The only differences are that sample C-400-2.5-T9 itself has fewer pores in the mentioned range, and has more contents of pores in the range of 1.0 to 1.2 nm, as opposed to sample C-700-5-T9. It seems likely the critical transition from poor to sufficient retention of capacitance in the pore size range is between 1.2 to 1.5 nm. Based on this, it is very likely the critical pore size itself is about 1.3 nm, corresponding to the size of TEA⁺ ions solvated in

acetonitrile. Thus, the pore size range, which promotes a high diffusion of the ions and thus leads to a high retention of the capacitance at high currents and frequencies, could be narrowed down.

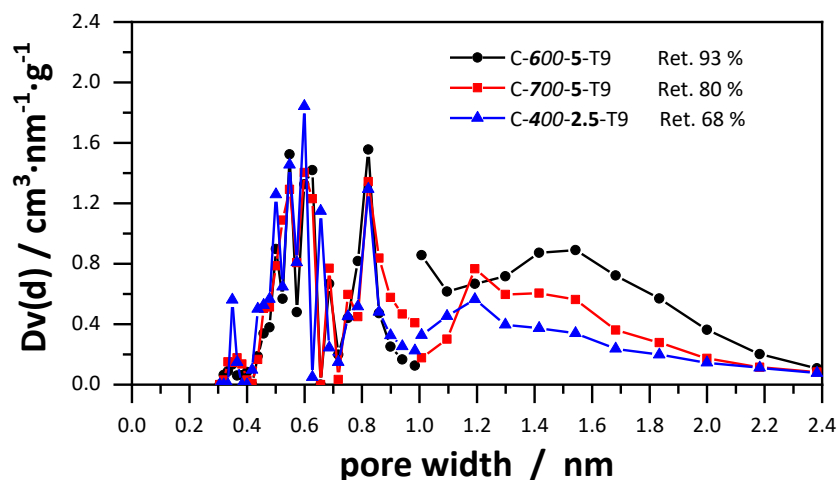


Figure 169: Pore size distributions calculated from carbon dioxide physisorption for pores up to 1 nm and calculated from nitrogen physisorption for pores larger than 1 nm, for the samples C-600-5-T9, C-700-5-T9 and C-400-2.5-T9 including their capacitance retention from galvanostatic charge discharge measurements.

Even if the critical pore size range could now be narrowed, it is still not quite clear in what ratio or in what frequency the critical pore sizes have to be present, in comparison to smaller and larger pores, in order to guarantee a sufficiently high diffusion of the ions. In order to investigate this aspect more accurately, Figure 170 shows the retention of the capacitance of all carbon samples as a function of the volume ratio. This is the ratio of the pore volume generated by pores above 1.30 nm to the pore volume generated by pores between 0.66 and 1.30 nm. It clearly shows that carbons with a high volume content through pores above 1.30 nm have a much better retention of capacitances, which is expressed by a high ratio. If the ratio is below 1, the retention of each of these carbons is also below 80 % and thus below the benchmark criteria. Interestingly, the three selected samples with a ratio around 1 are exactly in the transition range, which again underlines the usefulness of evaluating these three samples to find the transition range of the pore sizes. All in all, this means a carbon material should best generate more than 50% of the pore volume of pores larger than 1.30 nm in order to achieve good retention of capacitance, whereby this is only related to the accessible pore volume for pores larger than 0.66

nm. Apparently, this means that not only the critical pore size is present, but that it is also sufficiently well accessible in a pore network of larger pores. Thus the pore size dependent retention of the capacitance could be narrowed, and could range on average around 1.30 nm. With a sufficient amount of these pores, more than half of the pore volume must be generated by these or larger pores to enable electrolyte ion diffusion at high currents. Although the knowledge has now been expanded, this volume ratio is a rather complex quantity, which cannot be determined so easily from pore size distributions. Nor does it directly indicate the abundance of pores above 1.3 nm. A further volume-related size would therefore be desirable.

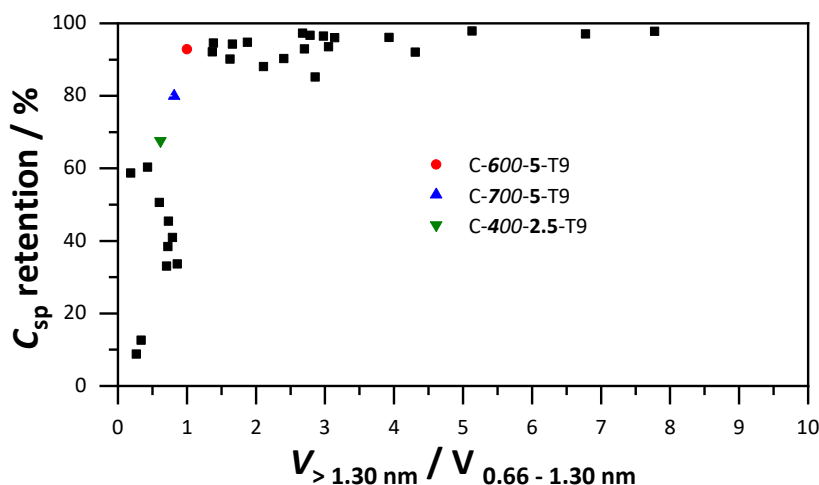


Figure 170: The retention of capacitance of the carbon samples from the entire work in dependence of the pore volume ratio of the volume generated by pores > 1.30 nm and the volume generated by pores in the range of 0.66 to 1.30 nm

The pore size range, which allows a good diffusion of the electrolyte ions and thus leads to a high retention of the capacitance, could be narrowed down very well. In addition, it was possible to determine the ratio in which these pore sizes must be present in the carbon material, since this also plays an important role. These two pieces of information are important, but relatively complex and difficult to obtain. Therefore, Figure 171 shows the volume-weighted average pore size of all carbon samples with the respective retention of capacitance. The volume-weighted average pore size should not be understood as a general average pore size, since almost all materials have a multimodal pore size distribution. However, it is still a good indicator of whether a material has a high content of larger or smaller pores. It is very

clear carbons with larger volume-weighted average pore sizes show a higher retention of capacitance. This is due to the fact a high average pore size implies, or is equivalent to, a high content of pores of 1.30 nm and larger, which promotes good retention of capacitance. Interestingly, the three selected samples also form the transition to capacitance retentions of over 80 %. Sample C-400-2.5-T9 has a pore size of less than 1 nm, and like all other carbon samples, which have an average pore size of less than 1 nm, the retention is well below 80 %, thus below the benchmark criteria. The pore size of sample C-700-5-T9 is 1.02 nm and that of sample C-600-5-T9 is 1.16 nm. It follows that carbon samples with a volume-weighted average pore size above 1.02 nm have sufficiently large pores for a good diffusion of the electrolyte ions and thus a good retention of the capacitance at high currents and frequencies. As a result, a size has been found which can be measured simply and quickly and at which it can be easily seen whether a carbon material has sufficiently large pores available to transport ions without loss of capacitance at high currents, since this cannot always be measured from pore size distributions. However, it should be emphasized once again 1.02 and 1.16 nm are not the actual critical pore sizes. This would also be rather unusual, since this corresponds to the size of the fully solvated BF_4^- ions in acetonitrile and the TEA^+ ions can only enter these pores desolvated. The pore size is only a volume average, which has been determined as being empirically sufficient.

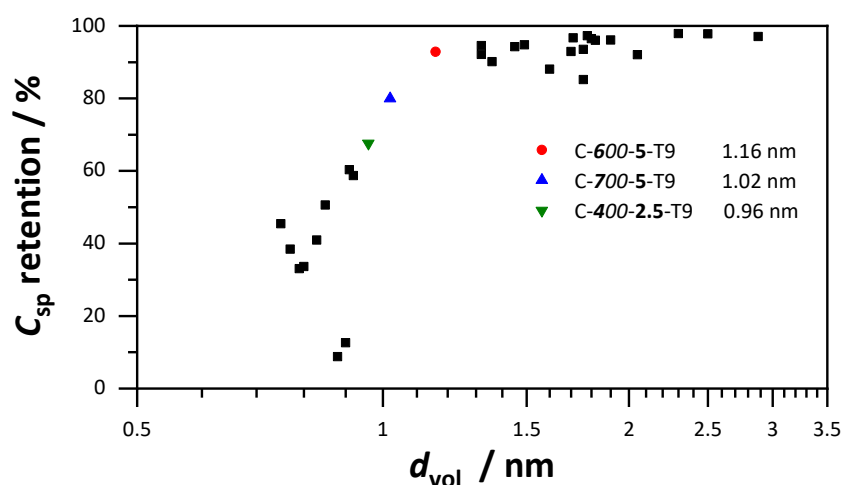


Figure 171: Capacitance retention from galvanostatic discharge measurements in dependence of the volume weighted average pore size for all carbon samples of the entire work.

In this section, knowledge about the relationship between pore sizes of carbon electrode materials of EDLCs and the retention of the capacitance of small currents in relation to large currents can be gained and expanded. Figure 172 shows the results graphically using the pore size distribution of sample C-700-5-T9. This particular sample was chosen, as it is the first carbon sample, which obtains the required porosity to provide a retention of capacitance of 80 %. The results of all carbon samples of this work were evaluated and a retention of capacitance of 80 % was specified as the benchmark criteria. The results were further refined on the basis of three samples whose retentions were on or around 80 %. It turned out, the critical pore size, which is the bottleneck with regard to the sufficient diffusion of the electrolyte ions, is in a pore size range of 1.2 to 1.5 nm. Averaged at 1.3 nm, this is reasonable, as it is the size of the solvated TEA⁺ ion, which is the larger of the two ions. So it seems pores with the size of the fully solvated electrolyte ions are already sufficient to ensure a good diffusion and retention of the capacitance. Another important factor, however, is the availability of critical pore sizes in the carbon material. The pore network must provide these sufficiently so the electrochemically active surface can be reached at any time. Here it has been established that a material whose accessible pore volume is generated to over 50 % by pores larger than 1.30 nm provides a sufficient amount of large pores to enable good retention of the capacitance. This is important information, as it clarifies the relationship of the critical pore sizes. However, one of the first pieces of information obtained from sorption measurements of carbon porosity is the pore size distribution itself. From this it is not so easy to determine in which ratio the corresponding pore volumes are. Therefore, it was of interest to find another parameter that summarizes the criteria in a compact fashion. Therefore, the volume-weighted average pore sizes of all carbons were evaluated in relation to the retention of capacitance, and it was found all carbons with an average pore size of approximately 1.1 nm and above had a retention of capacitance above 80 %. However, this does not mean this is the critical pore size, since the optimal size is likely closer to 1.3 nm. In conclusion, it can be said that nanoporous carbons with a volume-weighted average pore size of over 1.1 nm are well suited as electrode materials for EDLCs, as they generate more than 50 % of their accessible pore volume through pores larger than 1.3 nm in relation to TEABF₄ in ACN and thus have sufficient pores in the size range of 1.2 to 1.5 nm,

which are important for good diffusion of the electrolyte ions on and in the pores and thus ensure good retention of the capacitance at high currents.

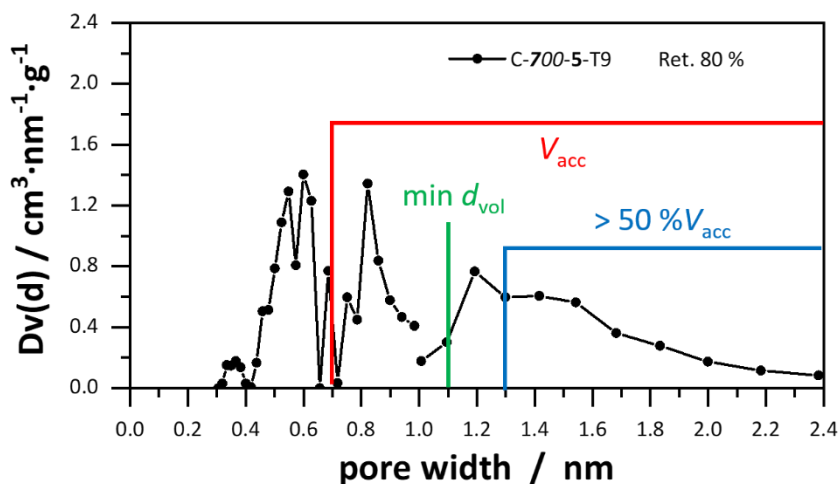


Figure 172: Summary of the requirements on pore sizes for a sufficient retention of capacitance, taking sample C-700-5-T9 as an example. It is highlighted in color that at least 50 % or more of the accessible pore volume (red) must be generated from pores above 1.3 nm (blue) or the sample must have a volume-weighted average pore size of at least 1.1 nm (green).

4.2.4 The perfect pore size for supercapacitors?

The last two sections dealt with the question to what extent the pore sizes of the carbon electrode materials of EDLCs influence the electrochemical properties. The focus was on the influence of the pore sizes on the electrochemical utilization of the pore walls or the surface capacitance and on determining which pore sizes are required at a minimum and how frequently to ensure good retention of the capacitance at high currents. Finally, the question remains, whether there is such a perfect pore size or pore size range, which not only provides the optimal capacitance, but it also enables a good diffusion of the electrolyte ions. It should at least be summarized again which pore size distribution would be the most reasonable for carbons as EDLC electrodes. Figure 173 shows again the result of the modified ESDCC model, which shows the progression of the surface capacitance with the pore size. Especially, the range between 0.6 and 4.0 nm shows clear differences in the electrochemical utilization of the carbon surface. The pores in the 0.7 to 0.9 nm range, which have been marked red, provide the best surface capacitance by far. The surface capacitances are 2 to 4 times higher than the average capacitance from 5 nm,

which is due to the confinement effect; the electrolyte ions must completely or partially remove their solvate shell or distort it strongly so the ions can enter the pores. This reduces the distance to the carbon surface, which in turn increases the energy in the electric double layer and thus the capacitance. However, it has been shown the pores in the 0.6 to 0.9 nm range cannot permit diffusion of the electrolyte ions at higher currents and thus lead to high capacitance losses. This is due the ions needing to remove or distort their solvate shell in order to enter these pores, since the size of the solvated ions in acetonitrile is 1.1 nm for BF_4^- and 1.3 nm for TEA^+ .

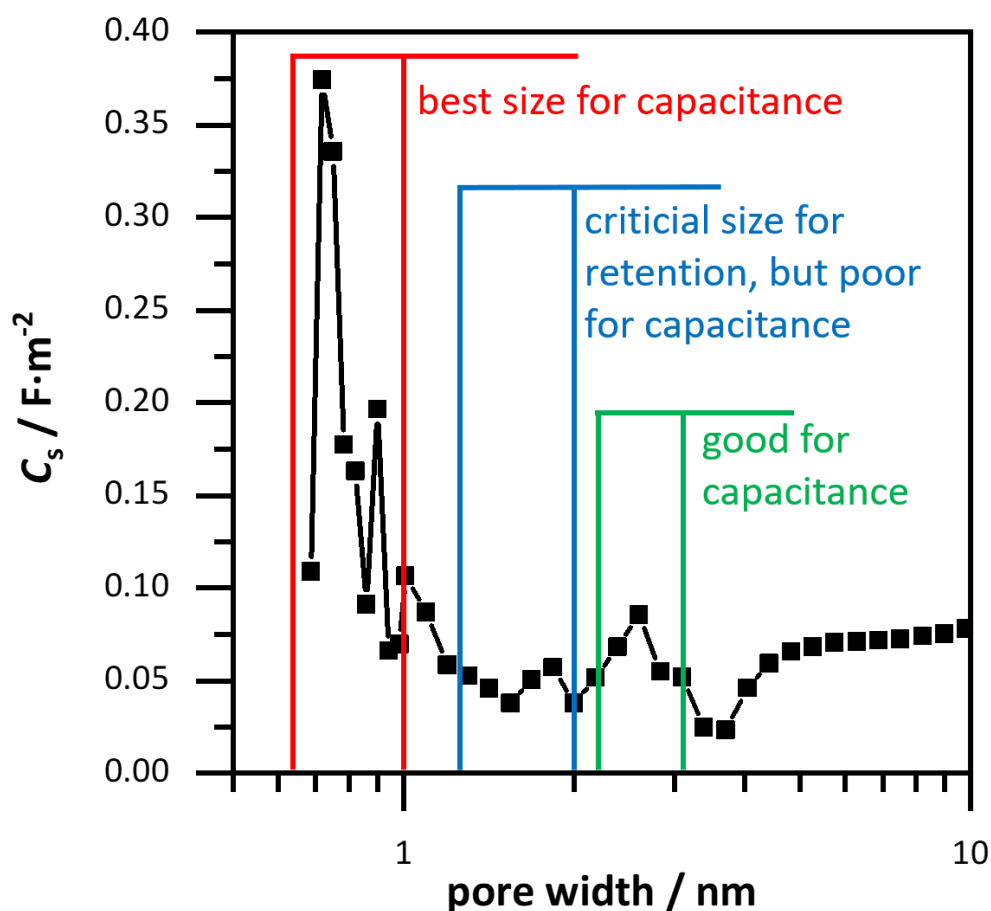


Figure 173: Surface capacitance in dependence of the pore size based on the modified ESDCC model and the best pore range for capacitance highlighted (red) along with the critical pore size range for capacitance retention (blue) and the second best pore size range for capacitance (green).

The pores around 1.3 nm have proven to be the so-called critical pore size range, since the ions can penetrate these pores with the solvate shell. In addition, it has been shown the pores have to be present in a sufficient abundance, otherwise they

cannot ensure sufficient ion diffusion. The important factor here is the ratio of the pore volume accessible to the electrolyte ions. This has to be generated to 50 % or more by pores which are larger than 1.3 nm, which points to the result of the corresponding carbons needing a significant number of pores in the 1 to 2 nm range. However, this pore size range marked in blue shows a significantly lower surface capacitance of the respective pore sizes compared to the pores below 1 nm and also to the larger pores. Thus, the ideal pore size range, which provides high capacitance and the corresponding retention at high currents, does not exist. Of course, carbon materials with additional pores in the range of 1 to 2 nm can have higher gravimetric capacitance values than materials with only pores below 1 nm, which is primarily due to the fact materials with larger pores usually provide more surface area, which, in the end, increases the net capacitance. However, the surface is not used as well as for pores in the 0.6 to 0.9 nm range. In order to further optimize the utilization of the carbon electrode surface and the capacitance, materials have been shown which, in addition to micropores, could exhibit further mesopores between 2 and 3 nm. This pore size range, marked in green, provides better surface capacitance values than the pores in the range of 1 to 2 nm and can increase the maximum gravimetric capacitance more effectively while at the same time allowing optimum diffusion of the electrolyte ions. Synthetically, this is certainly a challenge, especially since chemical activations generate even larger pores in a homogeneous distribution. Here, however, it has been shown that pores between 3 and 4 nm have by far the lowest surface capacitance and thus the poorest electrochemical utilization of this surface. This means although there may be more usable surface area available, which also allows the diffusion of ions at high currents, the gravimetric capacitance is not significantly increased, which has also been shown in the plot of the capacitance with the respective accessible surface area in this work. Thus, the content to pores between 3 and 4 nm should be kept at a minimum in a potential carbon electrode material, as smaller pores provide more capacitance. Larger mesopores from 5 nm would then again provide a constantly better surface capacitance, but still significantly lower than that of the pores in the 0.6 to 0.9 nm range. It can therefore be summarized that carbons, with pores in the range of 0.6 to 0.9 nm and in the range of 2 to 3 nm, would selectively deliver the highest capacitance values and could also maintain these in applications in the high current or frequency range. However, this is synthetically difficult to achieve by selectively generating carbons only with

these pore regions, in any case by means of carbonization and chemical activation methods, as was the case in this work. Nor are there any other synthesis methods known to date. It must also be noted that in addition to the optimal pore size distribution, the availability of these pores also plays an important role, meaning the specific surface area of the carbon materials is still an important factor. It turned out in this work that this is nevertheless decisive for whether the capacitance of the corresponding EDLC is high or low. This means as many pores as possible have to be generated, which is only possible by chemical or physical activation. As shown in this work, these pores always provide broad pore size distributions, including pores in the range of 1 to 2 nm or 3 to 4 nm, which do not provide good surface capacitance. A compromise must therefore always be sought in order to achieve the best possible electrochemical performance.

The clarification of the obtained insights is conveyed well by the capacitance and the pore size distribution of sample C-500-5-T8, is shown in Figure 174. Sample C-500-5-T8 was chosen again as an example, as it has the highest measured capacitance and also the highest simulated capacitance, which was calculated from the physisorption data using a modified ESDCC model. In addition to the decisive pore sizes, the number and availability of these is also of importance, which is expressed in a high accessible surface area. The basis for this is provided, since sample C-500-5-T8 with almost $2600 \text{ m}^2 \cdot \text{g}^{-1}$ has one of the highest accessible surface areas of this work. The size of the pores are then responsible for optimizing the electrochemical properties. The carbon material has a high pore content around 0.8 nm, which provides a high surface capacitance and thus a large contribution to the gravimetric capacitance. It can also be seen that a large amount of pores between 1 and 2 nm in size are present and no pore sizes larger than 3.0 nm. Although this ensures that diffusion in the pore network is also guaranteed at high currents (see section 4.2.3), it provides a relatively small contribution to the capacitance due to the limited surface capacitance. Furthermore, the sample shows significant pores with a size of 2 to 3 nm, which in turn show a significantly higher surface capacitance and thus contribute more to the gravimetric capacitance. A further decisive difference is the maximum pore size is actually 3 nm, since the pores have the lowest surface

capacitance in the 3 to 4 nm range. Sample C-500-5-T8 therefore has a high capacitance ultimately because it has a high accessible surface area and mainly has pore sizes which show a high electrochemical utilization of the carbon surface in order to combine high capacitance and good retention as properties.

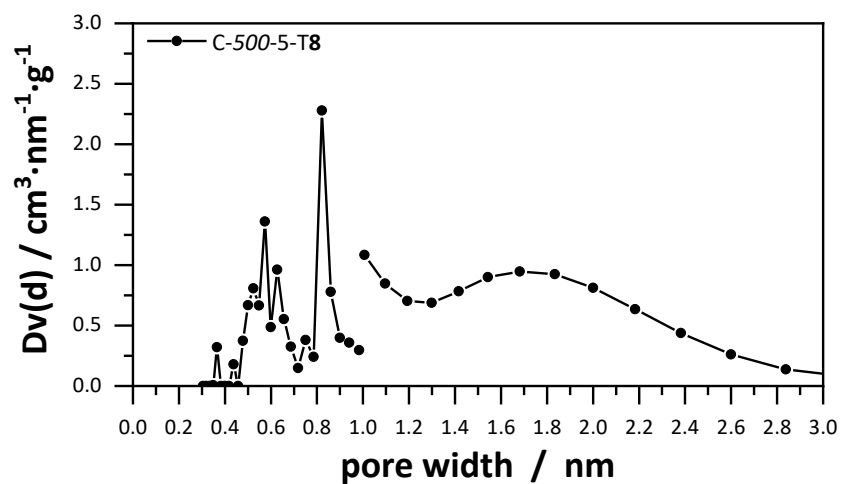


Figure 174: Combined pore size distribution calculated from carbon dioxide and nitrogen physisorption from the sample C-500-5-T8.

4.3 Influence of pore size on hydrogen uptake capacity

While in the last chapter the influence of the pore sizes of the carbon electrode materials of EDLCs on their performance was examined in detail, this chapter deals with the influence of the pore sizes on the hydrogen storage capacity at 77 K and 1 bar. Previous sections have shown even in hydrogen adsorption the utilization of the carbon surface is not the same for all materials, and there is a clear tendency for small pores, such as micropores, to show significantly better utilization. This is due to the overlapping of adsorption potentials and a classic phenomenon of low-temperature adsorption.^[7,210] The matter of investigating the influence of pore sizes on the gravimetric hydrogen uptake capacity will be addressed in a similar approach, by mining the collected data.

4.3.1 Mining the data

First, the collected data is evaluated to confirm already observed trends or to gain new insights. For this purpose, carbons from individual synthesis series are not discussed in isolated form, instead all synthesized carbons from chapter 5.1 are regarded as a joint convolute. Therefore it is assumed the hydrogen uptake capacity depends exclusively on the porous properties of the carbons and the surface morphology and the surface chemistry have no significant influence on the capacity. This assumption can be made to the extent that no clear correlation between heteroatom fractions and hydrogen uptake could be observed from the literature either, as already mentioned in section 1.5.

In the process of this work, it became very clear the surface of the carbon is a decisive factor for the hydrogen uptake capacity. Due to a higher specific surface of the adsorbent, more adsorption sites are available for the adsorptive, which increases the uptake capacity of the adsorbent. This can also be confirmed by considering all carbon samples, as shown in Figure 175. The hydrogen uptakes are plotted against the DFT surface areas and it can be seen that the uptakes increase with increasing specific surface area. However, one can also see the hydrogen uptake is not exclusively determined by the specific surface area. It can be recognized that starting from a surface of $2500 \text{ m}^2 \cdot \text{g}^{-1}$ the carbon materials show no clearer trend in their hydrogen uptake. For carbons with surface areas larger than $2500 \text{ m}^2 \cdot \text{g}^{-1}$, the hydrogen uptakes vary between 2.4 and 2.8 wt%. For carbons with surface areas between 1000 and $2500 \text{ m}^2 \cdot \text{g}^{-1}$ a clear increase of hydrogen capacity with increasing surface

area is recognizable. The two samples C-500-5-T6 and C-900-5-T10 stand out clearly, since these carbons show only hydrogen uptakes of 2.25 and 2.34 % despite their high specific surfaces of 1962 and 2335 $\text{m}^2\cdot\text{g}^{-1}$ respectively. Similar to EDLCs, there seems to be a limit value at which the specific surface no longer has any influence on the maximum hydrogen uptake, at least up to 1 bar. At higher pressures it can be assumed the surface again has a determining influence, since at 1 bar it is probably not completely covered with adsorptive.

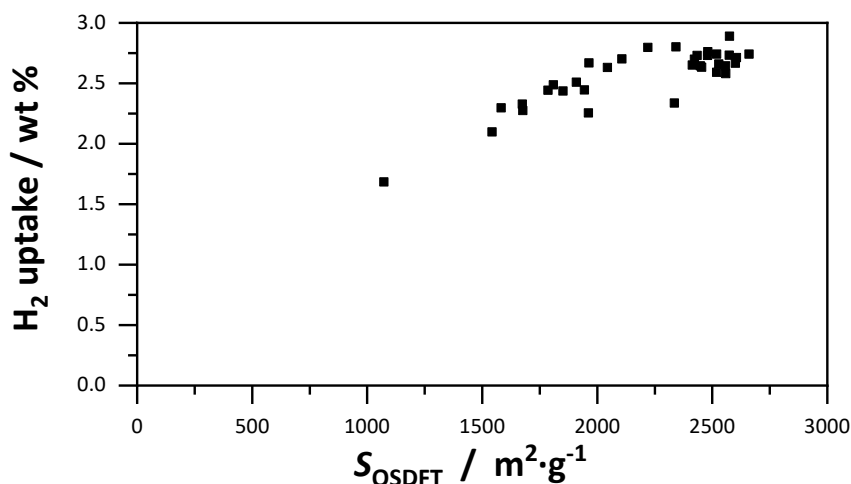


Figure 175: Gravimetric hydrogen uptake capacity in dependence of the total DFT surface area for all synthesized carbons.

The reason for the limiting influence of the specific surface area is probably the different utilization with regard to the hydrogen absorption of the surfaces in pores of different sizes. Micropores tend to have a higher usability due to the higher adsorption potential, as has already been shown.^[210] However, it is not yet known exactly for which pore range this applies. A more detailed insight into the utilization of hydrogen storage can be seen in Figure 176, where the surface area normalized hydrogen storage capacity is plotted against the total pore volume of all carbon samples. The total pore volume was selected because it correlates well with the average pore size of the respective carbon. It can be recognized clearly that the surface area normalized hydrogen uptake decreases with increasing pore volume and reaches a limit value from a pore volume of about $1.5 \text{ cm}^3\cdot\text{g}^{-1}$ onwards. This confirms that carbons with small pores can adsorb more hydrogen per surface. It is even the case that the carbon material with the smallest average pores and also the

smallest surface area and pore volume (sample C-900-5-T6) has the largest surface area normalized hydrogen uptake capacity. This suggests pores, especially those below 1 nm, show the highest usability regarding hydrogen uptake, since sample C-900-5-T6 almost exclusively has pores below 1 nm. The dependence of the normalized capacity on the pore volume suggests the usability of the pore walls becomes linearly lower with increasing pore size until it reaches a limit value after a certain pore size. This is further confirmed by the application of the surface normalized hydrogen uptake capacity against the volume-weighted average pore size provided in Figure 176. Here, too, a clearly decreasing hydrogen uptake per surface with increasing pores can be observed. It is assumed the adsorption potential of the pore walls becomes exponentially lower up to a limit value with decreasing pore size. However, it must be noted these applications are always average values. The volume-weighted average pore size also provides information about the abundance of the respective pores, but not about the uptake capacity of individual specific pore sizes. It should nevertheless be noted the reason for the stagnation of the uptake capacity with increasing pore size is related to the possibility of the decisive pores below 1 nm being present to a lesser extent than larger micro- and mesopores. It has already been discussed in detail that the increase of the surface area by the synthesis methods carried out in this thesis has always led to an enlargement of the pores and thus to a reduction of the abundance of the small micropores into which, capacity-increasing confinement effects take place.

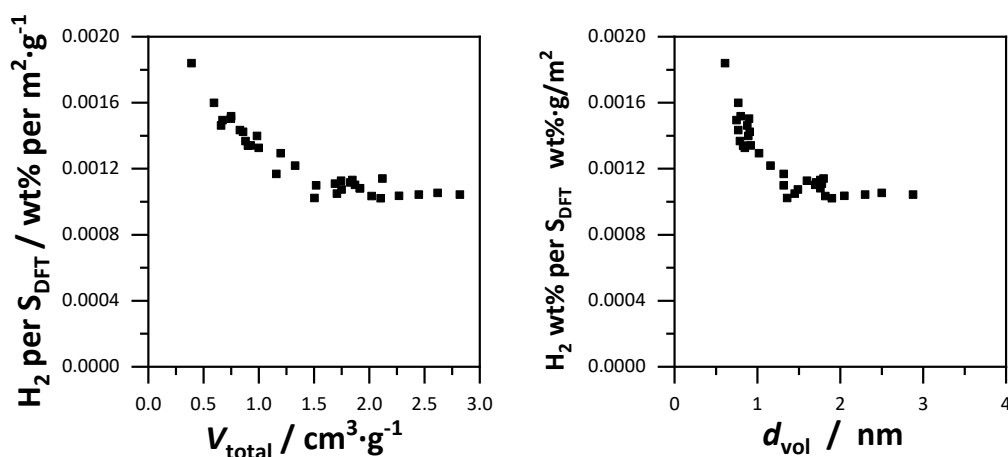


Figure 176: Surface area normalized gravimetric hydrogen uptake capacity applied against the total pore volume (left) and against the volume weighted average pore size (right) of all carbon samples.

4.3.2 Simulation of hydrogen uptake capacities

By evaluating the data of the carbon samples and the respective hydrogen uptake capacities it could be confirmed that the hydrogen adsorption per surface is higher in small micropores and decreases with increasing pores. Similar to chapter 4.2.2 for the capacities of EDLCs, a specific model has to be developed which shows the surface normalized hydrogen uptake capacity dependence on the specific pore size. With this model, gravimetric hydrogen uptakes can be calculated based on the porosity data and more precise insights into the pore size dependence of the hydrogen uptake can be gained. The simulation of the hydrogen uptake capacities will also be carried out here on the basis of the data from the physisorption measurements. Similar to equation (27), the uptake can be simulated by the following equation:

$$Uptake_{sim} = \sum \frac{Uptake}{S}(L) \cdot (S_L - S_{L-1}) \quad (29)$$

where $Uptake_{sim}$ is the simulated gravimetric hydrogen uptake and $Uptake/S$ the pore size specific hydrogen uptake normalized by the specific surface area. Pore sizes up to 10.7 nm were taken into account as no larger pores were observed in any carbon sample. Additionally, a minimum critical pore size of 0.35 nm was defined, since this corresponds to the kinetic diameter of the hydrogen molecule at 77 K.

Since the same strategy as in chapter 4.2.2 was followed, a base model was first established, which is an average value of the surface uptake for all pore sizes. It was obtained by calculating the average uptake per surface area of all carbon samples. The initial model is shown in Figure 177. The simulated capacity values based on this model deviated, of course, strongly from the measured values, since it has already been determined that not all pores can provide the same uptake per surface.

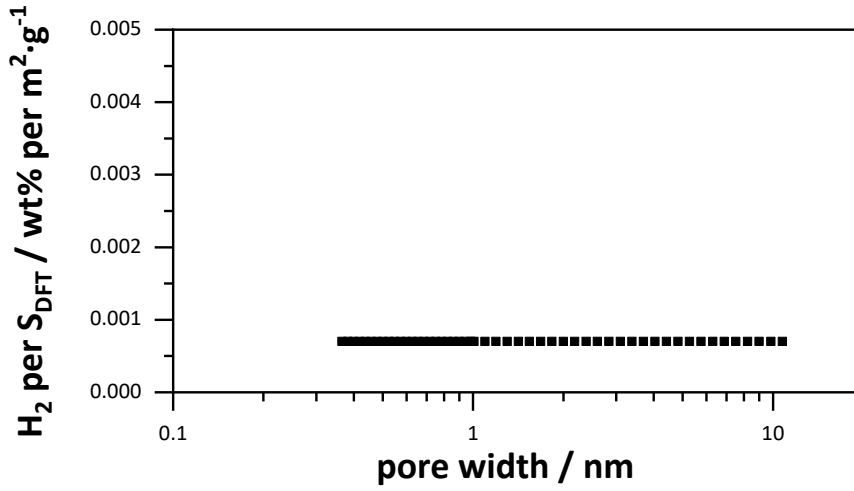


Figure 177: Base model for the simulation of gravimetric uptake capacities with an average value for the entire pore size range.

The uptake values simulated using the base model were compared with the measured values and the deviation calculated for the individual carbon samples. Then the average deviation (AD) was calculated again, as shown in the following equation:

$$AD = \frac{1}{n} \sum_{i=1}^n \left| 100 - \frac{Uptake_{meas,i}}{Uptake_{sim,i}} \cdot 100 \right| \quad (30)$$

where, $Uptake_{meas,i}$ are the measured gravimetric hydrogen uptake capacities and $Uptake_{sim,i}$ the simulated uptake capacities. Now a factor was again assigned to each surface uptake value that belonged to a pore size. These factors were again varied using the nonlinear GRG method to minimize the average deviation from equation (30). The result of this is shown in Figure 178 and shows a new complex dependence of pore size and surface uptake. The development of a more complex model was not necessary in this case, because the minimization of the AD was already successful based on the simple base model.

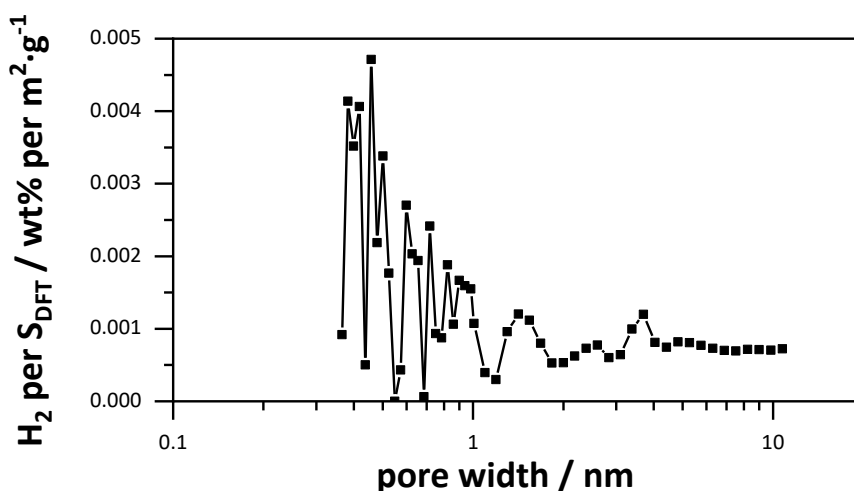


Figure 178: New pore size dependent progression of the specific surface area normalized gravimetric hydrogen uptake capacity, based on the minimization of the AD of simulated and measured capacity values for all carbon samples of the entire work.

The new model shows a very complex new progression of the surface normalized hydrogen uptake as a function of the pore sizes. The only general trend that can be observed is small pores from 0.35 nm have the highest uptake and this generally becomes exponentially smaller depending on the pore size. More specifically, pore sizes in the range of 0.35 to 0.60 nm provide the highest contribution to the uptake on average. Thus, the conclusion from the previous section, in which this trend has already been assumed, can be confirmed by the application of the surface normalized capacity against the pore volume. However, a closer look at Figure 178 also reveals very clearly that no simple trend can be derived from the further description, but rather a complex, oscillatory progression of the surface uptake capacity with increasing pores. Furthermore, the uptake capacity for pores is extremely low, and even down to the value of zero, which is unlikely, considering the adsorption potential of hydrogen and literature.^[6,201,203,213,290,309]

It should be reaffirmed the pore size dependent surface hydrogen uptake capacity in Figure 178 is a purely mathematical solution where no molecule and substrate-specific restrictions have been made, which is why the solution also has the corresponding oscillating form and must be interpreted accordingly. The validity of this solution is based only on the fact that the hydrogen uptakes of over 30 carbon samples can be simulated on the basis of physisorption data. However, this succeeds

with an enormously high accuracy, as shown in Figure 179. The AD is very low at 1.3 % and the maximum deviation from measured and simulated uptake capacity is just 10 %, which also applies to a single sample only. For all other carbons, uptake capacity can be simulated with a maximum accuracy and a percentage deviation of 6 % and less. It can therefore be assumed that this new model provide additional insights into the pore-specific adsorption of hydrogen in porous carbons.

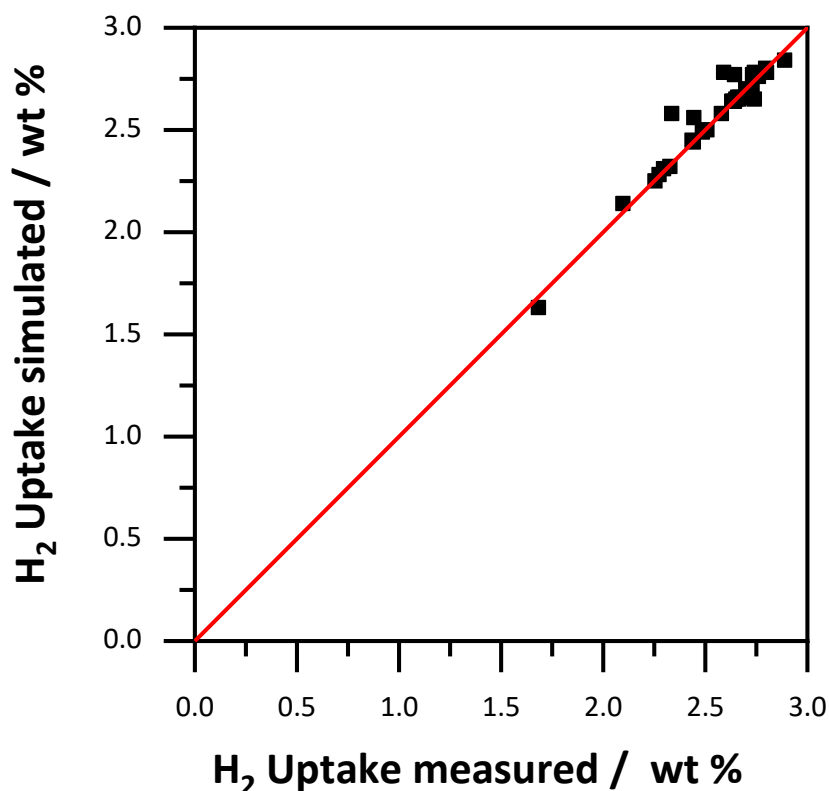


Figure 179: Comparison of simulated hydrogen uptake capacity values and measured uptake capacities for all carbon samples of the entire work.

Such a complex contribution of individual pore sizes to the hydrogen uptake capacity has never been postulated in this form, namely based on the theoretic simulation of hydrogen uptakes using experimentally determined sorption values. So far it is generally known from literature, that the hydrogen-adsorbent interaction is critical for the hydrogen uptake at 77 K and 1 bar. This was concluded from observations, in which porous carbons with an increased amount of pores below 1 nm exhibited superior hydrogen uptake storage capacities.^[206] Gogotsi *et al.* established that the carbon pore wall-hydrogen interaction differs significantly with the size of the

pores. The heat of adsorption of hydrogen at 77 K and ambient pressure is significantly higher, for carbons with a higher amount of pores below 1 nm, which again, possess a higher surface area normalized uptake capacity (7 compared to 6 kJ·mol⁻¹).^[209] The higher hydrogen-carbon interaction was ascribed to the fact hydrogen molecules, which are placed in small slit pores, are able to interact with a larger number of carbon atoms which increases the heat of adsorption (up to 7 kJ·mol⁻¹) along with the overlap of the adsorption potential from both pore walls. Thus, a higher uptake capacity can be obtained, because more available adsorption sites are addressed, compared to larger pores, which may not be able to exceed their full adsorption potential.^[310] This seems reasonable so far, as for this work, carbons with pores below 1 nm possess a higher normalized hydrogen uptake capacity, and the new model reveals the highest uptake for pores smaller than 1 nm. Gogotsi *et al.* eventually concluded, by evaluating a set of different microporous carbons and their respective average pore sizes and uptakes that the best effective pore size for hydrogen storage is below 0.75 nm, useful pore sizes are in the 0.75 to 1.30 nm in range and larger pores exhibit little or no significant contribution to the overall hydrogen uptake capacity.^[210] This is generally in accordance with the results from Figure 178, although the pore size ranges with their respective influence are a little bit different and the uptakes per surface area are oscillating within the pore size ranges, although the oscillating behavior is due to the pure mathematical approach and the best pores for hydrogen uptake are preferably below 0.6 nm. In addition to that, larger pores with the sizes of 1.4 nm may provide additional hydrogen uptake capacity, although no physical meaning can be addressed to this feature. Long *et al.* observed an unusual high heat of adsorption for a magnesia based metal organic framework, which indicated a stronger hydrogen-adsorbent interaction.^[311] They attributed this feature to an increased van der Waals contact area of hydrogen and adsorbent along with the adsorption potential overlap induced by pores as small as 0.36 nm. Additionally, the strong interaction of the hydrogen with the metal sited induces the strong increase of the heat of adsorption of hydrogen and metal organic frameworks.^[312] The van der Waals contact area should remain the same, since the carbon pore walls are considered evenly distributed regarding the atomic composition. However, the number of carbon atoms, which interact with the adsorptive may increase, as stated by Gogotsi *et al.* Lu *et al.* calculated just recently, that a force field, which attracts potential adsorptive molecules, differs with the size of the pores

and increases with decreasing pore radius of the pores.^[313] This force field predicts a continuously increase of adsorption energy of hydrogen and adsorbent, with decreasing pore size, which is basically the case for the new model. Kim *et al.* investigated the hydrogen adsorption mechanism on three synthesized microporous carbons, by comparing the hydrogen uptake with different pore volumes provided by different pore sizes.^[314] They concluded the highest impact on hydrogen uptake for pores in the range of 0.63 and 0.78 nm, with other pore ranges having a lower impact, simply by the fact that the uptake capacities give a linear correlation with the pore volumes. These results indicate a differentiated influence of different pore size ranges, even for pores below 1 nm, but are only based on three carbon samples and neglect the uptake capacities per surface area, which may be different compared to the overall uptake.

It is clear, the general trend of increasing hydrogen uptake per surface area with decreasing pore size of the respective carbons shown in Figure 178 can be explained with the increasing interaction of hydrogen and carbon in the confined pore. However, with the new model, it is possible to address new optimal pore sizes for hydrogen storage. (1) The best uptake capacity can be addressed to pores below 0.4 nm explained by the larger adsorption potential of hydrogen and carbon pore wall. (2) Pores below 0.9 nm can be considered as useful pore sizes, as their uptake per specific surface area is twice as large compared to pores larger than 0.9 nm. (3) Pores larger than 0.9 nm contribute to a lesser extent to the hydrogen uptake capacity, which can be addressed to the lower adsorption potential of hydrogen on the carbon pore walls. However, the oscillation of hydrogen uptake capacity per surface area, especially in the pore size range below 1 nm and for pore sizes around 1.40 and 3.7 nm is unusual. This is ascribed to the fact, that the approach is purely mathematical and does not consider molecule and substrate- specifically restrictions. In the case for the maximum around 1.4 nm, however, a layer of five molecules are able to enter these pores at pores around 1.5 nm, considering the kinetic diameter of the hydrogen molecule. Therefore, the fluid-fluid interaction becomes more prominent. Nevertheless, it is difficult to ascribe the pore size, at which point the fluid-fluid interaction is the primary adsorption parameter, compared the pore wall-fluid-interaction.

4.3.3 Applicability of the new model

The previous section showed that with the new model it is possible to simulate the gravimetric hydrogen uptake very accurately. In this section, the simulated pore size dependent cumulative uptake curves for the respective carbon samples will be evaluated in order to exemplify the new insights into the pore size dependent hydrogen uptake. The results are summarized in Table A.2.

The simulated cumulative gravimetric hydrogen uptake capacities of the carbon samples, synthesized with different KOH/carbon ratios and their respective measured uptake values are shown in Figure 180. It can be seen that the hydrogen uptakes for all samples could be simulated very well and only sample C-900-5-T9 shows a deviation of +3 % to the measured value, which is however also not a large deviation. It can also be observed that with increasing KOH/carbon ratio the hydrogen uptake, which is generated by pores up to 1 nm, clearly decreases.

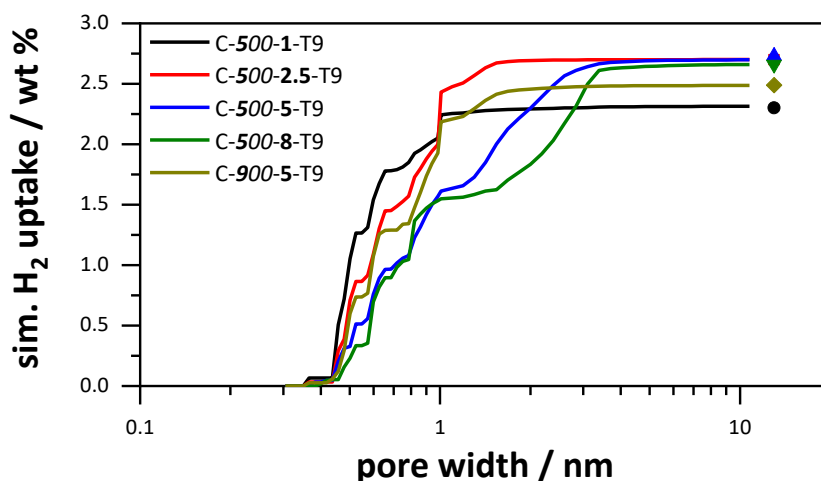


Figure 180: Simulated cumulative gravimetric hydrogen uptake capacity at 77 K and 1 bar in dependence of the pore width of the carbons synthesized with different KOH/carbon ratios and their respective measured uptake capacity in comparison.

This is due to the fact that with increasing KOH/carbon ratio the pores are enlarged and the proportion of pores with the size of less than 1 nm also decreases accordingly. This is even the case for sample C-500-1-T9 that the uptake for pores up to 1 nm is 2 wt%, which is due to the fact that small pores from 0.35 nm show the highest contribution to hydrogen uptake. For samples C-500-2.5-T9 and C-900-5-T9, the uptake up to pore sizes of 1 nm is approximately the same, as these also

show similar pore size distributions. The higher proportion of pores above 1 nm ultimately ensures that sample C-900-5-T9 can exhibit the higher uptake. Samples C-500-5-T9 and C-500-8-T9 have significantly less hydrogen capacity generated by pores up to 1 nm. These are nevertheless relatively large with 1.5 wt%, although a large part of the specific surface area of these carbons is generated by larger pores. This shows once again the higher contributions to the hydrogen uptake of pores below 1 nm. Nevertheless, samples C-500-5-T9 and C-500-8-T9 still show high total uptakes, which can be traced back to the pores between 1 and 4 nm, which are presented in both carbon samples in a higher frequency as seen in Figure 181. Therefore, both samples exhibit a high total hydrogen uptake. This exemplifies again, that carbon samples like C-500-5-T9 and C-500-8-T9, which lack pores below 1 nm, need to compensate with higher frequency of pores between 1 and 4 nm in order to exhibit high hydrogen uptakes. However, this also demonstrates that carbons which have been effectively activated with KOH and thus have high specific surfaces will rarely have high hydrogen absorption capacities of more than 3 wt% due to an unfavorable distribution of pores, specifically fewer pores below 1 nm.

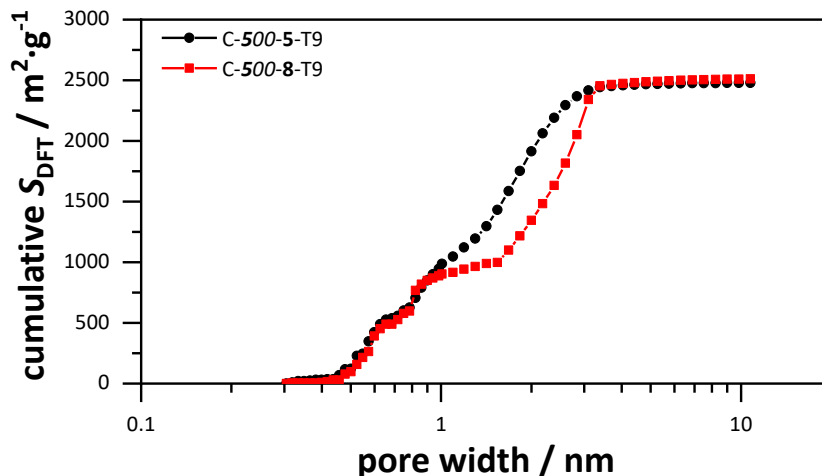


Figure 181: Combined cumulative surface area derived from carbon dioxide and nitrogen physisorption data of the carbon samples C-500-5-T9 and C-500-8-T9.

Evaluation of the cumulative hydrogen uptakes of the remaining carbon samples, which are displayed in Figure A.19 to Figure A.24, reveal information about the

respective pore size-dependent hydrogen uptake. Often the pores up to and including 1 nm provided more than half of the total hydrogen uptake. The pores in the 1 to 4 nm range are also important as they were present in higher frequencies for carbons with higher surface areas. However, the surface uptake capacities are significantly smaller compared to the smaller pores up to 1 nm. From a synthetic point of view, however, these were of importance. It was possible to increase the amount of pores and the content of the carbons below 1 nm by appropriate synthesis parameters, which then led to correspondingly high uptakes. However, the total specific surface area was often too small to obtain even higher uptakes than 2.65 wt% at 1 bar, although the uptake certainly increases with uptakes higher than 1 bar. To overcome this obstacle, changes in the synthesis parameters, which increased the specific surface area of the carbons, have the consequence that the pores are generally also enlarged and thus the number and content of micropores below 1 nm has decreased, whereby the capacity could not be maximized. To maximize the hydrogen uptake, a high specific surface area is needed, but this in turn is mainly formed by micropores up to and around 1 nm, which is difficult to achieve by chemical activation. These properties were best combined by sample FC-**PF**, whose pore size distribution is shown in Figure 182. In addition to a high specific surface area of $2575 \text{ m}^2\text{g}^{-1}$, it exhibited a large content of pores below 1 nm, more precisely around 0.6 nm, which led to an increase in hydrogen uptake. Thus a very high hydrogen uptake of 2.89 wt% could be achieved, which can also be well explained with the new model depending on the pore size.

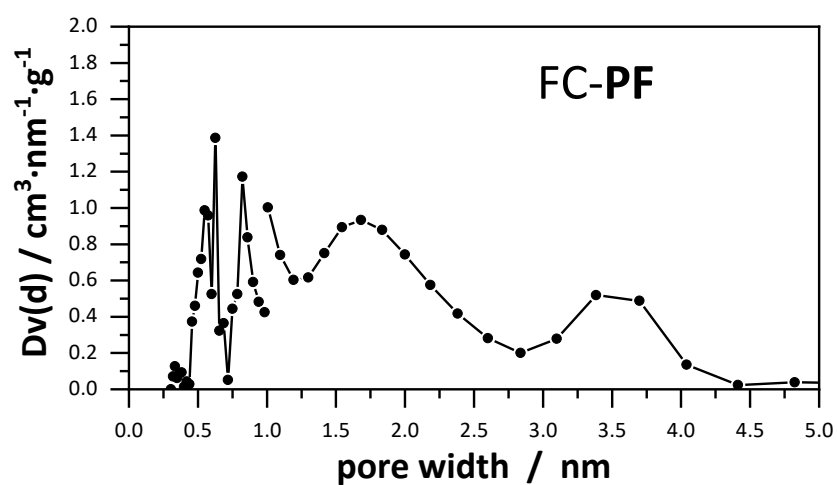


Figure 182: Pore size distribution calculated via NLDFT method from carbon dioxide physisorption and QSDFT method from nitrogen physisorption in combination.

5 Summary

Within the scope of the present thesis, a multitude of porous carbons were synthesized based on formaldehyde resins as precursor compounds. The materials differed with regard to their pore size and, accordingly, their specific surface area and pore volume. All carbon materials were investigated by SEM for their macroscopic morphology, Raman spectroscopy and P-XRD for their degree of graphitization. Carbon dioxide and nitrogen sorption were used to investigate porosity. In order to obtain the different carbons, phenol and formaldehyde were polymerized to resins under acidic conditions and then carbonized and chemically activated with KOH. The chemical activation with KOH is a more cost-effective alternative for the generation of pores compared to the template methods. Furthermore, a semi-carbonization step was introduced in the synthesis in order to increase the possibility of synthesis variation. In the progress of the work, the synthesis parameters were varied in order to determine their effect on the porosity of the carbons.

The variation of the amount of activation reactant used has clearly shown that a higher KOH/carbon ratio leads to materials with larger pores and thus larger pore volumes. The sample C-500-8-T9 showed pore sizes up to 4.0 nm. In addition, it was found that the specific surface area also increased with increasing KOH/carbon ratio, up to $2551 \text{ m}^2 \cdot \text{g}^{-1}$ for C-500-8-T9, showing that a higher KOH/carbon ratio not only generates more pores during chemical activation, but also leads to enlargement of existing micropores. A decisive influence on the porosity of the carbon materials could also be demonstrated for the semi-carbonization temperature. A lower semi-carbonization temperature led to a more effective chemical activation by KOH, which was expressed by carbons with larger pores, larger pore volumes and larger specific surfaces. The sample C-300-5-T9 showed pores with a size of up to 5 nm and a specific surface area of $2558 \text{ m}^2 \cdot \text{g}^{-1}$. This effect could also be shown clearly in the comparison of the samples C-500-2.5-T9 and C-900-2.5-T9. The higher effectiveness of the chemical activation is attributed to the larger amount of organic residues in the carbon, which leads to further pore formation during the chemical activation by carbonizing the remaining organic functional groups. For the activation temperature, it could be shown that with increasing activation temperature, carbons with larger pores and also larger specific surfaces were obtained. Sample C-500-5-T10 showed pore sizes of up to 4 nm and a specific surface area

of $2601 \text{ m}^2 \cdot \text{g}^{-1}$. Although pure KOH is already consumed at temperatures of 600°C , side reactions occur which lead to higher effectiveness of KOH activation. Regarding the application of carbon as electrode material in electrochemical double layer capacitors, pores with the size of desolvated electrolyte ions are of particular interest. Above all, the ion size of the tetraethylammonium cation of 0.67 nm represents a key parameter, since for carbon materials with smaller pores, the electrolyte ions cannot penetrate into the pores and thus barely contribute to the capacitance. In order to generate controlled pores below 1 nm , the effectiveness of the chemical activation had to be limited, which could be achieved by a higher semi-carbonization temperature, lower KOH/carbon ratio and lower activation temperature. Two parameters were investigated for each of two series of samples. In addition, the influence of the precursor compound on the porosity of the carbon was investigated. On the one hand, different ratios of resorcinol and phenol were used in the polymer synthesis, on the other hand the polymers were additionally cross-linked by Friedel-Crafts alkylation. Although a higher proportion of resorcinol in the polymer synthesis led to a change in the morphology of the carbons, the porosity did not change. As a result, it was possible to conclude that porosity is influenced exclusively by the carbonization and activation conditions.

All synthesized carbon materials were investigated as electrode materials for electrochemical double layer capacitors, with TEABF_4 in acetonitrile as electrolyte. The electrolyte ion sizes were particularly important in the desolvated state (0.45 nm for BF_4^- and 0.67 nm for TEA^+) as well as in the solvated state (1.2 nm for BF_4^- and 1.3 nm for TEA^+). The influence of the pore size and the specific surface area on the capacitance of the capacitors and the retention of the capacitance at high currents was investigated. Extensive electrochemical measurements were performed using cyclic voltammetry, galvanostatic charge/discharge and potentiostatic impedance spectroscopy. Basically, several materials showed high capacitances in the range of 140 to $160 \text{ F} \cdot \text{g}^{-1}$ and very high retentions of the capacitance with over 90% at a current density of $20 \text{ A} \cdot \text{g}^{-1}$. The maximum capacitance showed a general dependence of the specific surface area, but from a surface area of about $2000 \text{ m}^2 \cdot \text{g}^{-1}$ the specific surface area was not the decisive factor and the capacitances fluctuated very strongly. Therefore the accessible surface area was determined for each carbon sample. This is the surface area generated by pores larger than 0.67 nm . The acces-

sible surface area of the carbon is also a decisive factor for the maximum capacitance, since a larger surface area generally leads to a higher capacitance. However, saturation of the maximum capacitance with increasing accessible surface area was observed for all carbon materials. When considering the surface area normalized capacitances, it became clear that these were larger for carbons with smaller pores than for carbons with larger pores. This was a clear indication that smaller pores have a greater electrochemical usability of the surfaces, as already indicated in the literature.

In order to extend the existing insights, a model for the pore size-specific dependence of the surface capacitance was created. For this model a sandwich-type capacitor for pores up to 1.83 nm was postulated and a double-cylinder capacitor for larger pores was postulated. The decisive factor for the subdivision was the size of the bare and solvated electrolyte ions. The model was finally referred to as *enhanced sandwich double-cylinder capacitor* model or ESDCC model. Another special feature of the ESDCC model was that the relative permittivity of the solvent was also postulated to be pore size dependent. With the use of sorption data, gravimetric capacitances of each individual carbon material could now be simulated and compared with the measured capacitance values. For a selected series of carbons, the measured and simulated capacitance values were basically in agreement, but there were still deviations of 23 %. As a result, each pore size in the ESDCC model was assigned a factor that could be varied. The factors were varied in such a way that the average deviation of all measured and simulated capacitances of the carbons was minimized. The nonlinear GRG method was used and the solution obtained was the modified ESDCC model. Using the modified ESDCC model, all capacitance values of the carbons could be simulated with an accuracy of 10 %. In addition, new knowledge on the pore size dependence of the capacitance could be gained. It was shown that pores with a size between 0.72 and 0.75 nm provide the highest contribution to the capacitance of the carbons. This also corresponds to the findings and opinions of the literature, which could be confirmed in a new way. The reason for the increased capacitance in the small pores is the reduced distance between the electrolyte and the electrode wall, which is equivalent to an increased stored amount of charge per voltage. Furthermore, it was found that pores between 3.4 and 3.7 nm contribute to the capacitance in a lesser extent. This is attributed to the fact that a maximum of three electrolyte ions can penetrate into the pores of this

size, which leads to a lower degree of adsorbed ions on the surface of the pores and thus reduces the electrochemical usability of the corresponding pores.

Furthermore, the influence of pore size on the retention of capacitance at high currents should be investigated. From the results of the electrochemical investigations it could already be determined that carbons with a larger proportion of pores with a size of about 1.5 nm already showed very high retention. Thus it could already be determined that no larger mesopores are required to enable the diffusion of the electrolyte ions in the pores of the carbons. When applying the retention of the capacity against the ratio of the pore volumes $V_{>1.30\text{ nm}}/V_{0.66-1.30\text{ nm}}$ a corresponding dependence was found. As benchmark 80 % retention of the capacitance was defined and a clear dependence of the volume ratios on the volume-weighted average pore size could be determined. The exact critical pore size could not be extracted, since the frequency of this is also decisive. As criteria for the porosity of the carbons it could be determined that for an 80 % retention of the capacitance a volume-weighted average pore size of at least 1.1 nm must be present and 50 % of the volume accessible by the electrolyte ions must be generated by pores larger than 1.3 nm. The critical pore size could thus be set within a pore size range of 1.2 to 1.5 nm.

The influence of the specific surface area and pore size of the carbon materials on the hydrogen uptake capacity at 1 bar and 77 K was also investigated. High hydrogen uptake capacities of up to 2.89 wt% were observed. Here, too, it was shown that a higher specific surface area basically is beneficial for high uptake capacities, but a saturation effect is discernible from a surface area of $2200\text{ m}^2\cdot\text{g}^{-1}$. By evaluation of the specific surface area normalized capacities it could be shown that carbons with smaller pores have a higher adsorption capacity per surface compared to carbons with larger pores, which corresponds with the findings of the literature. Also for the pore size specific dependence of the capacity per surface a model was calculated using the nonlinear GRG method to simulate the average deviation of measured and simulated uptake capacities. The result shows some mathematical artifacts, but clearly shows that the highest uptake is generated by pores below 0.4 nm and pores in the range of 0.4 to 0.9 nm can also show high uptake capacities. The reason for this is the increased adsorption potential of hydrogen in pores of confined size.

In summary, it was found that the porosity of carbons can be strongly influenced by carbonization and activation conditions. At least with formaldehyde resins as precursor compounds, the composition merely has a minor influence. With regard to the influence of the pore sizes on the electrochemical double layer capacitance and hydrogen uptake capacity, the state of knowledge of the literature could be manifested by new models. For both capacities it could be shown that small pores below 1 nm provide higher contributions to the capacity and play an important role in the future design of electrode materials for capacitors and energy storage materials. However, the studies of this work have also shown that this is a synthetic challenge and will be difficult to realize by chemical activation. With regard to the retention of the double layer capacitance at high currents, however, it could be shown that pores in the range of 1.2 to 1.5 nm are sufficient to ensure the diffusion of the electrolyte ions, which could be shown in extensive electrochemical investigations. Thus, the prevailing opinion in the literature that mesopores are required for this effect has been refuted.

6 Zusammenfassung

Im Rahmen der vorliegenden Arbeit wurde eine Vielzahl von porösen Kohlenstoffen hergestellt, welche auf Formaldehydharzen als Vorläuferverbindungen basierten. Die Materialien unterschieden sich hinsichtlich ihrer Porengröße und dementsprechend auch ihrer spezifischen Oberfläche und Porenvolumen. Alle Kohlenstoffmaterialien wurden mittels REM hinsichtlich ihrer makroskopischen Morphologie sowie Ramanspektroskopie und P-XRD hinsichtlich ihres Grads der Graphitisierung untersucht. Zur Untersuchung der Porosität wurden Kohlenstoffdioxid- und Stickstoffsorption verwendet. Zur Realisierung der verschiedenen Kohlenstoffe, wurde Phenol und Formaldehyd zu Harzen unter sauren Bedingungen polymerisiert und diese anschließend carbonisiert und mit KOH chemisch aktiviert. Die chemische Aktivierung mittels KOH ist dabei eine kostengünstigere Alternative zur Generierung von Poren im Vergleich zu den Templatverfahren. Weiterhin wurde in der Synthese ein semi-Carbonisierungsschritt eingeführt, um die Variationsmöglichkeit weiter zu erhöhen. Im Laufe der Arbeit wurden die Syntheseparameter variiert um deren Auswirkung auf die Porosität der Kohlenstoffe zu untersuchen.

Bei der Variation der eingesetzten Menge an Aktivierungsmittel hat sich klar herausgestellt, dass ein höheres KOH/Kohlenstoffverhältnis zu Materialien mit größeren Poren und demnach größeren Porenvolumina führt. Die Probe C-500-8-T9 zeigte dabei Porengrößen bis zu 4.0 nm. Zudem konnte festgestellt werden, dass die spezifische Oberfläche ebenfalls mit zunehmenden KOH/Kohlenstoffverhältnis anstieg, bis $2551 \text{ m}^2 \cdot \text{g}^{-1}$ für C-500-8-T9, wodurch gezeigt werden konnte, dass ein höheres KOH/Kohlenstoffverhältnis nicht nur mehr Poren bei der chemischen Aktivierung generiert, sondern auch zur Vergrößerung bestehender Mikroporen führt. Ein entscheidender Einfluss auf die Porosität der Kohlenstoffmaterialien konnte auch für die semi-Carbonisierungstemperatur gezeigt werden. Eine geringere semi-Carbonisierungstemperatur führte dabei zu einer effektiveren chemischen Aktivierung mittels KOH, was sich durch Kohlenstoffe mit größeren Poren, größeren Porenvolumina und größeren spezifischen Oberflächen ausdrückte. Die Probe C-300-5-T9 zeigte dabei Poren mit einer Größe bis zu 5 nm und einer spezifischen Oberfläche von $2558 \text{ m}^2 \cdot \text{g}^{-1}$. Auch im Vergleich der Proben C-500-2.5-T9 und C-900-2.5-T9 konnte dieser Effekt deutlich gezeigt werden. Die höhere Effektivität der chemischen Aktivierung wird auf die größere Menge an organischen Resten in den

Kohlenstoffen zurückgeführt, wodurch es bei der chemischen Aktivierung zu weiteren Porenbildung kommt, indem die restlichen organischen funktionellen Gruppen carbonisiert werden. Für die Aktivierungstemperatur konnte gezeigt werden, dass mit steigender Aktivierungstemperatur, Kohlenstoffe mit größeren Poren und ebenfalls größeren spezifischen Oberflächen erhalten werden konnten. Probe C-500-5-T10 zeigte dabei Porengrößen bis zu 4 nm und eine spezifische Oberfläche von $2601 \text{ m}^2 \cdot \text{g}^{-1}$. Die das reine KOH wird zwar bereits bei Temperaturen von $600 \text{ }^\circ\text{C}$ verbraucht, jedoch finden weiter Nebenreaktionen statt, welche zur höheren Effektivität der KOH Aktivierung führen. Bezüglich der Anwendung der Kohlenstoffe als Elektrodenmaterialien in elektrochemischen Doppelschichtkondensatoren, sind besonders die Poren mit der Größe der unsolvatisierten Elektrolyt Ionen von Interesse. Vor allem die Ionengöße des Tetraethylammonium Kations von 0.67 nm stellt eine Kenngröße dar, da für Kohlenstoffe mit kleineren Poren, die Elektrolyt Ionen nicht in die Poren penetrieren können und somit kaum einen Beitrag zur Kapazität leisten. Um daher kontrollierter Poren unter 1 nm zu generieren, musste die Effektivität der chemischen Aktivierung eingegrenzt werden, was durch eine höhere semi-Carbonisierungstemperatur, geringerem KOH/Kohlenstoffverhältnis und niedrigerer Aktivierungstemperatur erreicht werden konnte. Dabei wurden für zwei Probenreihen jeweils zwei Parameter untersucht. Außerdem wurde der Einfluss der Vorläuferverbindung auf die Porosität der Kohlenstoffe untersucht. Dabei wurden zum einen, verschiedene Verhältnisse Resorcin und Phenol in der Polymersynthese eingesetzt, zum anderen wurden die Polymere zusätzlich mittels Friedel-Crafts-Alkylierung vernetzt. Zwar hat ein höherer Resorcinanteil in der Polymersynthese zu einer Veränderung der Morphologie der Kohlenstoffe geführt, die Porosität hat sich jedoch nicht verändert. Daraus konnte geschlossen werden, dass die Porosität ausschließlich durch die Carbonisierungs- und Aktivierungsbedingungen beeinflusst wird.

Alle dargestellten Kohlenstoffmaterialien wurden als Elektrodenmaterialien für elektrochemische Doppelschichtkondensatoren untersucht, mit TEABF₄ in Acetonitril als Elektrolyt. Dabei waren besonders die Elektrolytionengrößen von Bedeutung im unsolvatisierten (0.45 nm für BF₄⁻ und 0.67 nm für TEA⁺) als auch im solvatisierten Zustand (1.2 nm für BF₄⁻ und 1.3 nm für TEA⁺) im Fokus. Hierbei sollte besonders der Einfluss der Porengröße und der spezifischen Oberfläche auf die Ka-

pazität der Kondensatoren und die Retention der Kapazität bei hohen Strömen untersucht werden. Dafür wurden umfangreiche elektrochemische Messungen durchgeführt wobei Cyclovoltammetrie, galvanostatische Ladung/Entladung und potentiostatische Impedanz Spektroskopie eingesetzt worden sind. Grundsätzlich, zeigten viele Materialien hohe Kapazitäten im Bereich von 140 bis 160 F·g⁻¹ und sehr hohe Retentionen der Kapazität mit über 90 % bei einer Stromdichte von 20 A·g⁻¹. Die maximale Kapazität zeigte dabei eine generelle Abhängigkeit der spezifischen Oberfläche, jedoch wurde diese ab einer Oberfläche von etwa 2000 m²·g⁻¹ nicht mehr eindeutig und die Kapazitäten fluktuieren sehr stark. Daher wurde für jede Kohlenstoffprobe die erreichbare Oberfläche bestimmt. Dies ist die Oberfläche, welche durch Poren gebildet wird, welche größer sind als 0.67 nm. Auch die erreichbare Oberfläche der Kohlenstoffe ist ein entscheidender Faktor der maximalen Kapazität, da eine größere Oberfläche grundsätzlich zu einer höheren Kapazität führt. Jedoch konnte auch hier eine Sättigung der maximalen Kapazität mit steigender erreichbarer Oberfläche für alle Kohlenstoffmaterialien beobachtet werden. Bei der Betrachtung der oberflächennormierten Kapazitäten wurde deutlich, dass diese für Kohlenstoffe mit durchschnittlich kleineren Poren größer waren, als für Kohlenstoffe mit durchschnittlich größeren Poren. Dies war ein eindeutiger Hinweis darauf, dass kleinere Poren eine größere elektrochemische Nutzbarkeit der Oberflächen aufweisen, wie es auch schon in der Literatur gezeigt wurde.

Um die bestehenden Erkenntnisse zu erweitern, wurde ein Modell zur porengrößenspezifischen Abhängigkeit der Oberflächenkapazität erstellt. Für dieses Modell wurden ein Sandwich-Typ Kondensator für Poren bis 1.83 nm postuliert und der Doppelzylinderkondensator für größere Poren angenommen. Als entscheidender Faktor zur Unterteilung war dabei die Größe der nackten und solvatisierten Elektrolyt Ionen. Das Modell wurde schließlich *enhanced sandwich double-cylinder capacitor model* oder auch ESDCC Modell genannt. Eine weitere Besonderheit des ESDCC Modells war zudem, dass die relative Permittivität des Lösungsmittels ebenfalls porengrößenabhängig postuliert worden ist. Mithilfe der Sorptionsdaten konnten nun gravimetrische Kapazitäten jeder einzelnen Kohlenstoffmaterialien simuliert werden und mit den gemessenen Kapazitätswerten verglichen werden. Für eine ausgewählte Reihe von Kohlenstoffen zeigte sich grundsätzlich eine gute Übereinstimmung der gemessenen und simulierten Kapazitäten, jedoch gab es noch Abweichungen von 23 %. Daraufhin wurde jeder Porengröße im ESDCC Modell

ein Faktor zugewiesen welcher variiert werden konnte. Die Faktoren sollten dabei so variiert werden, dass die durchschnittliche Abweichung aller gemessener und simulierten Kapazitäten der Kohlenstoffe minimiert wurde. Dafür wurde die nicht-lineare GRG Methode verwendet und als Lösung wurde die das modifizierte ESDCC Modell erhalten. Mithilfe des modifizierten ESDCC Modells konnten alle Kapazitätswerte der Kohlenstoffe mit einer Genauigkeit von 10 % simuliert werden. Zudem konnte neue Erkenntnisse zur Porengrößenabhängigkeit der Kapazität gewonnen werden. Es zeigte sich, dass Poren mit der Größe zwischen 0.72 und 0.75 nm den höchsten Beitrag zur Kapazität der Kohlenstoffe liefern. Dies entspricht dabei auch den Erkenntnissen und Meinungen der Literatur, welche hiermit auf einer neuen Art und Weise bestätigt werden konnten. Der Grund für die erhöhte Kapazität in den kleinen Poren ist die verringerte Distanz zwischen Elektrolyt-Ion und Elektrodenwand, was gleichbedeutend mit einer erhöhten gespeicherten Ladungsmenge pro Spannung. Weiterhin konnte noch festgestellt werden, dass Poren zwischen 3.4 und 3.7 nm einen sehr geringen Beitrag zur Kapazität liefern. Dies wird darauf zurückgeführt, dass maximal drei Elektrolyt-Ionen in die Poren dieser Größe eindringen können, was zu einem geringeren Grad adsorbierten Ionen an der Porenoberfläche führt und damit die elektrochemische Nutzbarkeit der entsprechenden Poren geringer ist.

Weiterhin sollte der Einfluss der Porengröße auf die Retention der Kapazität bei hohen Strömen untersucht werden. Aus den Ergebnissen der elektrochemischen Untersuchungen konnte bereits festgestellt werden, dass Kohlenstoffe mit größeren Anteil an Poren mit der Größe um 1.5 nm bereits sehr gute Retentionen aufweisen konnten. Somit konnte bereits festgestellt werden, dass keine größeren Mesoporen benötigt werden um die Diffusion der Elektrolyt-Ionen in den Poren der Kohlenstoffe zu ermöglichen. Bei der Auftragung der Retention der Kapazität gegen das Verhältnis der Porenvolumina $V_{>1.30\text{ nm}}/V_{0.66-1.30\text{ nm}}$ zeigte sich eine entsprechende Abhängigkeit. Als Benchmark wurden 80 % Retention der Kapazität festgelegt und eine deutliche Abhängigkeit dieser von der volumengewichteten durchschnittlichen Porengröße konnte festgestellt werden. Die genaue kritische Porengröße konnte nicht bestimmt werden, da auch die Häufigkeit dieser entscheidend ist. Als Kriterien der Porosität der Kohlenstoffe konnte festgelegt werden, dass für eine 80 % ige Retention der Kapazität eine volumengewichtete durchschnittliche Porengröße von mindestens 1.1 nm vorhanden sein muss und 50 % des von den Elektrolyt-Ionen

erreichbaren Volumens von Poren größer als 1.3 nm generiert werden muss. Die kritische Porengröße konnte damit auf einen Bereich von 1.2 bis 1.5 nm festgelegt werden.

Auch der Einfluss der spezifischen Oberfläche und Porengröße der Kohlenstoffmaterialien auf die Wasserstoffaufnahmekapazität bei 1 bar und 77 K wurde untersucht. Dabei konnten hohe Wasserstoffaufnahmekapazitäten von bis zu 2.89 wt% festgestellt werden. Auch hier hat sich gezeigt, dass eine höhere spezifische Oberfläche grundsätzlich hohe Aufnahmekapazitäten ermöglicht, jedoch einen Sättigungseffekt ab einer Oberfläche von $2200 \text{ m}^2 \cdot \text{g}^{-1}$ erkennbar ist. Durch Auswertung der oberflächennormierten Kapazitäten konnte zudem gezeigt werden, dass Kohlenstoffe mit durchschnittlich kleineren Poren eine höhere Aufnahmekapazität pro Oberfläche aufweisen im Vergleich zu Kohlenstoffen mit größeren Poren, was damit Erkenntnissen der Literatur entspricht. Auch für die porengrößenspezifische Abhängigkeit der Kapazität pro Oberfläche wurde ein Modell mithilfe der nichtlinearen GRG Methode berechnet um die durchschnittliche Abweichung von gemessenen und simulierten Aufnahmekapazitäten zu simulieren. Das Ergebnis weist einige mathematische Artefakte auf, zeigt jedoch deutlich, dass die höchste Aufnahme durch Poren unter 0.4 nm generiert wird und Poren im Bereich von 0.4 bis 0.9 nm ebenfalls noch hohe Aufnahmekapazitäten aufzeigen können. Der Grund dafür liegt in dem erhöhten Adsorptionspotential von Wasserstoff in größenbeschränkten Poren.

Zusammenfassend lässt sich also sagen, dass die Porosität von Kohlenstoffen sehr stark durch Carbonisierungs- und Aktivierungsbedingungen beeinflusst werden kann. Dabei spielt zumindest bei Formaldehydharzen als Vorläuferverbindung, die Zusammensetzung nur eine untergeordnete Rolle. Bezüglich des Einflusses der Porengrößen auf die elektrochemische Doppelschichtkapazität und Wasserstoffaufnahmekapazität konnten der Wissenstand der Literatur anhand von neuen Modellen manifestiert werden. Für beide Kapazität konnte dabei gezeigt werden, dass kleine Poren unter 1 nm jeweils höhere Beiträge zur Kapazität liefern und dabei eine wichtige Rolle in der zukünftigen Gestaltung von Elektrodenmaterialien für Kondensatoren und Energiespeichermaterialien einnehmen. Es hat sich in den Studien dieser Arbeit jedoch auch gezeigt, dass dies synthetisch durchaus eine Herausforderung

darstellt und mittels chemischer Aktivierung schwierig zu realisieren sein wird. Bezüglich der Retention der Doppelschichtkapazität bei hohen Strömen konnte jedoch gezeigt werden, dass Poren im Bereich von 1.2 bis 1.5 nm ausreichend sind um die Diffusion der Elektrolyt-Ionen zu gewährleisten, was in umfangreichen elektrochemischen Untersuchungen gezeigt werden konnte. Damit ist die in der Literatur vorherrschende Meinung widerlegt worden, dass für diesen Effekt Mesoporen benötigt werden.

7 Experimental Section

7.1 Material syntheses

7.1.1 Synthesis of phenol formaldehyde-resins

In a typical synthesis of PF resins, 2.2 g (24 mmol) phenol (ABCR) were dissolved in 30 g ethanol. While stirring, 4.4 mL (58 mmol) of formaldehyde (Grüssing, 37 wt% in water) solution and 10 mL of hydrochloric acid (HCl, 37 wt%) were added. The mixture was heated to 95 °C for 24 h. The bright brown PF resin was filtered, washed with ethanol and dried for 12 h at 100 °C.

7.1.2 Synthesis of PF resins based carbons

In a typical carbon synthesis on the basis of a PF resin, the powdery dark red PF polymer was heated in a quartz tube furnace at temperatures of 300, 400, 500, 600, 700, 800 or 900 °C for 3 h under argon inert gas atmosphere with a heating rate of 5 °C·min⁻¹. The pre-carbonized material was mixed with potassium hydroxide in different ratios of 1, 2.5, 5 or 8 to 1 and dissolved in water and ethanol. The mixture was then dried at 100 °C for 24 h to ensure a good amalgamation of the pre-carbonized carbon and potassium hydroxide. The carbon/KOH mixture was activated at temperatures of 600, 700, 800, 900 or 1000 °C with no holding time under nitrogen gas atmosphere. The resulting product was washed with diluted HCl and distilled water to remove any impurities until the filtrate was pH neutral. The product was dried for 24 h at 100 °C.

7.1.3 Synthesis of phenol resorcinol formaldehyde resins

In a typical synthesis of PRF resins, phenol and resorcinol were dissolved in different ratios in 30 g ethanol. The different ratios were 1.47 g phenol (16 mmol) and 0.88 g resorcinol (8 mmol), 1.10 g phenol (12 mmol) and 1.32 g resorcinol (12 mmol), 0.73 phenol (8 mmol) and 1.76 g resorcinol (16 mmol) and 2.64 g resorcinol (24 mmol) only. While stirring, 4.4 mL (58 mmol) of formaldehyde (Grüssing, 37 wt% in water) solution and 10 mL of hydrochloric acid (HCl, 37 wt%) were added. The mixture was heated to 95 °C for 24 h. The bright brown to black PRF resins were filtered, washed with ethanol and dried for 12 h at 100 °C.

7.1.4 Synthesis of PRF resin based carbons

In a typical synthesis of PRF resin based carbons, the powdery resin was heated in a quartz tube furnace at a temperature 500 °C for 3 h under argon inert gas atmosphere with a heating rate of 5 °C·min⁻¹. The pre-carbonized material was mixed with potassium hydroxide in a ratio of 5 to 1 and dissolved in water and ethanol. The mixture was then dried at 100 °C for 24 h to ensure a good mixture of the pre-carbonized carbon and potassium hydroxide. The carbon/KOH mixture was activated at a temperature of, 900 with no holding time under nitrogen gas atmosphere. The resulting product was washed with diluted HCl and distilled water to remove any impurities until the filtrate was pH neutral. The product was dried for 24 h at 100 °C.

7.1.5 Synthesis of FC-cross-linked PRF resins

Either 2.2 g (24 mmol) phenol, 2.6 g (24 mmol) resorcinol or mixtures of them with the ratio of 0.47 g phenol (16 mmol) and 0.88 g resorcinol (8 mmol), 1.10 g phenol (12 mmol) and 1.32 g resorcinol (12 mmol), 0.73 phenol (8 mmol) and 1.76 g resorcinol (16 mmol) were dissolved in 50 mL carbon tetrachloride and while stirring, 4.4 mL (58 mmol) of formaldehyde (37 wt% in water) solution and 1 g Aluminum trichloride were added. The clear, colorless solution was heated at 90 °C for 30 minutes. In parallel, 12.0 g (90 mmol) AlCl₃ was suspended in 150 mL CCl₄ and heated at 90 °C for 60 minutes to form an orange suspension. The clear, pale yellow phenol-resorcinol/formaldehyde solution in CCl₄ was carefully added to the AlCl₃/CCl₄ solution and the mixture was heated for 2 days at 90 °C. To terminate the reaction, a mixture of 50 mL water, 25 mL ethanol and 5 mL 37 % HCl was added to the suspended purple solid. A brown solid was formed, which was filtered and washed with water and dried for 24 h at 100 °C.

7.1.6 Synthesis of FC cross-linked PRF resin based carbons

In a typical synthesis of FC-cross-linked PRF resin based carbons, the powdery resin was heated in a quartz tube furnace at a temperature 500 °C for 3 h under argon inert gas atmosphere with a heating rate of 5 °C·min⁻¹. The pre-carbonized material was mixed with potassium hydroxide in a ratio of 5 to 1 and dissolved in water and ethanol. The mixture was then dried at 100 °C for 24 h to ensure a good amalgamation of the pre-carbonized carbon and potassium hydroxide. The carbon/KOH mixture was activated at a temperature of, 900 °C with no holding time

under nitrogen gas atmosphere. The resulting product was washed with diluted HCl and distilled water to remove any impurities until the filtrate was pH neutral. The product was dried for 24 h at 100 °C.

7.2 Characterization methods

7.2.1 Physisorption

Nitrogen adsorption-desorption isotherms were obtained on a Quadrasorp SI-MP analyzer from Quantachrome at 77 K. Carbon dioxide and hydrogen adsorption-desorption isotherms were obtained on an Autosorb-iQ-MP analyzer from Quantachrome at 273 K for carbon dioxide and 77 K for hydrogen respectively. Prior to the measurement, the samples were degassed and dried at a Degasser Masterprep-station from Quantachrome for 24 h at 120 °C in vacuo (10^{-5} bar). The measured data were evaluated with the QuadraWin software from Quantachrome. For the calculation of the BET surface area, a relative pressure range of 0.05-0.3 was selected to ensure a positive line intersect of multipoint BET fitting ($C > 0$) was obtained and $V_{\text{ads}} (1-p/p_0)$ increased with p/p_0 . The pore size distributions, pore volumes and surface areas were calculated by the QSDFT method for nitrogen using the slit pore equilibrium kernel for nitrogen at carbon. For the evaluation of the pore range from 1 to 10.7 nm nitrogen sorption was used, because no larger pores were observed for any carbon sample. Carbon dioxide sorption was used to study the range of pores below 1 nm. Pore size distribution, pore volume and surface area were calculated by the NLDFT method using the slit pore equilibrium kernel for carbon dioxide at carbon. The micropore volume was collected from the cumulative pore volume at 2 nm from the nitrogen sorption.

7.2.2 Scanning electron microscopy

Scanning electron microscopy (SEM) images were taken on NTS LEO-1525 from Carl Zeiss Company. The acceleration voltage was 5 kV.

7.2.3 Powder X-Ray diffraction

X-ray diffraction patterns were obtained on a PANalytical X'Pert Pro in reflection mode. The X-ray tube was operated with a voltage of 40 kV and a current of 30 mA and Cu- K_{α} radiation with a wavelength of 1.54 Å was used. The step size was $0.1^{\circ} 2\theta$ with a measurement time of 72 seconds per step in the range of $2\theta = 10$ to

70°. For the evaluation of the measured data the software X'Pert HighScore Plus from PANalytical was used.

7.2.4 Raman spectroscopy

Raman spectra were recorded on a SENTERRA microscope from Bruker. The source of radiation was a laser operating at a wavelength of 633 nm. It was measured in a wavenumber range of 400 to 1800 cm^{-1} .

7.2.5 Thermal analysis

The thermal analysis of the carbon samples was carried out in a thermobalance STA 409 from Netzsch. The sample was heated to 900 °C in an Al_2O_3 crucible in an air stream with a flow rate of 50 $\text{mL}\cdot\text{min}^{-1}$ at a heating rate of 5 $^\circ\text{C}\cdot\text{min}^{-1}$.

7.2.6 Cell preparation and electrochemical measurements

Electrodes were prepared by mixing carbon active material with polyvinylidene fluoride (PVDF) binder (Sigma-Aldrich, 10 % suspension in N-methyl-pyrrolidone, NMP) and VULCAN XC72R (CABOT) as conductive additive in a ratio of 7:2:1 in a slurry with NMP. The slurry was coated on aluminum foil (Custom Cells, 20 μm) and dried at 100 °C in vacuo. The thickness of the electrodes of each sample was approximately 70 μm (including Al foil). Electrodes were cut out with a diameter of 1.8 cm with mass loadings from 0.50 to 1.05 $\text{mg}\cdot\text{cm}^{-2}$ of total active carbon material. The electrochemical measurements were performed in a two-electrode test cell setup (El-Cell) using stainless steel electrodes (1.8 cm diameter). Symmetrical electrochemical capacitors were built using two carbon electrodes of identical mass, electrically isolated by glassy fibrous separator (Whatman, 50 μm). A 1 M tetraethylammonium tetrafluoroborate (TEABF_4 , electrochemical grade, Sigma-Aldrich) solution in acetonitrile (AN, 99.999 %, Sigma-Aldrich) was used as electrolyte. The electrochemical characterization was performed using a computer-controlled potentiostat (Biologic VMP3). Before electrochemical tests were carried out, each test cell was cycled at a scan rate of 75 $\text{mV}\cdot\text{s}^{-1}$ 25 times to ensure wettability of the electrode and equilibrium state of electrolyte ions on the carbon electrode surface. All calculations regarding electrochemical tests were calculated by the means of the following equations (31) – (34).

CV was conducted between 0 and 2.5 V at increasing scan rates from 10 to 2500 mV·s⁻¹. The specific capacitance of both electrodes was calculated from the area of the voltammograms by the means of the following equations:

$$C_{CV} = \frac{4 \int_0^{2.5} I dV}{vm\Delta V} \quad (31)$$

where I is the current (mA), v the scan rate (mV·s⁻¹), ΔV the voltage window (V) and m the mass (g) of total active carbon material of both electrodes. Galvanostatic charge/discharge cycling was also performed in the 0 to 2.5 V range at current densities ranged between 1 and 20 A·g⁻¹, based on the total electrode mass of both electrodes. The specific capacitance of both electrodes determined from galvanostatic cycles was calculated by means of the equation:

$$C_{DC} = \frac{2I}{(dV/dt)m} \quad (32)$$

where dV/dt is the slope of the discharge curve (V·s⁻¹). Electrochemical impedance spectroscopy was carried out at open circuit voltage within the frequency range of 10 mHz to 500 kHz and a 5 Mv AC amplitude. Plots of the dependence of the capacitance on the frequency were recorded to characterize the impedance of the samples. The real specific capacitance of both electrodes C'_{EIS} was calculated according to the following equation and normalized with respect to the specific capacitance at 10 mHz:

$$C'_{EIS} = \frac{4|\text{Im}(Z)|}{2\pi f|Z|^2 m} \quad (33)$$

where f is the operating frequency (Hz), $\text{Im}(Z)$ the imaginary component of the impedance (Ohm) and Z the total impedance (Ohm). The imaginary specific capacitance of both electrodes C''_{EIS} was calculated by means of the following equation and normalized with respect to the highest imaginary capacitance:

$$C''_{EIS} = \frac{4|\text{Re}(Z)|}{2\pi f|Z|^2 m} \quad (34)$$

where $\text{Re}(Z)$ is the real part of the impedance (Ohm). The time relaxation constant τ_0 , which separates the capacitive behavior and the resistive behavior of the supercapacitor, was deduced from the frequency f_0 as follows: $\tau_0 = 1/f_0$, where f_0 is the peak frequency of the plot from the imaginary capacitance.

8 Bibliography

- [1] R. N. Carmody, R. W. Wrangham, *J. Hum. Evol.* **2009**, 57, 379–391.
- [2] L.-C. Sang, A. Vinu, M.-O. Coppens, *J. Mater. Chem.* **2011**, 21, 7410.
- [3] S. L. Candelaria, Y. Shao, W. Zhou, X. Li, J. Xiao, J.-G. Zhang, Y. Wang, J. Liu, J. Li, G. Cao, *Nano Energy* **2012**, 1, 195–220.
- [4] R. Nagar, B. P. Vinayan, S. S. Samantaray, S. Ramaprabhu, *J. Mater. Chem. A* **2017**, 5, 22897–22912.
- [5] M. Balat, H. Balat, *Appl. Energy* **2009**, 86, 2273–2282.
- [6] J. Ren, N. M. Musyoka, H. W. Langmi, M. Mathe, S. Liao, *Int. J. Hydrogen Energy* **2017**, 42, 289–311.
- [7] M. Thommes, K. Kaneko, A. V. Neimark, J. P. Olivier, F. Rodriguez-Reinoso, J. Rouquerol, K. S. W. Sing, *Pure Appl. Chem.* **2015**, 87, 1051–1069.
- [8] H. Giesche, *Part. Part. Syst. Charact.* **2006**, 23, 9–19.
- [9] H. P. Boehm, *Carbon N. Y.* **1994**, 32, 759–769.
- [10] A. Bentur, S. Mindess, *Fibre Reinforced Cementitious Composites*, CRC Press, London, **2006**.
- [11] E. Frackowiak, *Phys. Chem. Chem. Phys.* **2007**, 9, 1774–85.
- [12] G. Lota, K. Lota, E. Frackowiak, *Electrochem. Commun.* **2007**, 9, 1828–1832.
- [13] A. G. Pandolfo, A. F. Hollenkamp, *J. Power Sources* **2006**, 157, 11–27.
- [14] P. W. Ruch, R. Kötz, A. Wokaun, *Electrochim. Acta* **2009**, 54, 4451–4458.
- [15] Y. Zhai, Y. Dou, D. Zhao, P. F. Fulvio, R. T. Mayes, S. Dai, *Adv. Mater.* **2011**, 23, 4828–4850.
- [16] M. Inagaki, H. Konno, O. Tanaike, *J. Power Sources* **2010**, 195, 7880–7903.
- [17] G. Wang, L. Zhang, J. Zhang, *Chem. Soc. Rev.* **2012**, 41, 797–828.
- [18] A. F. Holleman, E. Wiberg, N. Wiberg, *Lehrbuch Der Anorganischen Chemie*, Walter De Gruyter, Berlin, **2007**.
- [19] M. Harry, F. Rodriguez-Reinoso, *Activated Carbon*, Elsevier Science & Technology Books, **2006**.
- [20] M. S. Whittingham, *Chem. Rev.* **2004**, 104, 4271–4302.
- [21] B. Scrosati, J. Garche, *J. Power Sources* **2010**, 195, 2419–2430.
- [22] R. Luque, A. M. Balu, *Producing Fuels and Fine Chemicals from Biomass Using Nanomaterials*, Taylor & Francis Group, LLC, Boca Raton, **2013**.

- [23] A. Corma, *Chem. Rev.* **1997**, 97, 2379–2419.
- [24] F. Caruso, R. A. Caruso, H. Möhwald, *Chem. Mater.* **1999**, 11, 3309–3314.
- [25] F. Rodríguez-reinoso, *Carbon N. Y.* **1998**, 36, 159–175.
- [26] E. Frackowiak, F. Béguin, *Carbon N. Y.* **2001**, 39, 937–950.
- [27] S.-Y. Lee, S.-J. Park, *J. Ind. Eng. Chem.* **2015**, 23, 1–11.
- [28] S. B. Yoon, K. Sohn, J. Y. Kim, C.-H. Shin, J.-S. Yu, T. Hyeon, *Adv. Mater.* **2002**, 14, 19–21.
- [29] R. C. Bansal, J.-B. Donnet, F. Stoeckli, *Active Carbon*, Dekker, New York, **1988**.
- [30] Z. Hu, H. Guo, M. P. Srinivasan, N. Yaming, *Sep. Purif. Technol.* **2003**, 31, 47–52.
- [31] A. Oya, S. Yoshida, J. Alcaniz-Monge, A. Linares-Solano, *Carbon N. Y.* **1995**, 33, 1085–1090.
- [32] C. Srinivasakannan, *Biomass and Bioenergy* **2004**, 27, 89–96.
- [33] Y. J. Kim, Y. Abe, T. Yanagiura, K. C. Park, M. Shimizu, T. Iwazaki, S. Nakagawa, M. Endo, M. S. Dresselhaus, *Carbon N. Y.* **2007**, 45, 2116–2125.
- [34] X. He, P. Ling, M. Yu, X. Wang, X. Zhang, M. Zheng, *Electrochim. Acta* **2013**, 105, 635–641.
- [35] Z. Jin, X. Yan, Y. Yu, G. Zhao, *J. Mater. Chem. A* **2014**, 2, 11706.
- [36] S. Bai, G. Tan, X. Li, Q. Zhao, Y. Meng, Y. Wang, Y. Zhang, D. Xiao, *Chem. - An Asian J.* **2016**, 11, 1828–1836.
- [37] M. Sevilla, G. A. Ferrero, A. B. Fuertes, *Carbon N. Y.* **2017**, 114, 50–58.
- [38] N. Patel, K. Okabe, A. Oya, *Carbon N. Y.* **2002**, 40, 315–320.
- [39] R. Kötz, M. Carlen, *Electrochim. Acta* **2000**, 45, 2483–2498.
- [40] R. W. Pekala, *J. Mater. Sci.* **1989**, 24, 3221–3227.
- [41] H. Teng, S.-C. Wang, *Carbon N. Y.* **2000**, 38, 817–824.
- [42] Y. Wan, Y. Shi, D. Zhao, *Chem. Mater.* **2008**, 20, 932–945.
- [43] C. Liang, Z. Li, S. Dai, *Angew. Chemie - Int. Ed.* **2008**, 47, 3696–3717.
- [44] J. Jang, B. Lim, *Adv. Mater.* **2002**, 14, 1390–1393.
- [45] A. Lu, A. Kiefer, W. Schmidt, F. Schüth, *Chem. Mater.* **2004**, 16, 100–103.
- [46] C. M. Yang, C. Weidenthaler, B. Spliethoff, M. Mayanna, F. Schüth, *Chem. Mater.* **2005**, 17, 355–358.
- [47] H. Nishihara, T. Kyotani, *Adv. Mater. (dearf. Beach, Fla.)* **2012**, 24, 4473–98.

-
- [48] S. Han, T. Hyeon, *Chem. Commun.* **1999**, 1955–1956.
- [49] R. Ryoo, S. H. Joo, S. Jun, *J. Phys. Chem. B* **1999**, *103*, 7743–7746.
- [50] A.-H. Lu, F. Schüth, *Adv. Mater.* **2006**, *18*, 1793–1805.
- [51] I. Moriguchi, A. Ozono, K. Mikuriya, Y. Teraoka, S. Kagawa, M. Kodama, *Chem. Lett.* **1999**, 1171–1172.
- [52] Y. Meng, D. Gu, F. Zhang, Y. Shi, H. Yang, Z. Li, C. Yu, B. Tu, D. Zhao, *Angew. Chemie Int. Ed.* **2005**, *44*, 7053–7059.
- [53] Y. Meng, D. Gu, F. Zhang, Y. Shi, L. Cheng, D. Feng, Z. Wu, Z. Chen, Y. Wan, A. Stein, et al., *Chem. Mater.* **2006**, *18*, 4447–4464.
- [54] R. Liu, Y. Shi, Y. Wan, Y. Meng, F. Zhang, D. Gu, Z. Chen, B. Tu, D. Zhao, *J. Am. Chem. Soc.* **2006**, *128*, 11652–62.
- [55] C. J. Brinker, Y. Lu, A. Sellinger, H. Fan, *Adv. Mater.* **1999**, *11*, 579–585.
- [56] D. Braun, G. Collin, *Chem. Unserer Zeit* **2010**, *44*, 190–197.
- [57] L. Pilato, *Phenolic Resins: A Century of Progress*, Springer Berlin Heidelberg, Berlin, Heidelberg, **2010**.
- [58] E. Breitmeier, G. Jung, *Organische Chemie*, Goerg Thieme Verlag, Stuttgart, **2009**.
- [59] C. Liang, K. Hong, G. A. Guiochon, J. W. Mays, S. Dai, *Angew. Chemie - Int. Ed.* **2004**, *43*, 5785–5789.
- [60] C. Liang, S. Dai, *J. Am. Chem. Soc.* **2006**, *128*, 5316–5317.
- [61] X. Wang, C. Liang, S. Dai, *Langmuir* **2008**, *24*, 7500–7505.
- [62] L.-C. Sang, A. Vinu, M.-O. Coppens, *J. Mater. Chem.* **2011**, *21*, 7410.
- [63] C. Zou, D. Wu, M. Li, Q. Zeng, F. Xu, Z. Huang, R. Fu, *J. Mater. Chem.* **2010**, *20*, 731.
- [64] Z. Li, D. Wu, Y. Liang, F. Xu, R. Fu, *Nanoscale* **2013**, *5*, 10824–8.
- [65] J. Wang, S. Kaskel, *J. Mater. Chem.* **2012**, *22*, 23710–23725.
- [66] T. M. Alslaibi, I. Abustan, M. A. Ahmad, A. A. Foul, *J. Chem. Technol. Biotechnol.* **2013**, *88*, 1183–1190.
- [67] J. Jin, S. Tanaka, Y. Egashira, N. Nishiyama, *Carbon N. Y.* **2010**, *48*, 1985–1989.
- [68] H. Hadoun, Z. Sadaoui, N. Souami, D. Sahel, I. Toumert, *Appl. Surf. Sci.* **2013**, *280*, 1–7.
- [69] H. Zhong, F. Xu, Z. Li, R. Fu, D. Wu, *Nanoscale* **2013**, *5*, 4678.
- [70] M. A. Lillo-Ródenas, J. Juan-Juan, D. Cazorla-Amorós, A. Linares-Solano, *Carbon N. Y.* **2004**, *42*, 1365–1369.

- [71] M. A. Lillo-Ródenas, D. Cazorla-Amorós, A. Linares-Solano, *Carbon N. Y.* **2003**, *41*, 267–275.
- [72] T. Otowa, R. Tanibata, M. Itoh, *Gas Sep. Purif.* **1993**, *7*.
- [73] B. J. Wood, K. M. Sancier, *Catal. Rev.* **1984**, *26*, 233–279.
- [74] J. Romanos, M. Beckner, T. Rash, L. Firlej, B. Kuchta, P. Yu, G. Suppes, C. Wexler, P. Pfeifer, *Nanotechnology* **2012**, *23*, 015401.
- [75] A. Attar, C. C. Baker, *Prep. - Am.Chem.Soc., Div. Energy Fuels* **1980**, *25*, 7–8.
- [76] A. L. Cabrera, H. Heinemann, G. A. Somorjai, *J. Catal.* **1982**, *75*, 7–22.
- [77] C. Liang, J. Bao, C. Li, H. Huang, C. Chen, Y. Lou, H. Lu, H. Lin, Z. Shi, S. Feng, *Microporous Mesoporous Mater.* **2017**, *251*, 77–82.
- [78] C. Zhang, R. Kong, X. Wang, Y. Xu, F. Wang, W. Ren, Y. Wang, F. Su, J.-X. Jiang, *Carbon N. Y.* **2017**, *114*, 608–618.
- [79] N. Díez, R. Mysyk, W. Zhang, E. Goikolea, D. Carriazo, *J. Mater. Chem. A* **2017**, *5*, 14619–14629.
- [80] T. Ouyang, K. Cheng, F. Yang, L. Zhou, K. Zhu, K. Ye, G. Wang, D. Cao, *J. Mater. Chem. A* **2017**, *5*, 14551–14561.
- [81] L. Hao, X. Li, L. Zhi, *Adv. Mater.* **2013**, *25*, 3899–904.
- [82] X. Li, C. Han, X. Chen, C. Shi, *Microporous Mesoporous Mater.* **2010**, *131*, 303–309.
- [83] W. Xing, S.-P. Zhuo, X. Gao, *Mater. Lett.* **2009**, *63*, 1311–1313.
- [84] N. Liu, J. Shen, D. Liu, *Microporous Mesoporous Mater.* **2013**, *167*, 176–181.
- [85] T. Cai, M. Zhou, G. Han, S. Guan, *J. Power Sources* **2013**, *241*, 6–11.
- [86] J. Choma, K. Jedynak, W. Fahrenholz, J. Ludwinowicz, M. Jaroniec, *Appl. Surf. Sci.* **2014**, *289*, 592–600.
- [87] L. K. C. de Souza, N. P. Wickramaratne, A. S. Ello, M. J. F. Costa, C. E. F. da Costa, M. Jaroniec, *Carbon N. Y.* **2013**, *65*, 334–340.
- [88] J. Górka, M. Jaroniec, *Carbon N. Y.* **2011**, *49*, 154–160.
- [89] X. Wang, C. Liang, S. Dai, *Langmuir* **2008**, *24*, 7500–7505.
- [90] X. Wang, J. S. Lee, C. Tsouris, D. W. DePaoli, S. Dai, *J. Mater. Chem.* **2010**, *20*, 4602–4608.
- [91] J. Górka, A. Zawislak, J. Choma, M. Jaroniec, *Carbon N. Y.* **2008**, *46*, 1159–1161.
- [92] J. Górka, A. Zawislak, J. Choma, M. Jaroniec, *Appl. Surf. Sci.* **2010**, *256*, 5187–5190.

- [93] Y. Liang, F. Liang, H. Zhong, Z. Li, R. Fu, D. Wu, *J. Mater. Chem. A* **2013**, *1*, 7000.
- [94] C. Breitkopf, K. Swider-Lyons, *Springer Handbook of Electrochemical Energy*, Springer Berlin Heidelberg, Berlin, Heidelberg, **2017**.
- [95] F. Béguin, E. Frackowiak, *Supercapacitors: Materials, Systems, and Applications*, WILEY-VCH, Weinheim, **2013**.
- [96] A. Burke, *J. Power Sources* **2000**, *91*, 37–50.
- [97] W. G. Pell, B. E. Conway, *J. Power Sources* **2001**, *96*, 57–67.
- [98] A. Burke, *Electrochim. Acta* **2007**, *53*, 1083–1091.
- [99] B. E. Conway, *J. Electrochem. Soc.* **1991**, *138*, 1539.
- [100] B. E. Conway, W. G. Pell, *J. Solid State Electrochem.* **2003**, *7*, 637–644.
- [101] V. Augustyn, P. Simon, B. Dunn, *Energy Environ. Sci.* **2014**, *7*, 1597–1614.
- [102] J. Liu, *Graphene-Based Composites for Electrochemical Energy Storage*, Springer Singapore, Singapore, **2017**.
- [103] E. Frackowiak, Q. Abbas, F. Béguin, *J. Energy Chem.* **2013**, *22*, 226–240.
- [104] H. Helmholtz, *Ann. der Phys. und Chemie* **1853**, *165*, 211–233.
- [105] H. Helmholtz, *Ann. der Phys. und Chemie* **1879**, *243*, 337–382.
- [106] M. Gouy, *J. Phys. Theor. Appl.* **1910**, *9*, 457–468.
- [107] D. L. Chapman, *London, Edinburgh, Dublin Philos. Mag. J. Sci.* **1913**, *25*, 475–481.
- [108] O. Stern, *Zeitschrift für Elektrochemie* **1924**, *30*, 508–516.
- [109] J. Liu, J. Wang, C. Xu, H. Jiang, C. Li, L. Zhang, J. Lin, Z. X. Shen, *Adv. Sci.* **2018**, *5*, 1700322.
- [110] A. V. Delgado, F. González-Caballero, R. J. Hunter, L. K. Koopal, J. Lyklema, *Pure Appl. Chem.* **2005**, *77*, 1753–1805.
- [111] H.-J. Butt, K. Graf, M. Kappl, *Physics and Chemistry of Interfaces*, Wiley-VCH Verlag GmbH & Co. KGaA, Weinheim, FRG, **2003**.
- [112] L. Zhang, X. Hu, Z. Wang, F. Sun, D. G. Dorrell, *Renew. Sustain. Energy Rev.* **2018**, *81*, 1868–1878.
- [113] A. González, E. Goikolea, J. A. Barrena, R. Mysyk, *Renew. Sustain. Energy Rev.* **2016**, *58*, 1189–1206.
- [114] Y. Wang, Y. Song, Y. Xia, *Chem. Soc. Rev.* **2016**, *45*, 5925–5950.
- [115] F. Béguin, V. Presser, A. Balducci, E. Frackowiak, *Adv. Mater.* **2014**, *26*, 2219–2251.
- [116] W. Gu, G. Yushin, *Wiley Interdiscip. Rev. Energy Environ.* **2014**, *3*, 424–

- [117] A. Lewandowski, A. Olejniczak, M. Galinski, I. Stepniak, *J. Power Sources* **2010**, *195*, 5814–5819.
- [118] K. Fic, M. He, E. J. Berg, P. Novák, E. Frackowiak, *Carbon N. Y.* **2017**, *120*, 281–293.
- [119] K. Fic, A. Platek, J. Piwek, E. Frackowiak, *Mater. Today* **2018**, *21*, 437–454.
- [120] P. Ratajczak, M. E. Suss, F. Kaasik, F. Béguin, *Energy Storage Mater.* **2019**, *16*, 126–145.
- [121] K. Fic, M. Meller, J. Menzel, E. Frackowiak, *Electrochim. Acta* **2016**, *206*, 496–503.
- [122] X. Zhang, X. Cheng, Q. Zhang, *J. Energy Chem.* **2016**, *25*, 967–984.
- [123] A. Hossain, P. Bandyopadhyay, P. S. Guin, S. Roy, *Appl. Mater. Today* **2017**, *9*, 300–313.
- [124] Z. Yu, L. Tetard, L. Zhai, J. Thomas, *Energy Environ. Sci.* **2015**, *8*, 702–730.
- [125] L. Guan, L. Yu, G. Z. Chen, *Electrochim. Acta* **2016**, *206*, 464–478.
- [126] T. Kou, B. Yao, T. Liu, Y. Li, *J. Mater. Chem. A* **2017**, *5*, 17151–17173.
- [127] K. Jurewicz, C. Vix-Guterl, E. Frackowiak, S. Saadallah, M. Reda, J. Parmentier, J. Patarin, F. Béguin, *J. Phys. Chem. Solids* **2004**, *65*, 287–293.
- [128] M. Sevilla, R. Mokaya, *Energy Environ. Sci.* **2014**, *7*, 1250–1280.
- [129] J. Wang, H. L. Xin, D. Wang, *Part. Part. Syst. Character.* **2014**, *31*, 515–539.
- [130] T. Liu, F. Zhang, Y. Song, Y. Li, *J. Mater. Chem. A* **2017**, *5*, 17705–17733.
- [131] A. Eftekhari, *J. Mater. Chem. A* **2018**, *6*, 2866–2876.
- [132] H. Teng, Y.-J. Chang, C.-T. Hsieh, *Carbon N. Y.* **2001**, *39*, 1981–1987.
- [133] X. Zhang, J. Wang, Z. Yu, R. Wang, H. Xie, *Mater. Lett.* **2009**, *63*, 2523–2525.
- [134] H. Chen, F. Wang, S. Tong, S. Guo, X. Pan, *Appl. Surf. Sci.* **2012**, *258*, 6097–6102.
- [135] Z. Wang, M. Zhou, H. Chen, J. Jiang, S. Guan, *Chem. - An Asian J.* **2014**, *9*, 2789–2797.
- [136] Y. Wang, B. Chang, D. Guan, X. Dong, *J. Solid State Electrochem.* **2015**, *19*, 1783–1791.
- [137] F. Sun, J. Gao, X. Liu, X. Pi, Y. Yang, S. Wu, *Appl. Surf. Sci.* **2016**, *387*, 857–863.
- [138] C. Lei, N. Amini, F. Markoulidis, P. Wilson, S. Tennison, C. Lekakou, *J. Mater. Chem. A* **2013**, *1*, 6037.

- [139] J. Du, L. Liu, Y. Yu, Y. Zhang, H. Lv, A. Chen, *J. Power Sources* **2019**, *434*, 226720.
- [140] V. Presser, M. Heon, Y. Gogotsi, *Adv. Funct. Mater.* **2011**, *21*, 810–833.
- [141] M. Sevilla, R. Mokaya, *J. Mater. Chem.* **2011**, *21*, 4727–4732.
- [142] D. a Ersoy, M. J. McNallan, Y. Gogotsi, *Mater. Res. Innov.* **2001**, *5*, 55–62.
- [143] Y. G. Gogotsi, I.-D. Jeon, M. J. McNallan, *J. Mater. Chem.* **1997**, *7*, 1841–1848.
- [144] Y. Gogotsi, A. Nikitin, H. Ye, W. Zhou, J. E. Fischer, B. Yi, H. C. Foley, M. W. Barsoum, *Nat. Mater.* **2003**, *2*, 591–594.
- [145] R. Dash, J. Chmiola, G. Yushin, Y. Gogotsi, G. Laudisio, J. Singer, J. Fischer, S. Kucheyev, *Carbon N. Y.* **2006**, *44*, 2489–2497.
- [146] A. E. Kravchik, J. A. Kukushkina, V. V. Sokolov, G. F. Tereshchenko, *Carbon N. Y.* **2006**, *44*, 3263–3268.
- [147] Y. Gogotsi, *Nanomaterials Handbook*, Taylor & Francis Group, LLC, Boca Raton, **2006**.
- [148] D. Salinas-Torres, R. Ruiz-Rosas, E. Morallón, D. Cazorla-Amorós, *Front. Mater.* **2019**, *6*, 1–24.
- [149] S. Najib, E. Erdem, *Nanoscale Adv.* **2019**, *1*, 2817–2827.
- [150] L. Permann, M. Lätt, J. Leis, M. Arulepp, *Electrochim. Acta* **2006**, *51*, 1274–1281.
- [151] J. Chmiola, G. Yushin, R. Dash, Y. Gogotsi, *J. Power Sources* **2006**, *158*, 765–772.
- [152] J. Chmiola, G. Yushin, Y. Gogotsi, C. Portet, P. Simon, P. L. Taberna, *Science* **2006**, *313*, 1760–1763.
- [153] J. Chmiola, C. Largeot, P.-L. Taberna, P. Simon, Y. Gogotsi, *Angew. Chemie Int. Ed.* **2008**, *47*, 3392–3395.
- [154] P. Simon, A. Burke, *Electrochem. Soc. Interface* **2008**, *17*, 38–43.
- [155] S. Talapatra, S. Kar, S. K. Pal, R. Vajtai, L. Ci, P. Victor, M. M. Shaijumon, S. Kaur, O. Nalamasu, P. M. Ajayan, *Nat. Nanotechnol.* **2006**, *1*, 112–116.
- [156] E. Frackowiak, S. Delpeux, K. Jurewicz, K. Szostak, D. Cazorla-Amoros, F. Beguin, *Chem. Phys. Lett.* **2002**, *361*, 35–41.
- [157] W. Gu, G. Yushin, *Wiley Interdiscip. Rev. Energy Environ.* **2013**, *3*, DOI 10.1002/wene.102.
- [158] C. Liu, F. Li, L.-P. Ma, H.-M. Cheng, *Adv. Mater.* **2010**, *22*, E28–E62.
- [159] A. K. Geim, K. S. Novoselov, *Nat. Mater.* **2007**, *6*, 183–191.
- [160] S. K. Tiwari, V. Kumar, A. Huczko, R. Oraon, A. De Adhikari, G. C. Nayak,

- [161] S. R. C. Vivekchand, C. S. Rout, K. S. Subrahmanyam, A. Govindaraj, C. N. R. Rao, *J. Chem. Sci.* **2008**, *120*, 9–13.
- [162] M. D. Stoller, S. Park, Y. Zhu, J. An, R. S. Ruoff, *Nano Lett.* **2008**, *8*, 3498–3502.
- [163] Y. Sun, Q. Wu, G. Shi, *Energy Environ. Sci.* **2011**, *4*, 1113–1132.
- [164] Y. Shao, M. F. El-Kady, L. J. Wang, Q. Zhang, Y. Li, H. Wang, M. F. Mousavi, R. B. Kaner, *Chem. Soc. Rev.* **2015**, *44*, 3639–3665.
- [165] W. K. Chee, H. N. Lim, Z. Zainal, N. M. Huang, I. Harrison, Y. Andou, *J. Phys. Chem. C* **2016**, *120*, 4153–4172.
- [166] S. Wang, Z. S. Wu, S. Zheng, F. Zhou, C. Sun, H. M. Cheng, X. Bao, *ACS Nano* **2017**, *11*, 4283–4291.
- [167] D. Li, M. B. Müller, S. Gilje, R. B. Kaner, G. G. Wallace, *Nat. Nanotechnol.* **2008**, *3*, 101–105.
- [168] X. Guo, S. Zheng, G. Zhang, X. Xiao, X. Li, Y. Xu, H. Xue, H. Pang, *Energy Storage Mater.* **2017**, *9*, 150–169.
- [169] Y. Xu, Z. Lin, X. Zhong, X. Huang, N. O. Weiss, Y. Huang, X. Duan, *Nat. Commun.* **2014**, *5*, 4554.
- [170] Y. Zhu, S. Murali, M. D. Stoller, K. J. Ganesh, W. Cai, P. J. Ferreira, A. Pirkle, R. M. Wallace, K. A. Cychosz, M. Thommes, et al., *Science (80-.)*. **2011**, *332*, 1537–1541.
- [171] Y. Deng, Y. Xie, K. Zou, X. Ji, *J. Mater. Chem. A* **2016**, *4*, 1144–1173.
- [172] A. Borenstein, O. Hanna, R. Attias, S. Luski, T. Brousse, D. Aurbach, *J. Mater. Chem. A* **2017**, *5*, 12653–12672.
- [173] C. Feng, H. Li, Y. Wan, *J. Nanosci. Nanotechnol.* **2009**, *9*, 1558–1563.
- [174] F. Jiang, Z. Ge, B. Niu, M. Yuan, S. Wei, M. Li, *J. Appl. Polym. Sci.* **2019**, *136*, 47816.
- [175] Z. Wu, P. A. Webley, D. Zhao, *J. Mater. Chem.* **2012**, *22*, 11379.
- [176] A. E. Allah, Y. Yamauchi, J. Wang, Y. Bando, H. Tan, A. A. Farghali, M. H. Khedr, A. Alshehri, Y. G. Alghamdi, D. Martin, et al., *ChemElectroChem* **2019**, celc.201900151.
- [177] E. Frackowiak, G. Lota, J. Machnikowski, C. Vix-Guterl, F. Béguin, *Electrochim. Acta* **2006**, *51*, 2209–2214.
- [178] Y.-H. Lee, K.-H. Chang, C.-C. Hu, *J. Power Sources* **2013**, *227*, 300–308.
- [179] L. Wei, M. Sevilla, A. B. Fuertes, R. Mokaya, G. Yushin, *Adv. Funct. Mater.* **2012**, *22*, 827–834.
- [180] E. Raymundo-Piñero, F. Leroux, F. Béguin, *Adv. Mater.* **2006**, *18*, 1877–

- 1882.
- [181] E. Raymundo-Piñero, M. Cadek, F. Béguin, *Adv. Funct. Mater.* **2009**, *19*, 1032–1039.
- [182] K. Jurewicz, K. Babel, A. Ziolkowski, H. Wachowska, *Electrochim. Acta* **2003**, *48*, 1491–1498.
- [183] F. Stoeckli, T. A. Centeno, *Phys Chem Chem Phys* **2012**, *14*, 11589–11591.
- [184] F. Stoeckli, T. A. Centeno, *J. Mater. Chem. A* **2013**, *1*, 6865.
- [185] B. Lobato, L. Suárez, L. Guardia, T. A. Centeno, *Carbon N. Y.* **2017**, *122*, 434–445.
- [186] G. Y. Gor, M. Thommes, K. a. Cychosz, A. V. Neimark, *Carbon N. Y.* **2012**, *50*, 1583–1590.
- [187] M. Thommes, K. A. Cychosz, A. V. Neimark, in *Nov. Carbon Adsorbents*, Elsevier, **2012**, pp. 107–145.
- [188] N. Jäckel, P. Simon, Y. Gogotsi, V. Presser, *ACS Energy Lett.* **2016**, *1*, 1262–1265.
- [189] N. Jäckel, M. Rodner, A. Schreiber, J. Jeongwook, M. Zeiger, M. Aslan, D. Weingarth, V. Presser, *J. Power Sources* **2016**, *326*, 660–671.
- [190] T. A. Centeno, O. Sereda, F. Stoeckli, *Phys. Chem. Chem. Phys.* **2011**, *13*, 12403.
- [191] A. García-Gómez, G. Moreno-Fernández, B. Lobato, T. A. Centeno, *Phys. Chem. Chem. Phys.* **2015**, *17*, 15687–15690.
- [192] V. Presser, J. McDonough, S.-H. Yeon, Y. Gogotsi, *Energy Environ. Sci.* **2011**, *4*, 3059.
- [193] W.-Y. Tsai, P.-L. Taberna, P. Simon, *J. Am. Chem. Soc.* **2014**, *136*, 8722–8728.
- [194] J. Huang, B. G. Sumpter, V. Meunier, *Chem. - A Eur. J.* **2008**, *14*, 6614–6626.
- [195] J. Huang, B. G. Sumpter, V. Meunier, *Angew. Chemie Int. Ed.* **2008**, *47*, 520–524.
- [196] H. Wang, L. Pilon, *J. Power Sources* **2013**, *221*, 252–260.
- [197] K. Urita, C. Urita, K. Fujita, K. Horio, M. Yoshida, I. Moriguchi, *Nanoscale* **2017**, *9*, 15643–15649.
- [198] G. Feng, R. Qiao, J. Huang, B. G. Sumpter, V. Meunier, *ACS Nano* **2010**, *4*, 2382–2390.
- [199] W. Hsieh, T.-L. A. Horng, H.-C. Huang, H. Teng, *J. Mater. Chem. A* **2015**, *3*, 16535–16543.
- [200] J. E. Zuliani, C. Q. Jia, D. W. Kirk, *J. Phys. Chem. C* **2017**, *121*, 20555–

- [201] X. Yu, Z. Tang, D. Sun, L. Ouyang, M. Zhu, *Prog. Mater. Sci.* **2017**, 88, 1–48.
- [202] Y. Xia, Z. Yang, Y. Zhu, *J. Mater. Chem. A* **2013**, 1, 9365.
- [203] M. Hirscher, B. Panella, *J. Alloys Compd.* **2005**, 404–406, 399–401.
- [204] J. O. Abe, A. P. I. Popoola, E. Ajenifuja, O. M. Popoola, *Int. J. Hydrogen Energy* **2019**, 44, 15072–15086.
- [205] J. Liu, R. Zou, Y. Zhao, *Tetrahedron Lett.* **2016**, 57, 4873–4881.
- [206] Y. Gogotsi, R. K. Dash, G. Yushin, T. Yildirim, G. Laudisio, J. E. Fischer, *J. Am. Chem. Soc.* **2005**, 127, 16006–16007.
- [207] K. M. Thomas, *Catal. Today* **2007**, 120, 389–398.
- [208] B. Panella, M. Hirscher, S. Roth, *Carbon N. Y.* **2005**, 43, 2209–2214.
- [209] G. Yushin, R. Dash, J. Jagiello, J. E. Fischer, Y. Gogotsi, *Adv. Funct. Mater.* **2006**, 16, 2288–2293.
- [210] Y. Gogotsi, C. Portet, S. Osswald, J. M. Simmons, T. Yildirim, G. Laudisio, J. E. Fischer, *Int. J. Hydrogen Energy* **2009**, 34, 6314–6319.
- [211] M. Felderhoff, C. Weidenthaler, R. Von Helmolt, U. Eberle, *Phys. Chem. Chem. Phys.* **2007**, 9, 2643–2653.
- [212] J. Germain, J. M. J. Fréchet, F. Svec, *Small* **2009**, 5, 1098–1111.
- [213] G. Sethia, A. Sayari, *Carbon N. Y.* **2016**, 99, 289–294.
- [214] Y. Xia, R. Mokaya, D. M. Grant, G. S. Walker, *Carbon N. Y.* **2011**, 49, 844–853.
- [215] E. Masika, R. A. Bourne, T. W. Chamberlain, R. Mokaya, *ACS Appl. Mater. Interfaces* **2013**, 5, 5639–5647.
- [216] F. Shayeganfar, R. Shahsavari, *Langmuir* **2016**, 32, 13313–13321.
- [217] T. S. Blankenship II, N. Balahmar, R. Mokaya, *Nat. Commun.* **2017**, 8, 1545.
- [218] C. Hou, Q. Xu, *Adv. Energy Mater.* **2019**, 9, 1801307.
- [219] E. Rivard, M. Trudeau, K. Zaghbi, *Materials (Basel)*. **2019**, 12, 1973.
- [220] H. Furukawa, K. E. Cordova, M. O’Keeffe, O. M. Yaghi, *Science (80-.)*. **2013**, 341, 1230444–1230444.
- [221] K. Koh, A. G. Wong-Foy, A. J. Matzger, *J. Am. Chem. Soc.* **2009**, 131, 4184–4185.
- [222] N. Klein, I. Senkovska, K. Gedrich, U. Stoeck, A. Henschel, U. Mueller, S. Kaskel, *Angew. Chemie Int. Ed.* **2009**, 48, 9954–9957.
- [223] Y. Yan, X. Lin, S. Yang, A. J. Blake, A. Dailly, N. R. Champness, P.

- Hubberstey, M. Schröder, *Chem. Commun.* **2009**, 1025.
- [224] L. Xia, Z. Bo, Q. Liu, X. Zhang, Y. Pei, *Comput. Mater. Sci.* **2019**, *166*, 179–186.
- [225] D. A. Gómez-Gualdrón, T. C. Wang, P. García-Holley, R. M. Sawelewa, E. Argueta, R. Q. Snurr, J. T. Hupp, T. Yildirim, O. K. Farha, *ACS Appl. Mater. Interfaces* **2017**, *9*, 33419–33428.
- [226] E. M. Kumar, S. Sinthika, R. Thapa, *J. Mater. Chem. A* **2015**, *3*, 304–313.
- [227] R. Ma, Y. Bando, H. Zhu, T. Sato, C. Xu, D. Wu, *J. Am. Chem. Soc.* **2002**, *124*, 7672–7673.
- [228] C. Tang, Y. Bando, X. Ding, S. Qi, D. Golberg, *J. Am. Chem. Soc.* **2002**, *124*, 14550–14551.
- [229] W. Lei, H. Zhang, Y. Wu, B. Zhang, D. Liu, S. Qin, Z. Liu, L. Liu, Y. Ma, Y. Chen, *Nano Energy* **2014**, *6*, 219–224.
- [230] H. Furukawa, O. M. Yaghi, *J. Am. Chem. Soc.* **2009**, *131*, 8875–8883.
- [231] S. Zheng, F. Fang, G. Zhou, G. Chen, L. Ouyang, M. Zhu, D. Sun, *Chem. Mater.* **2008**, *20*, 3954–3958.
- [232] M. Thommes, *Chem.-Ing.-Tech.* **2010**, *82*, 1059–1073.
- [233] K. S. W. Sing, *Pure Appl. Chem.* **1985**, *57*, 603–619.
- [234] K. S. W. Sing, *J. Porous Mat.* **1995**, *2*, 5–8.
- [235] P. A. Monson, *Langmuir* **2008**, *24*, 12295–12302.
- [236] M. Thommes, B. Smarsly, M. Groenewolt, P. I. Ravikovitch, A. V. Neimark, *Langmuir* **2006**, *22*, 756–764.
- [237] P. I. Ravikovitch, A. V. Neimark, *Langmuir* **2002**, *18*, 9830–9837.
- [238] S. Brunauer, P. Emmett, E. Teller, *J. Am. Chem. Soc.* **1938**, *407*, 309–319.
- [239] E. P. Barrett, L. G. Joyner, P. P. Halenda, *J. Am. Chem. Soc.* **1951**, *73*, 373–380.
- [240] D. Dollimore, G. R. Heal, *J. Appl. Chem.* **1964**, *14*, 109–114.
- [241] W. S. Ahn, M. S. Jhon, H. Pak, S. Chang, *J. Colloid Interf. Sci.* **1972**, *38*, 1–4.
- [242] P. I. Ravikovitch, S. C. O. Domhnaill, A. V. Neimark, F. Schueth, K. K. Unger, *Langmuir* **1995**, *11*, 4765–4772.
- [243] P. I. Ravikovitch, D. Wei, W. T. Chueh, G. L. Haller, A. V. Neimark, *J. Phys. Chem. B* **1997**, *101*, 3671–3679.
- [244] M. M. Dubinin, *Chem. Rev.* **1960**, *60*, 235–241.
- [245] M. M. Dubinin, in *Prog. Surf. Membr. Sci.*, ACADEMIC PRESS, INC.,

1975, pp. 1–70.

- [246] M. Polanyi, *Trans. Faraday Soc.* **1932**, 28, 316–333.
- [247] M. M. Dubinin, *Pure Appl. Chem.* **1989**, 61, 1841–1843.
- [248] M. M. Dubinin, F. Stoeckli, *J. Colloid Interface Sci.* **1980**, 75, 34–42.
- [249] G. Horvath, K. Kawazoe, *J. Chem. Eng. Japan* **1983**, 16, 470–475.
- [250] D. H. Everett, J. C. Powl, *J. Chem. Soc. Faraday Trans. 1 Phys. Chem. Condens. Phases* **1976**, 72, 619.
- [251] S. U. Rege, R. T. Yang, *AIChE J.* **2000**, 46, 734–750.
- [252] N. a. Seaton, J. P. R. B. Walton, N. Quirke, *Carbon N. Y.* **1989**, 27, 853–861.
- [253] C. Lastoskie, K. E. Gubbins, N. Quirke, *J. Phys. Chem.* **1993**, 97, 4786–4796.
- [254] P. I. Ravikovitch, A. V. Neimark, *Langmuir* **2002**, 18, 1550–1560.
- [255] P. I. Ravikovitch, A. V. Neimark, *Langmuir* **2006**, 22, 11171–11179.
- [256] J. Landers, G. Y. Gor, A. V. Neimark, *Colloids Surfaces A Physicochem. Eng. Asp.* **2013**, 437, 3–32.
- [257] A. V. Neimark, Y. Lin, P. I. Ravikovitch, M. Thommes, *Carbon N. Y.* **2009**, 47, 1617–1628.
- [258] P. I. Ravikovitch, A. Vishnyakov, R. Russo, A. V. Neimark, *Langmuir* **2000**, 16, 2311–2320.
- [259] S. K. Bhatia, *Langmuir* **2017**, 33, 831–847.
- [260] S.-S. Tzeng, Y.-G. Chr, *Mater. Chem. Phys.* **2002**, 73, 162–169.
- [261] F. Tuinstra, J. L. Koenig, *J. Chem. Phys.* **1970**, 53, 1126–1130.
- [262] A. C. Ferrari, J. Robertson, *Phys. Rev. B* **2000**, 61, 14095–14107.
- [263] S. Reich, C. Thomsen, *Philos. Trans. A. Math. Phys. Eng. Sci.* **2004**, 362, 2271–88.
- [264] C.-L. Liu, W.-S. Dong, J.-R. Song, L. Liu, *Mater. Sci. Eng. A* **2007**, 459, 347–354.
- [265] A. J. Bard, L. R. Faulkner, *Electrochemical Methods: Fundamentals and Applications*, John Wiley & Sons, Inc., New York, **2001**.
- [266] Y. Yamada, T. Tanaka, K. Machida, S. Suematsu, K. Tamamitsu, H. Kataura, H. Hatori, *Carbon N. Y.* **2012**, 50, 1422–1424.
- [267] G. Z. Chen, *Int. Mater. Rev.* **2017**, 62, 173–202.
- [268] M. M. Hantel, T. Kaspar, R. Nesper, A. Wokaun, R. Kotz, *ECS Electrochem. Lett.* **2012**, 1, A1–A3.

- [269] D. M. Anjos, J. K. McDonough, E. Perre, G. M. Brown, S. H. Overbury, Y. Gogotsi, V. Presser, *Nano Energy* **2013**, 2, 702–712.
- [270] D. Weingarth, M. Zeiger, N. Jäckel, M. Aslan, G. Feng, V. Presser, *Adv. Energy Mater.* **2014**, 4, 1400316.
- [271] M. D. Stoller, R. S. Ruoff, *Energy Environ. Sci.* **2010**, 3, 1294.
- [272] P. L. Taberna, P. Simon, J. F. Fauvarque, *J. Electrochem. Soc.* **2003**, 150, A292–A300.
- [273] R. Heimböckel, S. Kraas, F. Hoffmann, M. Fröba, *Appl. Surf. Sci.* **2018**, 427, 1055–1064.
- [274] L. Zhang, H. Liu, M. Wang, L. Chen, *Carbon N. Y.* **2007**, 45, 1439–1445.
- [275] A. M. ElKhatat, S. A. Al-Muhtaseb, *Adv. Mater.* **2011**, 23, 2887–2903.
- [276] Y. Liu, Z. Shi, Y. Gao, W. An, Z. Cao, J. Liu, *ACS Appl. Mater. Interfaces* **2016**, 8, 28283–28290.
- [277] A. Onodera, K. Terashima, T. Urushihara, K. Suito, H. Sumiya, S. Satoh, *J. Mater. Sci.* **1997**, 32, 4309–4318.
- [278] A. C. Juhl, Poröse Kohlenstoffe Für Lithium-Schwefel-Batterien: Darstellung Besonderer Morphologien Und Verwendung Als Wirtsstruktur Für Schwefel, University of Hamburg, **2017**.
- [279] S. Waluś, A. Robba, R. Bouchet, C. Barchasz, F. Alloin, *Electrochim. Acta* **2016**, 210, 492–501.
- [280] G. A. Ferrero, M. Sevilla, A. B. Fuertes, *Carbon N. Y.* **2015**, 88, 239–251.
- [281] H. Zhang, K. Wang, X. Zhang, H. Lin, X. Sun, C. Li, Y. Ma, *J. Mater. Chem. A* **2015**, 3, 11277–11286.
- [282] M. Härmas, T. Thomberg, H. Kurig, T. Romann, A. Jänes, E. Lust, *J. Power Sources* **2016**, 326, 624–634.
- [283] A. Eftekhari, *Mater. Today Chem.* **2018**, 7, 1–4.
- [284] M. Karthik, E. Redondo, E. Goikolea, V. Roddatis, S. Doppiu, R. Mysyk, *J. Phys. Chem. C* **2014**, 118, 27715–27720.
- [285] Q. Wang, J. Yan, Z. Fan, *Energy Environ. Sci.* **2016**, 9, 729–762.
- [286] T. Chou, C. Huang, R. Doong, C. Hu, *J. Mater. Chem. A* **2013**, 1, 2886.
- [287] J. Liu, X. Wang, J. Gao, Y. Zhang, Q. Lu, M. Liu, *Electrochim. Acta* **2016**, 211, 183–192.
- [288] N. Balahmar, R. Mokaya, *J. Mater. Chem. A* **2019**, 7, 17466–17479.
- [289] J.-S. M. Lee, M. E. Briggs, T. Hasell, A. I. Cooper, *Adv. Mater.* **2016**, 28, 9804–9810.
- [290] H. Frost, T. Düren, R. Q. Snurr, *J. Phys. Chem. B* **2006**, 110, 9565–9570.

- [291] O. Barbieri, M. Hahn, A. Herzog, R. Kötz, *Carbon N. Y.* **2005**, *43*, 1303–1310.
- [292] B. Dyatkin, O. Gogotsi, B. Malinovskiy, Y. Zozulya, P. Simon, Y. Gogotsi, *J. Power Sources* **2016**, *306*, 32–41.
- [293] R. Yan, T. Heil, V. Presser, R. Walczak, M. Antonietti, M. Oschatz, *Adv. Sustain. Syst.* **2018**, *2*, 1700128.
- [294] C. Portet, P. L. Taberna, P. Simon, E. Flahaut, C. Laberty-Robert, *Electrochim. Acta* **2005**, *50*, 4174–4181.
- [295] P. Ratajczak, K. Jurewicz, P. Skowron, Q. Abbas, F. Béguin, *Electrochim. Acta* **2014**, *130*, 344–350.
- [296] J. M. Griffin, A. C. Forse, W.-Y. Tsai, P.-L. Taberna, P. Simon, C. P. Grey, *Nat. Mater.* **2015**, *14*, 812–819.
- [297] D. H. Hromads'kyi, Y. F. Fateev, N. H. Stryzhakova, Y. a. Maletin, *Mater. Sci.* **2010**, *46*, 412–417.
- [298] P. W. Ruch, D. Cericola, A. Foelske-Schmitz, R. Kötz, A. Wokaun, *Electrochim. Acta* **2010**, *55*, 4412–4420.
- [299] P. Kurzweil, O. K. Dietlmeier, *Elektrochemische Speicher*, Springer Fachmedien Wiesbaden, Wiesbaden, **2018**.
- [300] M. Li, X. Chang, X. Han, W. Yin, M. Ren, *Synth. Met.* **2016**, *219*, 67–75.
- [301] H. Tamon, H. Ishizaka, M. Mikami, M. Okazaki, *Carbon N. Y.* **1997**, *35*, 791–796.
- [302] R. Heimböckel, F. Hoffmann, M. Fröba, *Phys. Chem. Chem. Phys.* **2019**, *21*, 3122–3133.
- [303] L. S. Lasdon, R. L. Fox, M. W. Ratner, *Rev. Fr. d'Automatique, Inform. Rech. Opérationnelle* **1974**, *3*, 73–104.
- [304] D. Jiang, Z. Jin, J. Wu, *Nano Lett.* **2011**, *11*, 5373–5377.
- [305] G. Feng, P. T. Cummings, *J. Phys. Chem. Lett.* **2011**, *2*, 2859–2864.
- [306] C. Liu, X. Yan, F. Hu, G. Gao, G. Wu, X. Yang, *Adv. Mater.* **2018**, *30*, 1705713.
- [307] Y. Zhang, S. Yu, G. Lou, Y. Shen, H. Chen, Z. Shen, S. Zhao, J. Zhang, S. Chai, Q. Zou, *J. Mater. Sci.* **2017**, *52*, 11201–11228.
- [308] C.-P. Elverfeldt, Y. J. Lee, M. Fröba, *ACS Appl. Mater. Interfaces* **2019**, *11*, 24423–24434.
- [309] T. Y. Wei, K. L. Lim, Y. S. Tseng, S. L. I. Chan, *Renew. Sustain. Energy Rev.* **2017**, *79*, 1122–1133.
- [310] S. H. Jung, H.-K. Kim, J. W. Yoon, J.-S. Chang, *J. Phys. Chem. B* **2006**, *110*, 9371–9374.

- [311] M. Dincă, J. R. Long, *J. Am. Chem. Soc.* **2005**, *127*, 9376–9377.
- [312] M. Fischer, B. Kuchta, L. Firlej, F. Hoffmann, M. Fröba, *J. Phys. Chem. C* **2010**, *114*, 19116–19126.
- [313] Y. Liu, J. Lu, J. Yang, Y. Zhang, J. Wang, C. Li, L. Xia, *Mater. Lett.* **2018**, *214*, 91–94.
- [314] H.-M. Lee, Y.-J. Heo, K.-H. An, S.-C. Jung, D. C. Chung, S.-J. Park, B.-J. Kim, *Int. J. Hydrogen Energy* **2018**, *43*, 5894–5902.

9 Appendix

9.1 Further information to the chapter “results and discussion”

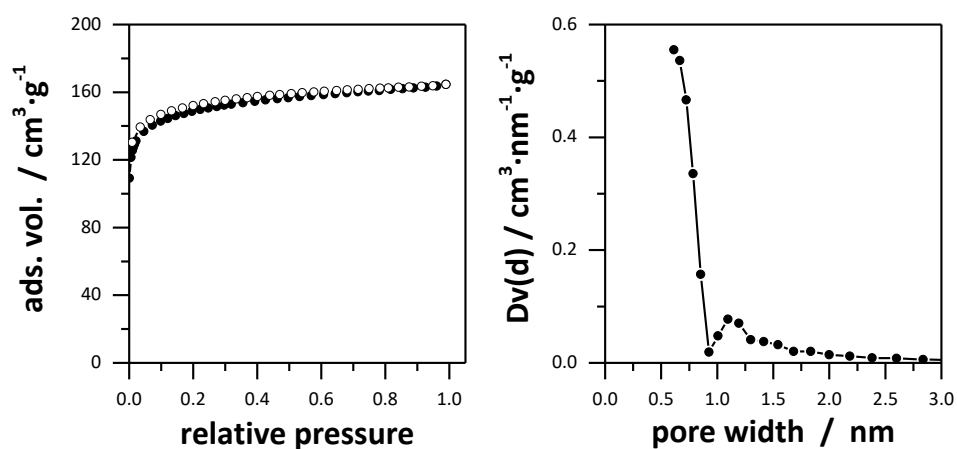


Figure A.1: Nitrogen adsorption-desorption isotherm (77 K) of the sample C-500-0-T9 (left) and the pore size distribution calculated by the QSDFT method (right).

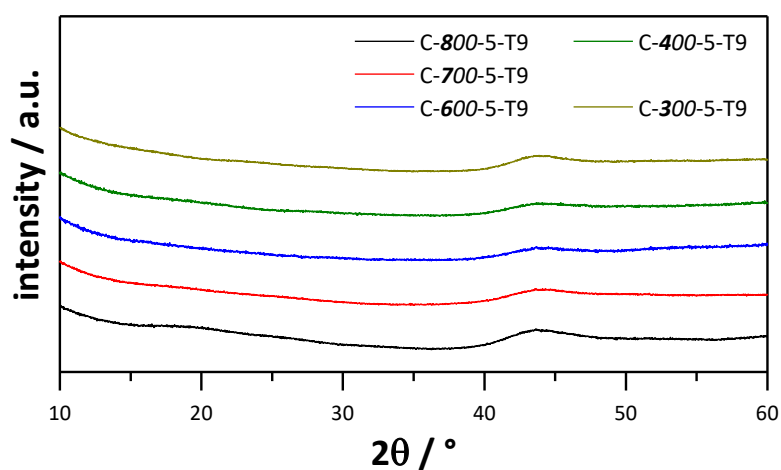


Figure A.2: P-XRD pattern of the activated carbons with different semi-carbonization temperatures.

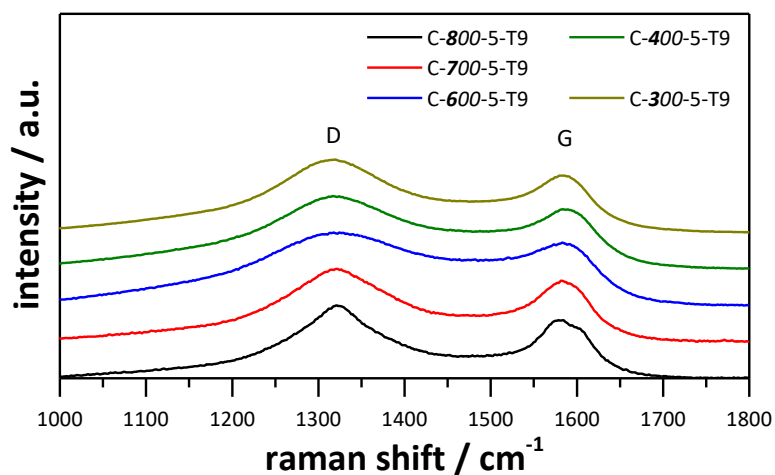


Figure A.3: Raman spectra of the activated carbons with different semi-carbonization temperatures.

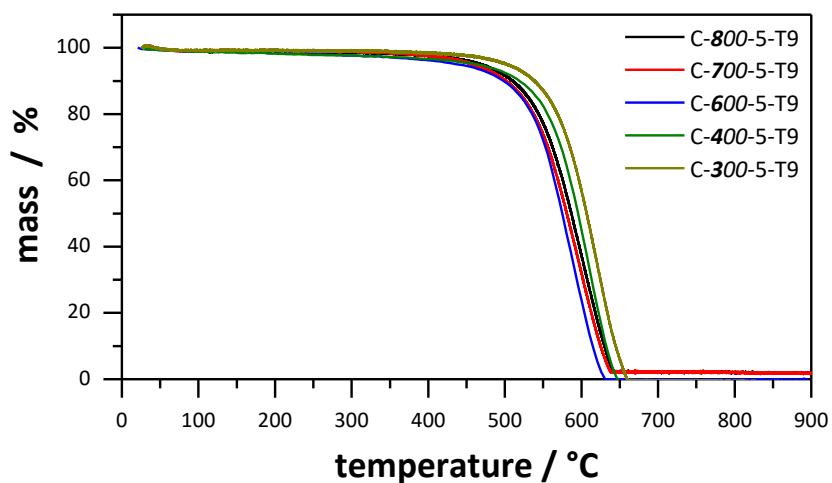


Figure A.4: Results of the thermogravimetry of the activated carbons with different semi-carbonization temperatures. The samples were heated to 900 $^{\circ}\text{C}$ in air steam with a flow rate of $50 \text{ mL} \cdot \text{min}^{-1}$.

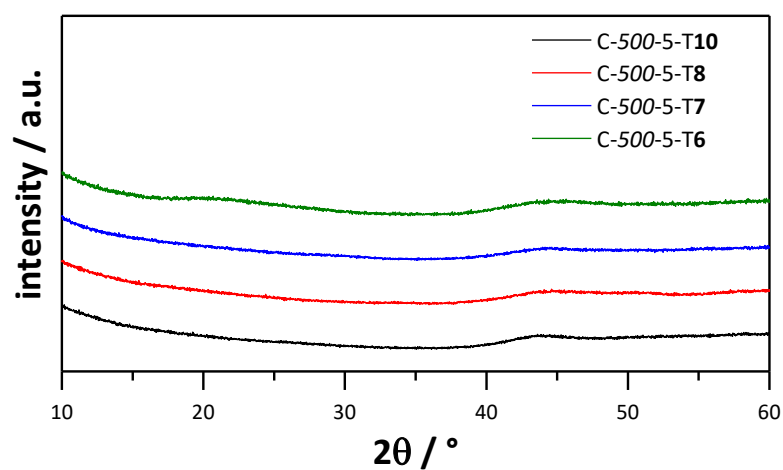


Figure A.5: P-XRD pattern of the activated carbons with different activation temperatures.

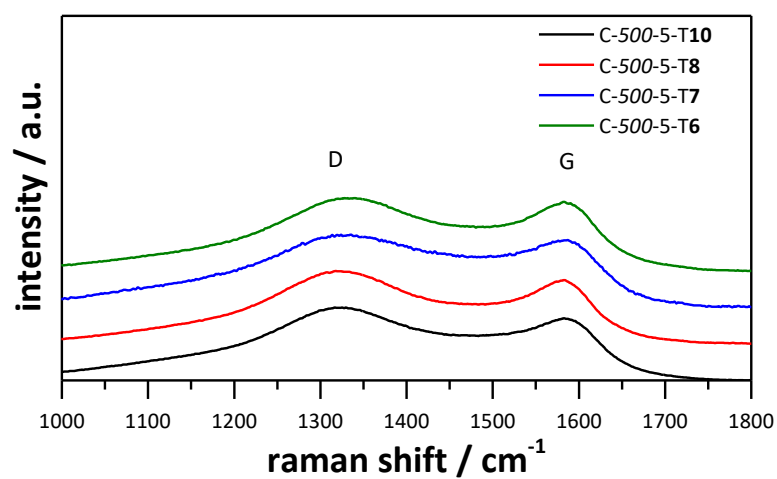


Figure A.6: Raman spectra of the activated carbons with different activation temperatures.

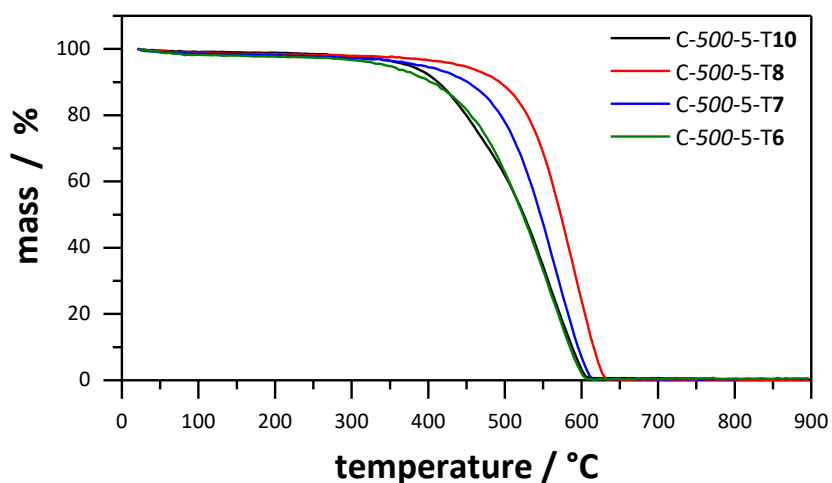


Figure A.7: Results of the thermogravimetry of the activated carbons with different activation temperatures. The samples were heated to 900 °C in air steam with a flow rate of 50 mL·min⁻¹.

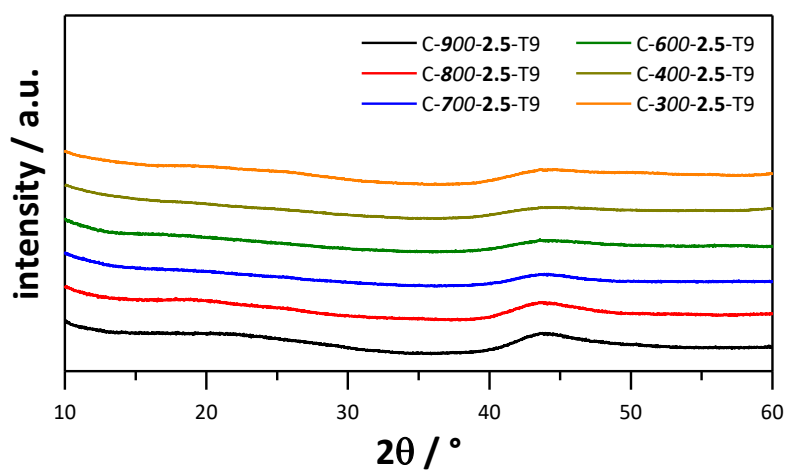


Figure A.8: P-XRD pattern of the activated carbons with different semi-carbonization temperatures and a KOH/carbon ratio of 2.5.

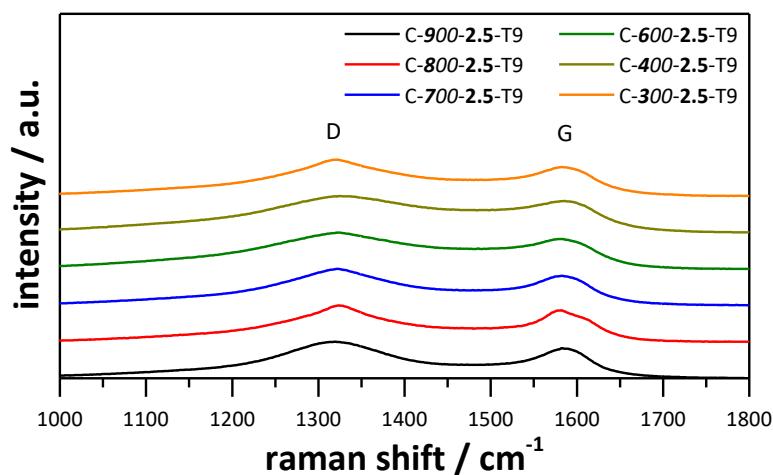


Figure A.9: Raman spectra of the activated carbons with different semi-carbonization temperatures and a KOH/carbon ratio of 2.5.

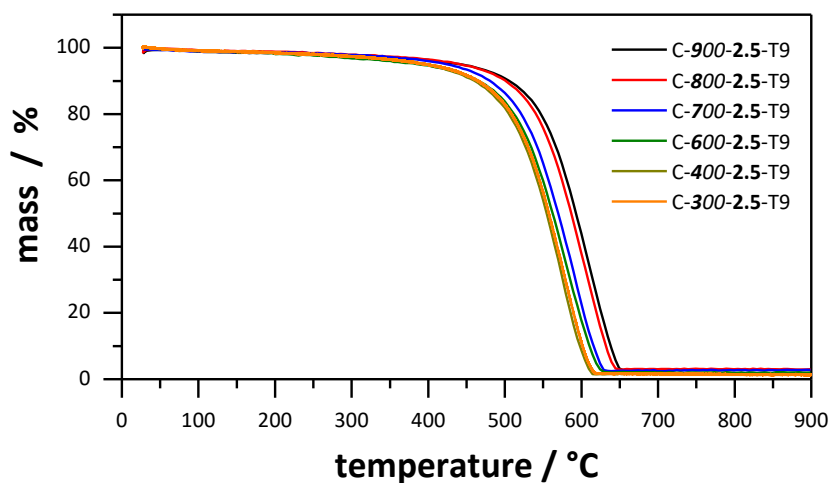


Figure A.10: Results of the thermogravimetry of the activated carbons with different semi-carbonization temperatures and a KOH/carbon ratio of 2.5. The samples were heated to 900 °C in air steam with a flow rate of 50 mL·min⁻¹.

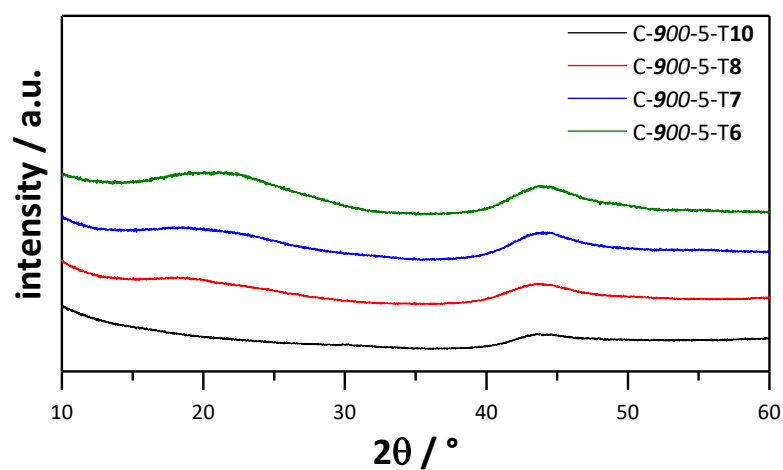


Figure A.11: P-XRD pattern of the activated carbons with different activation temperatures and a semi-carbonization temperature of 900 °C.

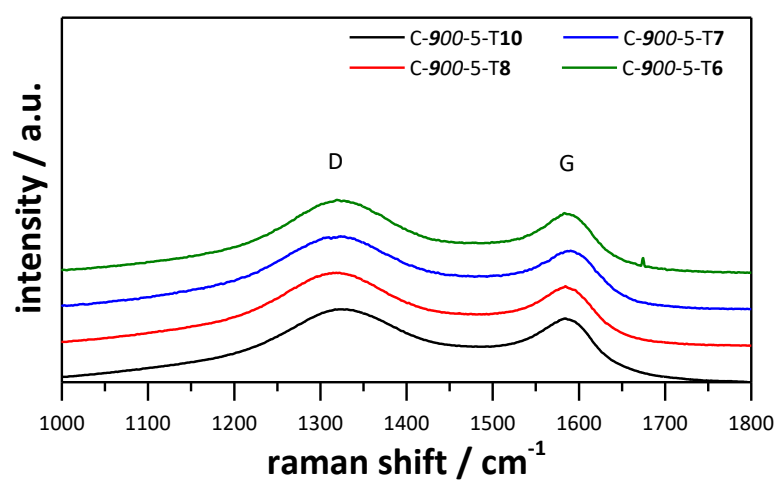


Figure A.12: Raman spectra of activated carbons with different activation temperatures and a semi-carbonization temperature of 900 °C.

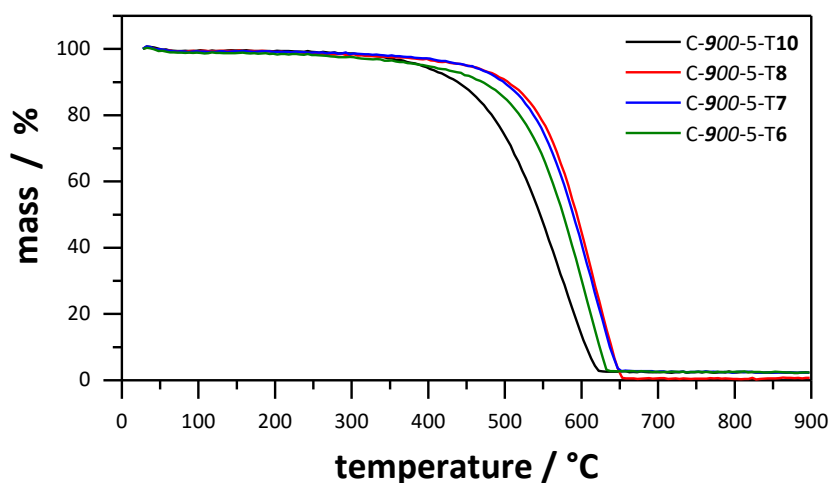


Figure A.13: Results of the thermogravimetry of the activated carbons with different activation temperatures and a semi-carbonization temperature of 900 °C. The samples were heated to 900 °C in air steam with a flow rate of 50 mL·min⁻¹.

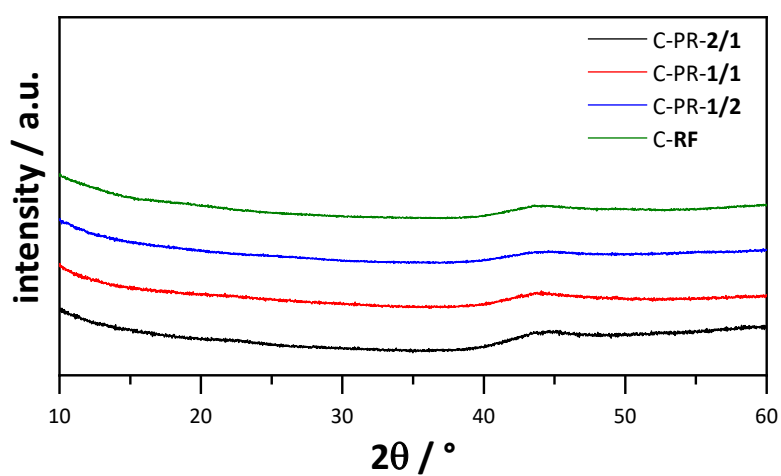


Figure A.14: P-XRD pattern of the activated carbons with different ratios of phenol and resorcinol for the resin precursor polymerization.

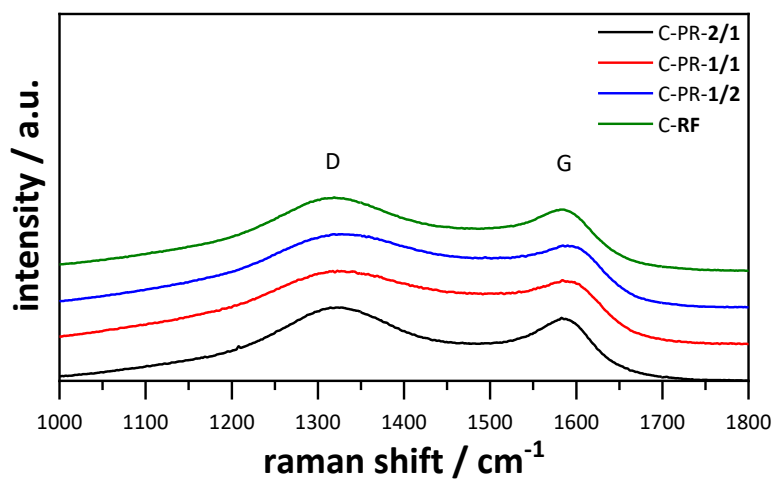


Figure A.15: Raman spectra of the activated carbons with different ratios of phenol and resorcinol for the resin precursor polymerization.

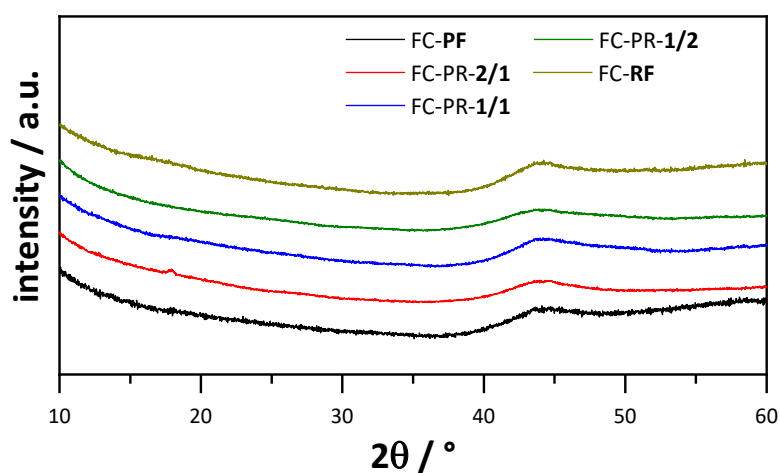


Figure A.16: P-XRD pattern of the activated carbons with different FC-cross-linked formaldehyde resins, synthesized with ratios of phenol and resorcinol.

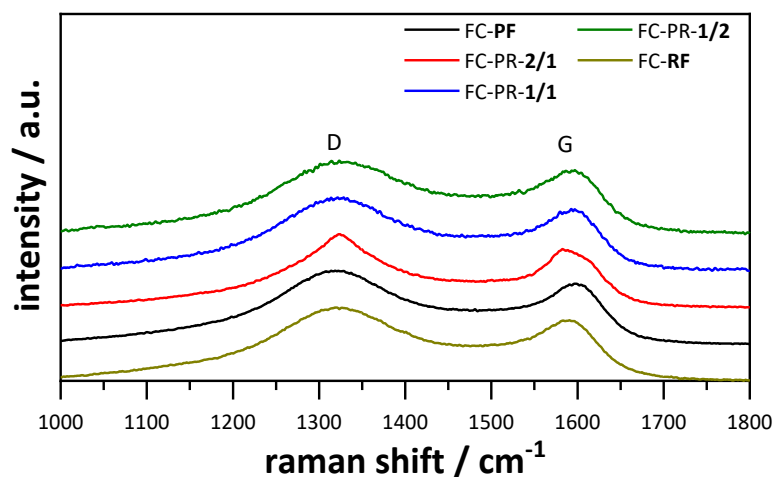


Figure A.17: Raman spectra of the activated carbons with different FC-cross-linked formaldehyde resins, synthesized with different ratios of phenol and resorcinol.

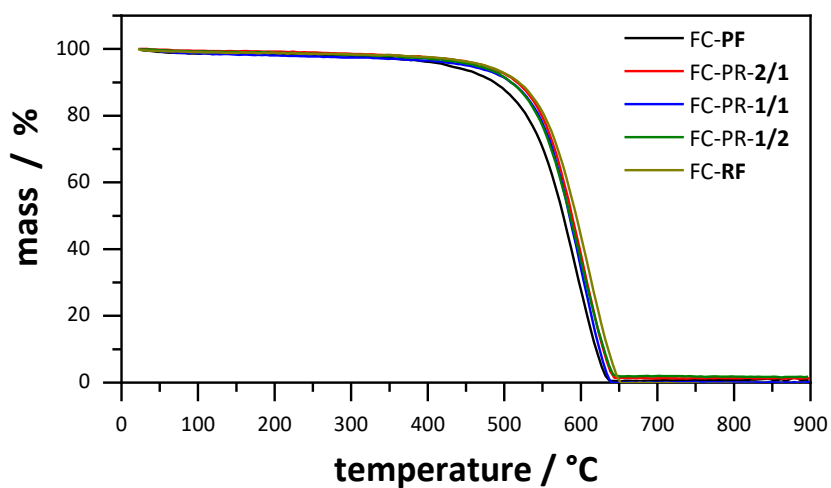


Figure A.18: Results of the thermogravimetry of the activated carbons with different FC-cross-linked formaldehyde resins, synthesized with different ratios of phenol and resorcinol. The samples were heated to 900 $^{\circ}\text{C}$ in air steam with a flow rate of 50 $\text{mL}\cdot\text{min}^{-1}$.

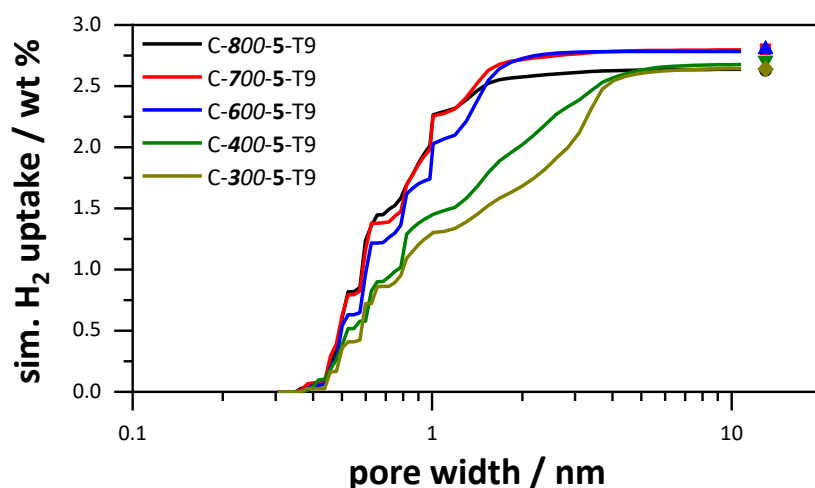


Figure A.19: Simulated cumulative gravimetric hydrogen uptake capacity at 77 K and 1 bar in dependence of the pore width of the carbons synthesized with different semi-carbonization temperatures and their respective measured uptake capacity in comparison.

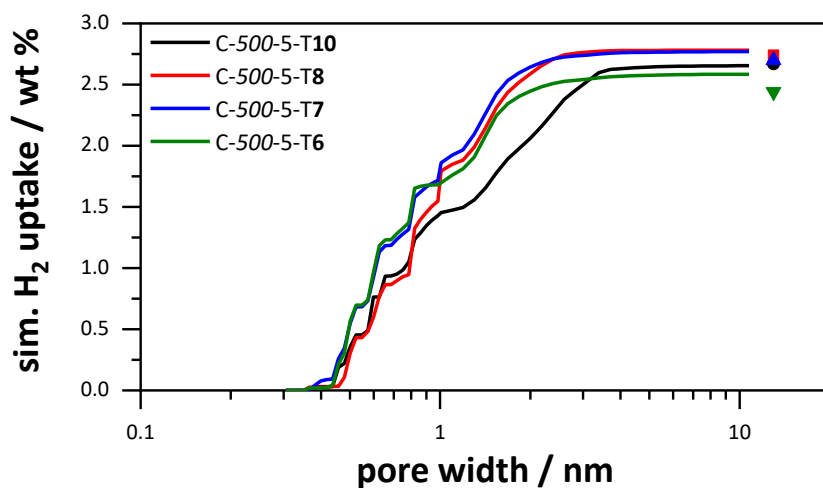


Figure A.20: Simulated cumulative gravimetric hydrogen uptake capacity at 77 K and 1 bar in dependence of the pore width of the carbons synthesized with different activation temperatures and their respective measured uptake capacity in comparison.

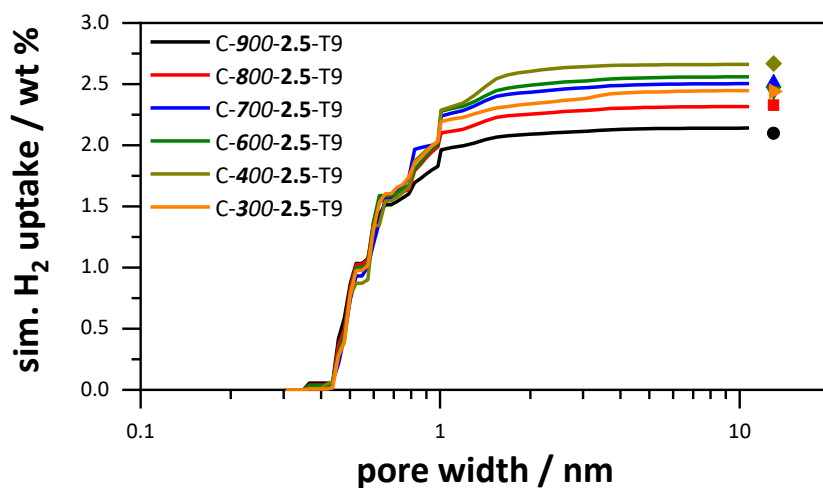


Figure A.21: Simulated cumulative gravimetric hydrogen uptake capacity at 77 K and 1 bar in dependence of the pore width of the carbons synthesized at different semi-carbonization temperatures and a KOH/carbon ratio of 2.5 and their respective measured uptake capacity in comparison.

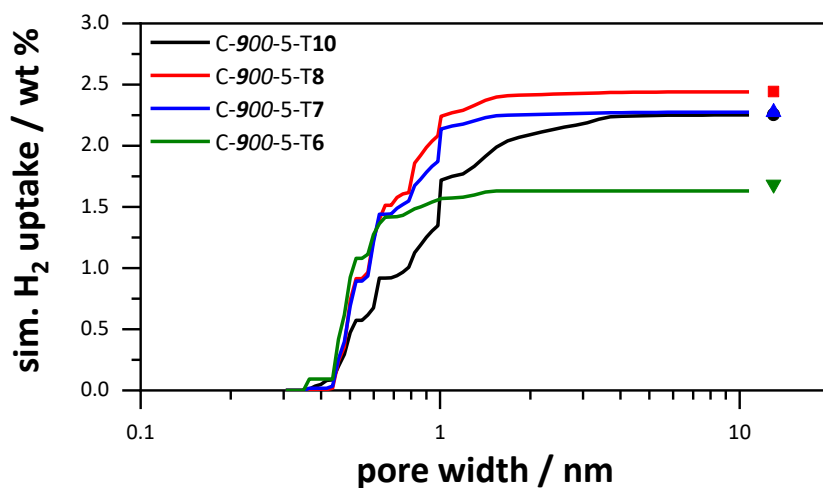


Figure A.22: Simulated cumulative gravimetric hydrogen uptake capacity at 77 K and 1 bar in dependence of the pore width of the carbons synthesized at different activation temperatures and a fixed semi-carbonization temperature of 900 °C and their respective measured uptake capacity in comparison.

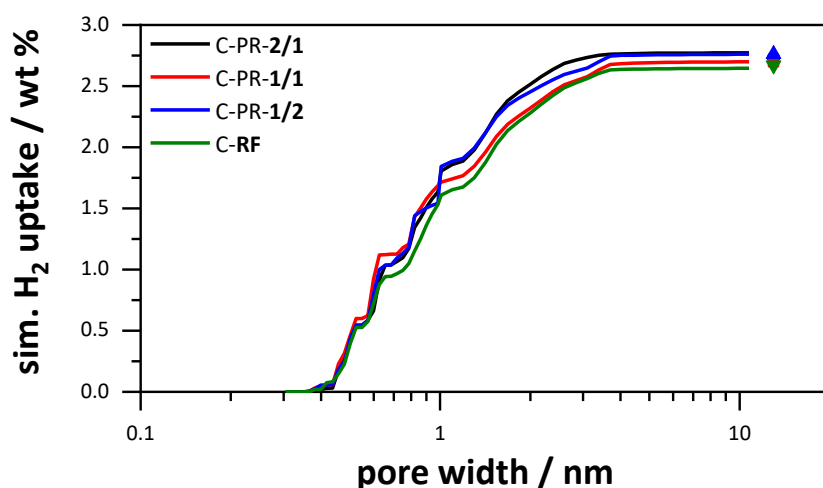


Figure A.23: Simulated cumulative gravimetric hydrogen uptake capacity at 77 K and 1 bar in dependence of the pore width of the carbons synthesized from formaldehyde resins with different phenol/resorcinol ratios for the polymerization and their respective measured uptake capacity in comparison.

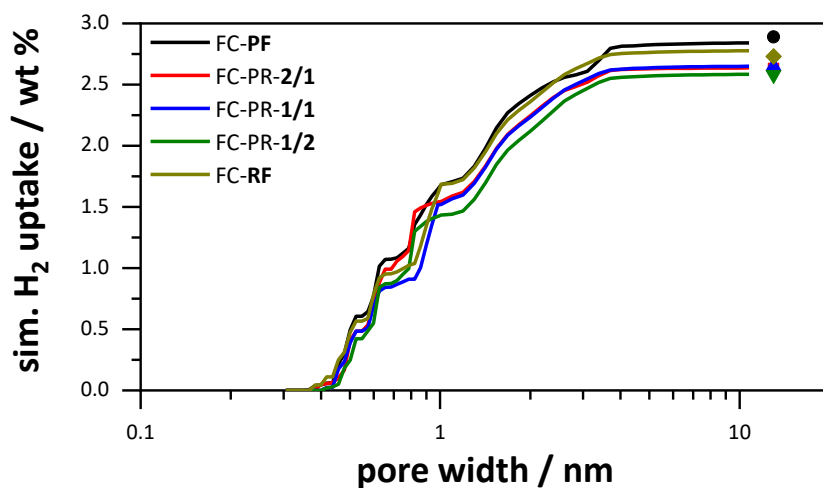


Figure A.24: Simulated cumulative gravimetric hydrogen uptake capacity at 77 K and 1 bar in dependence of the pore width of the carbons synthesized from FC-cross-linked formaldehyde resins with different phenol/resorcinol ratios for the polymerization and their respective measured uptake capacity in comparison.

Table A.1: Specific capacitance calculated from discharge tests of EDLC prepared from the carbon samples in 1 M TEABF₄/ACN and the simulated specific capacitance values based on the modified ESDCC model.




















	$C_{sp} / \text{F} \cdot \text{g}^{-1}$ measured	ESDCC modified	
		$C_{sp} / \text{F} \cdot \text{g}^{-1}$ simulated	percentage deviation
C-500-5-T10	147.6	155.2	+5 %
C-500-5-T8	164.1	172.0	+5 %
C-500-5-T7	154.4	162.4	+5 %
C-500-5-T6	140.3	133.5	−5 %
C-900-2.5-T9	9.4	70.1	+87 %
C-800-2.5-T9	82.7	79.7	−4 %
C-700-2.5-T9	109.5	105.2	−4 %
C-600-2.5-T9	118.2	103.5	−14 %
C-400-2.5-T9	123.0	114.8	−7 %
C-300-2.5-T9	89.9	91.7	+ 2%
C-900-5-T10	121.7	127.8	+5 %
C-900-5-T8	89.5	96.0	+7 %
C-900-5-T7	84.8	93.7	+10 %
C-900-5-T6	1.9	24.1	+92 %
C-PR-2/1	148.9	161.2	+8 %
C-PR-1/1	129.2	143.3	+10 %
C-PR-1/2	154.4	162.4	+5 %
C-RF	144.2	151.2	+5 %
FC-PF	148.5	143.3	−4 %
FC-PR-2/1	138.9	149.7	+7 %
FC-PR-1/1	147.5	147.5	±0 %
FC-PR-1/2	144.9	154.7	+6 %
FC-RF	142.9	149.0	+4 %

Table A.2: Measured gravimetric hydrogen uptake capacities of the carbon samples at 77 K and 1 bar and the simulated capacities based on the modified model.


















	Uptake / wt % measured	Modified model	
		Uptake / wt % simulated	percentage deviation
C-500-5-T10	2.67	2.67	±0 %
C-500-5-T8	2.74	2.88	+5 %
C-500-5-T7	2.64	2.73	+3 %
C-500-5-T6	2.34	2.60	+10 %
C-900-2.5-T9	2.10	2.14	+2 %
C-800-2.5-T9	2.33	2.33	±0 %
C-700-2.5-T9	2.51	2.50	±0 %
C-600-2.5-T9	2.44	2.59	+6 %
C-400-2.5-T9	2.67	2.60	−2 %
C-300-2.5-T9	2.44	2.43	±0 %
C-900-5-T10	2.25	2.25	±0 %
C-900-5-T8	2.44	2.44	±0 %
C-900-5-T7	2.28	2.28	±0 %
C-900-5-T6	1.68	1.65	−2 %
C-PR-2/1	2.73	2.74	±0 %
C-PR-1/1	2.70	2.69	±0 %
C-PR-1/2	2.76	2.76	±0 %
C-RF	2.67	2.66	±0 %
FC-PF	2.89	2.82	−3 %
FC-PR-2/1	2.63	2.64	±0 %
FC-PR-1/1	2.65	2.65	±0 %
FC-PR-1/2	2.58	2.64	+2 %
FC-RF	2.59	2.69	+4 %
C-300-5-T9	2.64	2.66	+1 %
C-400-5-T9	2.71	2.65	+2 %
C-500-5-T9	2.73	2.66	−3 %
C-600-5-T9	2.80	2.74	−2 %
C-700-5-T9	2.80	2.76	−1 %
C-800-5-T9	2.63	2.63	±0 %
C-900-5-T9	2.49	2.56	+3 %
C-500-2.5-T9	2.70	2.70	±0 %
C-500-8-T9	2.66	2.66	±0 %
C-500-1-T9	2.30	2.32	+1 %

9.2 Safety

Table A.3: Used substances, their H- and P-statements as well as disposal procedure

<i>Substance</i>	<i>Pictogram</i>	<i>H-Statement</i>	<i>P-Statement</i>	<i>Disposal</i>
<i>Acetone</i>	 	255-319-336-EU066	210-233-305+351+338	1
<i>Acetonitrile</i>	 	225-332-312-319	210-305+351+338-403+234	1
<i>Aluminum tri-chloride</i>		314	260-280-301+330+331-305+351+338-309-310	3
<i>Aluminum foil</i>	No hazardous substance according to GHS			5
<i>Argon</i>		280	403	-
<i>Ethanol</i>		225	210	1
<i>Hydrofluoric acid (40%)</i>	 	300+310+330-314	280-301+330+331-302+352-304+340-305+351+338	6
<i>Formaldehyde</i>	  	330-301-311-314-351-317	301+310-303+361+353-305+351+338-361-405	1
<i>Potassium carbonate</i>		315-319-335	302+352-305+351+338	4
<i>Potassium hydroxide</i>	 	314-302-290	280-301+330+331-305+351+338	4
<i>Carbon</i>	No hazardous substance according to GHS			5
<i>Carbon dioxide</i>		280	403	-
<i>N-Methyl-2-pyrrolidon</i>	 	360D-319-335-315	201-308+313-305+351+338-302+350	1
<i>Sodium hydroxide</i>		290-314	280-301+330+331-305+351+338	4

9 Appendix

<i>Phenol</i>	  	301-311-314-331-341-373	280-301+330+331-302+352-305+351+338-309-310	1
<i>Phenol-Formaldehyde-Resin</i>	Substance not fully studied			1
<i>Phenol-Formaldehyde-Polymer</i>	Substance not fully studied			5
<i>Phloroglucinol</i>		341-361	281	1
<i>Phloroglucinol-Formaldehyde-Polymer</i>	Substance not fully studied			5
<i>Polystyrene</i>	No hazardous substance according to GHS			5
<i>Polyvinylidenfluoride</i>	Substance not fully studied			5
<i>Resorcinol</i>	 	302-315-319-400	273-302+352-305+351+338	1
<i>Resorcinol-Formaldehyde-Polymer</i>	Substance not fully studied			5
<i>Hydrochloric acid (37%)</i>	  	314-335	260-301+330+331-303+361+353-405-501	3
<i>Nitrogen</i>		280	403	-
<i>Carbon tetrachloride</i>	 	301+311+331-351-372-412-420	261-273-280-301+310-311	2
<i>Tetraethylammonium tetrafluoroborate</i>	 	318-315-335	280-305+351+338-302+352-313	2
<i>Zinc chloride</i>	  	302-314-335-410	273-280-301+330+331-305+351+338-309+310	3

Disposal

- 1 If necessary dissolved in the container for halogen-free organic solvents.
- 2 If necessary dissolved in the container for halogen-containing organic solvents.
- 3 If necessary dissolved in container HCl-/H₂SO₄-containing acids.
- 4 If necessary dissolved in container for inorganic bases.
- 5 Disposal in solids container for contaminated substances.
6. Precipitate with CaCl₂ and dispose of in container for wastes containing hydrofluoric acid.

Table A.4: CMR substances

substance	carcinogenic	mutagenic	reprotoxic
Formaldehyde	1B	2	
N-Methyl-2-pyrrolidon			1B
Phenol		2	
Carbon tetrachloride	2		2

9.3 Publications

R. HEIMBÖCKEL, S. KRAAS, F. HOFFMANN, M. FRÖBA

Insights into the influence of pore size and surface area of activated carbons on the energy storage of electric double layer capacitors with a new potentially universally applicable capacitor model

Phys. Chem. Chem. Phys. **2019**, 21, 3122-3133.

R. HEIMBÖCKEL, S. KRAAS, F. HOFFMANN, M. FRÖBA

Increase of porosity by combining semi-carbonization and KOH activation of formaldehyde resins to prepare high surface area carbons for supercapacitor applications

Appl. Surf. Sci. **2018**, 427, 1055-1064.

R. ORTMANN, C. PASEL, M. LUCKAS, R. HEIMBÖCKEL, S. KRAAS, J. BENTGENS, M.

FRÖBA, D. BATHEN

Adsorption and Desorption of Isoflurane on Carbonaceous Adsorbents and Zeolites at Low concentrations in Gas Phase

Chem. Eng. Data **2016**, 61, 686-692.